Fakultät für Maschinenwesen
Lehrstuhl für Aerodynamik und Strömungsmechanik

Modeling Interfacial Instabilities with the Level Set Method

Jakob Wolfgang Josef Kaiser

Vollständiger Abdruck der von der Fakultät für Maschinenwesen der Technischen Universität München zur Erlangung des akademischen Grades eines

Doktor-Ingenieurs (Dr.-Ing.)

genehmigten Dissertation.

Vorsitzende: Prof. Dr.-Ing. Katrin Wudy

Prüfer der Dissertation:

1. Prof. Dr.-Ing. Nikolaus A. Adams
2. Prof. Dr. Iskander Akhatov

Die Dissertation wurde am 17.11.2020 bei der Technischen Universität München eingereicht und durch die Fakultät für Maschinenwesen am 30.03.2021 angenommen.

jakob.kaiser@tum.de

Typesetting LaTeX

Abstract

The aim of this work is to extend level-set modeling approaches for multi-phase flows with interfacial instabilities, coupled with spatial and temporal adaptation techniques. The multi-phase flow configurations investigated in this work - aerodynamic fragmentation and liquid-solid phase transition - are important for a wide range of technical applications, such as the manufacturing of drugs and additive manufacturing, respectively. Multi-phase flows often pose multi-scale problems. Therefore, spatial and temporal adaptation techniques are required to solve such problems efficiently. Special care is necessary to suppress potentially incurred numerical errors, which may result in decreasing numerical stability and perturbed simulation results. Therefore, the first goal of this work is to improve the overall stability and efficiency of such adaptation techniques for multi-phase flows, in particular of local time-stepping schemes. Second, the model is applied to perform high-resolution simulations of aerodynamic fragmentation in the high-Weber number regime, i.e. shear induced entrainment, with focus on interface deformation dynamics and the interaction of the interface with the surrounding flow field. The goal of this study is to improve the understanding of the breakup mechanism, since the physical mechanisms driving the transient interface deformation remain to this day unknown. Third, the applied level-set approach is extended to model non-equilibrium liquid-solid phase transition of pure melts. Crystal growth exhibits physical interface instabilities - side branching and tip splitting -, which influence the resulting microstructure. An accurate numerical model allows for prediction and, in the long term, targeted modification of the crystal growth process, thus mechanical part properties resulting from this microstructure could be controlled.

This publication-based thesis is structured as follows:
An overview of multi-phase flows and corresponding modeling approaches is given in chapter 1, together with an introduction to aerodynamic fragmentation and non-equilibrium liquid-solid phase transition. In chapter 2, the fundamental mathematical and numerical models are presented. The main findings of this work are presented in chapter 3, together with a short literature review of the issues addressed in each publication. A list of all publications, including peer-reviewed journal publications and conference proceedings, is provided in chapter 4. The conclusion is given in chapter 5. The main publications are attached in the appendix.

Kurzfassung

Das Ziel dieser Arbeit ist die Weiterentwicklung der level-set basierten Modellierung von Mehrphasenströmungen unter Einfluss von Grenzflächen-Instabilitäten, gekoppelt mit räumlich und zeitlich adaptiven Verfahren. Die Strömungskonfigurationen, die in dieser Arbeit untersucht werden - sekundärer Tropfenzerfall und Kornwachstum -, sind für viele technische Anwendungsbereiche relevant, beispielsweise die Medikamenten-Herstellung oder die additive Fertigung. Solche Strömungen stellen Mehr-Skalen Probleme dar, weswegen adaptive Verfahren für zeitliche und räumliche Diskretisierung für eine effiziente Lösung benötigt werden. Adaptive Verfahren können jedoch zu numerischen Fehlern führen, die die Stabilität der Methode potentiell reduzieren. Das erste Ziel dieser Arbeit ist daher die Verbesserung der Stabilität und Effizienz solcher adaptiver Verfahren. Der Fokus liegt hierbei auf lokalen Zeitschrittverfahren. Das zweite Ziel ist die Untersuchung von sekundärem Tropfenzerfall bei hohen Weber-Zahlen mit hoch-aufgelösten Simulationen. Besonderer Fokus liegt dabei auf der transienten Grenzflächenverformung sowie der Interaktion der Grenzfläche mit dem umgebenden Strömungsfeld. Das Ziel dieser Untersuchungen ist, ein besseres Verständnis des Tropfenzerfalls zu erlangen. Das dritte Ziel dieser Arbeit ist die Weiterentwicklung des Modells auf die Berechnung von Kornwachstum. Solche Kristallwachstumsvorgänge sind physikalisch instabil. Instabilitäten können sowohl an der Spitze des Kristalls als auch an der Seite auftreten. Diese Instabilitäten beeinflussen das resultierende Kristallgefüge. Eine numerische Modellierung ermöglicht somit die Vorhersage des Kristallwachstums und langfristig auch deren gezielte Beeinflussung. Somit können mechanische Bauteileigenschaften durch die kristalline Mikrostruktur gezielt erzeugt werden.

Diese publikationsbasierte Dissertation ist wie folgt aufgebaut:
Ein Überblick über Mehrphasenströmungen und entsprechende Modellierungsansätze erfolgt in Kapitel 1, zusammen mit einer Übersicht über sekundären Tropfenzerfall und Kornwachstum. Die grundlegenden mathematischen und numerischen Modelle werden in Kapitel 2 vorgestellt. Die Ergebnisse der Publikationen in dieser Arbeit werden in Kapitel 3 erörtert. Es erfolgt ebenfalls ein kurzer Überblick über bisherige Ergebnisse, wobei die offenen Punkte herausgearbeitet werden, die in der jeweiligen Publikation untersucht werden. Eine tabellarische Übersicht über alle Publikationen, die im Rahmen dieser Arbeit veröffentlicht wurden (Zeitschriftenaufsätze, Konferenzbeiträge), erfolgt in Kapitel 4. In Kapitel 5 werden die Ergebnisse zusammengefasst. Die Zeitschriftenaufsätze sind im Anhang aufgeführt.

Danksagung

Die vorliegende Arbeit ist während meiner Zeit als wissenschaftlicher Mitarbeiter am Lehrstuhl für Aerodynamik und Strömungsmechanik von 2016 bis 2020 entstanden. Ich möchte mich an dieser Stelle ganz herzlich bei all jenen bedanken, die mich auf diesem Weg begleitet und unterstützt haben und somit in besonderer Weise zum Erfolg meiner Arbeit beigetragen haben.

Zuallererst möchte ich mich bei meinem Doktorvater, Prof. Dr.-Ing. Adams, für seine Betreuung und die vielen Möglichkeiten, die er mir während meiner Zeit am Lehrstuhl geboten hat, bedanken. Dank der guten Atmosphäre am Lehrstuhl konnte ich mich in den vergangenen fünf Jahren am Lehrstuhl sowohl fachlich als auch persönlich in einer Art weiterentwickeln, die ich zu Beginn meiner Dissertation nicht für möglich gehalten hätte. Insbesondere möchte ich mich auch für die vielen Freiheiten bedanken, die mir sowohl einen Auslandsaufenthalt in Russland als auch das Kennenlernen des Innersten der TUM ermöglicht haben.

I want to thank my co-examiner and host at Skoltech, Prof. Akhatov, for the great opportunity to spent three months at CDMM. The time in Moscow was among the most interesting in my life, and I had the chance to develop new skills and learn more about Russia, its people, and its culture. I am glad that I had the opportunity to come back to CDMM regularly after my stay, and hope that this continues in the future. I also want to thank all my colleagues at Skoltech - Yulia, Oleg, Iurii, Eldar, Alexei, and Evgeny - for the great time I had in Russia. Thanks for introducing me to the Russian way of life, and welcoming me back after my stay.

Mein besonderer Dank gilt allen Kollegen am Lehrstuhl, insbesondere der Nanoshock-Gruppe. Vielen Dank, Stefan, für die Betreuung und Unterstützung in den vergangenen fünf Jahren. Vielen Dank an Josef, Nico, Nils, Thomas, Christian, Deniz, Aaron, Ludger, Felix, Naeimeh, Vladimir und Aleksandr, dass ihr die Zeit am Lehrstuhl zu etwas Besonderem und insbesondere die immer wiederkehrenden Code- und Cluster-Probleme mit regelmäßigen Kaffee-Pausen überbrückt habt.

Natürlich möchte ich mich auch bei allen Studenten bedanken, die in den vergangenen Jahren ihre Arbeiten bei mir geschrieben haben, insbesondere bei Rim, Franziska, Antonia, Fabian, Alex, Daniel, Chris und Paul. Ihr habt mich mit eurer Arbeit sehr unterstützt, und es freut mich ganz besonders, dass einige von euch trotz meiner Betreuung den Weg als Doktoranden an den Lehrstuhl gefunden haben.

Einen großen Anteil an meiner Arbeit hatte meine Familie - meine Eltern, mein Bruder und Franzi, und natürlich Theo, der insbesondere die letzten eineinhalb Jahre ein großartiger Motivator war. Vielen Dank für eure Unterstützung und eure Ermutigungen in den vergangenen Jahren. Ebenso möchte ich mich bei Clara, Dani, Daniel und Martin bedanken, die mich seit vielen Jahren in München begleitet haben.

Mein größter Dank gilt natürlich Sonja. Ohne deine Geduld, deine regelmäßigen Hinweise auf meine Work-Life Balance und natürlich ohne das gemeinsame Schreiben am Ende hätte das alles nicht geklappt. Vielen Dank, dass du meine schlechte Laune am Abend und meine gute Laune am Morgen auch weiterhin erträgst!

Contents

1 Introduction **1**
- 1.1 Motivation . . . 1
- 1.2 Aerodynamic fragmentation . . . 3
- 1.3 Liquid-solid phase transition under non-equilibrium conditions . . . 6

2 Mathematical and Numerical Model **9**
- 2.1 Governing equations . . . 9
- 2.2 Spatial and temporal discretization . . . 10
  - 2.2.1 Spatial discretization . . . 10
  - 2.2.2 Temporal discretization . . . 11
- 2.3 Multi-phase treatment . . . 12
  - 2.3.1 Level-set approach . . . 12
  - 2.3.2 Sharp-interface method with conservative interface interaction . . . 13
  - 2.3.3 Ghost-fluid method . . . 16
  - 2.3.4 Small-cell mixing . . . 18
- 2.4 Spatial and temporal adaptivity . . . 18
  - 2.4.1 Wavelet-based multiresolution scheme . . . 18
  - 2.4.2 Block-based data structure . . . 20
  - 2.4.3 Local time-stepping approach . . . 20

3 Accomplishments **23**
- 3.1 Adaptive local time-stepping . . . 23
- 3.2 Cylindrical droplet breakup at high Weber number . . . 26
- 3.3 Conservative sharp-interface method for liquid-solid phase transition . . . 28

4 List of Publications **31**
- 4.1 Peer-reviewed journal publications . . . 31
- 4.2 Conference proceedings . . . 31

5 Discussion with Respect to the State of the Art and Conclusion **33**

A Peer-Reviewed Journal Publications **35**
- A.1 An adaptive local time-stepping scheme for multiresolution simulations of hyperbolic conservation laws . . . 35
- A.2 Investigation of interface deformation dynamics during high-Weber number cylindrical droplet breakup . . . 52
- A.3 A semi-implicit conservative sharp-interface method for liquid-solid phase transition . . . 70

B Copyright Permission for Adopted and Reproduced Material **87**

Nomenclature

Greek letters:

α	Volume fraction
$\Delta\Gamma$	Interface segment
ϵ_u	Kinetic coefficient
γ	Ratio of specific heats
κ	Interface curvature
μ	Shear viscosity
Ω	Domain
ϕ	Level set
ψ	Phase-field parameter
ρ	Density
σ	Surface-tension coefficient
τ	Pseudo time-step size
ε	Multiresolution error
ε_{ref}	Multiresolution reference error

Roman letters:

Δt	Time-step size
Δx	Cell size
$\dot{\mathbf{q}}$	Heat flux
$\dot{m}$	Mass flow rate
$\mathbf{F}$	Flux vector
$\mathbf{I}$	Identity matrix
$\mathbf{n}$	Normal vector
$\mathbf{S}$	Shear rate tensor
$\mathbf{T}$	Cauchy stress tensor

$\mathbf{U}$ Conservative state vector

$\mathbf{X}$ Interface exchange fluxes

A Cell-face aperture

c Specific heat capacity

D Dimension

d Multiresolution details

D_0 Initial drop diameter

E Total energy

e Internal energy

e_∞ Fitting parameter for the equation of state

e_t Fitting parameter for the equation of state

k Thermal conductivity

L Latent heat

l Multiresolution level

l_{max} Maximum multiresolution level

Oh Ohnesorge number

P Fluid prime state

p Pressure

p_∞ Fitting parameter for the equation of state

R Specific gas constant

Re Reynolds number

T Temperature

t Time

u Velocity

V Cell volume

We Weber number

Super- and subscripts:

$(*)$ Quantity at first intermediate stage of time integration

$(**)$ Quantity at second intermediate stage of time integration

(i, j, k) Property of cell (i, j, k)

(n)	Quantity at time (n)
$+$	Positive fluid
$-$	Negative fluid
Γ	Interface-related property
$\mathbf{u}$	Convective
μ	Viscous
g	Gas phase
k	Thermal
l	Liquid phase
l	Multiresolution level
m	Property at melt point
n	Property in interface-normal direction
s	Solid phase
T	Threshold
v	Vapour

Chapter 1

Introduction

1.1 Motivation

In this thesis, I give an overview about my research on the numerical modeling of multi-phase flow problems with interfacial instabilities using the level-set approach. The focus has been on three topics: improving the efficiency of adaptation techniques to simulate such multi-scale flow problems, the numerical investigation of aerodynamic fragmentation, and the modeling of crystal growth with level set.

My research is based on the German Research Foundation (Deutsche Forschungsgesellschaft, DFG) project *Direkte numerische Simulation des aerodynamischen Zerfalls flüssiger Tropfen* (direct numerical simulation of aerodynamic fragmentation of liquid drops; project number 277161739). This project is on multi-phase flow modeling with focus on phenomenological investigations of interface instabilities, and in particular how these instabilities result in various breakup mechanisms of liquid drops in an ambient air flow.

Such multi-phase flows are at the core of many phenomena in nature and in technical applications, and are essential for every-day life. They include the mixture of gas and small water droplets in breathable air, the air-water surface of the oceans, the mixture of fuel and oxidizer in combustion engines, or simply stirring milk foam in a cappuccino. All of them have in common that at least two different aggregate states - gaseous, liquid, or solid - occur.

Various schemes exist for the categorization of multi-phase systems. Based on the structure of the interface, three systems may be distinguished: separated-phase, mixed-phase, and dispersed systems [22]. *Separated-phase* systems comprise two immiscible phases, which are separated by a clearly defined geometrical interface. Modeling of such systems requires an accurate representation of the phase interface. To the contrary, in *dispersed* systems, one phase is dispersed in a continuous phase, and the potential change of the interface structure is commonly neglected. The dispersed phase may be modeled by tracking single particles, or by assuming a homogeneous or heterogeneous mixture of the two phases. The *mixed-phase* systems describe the gradual transition from separated-phase to dispersed systems. The required accuracy of the interface structure directly impacts the choice of mathematical and numerical models, since they differ in their applicability to obtain an accurate prediction of the flow-field behavior for each of these multi-phase systems.

Two frames-of-reference are commonly distinguished in mathematical and numerical modeling of flow problems: Lagrangian and Eulerian. In the Lagrangian frame-of-reference, the evolution of the state variables is analyzed for a fluid element which moves in space and time. For a numerical model, this means that the nodes of the computational grid may alter their location in time. An example is the Smoothed Particle Hydrodynamics (SPH) approach, which evolves the governing equations on a set of moving particles. Examples for the simulation of multi-phase flows are given, e.g., in Monaghan [84]. Yet, due to stability and convergence issues, the use of SPH in the Computational-Fluid-Dynamics (CFD) community is still limited [2]. More widespread is the use of mesh-based approaches with fixed grid points in the Eulerian frame-of-reference, where the evolution of the state variables is analyzed for a

control volume at a fixed location. As the fluid passes through a parcel, its state variables change. The focus of this work is on multi-phase modeling in the Eulerian frame-of-reference.

For dispersed systems, the structures of the dispersed phase are usually too fine to be resolved on the numerical grid. Thus, such systems may be resolved by an averaged or homogenized description of the flow field, or by tracking the dispersed phase in a Lagrangian description. If the two phases can both be resolved reasonably well on the numerical mesh, appropriate interface-tracking or capturing schemes are required. Three classes of schemes may be distinguished [111]: In the first scheme, the interface is explicitly represented by adapting the mesh to the progressing evolution front [46, 89]. These methods have yet limitations when the interface is strongly distorted. The second class maintains a fixed mesh and tracks the evolving interface by Lagrangian marker particles [34, 63]. However, these so-called interface-tracking schemes are also limited for growing interface distortion. In the third class, the interface is implicitly tracked by an Eulerian order function. The most common variants of these interface-capturing schemes are the volume-of-fluid, phase-field, and level-set methods.

The volume-of-fluid method introduces the volume fraction α as additional order parameter which needs to be evolved in time. The phase interface is smeared across multiple cells for which $0 < \alpha < 1$, i.e. those cells which are occupied by more than one fluid. It is therefore also denoted as diffuse-interface method. First proposed by Hirt and Nichols [47] for incompressible flows, it has been further extended to compressible flows [69, 110]. In its original form, conservation equations for mass, momentum, energy, and volume fraction need to be solved for each phase separately. Simplified models have been developed, which rely, for example, on four [69] or five [3] equations only. These reduced models assume, e.g., an infinite relaxation, i.e. that pressure and velocity immediately reach equilibrium at the interface. Yet, the major drawbacks of such diffuse-interface methods are that the interface cannot be exactly determined, and that excessive numerical diffusion may deteriorate results. For an extensive review on the volume-of-fluid approach, the reader is referred to Saurel and Pantano [111].

Similarly to the volume-of-fluid method, the phase-field method is in general a diffuse-interface method [134]. It applies one or multiple phase-field parameters as order parameter, which indicate the phase state at the location of interest. Therefore, it has been widely used for multi-phase simulations including phase change, in particular for solidification processes in the material sciences. Comprehensive reviews have been published by Boettinger et al. [11] and Tonks and Aagesen [134]. The evolution of the phase-field parameters is driven by thermodynamic forces causing phase change. One or multiple conservative and non-conservative parameters may be used to describe the interface. The Cahn-Hilliard equation [12] describes the evolution of conservative parameters, and the Allen-Cahn equation [4] that of non-conservative parameters. For example, the solidification of multi-component alloys may be represented by multiple conserved variables C_i describing the concentration of constituent i and multiple non-conserved variables ψ describing the location of the grain boundaries [134]. The variable ψ is an order parameter with, e.g., $0 \leq \psi \leq 1$, where $\psi = 0.5$ denotes the interface and $0 < \psi < 1$ the transition zone between the phases. This width of this transition zone is a model parameter. Yet, the application of phase-field models on a specific problem is complicated by multiple barriers. In particular, the model requires extensive calibration of multiple model parameters for quantitative predictions, and the interface needs high spatial resolution for accurate solutions [134].

This difficulty is overcome by the level-set method, which is a sharp-interface method. The interface can be accurately located on the underlying numerical grid, which allows for computing geometrical parameters, such as the surface normal or the curvature, in a straightforward manner. The level-set method was first introduced by Osher and Sethian [93]. The interface is represented implicitly as the zero contour of a higher dimensional function, the level set ϕ. The level-set function is defined as a signed distance function, i.e. the sign of the level set indicates the fluid, and the absolute value the normal distance to the interface. This property is used to compute interface normal and mean curvature as gradient and Laplacian of the level-set field, respectively. The level-set field is evolved by solving an advection equation, and requires subsequent reinitialization to maintain the signed-distance property [124]. The level-set method has been widely used to solve incompressible and compressible multi-fluid

flow configurations, such as the melting of metal powder in laser-based additive manufacturing [145], to simulate near-wall bubble collapse as model of extracorporeal shock wave lithotripsy [73], or to predict growth rates of interfacial instabilities [91]. For an extensive review, the reader is referred to Gibou et al. [32]. Note that in its general form, the level-set method is limited to model the interaction of two fluids. An extension to an arbitrary number of fluids is focus of ongoing research (e.g. [94, 95]).

The level-set method requires appropriate fluid-field boundary conditions to be prescribed on the interface, which represents an irregular free boundary. This is paramount to accurately determining the exchange of mass, momentum, and energy across the interface. The ghost-fluid method (GFM) of Fedkiw et al. [23] has been commonly used, since it allows for a sharp treatment of the interface. It relies on defining ghost values for each fluid on the opposite side of the interface, and the interaction problem degenerates to determining these ghost values. The major advantage of the ghost fluid method is its sharp treatment of the boundary conditions at the interface, since each fluid can be treated separately. A detailed overview of the GFM is given by Gibou et al. [32]. Further simplifying the determination of ghost-fluid values, Hu et al. [51] introduced a conservative interface-interaction method by deriving explicit interface exchange terms. These terms are based on the solution of a two-material Riemann problem at the interface. Ghost cells are solely required for single-phase discretization of cell-face fluxes near the phase interface, and can be obtained by extrapolation from the real fluid. The interface-exchange terms may include inviscid [51], viscous [81], and thermal [98] exchange, as well as mass transfer due to evaporation [78]. The main advantages of the method are that the flux-based formulation enforces conservation at the interface, and that including additional physical effects is straightforward. Therefore, this method is used in the following.

This work aims at extending level-set based models for separated-phase systems with focus on interfacial instabilities, and includes three contributions:

1. A novel temporal adaptation approach with local time stepping for the multiresolution scheme of Harten [42], which improves stability and robustness as compared to previous local time-stepping approaches, see section 3.1.

2. High-resolution numerical simulation results of aerodynamic fragmentation, which highlight the influence of near-interface flow field phenomena on the interface deformation, see section 3.2.

3. A novel model to simulate liquid-solid phase transition with the conservative interface-interaction approach, see section 3.3.

In the following two sections 1.2 and 1.3, a short introduction is given on the physical phenomena investigated within the scope of my work: aerodynamic fragmentation of liquid drops and solidification of undercooled melts. In chapter 2, the governing equations and the fundamental approach of the level-set model are introduced, including spatial and temporal adaptation techniques, which are required for the efficient solution of such multi-scale problems. In the subsequent chapter 3, I give an overview of the novelties presented in the three publications included in this work. Each of these publications is motivated with a short review on the state-of-the-art, indicating the particular issues that have been overcome in the corresponding publication. A list of all publications is provided in section 4. Finally, chapter 5 gives a conclusion and outlook on possible future work.

1.2 Aerodynamic fragmentation

The fragmentation of coherent liquid structures into smaller sized, disjointed, stable fragments is a complex multi-phase flow problem. A concise review on fragmentation processes is offered by Villermaux [136], highlighting the relevance of this feature for a variety of applications, such as internal liquid-fuel combustion engines and manufacturing of medical drugs. To optimize the outcome of such applications, a-priori knowledge of the dependency of final fragment sizes on control parameters such as the flow velocity is desirable.

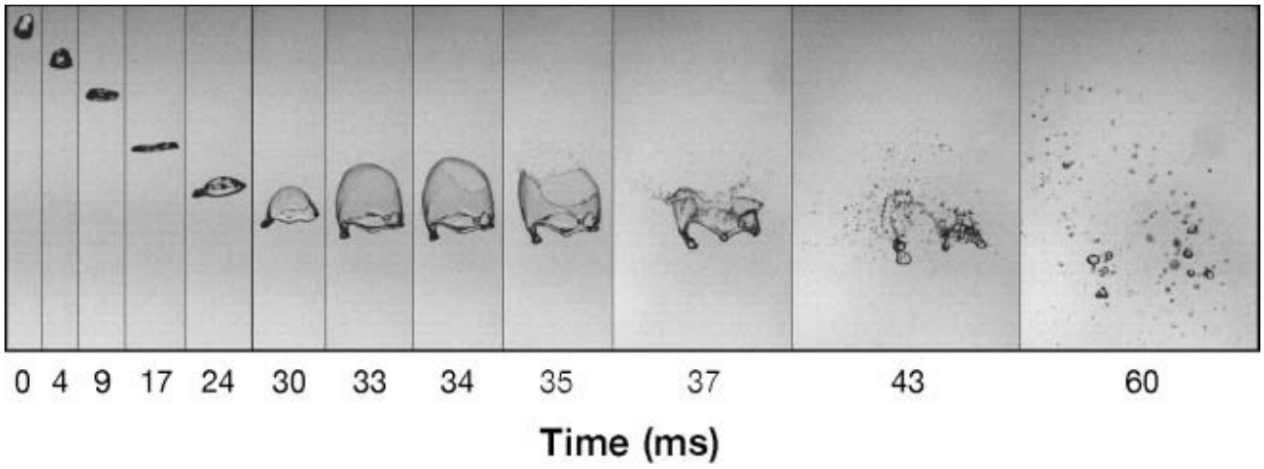

Figure 1.1: Fragmentation of a liquid drop with formation of a characteristic bag-like structure. Reprinted from Villermaux [136] with permission from Annual Reviews.

In general, two types of liquid fragmentation are distinguished. Primary atomization describes the breakup of a bulk fluid into drops. Secondary atomization denotes then the fragmentation of these drops into smaller droplets, and is investigated in this work. An example for the aerodynamic fragmentation of a drop is given in Fig. 1.1. The deformation process is initiated by a relative velocity of the liquid drop with regard to the ambient gas phase, and shows several distinct stages: the flattening of the drop ($t \leq 17\,\text{ms}$), the formation of the bag ($17\,\text{ms} < t \leq 33\,\text{ms}$), and, finally, the breakup of the bag and the rim into smaller fragments ($t > 33\,\text{ms}$). This so-called bag breakup is one potential breakup mode of secondary atomization. The relative velocity of the drop with regard to the ambient gas phase drives the deformation and, finally, fragmentation of the drop. Viscous forces delay the deformation, and capillary forces force the drop to maintain a spherical shape. This motivates the description of the breakup mechanism by a set of non-dimensional numbers, see Guildenbecher et al [38]:

- the Weber number

$$We = \frac{\rho_g u_g^2 D_0}{\sigma} \tag{1.1}$$

  denoting the ratio of inertial to capillary forces,

- the Ohnesorge number

$$Oh = \frac{\mu_l}{\sqrt{\rho_l D_0 \sigma}} \tag{1.2}$$

  describing the ratio of viscous forces to capillary forces in the liquid phase,

- the Reynolds number

$$Re = \frac{\rho_g u_g D_0}{\mu_g} \tag{1.3}$$

  giving the ratio of inertial forces to viscous forces in the gas phase, and

- the density ratio

$$\tilde{\rho} = \frac{\rho_l}{\rho_g} \tag{1.4}$$

  relating the densities of liquid and gas phase.

In the equations given above, ρ denotes the density, u the velocity, D_0 the initial drop diameter, σ the surface tension coefficient, μ the shear viscosity, and the subscripts l and g denote the liquid and gas phase, respectively.

Historically, the Weber number We was considered to be the characteristic parameter for liquid drop breakup [132]. Hinze [45] found that breakup occurs only once the Weber number exceeds a critical value, i.e. once inertial forces strongly exceed capillary forces to cause the breakup of the droplet. Since this critical Weber number We_{crit} varies with the liquid viscosity, the Ohnesorge number Oh is expected to affect the breakup mechanism as well. Therefore, breakup-mode classification considers We and Oh in later works [38, 49, 99]. Typically, five breakup modes have been distinguished: vibrational, bag, multimode, sheet-stripping or shear, and catastrophic. Their dependency on We and Oh is shown in Fig. 1.2. For $Oh < 10^{-1}$, the Weber number ranges for these breakup modes are basically constant while changing drastically for increasing Oh. Note that the transition from shear to catastrophic breakup is not shown in this graph, since recent work states that this regime was erroneously derived from shadowgraph visualizations [130, 132].

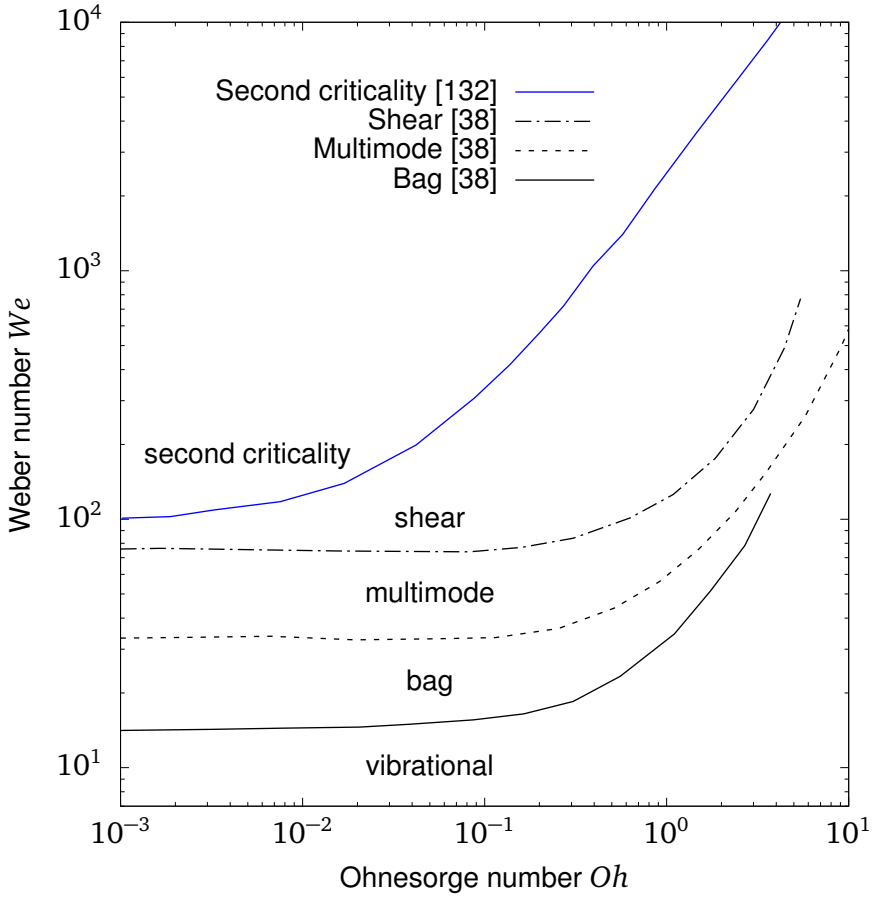

Figure 1.2: Breakup-mode evolution for changing We and Oh. The solid black line denotes the transition from vibrational to bag breakup, the dashed line from bag to multimode brekaup, and the dash-dotted line from multimode to sheet-stripping breakup [38]. The solid blue line denotes the onset of the second criticality, i.e. the onset of shear induced entrainment [132].

This traditional classification has been reformulated by Theofanous [132]. He suggested a system based on the dominating interface instability mechanisms. During its deformation, the drop is subjected to Rayleigh-Taylor instabilities near the upstream stagnation point, and Kelvin-Helmholtz instabilities at the equator [96]. These two instability modes relate to the Rayleigh-Taylor piercing (RTP) and the shear-induced entrainment (SIE) breakup regimes, respectively. Assuming small Ohnesorge numbers, $Oh \ll 1$, RTP is the dominating instability mechanisms for small Weber numbers. After the flattening of the drop, surface waves grow on the upstream side near the stagnation point, and ambient gas pierces the

liquid mass of the drop. This results in the well-known formation of the bag, which eventually disintegrates [131]. The transition from RTP to SIE starts for $We \sim 100$, and is completed for $We \sim 1000$. For larger Weber numbers, SIE is the terminal instability mode [130]. This breakup regime evolves as rapid deformation process, that is characterized by Kelvin-Helmholtz instabilities near the droplet equator, which occur already during the flattening stage of the drop. These shear forces result in the peeling of a water sheet from the rim of the drop, which later fragments due to capillary breakup. For increasing Oh, the transition from RTP to SIE is delayed to larger We, see also Fig. 1.2.

Despite extensive research on secondary atomization, many aspects of the breakup process remain unknown due to the overall complexity of the problem. In particular, a concise understanding of the interaction of Rayleigh-Taylor and Kelvin-Helmholtz instabilities, and of the interplay of flow field and interface deformation are aspects of ongoing research. In this context, numerical simulations appear as helpful tool, since small spatial and temporal scales limit detailed experimental investigations. A concise literature review on previous numerical investigations of aerobreakup and a summary of my contributions are given in section 3.2.

1.3 Liquid-solid phase transition under non-equilibrium conditions

Phase transition from liquid to solid state under non-equilibrium conditions is a complex multi-phase phenomenon. The inherent instability of the process complicates its experimental and numerical investigation. Growth patterns are thereby dominated by the interplay of macroscopic thermodynamics and microscopic interface dynamics. Most commonly known is dendritic growth, due to its ubiquity in nature, e.g. in the growth of a snowflake. The name dendritic thereby derives from the Greek δενδρον, which translates to tree and refers to the branched structure of the resulting crystal.

In his seminal work, Ivantsov [58] investigated the shape of solidification fronts propagating into undercooled melts, i.e. melts at a temperature below the equilibrium temperature of the material. He derived that for heat-diffusion dominated processes, the solidification front is parabolic. The model is, however, limited since it provides information only on the product of the tip radius and the velocity of such a dendrite, but does not allow for specifying each one of them separately. This poses the selection problem of dendritic growth, since the Ivantsov solution indicates a family of potential dendrites for an arbitrary undercooling. Glicksman et al. [33] showed that each undercooling corresponds to exactly one tip radius and velocity. Langer and Müller-Krumbhaar [75–77, 87] derived a solution to find the selected tip radius and velocity as marginally stable solution that is stabilized by surface tension. They found that dendrites experience tip-splitting instabilities once tip curvature and velocity drop below critical val-

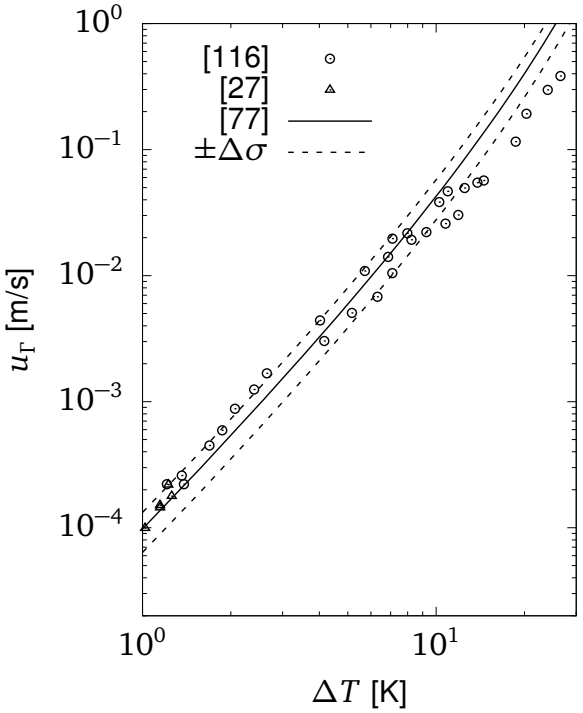

Figure 1.3: Analytical solution of Langer and Müller-Krumbhaar [77] with stability range $\pm\Delta\sigma$, and experimental results of Furukawa and Shimada [27] and Shibkov et al. [116]. The x-axis denotes the undercooling of the melt, and the y-axis the tip velocity of the dendrite.

ues. Side-branching instabilities occur if the dendrite is too fast and too sharp. These two interfacial instabilities finally result in the typically known tree-like pattern that emerges during dendritic solidification. Their model shows excellent agreement with experimental reference data for heat-diffusion dominated growth. Yet, once interface kinetics dominate the growth process, their theory overestimates the growth velocity, see Fig. 1.3. The diagram shows values for the solidification of water, which experiences kinetics-driven solidification starting from approximately $\Delta T > 10\,\mathrm{K}$.

A comprehensive model of liquid-solid phase transition needs to accurately consider the interplay of microscopic interface forces with the macroscopic diffusion field to predict the interface instabilities correctly. The microscopic forces at the interface are mathematically described by the Gibbs-Thomson relation, expressing an equilibrium between minimal bulk and surface energies [5]. It reads

$$T_\Gamma = T_m - \frac{\sigma T_m}{\rho L}\kappa - \epsilon_u ||\mathbf{u}_\Gamma|| \tag{1.5}$$

with T_Γ denoting the temperature at the phase interface, T_m the equilibrium melting temperature at a flat interface, L the latent heat, κ the interface curvature, ϵ_u the kinetic coefficient, and $\mathbf{u}_\Gamma$ the local velocity of the phase front. Surface tension effects, modeled by the second term on the right-hand-side of eq. (1.5), are intended to model the local equilibrium of a curved interface, where the free energy of solid and melt are the same [10]. The last term of eq. (1.5), $\epsilon_u ||\mathbf{u}_\Gamma||$, describes the microscopic dynamics of surface kinetics, to model the inherent non-equilibrium of the phase-change process. Both surface-tension and kinetic effects may experience strong anisotropies. The surface-tension anisotropy reflects that the interface orientation affects the average bonding energy between atoms. Similarly, the kinetic anisotropy represents that the interface orientation also affects the attach rate of atoms to the interface [10]. These anisotropies may result in preferred crystal-growth directions. In addition, the melt temperature may vary with the local solute concentration for alloys, and can be determined from a phase diagram. This is intentionally neglected in this work, since the model is limited to the solidification of pure melts.

The macroscopic, thermodynamic behavior is modeled by the Stefan condition

$$\dot{m}\left[L + (T_\Gamma - T_m)(c_l - c_s)\right] = (k_s \nabla_n T_s - k_l \nabla_n T_l) \cdot \mathbf{n}_\Gamma \,. \tag{1.6}$$

Here, $\dot{m}$ denotes the solidified mass of melt, c the specific heat capacity, k the thermal conductivity, $\nabla_n T$ the interface-normal temperature gradient, and the indices s and l denote the solid and melt, respectively. The Stefan condition describes the thermal equilibrium at the advecting phase front. The heat released by the phase-change process (left-hand-side) has to be in equilibrium with the heat flux from the interface into solid and liquid phase (right-hand-side). The square brackets on the left-hand-side thereby include heat release due to latent heat (first term) and varying specific heat capacities in solid and melt (second term). The interplay of macroscopic and microscopic effects is taken into account on the right-hand-side of eq. (1.6), since the interface temperature, eq. (1.5), influences the local interface-normal temperature gradients $\nabla_n T_{s/l}$.

Including the Gibbs-Thomson relation (1.5) and the Stefan condition (1.6) in a numerical model requires an accurate representation of the interface. Reconstructing the surface curvature in eq. (1.5) and the interface-normal temperature gradient in eq. (1.6) are of particular interest, since both directly affect the interface propagation and, therefore, the evolution of interface instabilities. In section 3.3, a review on previous modeling approaches and a summary of my contributions are given.

Chapter 2

Mathematical and Numerical Model

2.1 Governing equations

The multi-phase problems investigated within this work are governed by the full Navier-Stokes equations including viscous, capillary, and thermal effects. The governing equations read in vector notation

$$\frac{\partial \mathbf{U}}{\partial t} + \nabla^T \cdot \mathbf{F}_\mathbf{u} + \nabla^T \cdot \mathbf{F}_\mu + \nabla^T \cdot \mathbf{F}_k = \mathbf{X}. \tag{2.1}$$

Here,

$$\mathbf{U} = \begin{bmatrix} \rho \\ \rho\mathbf{u} \\ E \end{bmatrix}, \qquad \mathbf{F}_\mathbf{u} = \begin{bmatrix} \mathbf{u}\rho \\ \rho\mathbf{u}\otimes\mathbf{u} + p\mathbf{I} \\ \mathbf{u}(E+p) \end{bmatrix}, \qquad \mathbf{F}_\mu = \begin{bmatrix} 0 \\ \mathbf{T} \\ \mathbf{T}\cdot\mathbf{u} \end{bmatrix} \quad \text{and} \quad \mathbf{F}_k = \begin{bmatrix} 0 \\ \mathbf{0} \\ k\nabla T \end{bmatrix}$$

denote the vector of conservative states, the convective flux vector, the viscous flux vector, and the thermal flux vector, respectively, t the time, $\mathbf{u}$ the velocity vector, p the pressure, $\mathbf{I}$ the identity matrix, $\mathbf{T}$ the Cauchy stress tensor, and E the total energy

$$E = \rho e + \frac{1}{2}\rho\mathbf{u}\cdot\mathbf{u}, \tag{2.2}$$

composed of the internal energy (ρe) and the kinetic energy ($1/2\rho\mathbf{u}\cdot\mathbf{u}$). The Cauchy stress tensor for Newtonian fluids follows from

$$\mathbf{T} = 2\mu\mathbf{S} - \frac{2}{3}\mu(\nabla\cdot\mathbf{u})\mathbf{I}, \tag{2.3}$$

where

$$\mathbf{S} = \frac{1}{2}\left(\nabla\mathbf{u} + (\nabla\mathbf{u})^T\right) \tag{2.4}$$

is the shear-rate tensor. The vector $\mathbf{X}$ denotes exchange terms between two fluids including capillary, viscous, and thermal effects. Note that eq. (2.1) can be simplified for different flow configurations by suppressing single physical effects.

The governing equations need to be closed by an equation of state (EOS), which relates the internal energy with pressure, density, and temperature. The stiffened-gas equation of state

$$p = (\gamma - 1)\rho e - \gamma p_\infty \tag{2.5}$$

has been widely used for numerical simulations of compressible fluid flow with multiple immiscible fluids. The parameters γ and p_∞ are empirically determined fitting parameters, and allow for applying this EOS for both gases and liquids. For $p_\infty = 0$, the stiffened-gas EOS degenerates to the ideal-gas EOS.

Yet, the drawback of this EOS is the inaccurate prediction of the temperature field. If heat transfer is considered, an extended stiffened-gas equation of state needs to be applied as given by Hawker and Ventikos [43] with

$$p + (\gamma + 1)p_\infty = (\gamma + 1)\rho(e + e_\infty) \tag{2.6}$$

and

$$RT = \frac{p + p_\infty}{\rho} + (\gamma + 1)e_t\rho^{\gamma+1}, \tag{2.7}$$

where e_∞ and e_t are additional empirically determined fitting parameters, and R is the gas constant.

2.2 Spatial and temporal discretization

2.2.1 Spatial discretization

The governing equations (2.1) are discretized in the domain Ω with a finite volume approach. The domain is split into a set of finite volumes $\Omega_{(i,j,k)}$, $\bigcup_{(i,j,k)\in\mathbb{N}^3}\Omega_{(i,j,k)} = \Omega$, which are equivalent to a computational cell with cell volume $V_{(i,j,k)}$. In each cubic cell (i,j,k) with edge length Δx, the discretized governing equations (2.1) without interface exchange terms $\mathbf{X}$ read as

$$\begin{aligned}
\frac{\partial\overline{\mathbf{U}}_{(\mathbf{i},\mathbf{j},\mathbf{k})}}{\partial t} &= \mathcal{D}\left(\overline{\mathbf{U}}_{(i,j,k)}\right) \qquad (2.8)\\
&= \frac{(\mathbf{F}_{\mathbf{u},(i-1/2,j,k)} - \mathbf{F}_{\mathbf{u},(i+1/2,j,k)}) + (\mathbf{F}_{\mu,(i-1/2,j,k)} - \mathbf{F}_{\mu,(i+1/2,j,k)}) + (\mathbf{F}_{k,(i-1/2,j,k)} - \mathbf{F}_{k,(i+1/2,j,k)})}{\Delta x}\\
&+ \frac{(\mathbf{F}_{\mathbf{u},(i,j-1/2,k)} - \mathbf{F}_{\mathbf{u},(i,j+1/2,k)}) + (\mathbf{F}_{\mu,(i,j-1/2,k)} - \mathbf{F}_{\mu,(i,j+1/2,k)}) + (\mathbf{F}_{k,(i,j-1/2,k)} - \mathbf{F}_{k,(i,j+1/2,k)})}{\Delta x}\\
&+ \frac{(\mathbf{F}_{\mathbf{u},(i,j,k-1/2)} - \mathbf{F}_{\mathbf{u},(i,j,k+1/2)}) + (\mathbf{F}_{\mu,(i,j,k-1/2)} - \mathbf{F}_{\mu,(i,j,k+1/2)}) + (\mathbf{F}_{k,(i,j,k-1/2)} - \mathbf{F}_{k,(i,j,k+1/2)})}{\Delta x}.
\end{aligned}$$

The overbar indicates cell-averaged quantities, i.e.

$$\overline{\mathbf{U}}_{(\mathbf{i},\mathbf{j},\mathbf{k})} = \frac{1}{V_{(i,j,k)}}\int_{\Omega_{(i,j,k)}} \mathbf{U}d\Omega, \tag{2.9}$$

and $\mathcal{D}\left(\overline{\mathbf{U}}_{(i,j,k)}\right)$ denotes the divergence of the numerical flux functions $\mathbf{F}$. The flux functions $\mathbf{F}$ are evaluated at the cell patches, balancing in- and outgoing fluxes. Since the flux going out of one cell is identical to the flux going into the neighbor cell, the finite volume discretization is exactly conservative - the global mass, momentum and energy are conserved. For a more detailed discussion on the finite-volume method, the reader is referred to the standard references of LeVeque [79] and Toro [135].

The fifth-order weighted essentially non-oscillatory (WENO) scheme of Jiang and Shu [60] is applied for convective flux reconstruction of eq. 2.8. Is uses a weighted combination of multiple third-order stencils S_i, see Fig. 2.1. A fifth-order accurate reconstruction with low dissipation is obtained in smooth flow regions. In regions with large local gradients, a non-linear combination of these third-order stencils is applied. The weight of each stencil is computed from smoothness indicators of all stencils. For a more detailed introduction to WENO schemes and further developments,

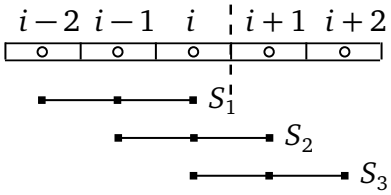

Figure 2.1: Stencil selection for the fifth-order WENO scheme of Jiang and Shu [60].

the reader is referred to Fu et al. [25]. Note that in this work the WENO scheme for convective flux-reconstruction is applied on the characteristic projection of the convective term based on the work of Roe [103]. For a description of this "Roe" solver, the reader is referred to the original publication of Roe [103]. Reconstruction of viscous and thermal fluxes requires computation of velocity and temperature gradients. In this work, these gradients are computed by the second order central differencing scheme

$$\left.\frac{\partial U}{\partial x}\right|_{i+1/2} = \frac{U_{i+1} - U_i}{\Delta x} \tag{2.10}$$

and the fourth order central differencing scheme

$$\left.\frac{\partial U}{\partial x}\right|_{i+1/2} = \frac{27(U_{i+1} - U_i) - (U_{i+2} - U_{i-1})}{24\Delta x}. \tag{2.11}$$

2.2.2 Temporal discretization

Strongly-stable Runge-Kutta schemes are used to evolve the finite volume discretization of the governing equations (2.8) in time, see Gottlieb and Shu [36]. We apply both the second-order formulation

$$\begin{aligned} \overline{\mathbf{U}}^{(*)} &= \overline{\mathbf{U}}^{(n)} + \Delta t^{(n)} \mathcal{D}\left(\overline{\mathbf{U}}^{(n)}\right) \\ \overline{\mathbf{U}}^{(n+1)} &= \overline{\mathbf{U}}^{(n)} + \frac{1}{2}\Delta t^{(n)}\left(\mathcal{D}\left(\overline{\mathbf{U}}^{(n)}\right) + \mathcal{D}\left(\overline{\mathbf{U}}^{(*)}\right)\right) \end{aligned} \tag{2.12}$$

and the third-order formulation

$$\begin{aligned} \overline{\mathbf{U}}^{(*)} &= \overline{\mathbf{U}}^{(n)} + \Delta t^{(n)} \mathcal{D}\left(\overline{\mathbf{U}}^{(n)}\right) \\ \overline{\mathbf{U}}^{(**)} &= \overline{\mathbf{U}}^{(n)} + \frac{1}{4}\Delta t^{(n)}\left(\mathcal{D}\left(\overline{\mathbf{U}}^{(n)}\right) + \mathcal{D}\left(\overline{\mathbf{U}}^{(*)}\right)\right) \\ \overline{\mathbf{U}}^{(n+1)} &= \overline{\mathbf{U}}^{(n)} + \frac{1}{6}\Delta t^{(n)}\left(\mathcal{D}\left(\overline{\mathbf{U}}^{(n)}\right) + \mathcal{D}\left(\overline{\mathbf{U}}^{(*)}\right)\right) + \frac{2}{3}\Delta t^{(n)}\mathcal{D}\left(\overline{\mathbf{U}}^{(**)}\right). \end{aligned} \tag{2.13}$$

The time-step size is controlled according to the Courant-Friedrichs-Lewy (CFL) condition. The advective time-step size follows

$$\Delta t^u = \frac{\Delta x}{\max\left(\sum_i |u_i \pm c|\right)}, \tag{2.14}$$

the time-step size due to viscous diffusion

$$\Delta t^\mu = \frac{3}{14}\frac{\Delta x^2 \rho}{\mu} \tag{2.15}$$

[124], and the time-step size due to thermal diffusion

$$\Delta t^k = \frac{1}{10}\frac{\Delta x^2 \rho c}{k}. \tag{2.16}$$

For multi-phase flows, also the time-step size due to surface waves at phase interfaces

$$\Delta t^\sigma = \sqrt{\frac{\rho_+ + \rho_-}{8\pi\sigma}\Delta x^3}, \tag{2.17}$$

with ρ_+ and ρ_- being the densities of the two fluids [124], and the time-step size based on the phase-interface advection velocity $\mathbf{u}_\Gamma$

$$\Delta t^\Gamma = \frac{\Delta x}{||\mathbf{u}_\Gamma||_\infty} \tag{2.18}$$

[64] are included. The global time-step size is finally determined with the global minimum of all time-step size limits

$$\Delta t = \text{CFL} \cdot \min\left(\Delta t^u, \Delta t^\mu, \Delta t^k, \Delta t^\sigma, \Delta t^\Gamma\right) \tag{2.19}$$

with CFL being the CFL-number. The maximum admissible CFL number depends on the temporal discretization scheme. In this work, varying CFL numbers are used depending on the simulated setup.

2.3 Multi-phase treatment

2.3.1 Level-set approach

In the level-set approach, the material interface is prescribed by the zero-contour of a multi-dimensional continuous function ϕ

$$\begin{aligned} \mathbf{x} \in \Omega_+ &\rightarrow \phi(\mathbf{x}) > 0\,, \\ \mathbf{x} \in \Omega_- &\rightarrow \phi(\mathbf{x}) < 0\,, \text{ and} \\ \mathbf{x} \in \Gamma &\rightarrow \phi(\mathbf{x}) = 0\,. \end{aligned}$$

An example is shown in Fig. 2.2 for a two-dimensional contracting circular interface, for which the corresponding multi-dimensional function is conically shaped. The circular interface contracts, thus the isoline (green) representing the cut of the multi-dimensional function (black) with the two-dimensional planar domain (blue) shrinks.

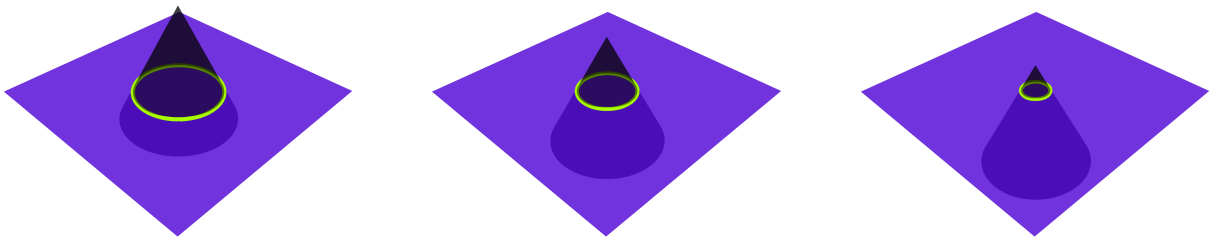

Figure 2.2: Multi-dimensional function for a two-dimensional contracting circular interface. The multi-dimensional level-set function is shown in black, the two-dimensional domain in blue, the zero-level-set marking the interface in green. From left to right, the circular interface shrinks.

The level-set function is chosen to have a signed-distance property $|\nabla\phi| = 1$, i.e. the absolute value of ϕ describes the normal distance of the cell center $\mathbf{x}$ to the interface Γ, and the level-set sign indicates the sub-domain the cell center belongs to. The signed-distance property allows for straightforward computation of geometrical characteristics of the interface. The interface normal unit vector $\mathbf{n}_\Gamma$ is the gradient of the level-set field, and the interface curvature κ the Laplacian of the level-set field

$$\mathbf{n}_\Gamma = \nabla\phi \quad \text{and} \quad \kappa = \nabla \cdot \nabla\phi\,. \tag{2.20}$$

The level-set field is evolved in time by solving the advection equation

$$\frac{\partial \phi}{\partial t} + \mathbf{u}_\Gamma \cdot \nabla\phi = 0 \tag{2.21}$$

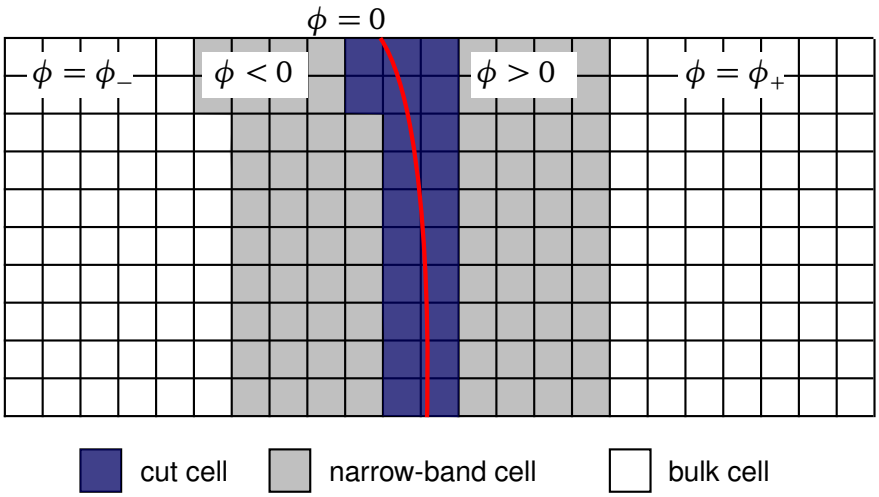

Figure 2.3: Cut cells and narrow band for a curved interface.

where $\mathbf{u}_\Gamma$ is the level-set advection velocity, i.e. the velocity at the interface. This velocity is obtained from the surrounding fluid field, which is further explained in section 2.3.2. When the level-set field is evolved in time, in general the signed-distance property is not maintained. Since the accuracy of the level-set method relies on the reconstruction of geometrical characteristics as described above, reinitializing the level-set field is paramount to maintain the accuracy of the overall scheme. Reinitialization is achieved by iterating the modified level-set advection equation

$$\frac{\partial \phi}{\partial \tau} + \text{sign}(\phi_0)\,(|\nabla \phi| - 1) = 0 \tag{2.22}$$

in pseudo-time τ to steady-state, where ϕ_0 is the level-set field prior reinitialization. In the second term on the left-hand side, the first contribution $\text{sign}(\phi_0)$ enforces that the level-set sign at each cell center does not alter during the iteration steps. The second contribution $(|\nabla \phi| - 1)$ enforces the linear distance property. Note that reinitializing cells that are cut by the interface requires special treatment. As shown e.g. by Russo et al. [109], performing reinitialization is necessary even in such cells to maintain the signed-distance property. Yet, it may alter the position of the interface and violate the conservation property of this method. This issue is addressed in section 3.3.

To improve the overall efficiency of the level-set approach, level-set related operations like advection or reinitialization are only performed within a small area around the interface. Three types of cells need to be distinguished:

- **Cut cells**: cells that are cut by the interface. Cut-cells are defined based on their level-set sign. If any neighboring cell has a different level-set sign than the target cell, this cell is assumed to be a cut cell.
- **Narrow-band cells**: cells which are located in a pre-defined distance to all cut-cells. The width of the narrow band depends on the chosen temporal and spatial discretization schemes.
- **Bulk cells**: cells that are far away from the interface, i.e. outside the narrow band. Note that the level-set value in the bulk cells can be chosen arbitrarily to have the correct sign, while the absolute value is irrelevant.

The cell types for a narrow-band width of four cells are shown exemplary for a curved interface in Fig. 2.3. This pre-selection drastically reduces the computational cost of the level-set method.

2.3.2 Sharp-interface method with conservative interface interaction

Determining the exchange between the two fluids across the interface is at the core of multi-phase flow modeling. In the level-set based conservative interface interaction method of Hu et al. [51], the interaction

is modeled by explicit exchange fluxes across the interface. The fluxes are related to the local interface segment of each cut cell. Otherwise, each fluid is solved separately, reconstructing local cell-face fluxes based on real and ghost-fluid cells (see section 2.3.3). This enforces the sharp-interface property of the method - the effect of the interface is limited to cut cells, but does not affect the flux reconstruction in cells that are not cut by the interface. The discretized Navier-Stokes equations, eq. (2.8), are extended by the interface exchange term

$$\frac{\partial\, \alpha_{(i,j,k)} \overline{\mathbf{U}}_{(i,j,k)}}{\partial\, t} = \mathcal{D}\left(\alpha_{(i,j,k)} \overline{\mathbf{U}}_{(i,j,k)}\right) + \frac{\mathbf{X}_{(i,j,k)}(\Delta\Gamma_{(i,j,k)})}{(\Delta x)^3} \tag{2.23}$$

where $\alpha_{(i,j,k)}$ denotes the volume fraction of cell (i,j,k) and $\Delta\Gamma_{(i,j,k)}$ the interface segment in this cell. A two-dimensional sketch of the cut-cell discretization with geometrical parameters is given in Fig. 2.4.

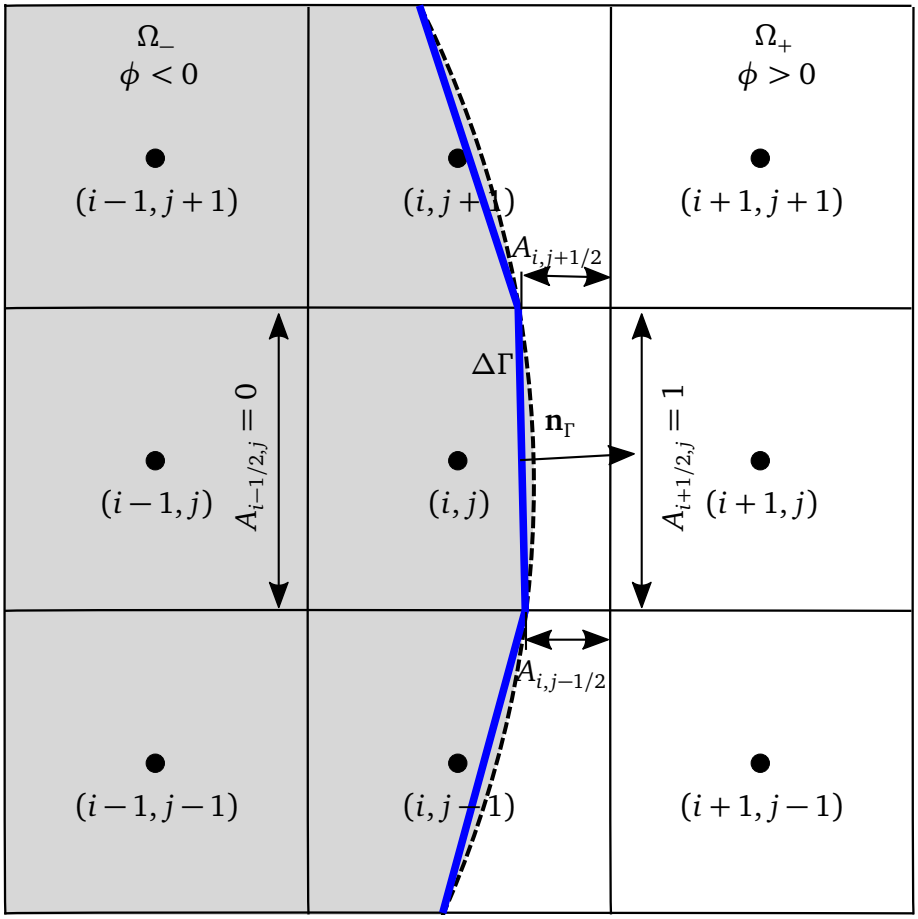

Figure 2.4: Two-dimensional schematic of cut-cell discretization. The interface is indicated by the dashed black line, the linearized interface obtained from the level set by the blue solid line.

The method of Hu et al. [51] relies on an accurate definition of interface states to calculate interface fluxes. For compressible flows without heat transfer, relevant interface states are the interface pressure p_Γ and the interface velocity $\mathbf{u}_\Gamma = u_\Gamma \mathbf{n}_\Gamma$. Hu and Khoo [50] suggested to solve a two-material Riemann problem to determine the interaction of the two fluids at the interface. Based on the method of characteristics, a formulation for the interface velocity and pressure can be found for each of the two fluids, which are then combined and solved iteratively using Newton's method. Alternatively, linearization results in explicit algebraic formulations for u_Γ and p_Γ, namely

$$u_\Gamma = \frac{\rho_- c_- u_- + \rho_+ c_+ u_+ + p_- - p_+}{\rho_+ c_+ + \rho_- c_-}, \tag{2.24}$$

$$p_\Gamma = \frac{\rho_- c_- p_+ + \rho_+ c_+ p_- + \rho_- c_- \rho_+ c_+ (u_- - u_+)}{\rho_+ c_+ + \rho_- c_-} \tag{2.25}$$

This model was extended for capillary effects by Luo et al. [81]. Assuming that the positive level set represents the surrounding fluid, and the negative level set the fluid inside the curved interface, the mechanical equilibrium at the interface follows from

$$\Delta p_\Gamma = p_{\Gamma,-} - p_{\Gamma,+} = \sigma\kappa\,. \tag{2.26}$$

The linearized interface states including the pressure jump now read as

$$u_\Gamma = \frac{\rho_- c_- u_- + \rho_+ c_+ u_+ + p_- - p_+ - \sigma\kappa}{\rho_+ c_+ + \rho_- c_-}, \tag{2.27}$$

$$p_{\Gamma,-} = \frac{\rho_- c_- (p_+ + \sigma\kappa) + \rho_+ c_+ p_- + \rho_- c_- \rho_+ c_+ (u_- - u_+)}{\rho_+ c_+ + \rho_- c_-}, \tag{2.28}$$

$$p_{\Gamma,+} = \frac{\rho_- c_- p_+ + \rho_+ c_+ (p_- - \sigma\kappa) + \rho_- c_- \rho_+ c_+ (u_- - u_+)}{\rho_+ c_+ + \rho_- c_-}. \tag{2.29}$$

Based on these interface states, Hu et al. [51] proposed interface-exchange terms for the Euler equations, and Luo et al. [81] for viscous exchange. This model includes momentum and energy transfer, but neglects mass transfer. Inviscid exchange due to the pressure forces between the two fluids are computed following

$$\mathbf{X}_{p,+} = -p_{\Gamma,+}[0,\, \Delta\Gamma\mathbf{n}_\Gamma,\, \Delta\Gamma\mathbf{n}_\Gamma \cdot \mathbf{u}_\Gamma]^T\,, \tag{2.30}$$

$$\mathbf{X}_{p,-} = p_{\Gamma,-}[0,\, \Delta\Gamma\mathbf{n}_\Gamma,\, \Delta\Gamma\mathbf{n}_\Gamma \cdot \mathbf{u}_\Gamma]^T\,. \tag{2.31}$$

The viscous exchange terms follow

$$\mathbf{X}_\mu = [0,\, \mathbf{T}_\Gamma \cdot \mathbf{n}_\Gamma \Delta\Gamma,\, (\mathbf{T}_\Gamma \cdot \mathbf{n}_\Gamma) \cdot \mathbf{u}_\Gamma \Delta\Gamma]^T \tag{2.32}$$

where the Cauchy stress tensor at the interface $\mathbf{T}_\Gamma$ is computed following eq. (2.3) using the harmonic mean of the viscosity

$$\mu_\Gamma = \frac{\mu_+ \mu_-}{\alpha\mu_- + (1-\alpha)\mu_+} \tag{2.33}$$

and real-fluid velocities from both fluids.

Piper [98] proposed an analogous model to include heat conduction across the interface. The interface exchange term reads

$$\mathbf{X}_\mathbf{k} = [0, \mathbf{0}, \dot{\mathbf{q}}_\Gamma \cdot \mathbf{n}_\Gamma]^T\,. \tag{2.34}$$

Here, $\dot{\mathbf{q}}_\Gamma$ denotes the interface heat flux, that is computed from real fluid temperatures on both sides of the interface.

Lauer et al. [78] extended the original method of Hu et al. to include mass transfer due to evaporation. Assuming that the liquid is the positive phase and vapor the negative phase, the exchange term of the vapor phase reads for evaporation

$$\mathbf{X}_{m,-} = \left[\dot{m}\Delta\Gamma,\, \dot{m}\Delta\Gamma\mathbf{u}_+,\, \dot{m}\Delta\Gamma\left(e_v + \frac{1}{2}||\mathbf{u}_+||^2\right) + p_\Gamma \Delta q^* \Delta\Gamma\right]^T, \tag{2.35}$$

and for condensation

$$\mathbf{X}_{m,-} = \left[\dot{m}\Delta\Gamma,\, \dot{m}\Delta\Gamma\mathbf{u}_-,\, \dot{m}\Delta\Gamma\left(e_v + \frac{1}{2}||\mathbf{u}_-||^2\right) + p_\Gamma \Delta q^* \Delta\Gamma\right]^T. \tag{2.36}$$

Here, $\dot{m}$ is the rate of evaporation or condensation, e_v the internal energy of vapor, and Δq^* the phase-change induced interface velocity. To satisfy conservation, the exchange term for the liquid phase follows from

$$\mathbf{X}_{m,+} = -\mathbf{X}_{m,-}\,. \tag{2.37}$$

For a detailed discussion of calculating the evaporation or condensation rate $\dot{m}$ and the phase-change induced interface velocity Δq^* the reader is referred to Lauer et al. [78]. Note that the evaporation model of Lauer et al. serves as foundation for the new interface-exchange model for liquid-solid phase transition presented in section 3.3.

The interface segment $\Delta\Gamma_{(i,j,k)}$ is computed from the level-set field, assuming the linear signed-distance property. The original two-dimensional approach of Hu et al. [51] is based on cell-face apertures A, see Fig. 2.4. Lauer et al. [78] proposed its three-dimensional formulation. For cubic cells, the interface segment follows from

$$\begin{aligned}\Delta\Gamma_{(i,j,k)} = (\Delta x)^2 \Big(\big(A_{(i+1/2,j,k)} - A_{(i-1/2,j,k)}\big)^2 \quad &+ \quad \big(A_{(i,j+1/2,k)} - A_{(i,j-1/2,k)}\big)^2 \\ &+ \quad \big(A_{(i,j,k+1/2)} - A_{(i,j,k-1/2)}\big)^2 \Big)^{1/2} . \end{aligned} \tag{2.38}$$

The volume fraction $\alpha_{(i,j,k)}$ is approximated with seven pyramids following Lauer et al. [78], which results for cubic cells in

$$\begin{aligned}\alpha_{(i,j,k)} = \quad & \frac{A_{(i-1/2,j,k)} + A_{(i+1/2,j,k)} + A_{(i,j-1/2,k)} + A_{(i,j+1/2,k)} + A_{(i,j,k-1/2)} + A_{(i,j,k+1/2)}}{6} \\ + \quad & \frac{\Delta\Gamma_{(i,j,k)} \phi_{(i,j,k)}}{3(\Delta x)^3} . \end{aligned} \tag{2.39}$$

2.3.3 Ghost-fluid method

The *ghost-fluid method* was originally introduced by Fedkiw et al. [23] for a sharp-interface model of the interaction of two fluids. The fundamental idea is to treat each fluid separately, and define ghost values at the opposite side of the interface for each fluid to model the interaction, thus enforcing the sharp-interface property of the method. The solution of the multi-phase problem degenerates to an accurate prescription of the ghost cells. The major challenges of the ghost-fluid method are the accurate definition of the ghost-fluid states, and the selection of ghost-fluid cells (or nodes in the finite difference scheme of Fedkiw et al. [23]).

In the original approach, the ghost-fluid states are determined to model the interaction of the two fluids at the interface. Thus, different types of fluid-fluid boundary conditions can be enforced by varying the ghost states. Details on the approach and further developments are discussed by Gibou et al. [32]. However, imposing ghost values may be challenging for flux-based boundary conditions [32]. This problem does not occur for the conservative interface-exchange model of Hu et al. [51], since interface exchange fluxes are prescribed to model the fluid-fluid interface interaction, see section 2.3.2. The definition of the ghost states reduces to an extrapolation of real-fluid states across the interface by iterating the extrapolation equation

$$\frac{\partial P}{\partial \tau} + \mathbf{n}_\Gamma \cdot \nabla P = 0 \tag{2.40}$$

to steady state. Here, P denotes the primitive fluid states, i .e. density ρ, pressure p, velocity $\mathbf{u}$, or temperature T, and τ a pseudo-time. Higher-order extrapolation schemes have been proposed by Aslam et al. [7].

In a finite-difference discretization as employed by Fedkiw et al., ghost fluid nodes are defined by the sign of the local level-set field. For the positive fluid $\phi > 0$, all nodes in the vicinity of the interface with $\phi < 0$ are ghost cells (and vice versa all nodes with $\phi > 0$ for the negative fluid). This definition has been applied not only to finite-difference schemes [20], but also to finite-volume schemes (e.g. [26, 30, 51, 73, 115]). However, it may alter the interface evolution due to erroneous fluid values at the interface. In the finite volume discretization, a cell that is cut by the interface may contain real fluid, even though the level-set sign at the cell center differs from the sign of the fluid. With the standard definition of the

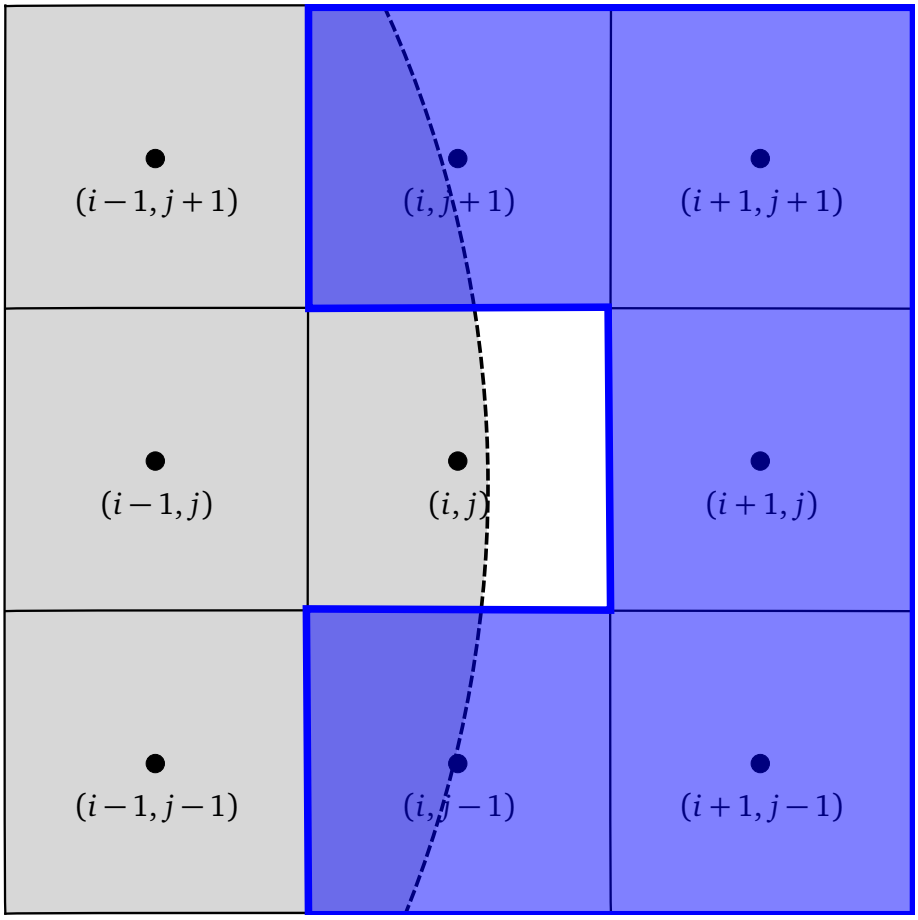

Figure 2.5: Ghost cells for a curved interface. Real fluid is shown in grey, cells tagged as ghost cells in blue.

ghost fluid, these cells are nevertheless treated as ghost cells, and their states are overwritten. This is shown in Fig. 2.5. The grey area marks real fluid, the blue area marks ghost cells. Cells $(i, j-1)$ and $(i, j+1)$ contain real fluid, but are flagged as ghost cells. Depending on the order of the extrapolation scheme and local flow field gradients, prescribing a value in these cells by solving eq. (2.40) instead of using the physical ones may result in wrong solutions of the two-material Riemann problem, see section 2.3.2. Therefore, a new definition for cells requiring extrapolation may be used: Instead of the level-set value at the cell center, the cell volume fraction α is considered. Defining a volume fraction threshold α_T, all cells with $\alpha < \alpha_T$ in the narrow band of the interface are tagged a ghost cells. The original definition of Fedkiw et al. is obtained for $\alpha_T = 0.5$. For $\alpha_T = 0$, extension is enforced for cells that contain only the opposite fluid, yet it may be numerically unstable. By extensive numerical tests it was found that $\alpha_T = 10^{-3}$ delivers accurate results and provides similar numerical stability as compared to the original definition. As example, numerical shadowgraphs of the expansion of a single bubble near a wall are given in Fig. 2.6. The left half shows results for the standard ghost-fluid definition with differing level-set sign ($\alpha_T = 0.5$), and the right half for the modified definition with $\alpha_T = 10^{-3}$. Prime states are extrapolated into ghost cells by iterating eq. (2.40) to steady state. The setup is aligned to the numerical investigation of Zeng et al. [146], who analyzed laser-induced bubble expansion and collapse near a rigid wall. A small bubble filled with air at high-pressure is initialized at $t = 0$ in a domain filled with water at ambient conditions. The bubble expands to its maximum radius at $t \approx 100\,\mu s$. The influence of the wall on the flow field results in a flattening of the expanding bubble on the near-wall hemisphere, which is clearly visible for both simulations. However, for $\alpha_T = 0.5$, also distinct grid effects are observed in diagonal direction, resulting in a strongly disturbed interface. For the modified version with $\alpha_T = 10^{-3}$, the surface remains smooth.

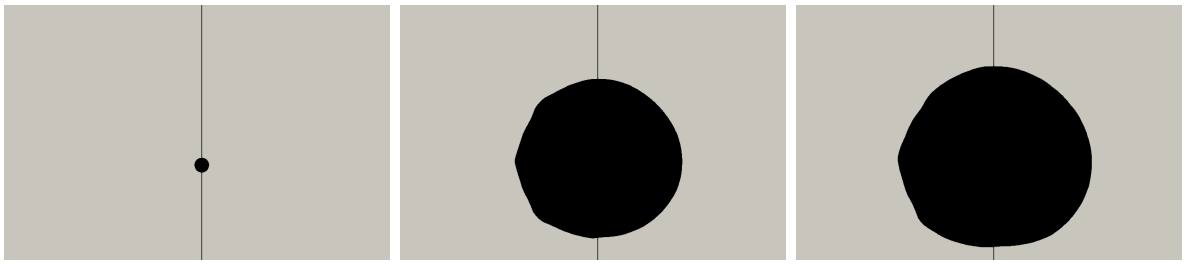

(a) $t = 0\,\mu s$ (b) $t = 50\,\mu s$ (c) $t = 100\,\mu s$

Figure 2.6: Bubble expansion for $\alpha_T = 0.5$ (left half) and $\alpha_T = 10^{-3}$ (right half) at multiple instants.

2.3.4 Small-cell mixing

A stable time integration based on the CFL condition assumes a full cell size Δx, see section 2.2.2. If a cell is cut by the interface, the time-step constraint of the full cell may be insufficient to guarantee a stable numerical integration. Therefore, such small cells pose severe stability issues for the entire numerical scheme. A more restrictive constraint, e.g. a sufficiently small CFL number, may remedy this issue, yet results in prohibitively small time-step sizes. As a remedy, Hu et al. [51] introduced a small-cell mixing procedure.

The general idea of mixing is to avoid integration of small cells and, instead, mix their conservative states with surrounding cells with sufficiently large fluid volume fraction. These neighboring cells are denoted as *target cells*. In the original version, all direct neighbors are possible target cells, and diagonal neighbors are neglected. Later, Lauer et al. [78] extended the mixing also for diagonal neighbors as possible target cells. After evolving the fluid from $t^{(n)}$ to $t^{(n+1)}$, three types of cells undergo mixing:

- Cells that are small cells at $t^{(n+1)}$.
- Cells that become empty at $t^{(n+1)}$, but contained fluid at $t^{(n)}$.
- Cells that did not contain fluid at $t^{(n)}$, but do at $t^{(n+1)}$.

The mixing contribution of each target cell is based on the volume fractions of mixed and target cell, their conservative states, and some weighting factor. The weighting factor may be based on the interface-normal unit vector of the cell to be mixed [51, 78], or the cell face aperture [48]. Finally, the mixing contributions are added to the small cell and subtracted from the target cell, thus ensuring overall conservation.

2.4 Spatial and temporal adaptivity

2.4.1 Wavelet-based multiresolution scheme

The large range of temporal and spatial scales in multi-phase flow simulations poses a challenge even for high-performance computing systems [105]. As a remedy, resolution-adaptation techniques are developed to reduce computational cost. For spatial adaptivity, Harten [42] proposed a multiresolution framework to improve the efficiency of the finite-difference and finite-volume discretization of hyperbolic conservation laws. This concept has been further developed by Cohen et al. [16]. In comparison to other spatial adaptation methods, such as adaptive mesh refinement (AMR), multiresolution exhibits improved CPU and memory compression rates for the same truncation-error order [19]. The multiresolution scheme relies on a wavelet-based representation of the flow field. Each flow-field variable can be represented by the solution on a coarse grid and higher-order wavelet coefficients on successively

finer meshes. This allows for implicit mesh refinement. In smooth flow regions, only few wavelet coefficients are required for representing all flow-field details. In regions with strong local gradients, high-wavenumber wavelets are necessary for an accurate representation, resulting in a locally refined grid. This concept is laid out in more detail in the following.

Assume that the cell-averaged solution $\overline{U}_{l,(i,j,k)}$, eq. (2.9), of the governing equations (2.1) represents the solution on a Cartesian grid with global cell indices (i,j,k) at a refinement level l. The cell may be refined dyadically into 2^D children cells. For the parent state $\overline{U}_{l,(i,j,k)}$ at refinement level l, the children at the next-finer level $l+1$ are $\overline{U}_{l+1,(2i+\alpha,2j+\beta,2k+\gamma)}$, $\alpha,\beta,\gamma \in \{0,1\}$. Two basic operations allow for data exchange between two consecutive levels l and $l+1$ [42]. To obtain data at level l from the child level $l+1$, the *projection* operation $\mathcal{Q}(l+1 \rightarrow l)$ is used. In its general three-dimensional formulation, it reads

$$\begin{aligned} \overline{U}_{l,(i,j,k)} &= \mathcal{Q}\overline{U}_{l+1} && (2.41)\\ &= \frac{1}{2^D}\sum_{\alpha=0}^{1}\sum_{\beta=0}^{1}\sum_{\gamma=0}^{1}\overline{U}_{l+1,(2i+\alpha,2j+\beta,2k+\gamma)}\,. && (2.42)\end{aligned}$$

This operation is exact for cell-averaged data. To estimate data on level $l+1$ from the parent level l, the *prediction* operation $\mathcal{P}(l \rightarrow l+1)$ is used. In three dimensions, it is given by

$$\begin{aligned} \hat{U}_{l+1,(2i+i_0,2j+j_0,2k+k_0)} &= \mathcal{P}\overline{U}_l \\ &= \overline{U}_{l,(i,j,k)} + (-1)^{i_0}Q^s_x + (-1)^{j_0}Q^s_y + (-1)^{k_0}Q^s_z + \\ &\quad (-1)^{(i_0+j_0)}Q^s_{xy} + (-1)^{(i_0+k_0)}Q^s_{xz} + \\ &\quad (-1)^{(j_0+k_0)}Q^s_{yz} + (-1)^{(i_0+j_0+k_0)}Q^s_{xyz} \end{aligned} \qquad (2.43)$$

with

$$\begin{aligned} Q^s_x &= \sum_{m=1}^{s}\gamma_m\left(\overline{U}_{l,(i+m,j,k)} - \overline{U}_{l,(i-m,j,k)}\right),\\
Q^s_y &= \sum_{n=1}^{s}\gamma_n\left(\overline{U}_{l,(i,j+n,k)} - \overline{U}_{l,(i,j-n,k)}\right),\\
Q^s_z &= \sum_{o=1}^{s}\gamma_o\left(\overline{U}_{l,(i,j,k+o)} - \overline{U}_{l,(i,j,k-o)}\right),\\
Q^s_{xy} &= \sum_{m=1}^{s}\gamma_m\sum_{n=1}^{s}\gamma_n\left(\overline{U}_{l,(i+m,j+n,k)} - \overline{U}_{l,(i+m,j-n,k)} - \overline{U}_{l,(i-m,j+n,k)} + \overline{U}_{l,(i-m,j-n,k)}\right),\\
Q^s_{xz} &= \sum_{m=1}^{s}\gamma_m\sum_{o=1}^{s}\gamma_o\left(\overline{U}_{l,(i+m,j,k+o)} - \overline{U}_{l,(i+m,j,k-o)} - \overline{U}_{l,(i-m,j,k+o)} + \overline{U}_{l,(i-m,j,k-o)}\right),\\
Q^s_{yz} &= \sum_{n=1}^{s}\gamma_n\sum_{o=1}^{s}\gamma_o\left(\overline{U}_{l,(i,j+n,k+o)} - \overline{U}_{l,(i,j+n,k-o)} - \overline{U}_{l,(i,j-n,k+o)} + \overline{U}_{l,(i,j-n,k-o)}\right),\\
Q^s_{xyz} &= \sum_{m=1}^{s}\gamma_m\sum_{n=1}^{s}\gamma_n\sum_{o=1}^{s}\gamma_o\left(\overline{U}_{l,(i+m,j+n,k+o)} - \overline{U}_{l,(i+m,j+n,k-o)} - \overline{U}_{l,(i+m,j-n,k+o)}\right.\\
&\quad -\overline{U}_{l,(i-m,j+n,k+o)} + \overline{U}_{l,(i+m,j-n,k-o)} + \overline{U}_{l,(i-m,j+n,k-o)} + \overline{U}_{l,(i-m,j-n,k+o)}\\
&\quad \left.-\overline{U}_{l,(i-m,j-n,k-o)}\right)\end{aligned}$$

and $i_0, j_0, k_0 \in \{0,1\}$ for all child cells. The interpolation order of the prediction operation is $r = 2s+1$, where s is the stencil half-width. For a fifth-order scheme ($s = 2$), the interpolation coefficients are $\gamma_i = \{-22/128, 3/128\}$. For the lower-dimensional formulation of projection and prediction, see e.g. Kaiser et al. [65].

Projection and prediction operations are local and consistent ($\mathcal{Q} \circ \mathcal{P} = Id$), but not commutative ($\mathcal{P} \circ \mathcal{Q} \neq Id$):

- Consistent: if, first, prediction is performed to obtain data on level $l+1$ from level l and, second, projection is applied to obtain data on level l from level $l+1$, exactly the same solution is obtained on level l.
- Not commutative: if, first, projection is applied to obtain data on level l from level $l+1$ and, second, prediction is performed to obtain data on level $l+1$ from level l, the predicted solution on level $l+1$ deviates from the exact solution.

This interpolation error motivates the definition of the so-called details d. The details quantify the difference of the exact solution $\overline{U}_{l,(i,j,k)}$ and the predicted solution $\hat{U}_{l,(i,j,k)}$

$$d_{l,(i,j,k)} = \overline{U}_{l,(i,j,k)} - \hat{U}_{l,(i,j,k)} \,. \tag{2.44}$$

Thus, the cell-averaged solution on an arbitrary level $\tilde{l}$ can be represented in a tree-like structure by the solution on the coarsest level $l = 0$ and the details of all subsequent levels $0 < l \leq \tilde{l}$. This enables implicit mesh refinement, since only those details need to be considered that are larger than a pre-defined error threshold and, therefore, result in significantly better results than interpolation from a coarser grid. This level-dependent error-threshold is computed following

$$\varepsilon_l = \varepsilon_{\text{ref}} \cdot \mathrm{e}^{-D(l_{\text{max}}-l)} \tag{2.45}$$

where l_{max} denotes the maximum multiresolution refinement level, and ε_{ref} the maximum admissible error for refinement from level $l_{\text{max}} - 1$ to l_{max}.

2.4.2 Block-based data structure

For efficiency reasons, Rossinelli et al. [106] and Han et al. [40] suggested to apply all multiresolution operations, such as projection and prediction, refinement and coarsening of cells, or the evolution of the flow field, on sets of multiple cells, so called blocks. Refinement is thereby triggered once the details of one single cell in the block exceeds the level-dependent threshold. Halo cells are introduced at the edges of the block since the operations mentioned above require data from neighboring blocks. To facilitate data transfer, cell data is stored in these overlapping halo cells. This is shown in Fig. 2.7 for two neighboring blocks on the same refinement level with eight internal cells and four halo cells in each spatial direction. Halo cells are filled by copying data from the internal cells of the neighboring block prior to performing the operations mentioned above. Note that block refinement is also triggered when details in halo cells exceed the level-dependent threshold, therefore the resolution of internal cells is always sufficient to accurately resolve the approaching flow field.

The governing equations (2.1) are only evolved on blocks that are not further refined, the so-called leaves. All other blocks receive their values from their children by the projection operation eq. (2.41). As emphasized by Roussel et al. [108], conservation may be violated at resolution jumps between leaves at two different refinement levels. Assuming that for two neighboring leaves at level l and $l + \Delta l$ ingoing fluxes are computed at level l and out-going fluxes at level $l + \Delta l$, the different cell sizes result in a mismatch of the reconstructed fluxes. To correct this mismatch, fluxes of the coarser level are overwritten by fluxes of the finer level at any resolution jump [108].

2.4.3 Local time-stepping approach

Temporal integration of the finite-volume discretization of the governing equation (2.8) is affected by a varying spatial grid resolution. Local adaptation techniques may exploit that the stability criterion, eq. (2.19), depends on the local grid size.

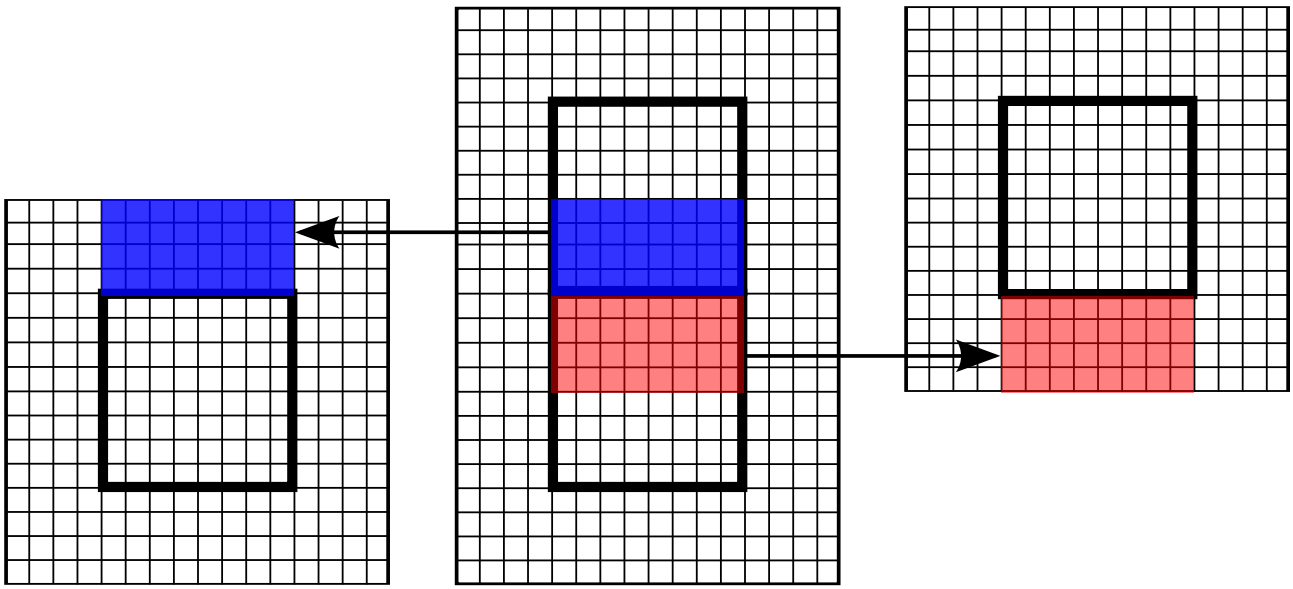

Figure 2.7: Halo cells for two neighboring blocks on the same level. The center shows the full domain, the single blocks are shown on the left and right. The thick black line marks the internal cells. The internal cells that are sent into the halo cells are marked in blue and red. Adapted from Kaiser et al. [65].

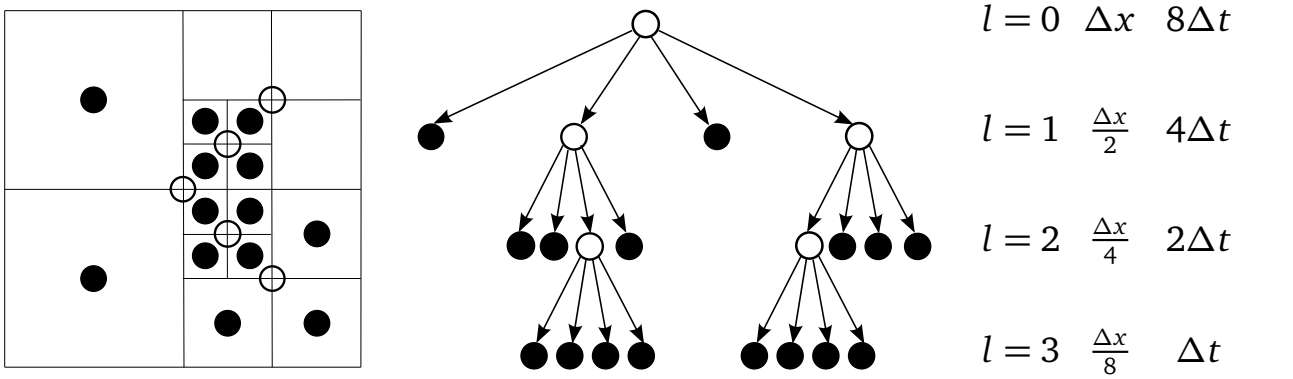

Figure 2.8: Two-dimensional domain with multiresolution refinement (left), sketched multiresolution tree-like data structure (center), and corresponding level, cell size, and time-step size relations (right). Adapted from Kaiser et al. [65].

A straightforward definition of a stable time-step size based on the CFL condition (see section 2.2.2) relies on the globally smallest occurring cell size [35, 108]. This constant time-stepping approach is algorithmically simple, since the entire domain is always evolved synchronously. Yet, overall efficiency could be further increased since larger cells could be evolved in time by larger time-step sizes. To overcome this issue, local time-stepping approaches can be used. Local time stepping was first introduced by Osher and Sanders [92] to solve one-dimensional scalar conservation laws on grids with varying spatial cell sizes. In their approach, the fluid field is evolved on each refinement level l with a level-dependent time-step size Δt_l. In multiresolution schemes with dyadic refinement strategies, level-dependent time-step sizes Δt_l can be easily formulated by scaling from the finest admissible time-step size at the maximum refinement level $\Delta t_{l_{\text{max}}}$

$$\Delta t_l = \Delta t_{l_{\text{max}}} \cdot 2^{l_{\text{max}} - l} \tag{2.46}$$

[21, 41]. Level-dependent time-step sizes are shown for a two-dimensional domain together with a sketched multiresolution tree in Fig. 2.8. For the given example of three levels, the coarsest level $l = 0$ is updated once, while the finest level l_{max} is updated eight times. This drastically decreases the computational effort in comparison to constant time stepping. Previous works [1, 9, 21, 41, 44, 97, 107]

underline the advantages of the method. In section 3.1, an overview about potential issues of such local time-stepping schemes and a summary of my contributions are given.

Chapter 3

Accomplishments

3.1 An adaptive local time-stepping scheme for multiresolution simulations of hyperbolic conservation laws

Local time-stepping schemes for instationary problems as introduced in section 2.4.3 have two major drawbacks [21], see Fig. 3.1: First, synchronization is required at resolution jumps between two neighboring blocks to use only data at the same time instant for reconstructing cell-face fluxes. Second, the time-step size has to remain constant until the coarsest level has evolved in time by one time-step size, since all levels advance to the first stage within the first evolution step. Thus, the efficiency of the time-step size adaptation decreases with increasing number of maximum refinement levels l_{max}, since the time-step size on the finest level is only updated after $2^{l_{\text{max}}}$ cycles. In the event of strong temporal wave-speed gradients, such as during bubble collapse, this may result in severe stability issues, since the CFL stability criterion is potentially violated. As remedy, small CFL numbers may be used to compute the maximum admissible time-step size, decreasing the overall efficiency of the method.

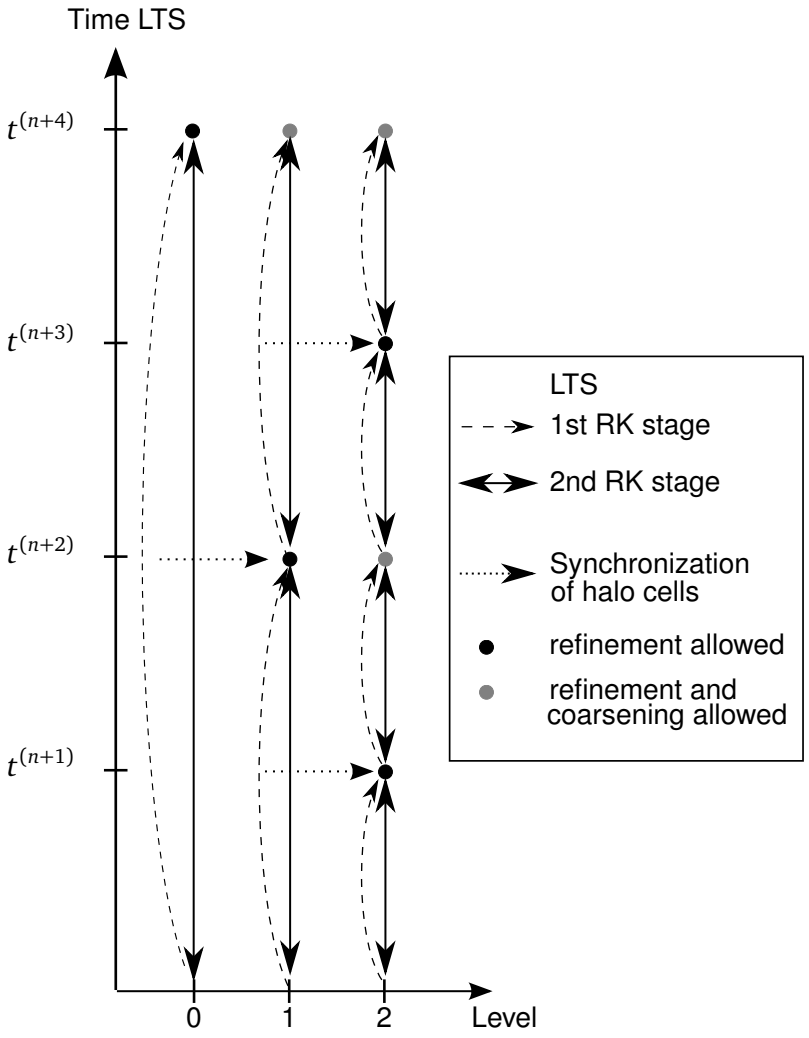

Figure 3.1: Sketch of the steps in the local time-stepping approach, see also Domingues et al. [21] or Kaiser et al. [65].

A first approach to overcome this difficulty was proposed by Müller and Stiriba [86]. They introduced transition zones between coarser and finer grids for synchronization. Evolving the solution in time from

finer to coarser grids allowed to update the time-step size after each full cycle on the finest level. The approach was extended to multi-fluid simulations by Coquel et al. [17]. Yet the approach is limited to stepwise grid refinements and low-order flux-reconstruction schemes.

Jakob W. J. Kaiser, **Nils Hoppe**, **Stefan Adami**, **Nikolaus A. Adams**: *An adaptive local time-stepping scheme for multiresolution simulations of hyperbolic conservation laws*. Journal of Computational Physics: X, Volume 4, 100038, 2019 [65]

In this publication, a novel algorithm is proposed for a block-based multiresolution method with local time stepping that allows for instantaneous time-step size adaptation. The method is not limited with regard to the order of the flux-reconstruction scheme or the level difference between neighboring blocks. To synchronize flow field data at resolution jumps between neighboring leaves, projection and prediction operations are applied on the divergence of the numerical flux function. By sending the divergence first into halo cells of resolution jumps and, second, evolving them in time on the finer level with the level-dependent time-step size, data on different levels are synchronized without prior temporal evolution on a coarser level. This is possible since, as derived mathematically in the publication, applying projection and prediction on the divergence and afterwards evolving it in time on the target level is equivalent to performing the projection and prediction on the already integrated conservative states. This approach allows for evolving coarser resolution levels only when they reach the same instant in time as all subsequent finer levels, thus the time-step size can be adapted efficiently after each full Runge-Kutta cycle on the finest level. Therefore, the prescribed CFL stability criterion is always enforced, including in the event of strong wave-speed changes.

Projection and prediction of the flux divergence do not deteriorate the convergence order of the overall scheme. Spatial and temporal error analyses are presented for a linear wave-advection case and a non-linear wave-steepening case.

The instantaneous time-step size adaptivity enables the use of larger CFL numbers than for standard local time-stepping schemes, even in the case of strong temporal wave-speed gradients. This is shown for the one-dimensional test cases of Sod [119] and Woodward and Colella [140] with discontinuities in the initial flow states. Standard local time stepping becomes unstable for large CFL numbers since the wave speed increases drastically during the first few iterations, which is not accounted for by the time-step size. In contrast, the new approach allows for time-step size adaptation corresponding to the wave speed increase, and the method remains stable.

The applicability of the new scheme to real-life problems is presented for an axisymmetric description of a biomedical application modeling non-invasive targeted drug delivery [120]. A bubble located near a solid wall is subjected to a lithotripter pulse, initiating the collapse of the bubble and finally resulting in a radial pressure wave and a water hammer impinging on the wall post-collapse. For more details on this case, see Johnsen and Colonius [61]. The new method shows improved stability properties for high CFL numbers as compared to the standard local time-stepping scheme. At collapse time, strong temporal wave speed gradients occur. These cause numerical instabilities for the standard local time stepping approach. For the novel scheme, the on-time time-step size adaptivity enables stable simulations. The accuracy of the method is shown by a comparison of the detected wall pressure with the empirical formula of Johnsen and Colonius [61].

Finally, the overall computational efficiency is analyzed for the one-dimensional, single-fluid shock tube case of Sod [119] and the two-dimensional, multi-phase case of Johnsen and Colonius [62]. The additional operations account for an overall compute time increase of approximately 10% and 5% of the total compute time, respectively, which is considered acceptable for the significantly improved stability of the method.

My contribution to this work lies in developing the algorithm of the adaptive local time-stepping scheme and deriving the mathematical foundation. I implemented the approach in our in-house code and performed the validation and verification of the method through numerical simulations. I selected the simulation setups presented in the paper, and post-processed the results. Finally, the manuscript for the publication was written predominantly by me.

3.2 Investigation of interface deformation dynamics during high-Weber number cylindrical droplet breakup

Systematic experimental investigations have improved the knowledge about the breakup of liquid drops. Extensive reviews have been published by Guildenbecher et al. [38] and Theofanous [132]. However, small temporal and spatial scales of the dominating instability modes hinder detailed experimental investigations of the breakup modes and the interplay of the occurring interface instability mechanisms. This, as well as increasing computational resources, motivates numerical investigations.

The first three-dimensional simulations in the low-Weber number regime have been presented by Khosla et al. [71]. More recently, further three-dimensional studies have been performed in the RTP regime by Yang et al. [144] assuming incompressible flow, and by Meng and Colonius [83] in the SIE regime, assuming compressible flow. Yet, these studies are limited in the applied spatial resolution since the number of degrees-of-freedom required to simulate three-dimensional drop breakup events exceeds the compute power even of modern supercomputers. To limit the numerical effort, many studies therefore decrease the setup size by assuming axisymmetry or choosing two-dimensional setups. The latter is motivated by the work of Igra et al. [52] and Igra and Takayama [55]. They reported phenomenological similarity of early-stage interface deformation of quasi two-dimensional water columns and three-dimensional spherical drops in crossflow in the SIE regime. Also, experimental results of the quasi two-dimensional breakup of liquid columns in crossflow [52, 54, 56, 113] are available for model validation [29, 53, 57, 90, 112, 128, 137, 138, 141, 143].

In a detailed analysis, Meng and Colonius [82] investigated two-dimensional cylindrical drop breakup in the SIE regime based on the setup of Igra and Takayama [52, 54], applying a volume-of-fluid approach. They highlighted the important role of local recirculation zones in the wake and at the equator of the drop for the peeling of sheets at the drop equator. In their study, they neglected viscous and capillary forces, assuming that the breakup mechanism is basically independent of these forces at large Weber and small Ohnesorge numbers. However, due to the applied diffuse interface multi-phase model, small scales at the interface were suppressed, and the interface remained smooth during the entire deformation.

Jakob W. J. Kaiser, **Josef M. Winter**, **Stefan Adami**, **Nikolaus A. Adams**: *Investigation of interface deformation dynamics during high-Weber number cylindrical droplet breakup*. International Journal of Multiphase Flow, Volume 132, 103409, 2020 [66]

In this publication, high-fidelity simulations are performed for the experimental setup of Igra and Takayama [52, 54]. The Weber number of this case is $We = 7.3 \times 10^3$, the Ohnesorge number $Oh = 1.7 \times 10^{-3}$, the Reynolds number $Re = 1.3 \times 10^5$, and the density ratio $\varepsilon = 459$. Hence, the expected breakup regime is shear-induced entrainment. The previously presented level-set sharp-interface approach with conservative interface interaction provides low numerical dissipation and high-order shock capturing. This enables an accurate prediction of interface waves during the deformation process, and the interaction of these interface waves with local flow field disturbances. In addition, viscous and capillary forces are considered in the setup by applying the extended conservative interface-interaction model of Luo et al. [81].

The setup is first validated using experimental data of Igra and Takayama [52, 54] and numerical data of Meng and Colonius [82]. Integral parameters, such as the upstream stagnation point drift and the center-of-mass drift, and schlieren images of the wave patterns near the cylinder agree well with the reference data, underlining the accuracy of the setup. A grid convergence study indicates that grid resolutions used in previous work were insufficient to capture small scale details of the deformation process. Yet, integral parameters are accurately reproduced already for fairly coarse grid resolutions.

The simulation accurately predicts the flattening of the cylindrical drop and the subsequent shearing of a water sheet from the drop equator, as expected for breakup in the shear induced entrainment regime. Small scale interface waves form already during the flattening of the droplet after shock passage near the drop equator. These waves grow to a hat-like structure on the windward side of the cylinder, which remains smooth during the entire simulation time. Both the hat-like structure and the smooth windward side were observed in experimental investigations of Theofanous [133]. Resolving early-stage interface waves is critical for hat-formation. For coarser grid resolutions or more dissipative schemes, these waves are not resolved, and the hat does not form during later deformation stages. The interface waves are linked to pressure waves at the droplet equator. These form in a local supersonic flow region shortly after shock passage, and disappear once the supersonic flow regions dissolve.

Multiple local recirculation zones are found along the circumference of the cylindrical droplet. In addition to the recirculation zones in the wake and at the equator, which were reported by Meng and Colonius [82], recirculation zones form near the hat and further downstream near the tip of the water sheet. This underlines the conclusion of Meng and Colonius, who emphasized the importance of such recirculation zones for the overall breakup process.

As new integral parameter, the skewness of the axial droplet displacement is introduced to characterize the transient droplet deformation. The skewness allows for distinguishing subsequent deformation stages of the droplet - flattening, hat formation, and sheet stripping. Flattening results in an increase of skewness. During hat formation, skewness decreases, before increasing again once the sheet is advected downstream. In addition, this quantity is also sensitive to small-scale interface structures, and therefore can be used to estimate the overall convergence of the spatial grid resolution.

Finally, simulation results are presented for a reduced setup, intentionally neglecting the effect of viscous and capillary forces on the breakup mechanism. These results show only minor differences to the full model with viscous and capillary effects. Thus, the usual assumption that these effects are negligible can be confirmed for the chosen spatial and temporal discretization schemes and resolution.

My contribution to this work is the calibration of the modeling parameters in our in-house code for this setup. Moreover, I performed the simulations and post-processed the simulation results, and validated the setup against experimental and numerical reference data. Finally, the manuscript for the publication was written predominantly by me.

3.3 A semi-implicit conservative sharp-interface method for liquid-solid phase transition

Liquid-solid phase transition poses an initial-boundary value problem with moving boundary, a so-called Stefan problem. The boundary conditions at the interface are the Gibbs-Thomson relation, eq. (1.5), and the Stefan condition, eq. (1.6). The numerical solution of the interface dynamics of the Stefan problem requires accurate predictions of the topologically complex, time-dependent solidification front. In literature, both mesh-free [85, 121–123, 147] and mesh-based methods have been proposed to solve the Stefan problem. The mesh-based methods can be considered to be either front-tracking [37, 63, 104] or front-capturing [6, 8, 15, 18, 28, 31, 39, 70, 72, 74, 88, 101, 102, 118, 125–127, 129, 142] methods. A review on front-capturing methods was recently published by Jaafar et al. [59], naming the phase-field method and the level-set method as most common front-capturing methods to solve solidification problems.

As introduced in section 1.1, phase-field models are widely used to simulate phase-change processes such as liquid-solid phase transition [6, 8, 28, 39, 70, 74, 88, 118, 142]. Comprehensive reviews are given by Singer-Loginova and Singer [117] and Boettinger et al. [11]. A major challenge regarding phase-field models is an appropriate choice of the interface thickness, which is a free model parameter. For quantitatively accurate predictions, the interface thickness needs to be sufficiently small. Since the cell size must be comparable to the interface thickness, this may incur prohibitively high computational cost [59].

The level-set method does not suffer from this limitation. Instead, its sharp-interface property allows for accurately computing the local interface geometry (interface normal and curvature). The first approach to model solidification processes with level set stems from Osher and Sethian [93]. They introduced a curvature-dependent interface-velocity formulation, which is a first step to model the Gibbs-Thomson relation and the Stefan condition. Such a model was presented by Sethian and Strain [114], and extended by Chen et al. [15] with focus on crystal growth. In their approach, the thermal diffusion equation is approximated by a finite-difference scheme on a homogeneous grid with implicit time integration. They show good results for the Stefan problem and unstable crystal growth. A validation of their approach with the solvability theory was performed by Kim et al. [72]. Gibou et al. [31] showed that the overall accuracy and convergence rate of the method can be improved by applying high-order stencils. To improve computational efficiency, Chen et al. [14] applied a local mesh adaptation approach, refining the mesh only near the phase interface. An extension to non-isothermal solidification of binary alloys was presented by Theillard [129]. Tan and Zabaras combined the level-set method with a front tracking approach to model the growth of melts [126, 127] and multi-component alloys [125]. Ramanuj et al. [101] applied a second-order level-set approach [100], underlining the advantages of high-order reconstruction schemes for overall accuracy and convergence rate. Criscione et al. [18] and Rauschenberger et al. [102], to the contrary, used a finite-volume discretization, which improves overall conservation. Yet, they relied on finite-difference based interface treatment, which may violate local conservation at the interface. Such non-conservative interface treatment may result in physically incorrect interface evolution.

Jakob W. J. Kaiser, **Stefan Adami**, **Iskander S. Akhatov**, **Nikolaus A. Adams**: *A semi-implicit conservative sharp-interface method for liquid-solid phase transition*. International Journal of Heat and Mass Transfer, Volume 155, 119800, 2020 [64]

In this publication, a sharp-interface method with conservative interface interaction is proposed to model liquid-solid phase transition. The developed model is based on the original approach of Hu et al. [51] and the extension of Lauer et al. [78] for phase change, see section 2.3.2. To focus on the phase-change process, convection is neglected in the model and all validation cases.

The Gibbs-Thomson relation, eq. (1.5), is prescribed as Dirichlet boundary condition, which allows for simple consideration of surface-tension, kinetic, and anisotropic effects on the interface temperature. The Stefan condition, eq. (1.6), is reformulated as interface exchange flux of the conservative interface interaction method. The reconstruction of the interface-normal temperature gradient, which is required for the Stefan condition, is a known challenge for this application [18]. In the presented model, a weighting based on WENO smoothness indicators is applied. This approach suppresses numerically induced oscillations. The high-order reconstruction, together with an explicit third-order strongly stable Runge-Kutta time integration scheme, provides low numerical dissipation.

A standard explicit level-set approach as used in the previous work of Lauer et al. [78] turned out to be insufficient to correctly predict the interface evolution in more than one dimension. This results from inaccurate solidification mass flux computations when the interface moves diagonally through a cell. Therefore, we propose a semi-implicit approach, splitting the integration of level-set and fluid fields in the algorithm. This enables a semi-implicit treatment of the level-set field in the computation of the interface exchange terms, since the interface position of the old and the new time instant can be used. The approach allows for an exact computation of solidification mass fluxes, which drastically improves stability and enforces conservation. Since the level-set field is reinitialized prior to computing interface exchange fluxes, numerical errors introduced by cut cell reinitialization are suppressed. The conservation property is presented for a two-dimensional complex crystal growth case, in which the total mass is conserved during the simulated time.

The model is validated for the one-dimensional Stefan problem with the analytical solution of Carslaw and Jaeger [13]. The interface propagation and the temperature field are accurately resolved, and the convergence order for spatial refinement is one for both the interface location and the temperature field. Comparison with the marginal stability hypothesis for a growing parabolic dendrite yields good agreement with the model of Langer and Müller-Krumbhaar [77]. For this case kinetic effects are not considered, resulting in good agreement with the model also for large undercoolings. The advantages of high-order, low-dissipation schemes are demonstrated for a two-dimensional crystal-growth problem with tip-splitting instability, which occurs earlier for our presented method than for previous approaches.

Finally, a multi-crystal growth case underlines the capabilities of the method to simulate complex microstructures. Anisotropic surface tension results in the growth of each crystal along four main axes. The low-dissipation spatial and temporal discretization schemes allow for resolving small scale structures, especially in those areas where crystals interfere in their growth. Yet, the crystals do not merge artificially.

My contribution to this work is the development of the phase-change model, its implementation, verification and validation. I have chosen the test cases and performed the post-processing. Finally, the manuscript for the publication was written predominantly by me. A significant part of this work was done during my research stay at the Skolkovo Institute of Science and Technology (Skoltech) in Moscow, Russia. This stay was supported by the TUM-Skoltech cooperation agreement, and my host at Skoltech, Prof. Iskander S. Akhatov, is co-author of this publication.

Chapter 4

List of Publications

4.1 Peer-reviewed journal publications

- **Jakob W. J. Kaiser**, **Stefan Adami**, **Iskander S. Akhatov**, **Nikolaus A. Adams**: *A semi-implicit conservative sharp-interface method for liquid-solid phase transition*. International Journal of Heat and Mass Transfer, Volume 155, 119800, 2020. [64]

- **Jakob W. J. Kaiser**, **Josef M. Winter**, **Stefan Adami**, **Nikolaus A. Adams**: *Investigation of interface deformation dynamics during high-Weber number cylindrical droplet breakup*. International Journal of Multiphase Flow, Volume 132, 103409, 2020. [66]

- **Jakob W. J. Kaiser**, **Nils Hoppe**, **Stefan Adami**, **Nikolaus A. Adams**: *An adaptive local time-stepping scheme for multiresolution simulations of hyperbolic conservation laws*. Journal of Computational Physics: X, Volume 4, 100038, 2019. [65]

4.2 Conference proceedings

- **Jakob W. J. Kaiser**, **Stefan Adami**, **Nikolaus A. Adams**: *Three-dimensional direct numerical simulation of shock-induced bubble collapse near gelatin*. 11th International Symposium on Turbulence and Shear Flow Phenomena, TSFP 11, 2019. [67]

- **Josef M. Winter**, **Jakob W. J. Kaiser**, **Stefan Adami**, **Nikolaus A. Adams**: *Numerical investigation of 3D drop-breakup mechanisms using a sharp interface level-set method*. 11th International Symposium on Turbulence and Shear Flow Phenomena, TSFP 11, 2019. [139]

- **Jakob W. J. Kaiser**, **Stefan Adami**, **Nikolaus A. Adams**: *Direct numerical simulation of shock-induced drop breakup with a sharp-interface-method*. 10th International Symposium on Turbulence and Shear Flow Phenomena, TSFP 10, 2017. [68]

Chapter 5

Discussion with Respect to the State of the Art and Conclusion

Simulating flow problems for dispersed systems with multiple immiscible fluids remains still today a challenge in computational fluid dynamics. An accurate representation of the interface and the interaction between the two fluids in a conservative formulation are required for a consistent representation of interfacial instabilities, which are paramount to an accurate physical model. In addition, the development of spatial and temporal adaptation techniques is required since the multi-scale nature of such multi-phase flow configurations complicates numerical investigations. Such techniques offer vast opportunities since experimental investigations are often limited due to the small temporal and spatial scales of multi-phase phenomena. In this work, contributions are presented improving stability and robustness of temporal adaptation techniques for single- and multi-phase simulations in an Eulerian frame of reference. This approach is applied for high-fidelity simulations of secondary atomization, which is a problem driven by the growth of Rayleigh-Taylor and Kelvin-Helmholtz instabilities at the gas-liquid interface [132]. Furthermore, a model for non-equilibrium liquid-solid phase transition is proposed for the conservative interface interaction method of Hu et al. [51]. Such liquid-solid phase-transition problems are dominated by the interplay of tip-splitting and side-branching instabilities at the progressing solidification front, which determine the resulting crystalline microstructure. High-fidelity models as the one presented in this work are required for validation of low-fidelity microstructure simulation tools, which play an important role in modern manufacturing.

Time-step size adaptivity is a widely discussed topic in computational fluid dynamics, since such adaptation techniques are paramount to the efficient simulation of real-life flow problems. The algorithm with full time-step size adaptivity presented in the first publication, see section 3.1, extends previous local time-stepping approaches for the multiresolution scheme of Harten [42], as given by, e.g., Domingues et al. [21] and Han et al. [41]. The novel scheme provides improved stability and robustness, while the incurred increase of computational cost is considered to be negligible. The proposed method can be implemented in a straightforward way in an already existing multiresolution code framework, since only standard operations of the multiresolution approach - projection and prediction - are used, without significant changes in the main evolution algorithm. The method was used in multiple subsequent investigations [24, 48, 64, 66, 67, 139], underlining its general applicability beyond the setups presented in the publication.

The multiresolution scheme with improved local time-stepping was applied for high-fidelity simulations of cylindrical droplet breakup in the high-Weber number regime (shear induced entrainment) in the second publication, see section 3.2. Previous work by Meng and Colonius [82, 83] on this setup underlined the importance of locally varying grids to obtain sufficient spatial resolution near the phase interface or in areas with large spatial flow-field gradients. Due to run-time spatial and temporal adaptation provided by the method, even higher resolutions are obtained in this work. Cells are added in areas of interest, but removed once the droplet moves away or local gradients flatten. This enables finer effective grid resolutions than in any previous study, resulting in an improved representation of the flow

field. In addition, the level-set approach yields lower numerical diffusion than the volume-of-fluid diffuse-interface approach [111] which was used by Meng and Colonius [82, 83]. In their study, the excess numerical diffusion of the volume-of-fluid method artificially smoothened the interface. This has little effect on integral parameters, which agree well with experimental reference data of Igra and Takayama [52, 54] for both studies. Yet, low numerical dissipation is required to accurately resolve small-scale interface features. In particular, the close connection of local interface disturbances and pressure waves in the flow field was observed for the first time. The disturbances later result in the formation of the hat-like interface structure on the windward side of the droplet, which is known from experimental visualizations of the shear-induced-entrainment breakup mode [132]. These findings have motivated ongoing investigations on the influence of ambient gas flow parameters on the breakup evolution. In addition, a more detailed investigation of low-Weber number breakup is required to investigate the transition from shear-induced-entrainment breakup to Rayleigh-Taylor-piercing breakup.

Finally, a novel approach to simulate non-equilibrium liquid-solid phase transition of pure melts is presented in the third publication, see section 3.3. A two-phase Stefan problem is solved at the interface, coupled with the Gibbs-Thomson relation as local Dirichlet boundary condition. The spatial and temporal adaptivity of the multiresolution approach with adaptive local time stepping is advantageous to model the inherent multiscale nature of the crystallization process efficiently, as was already shown in previous literature [14, 129]. At the same time, the conservation property of the sharp-interface approach with semi-implicit level-set treatment provides a physically consistent evolution of the interface instabilities. In contrast to previous level set-based schemes prescribing the interface boundary conditions using ghost cells (e. g. [18, 102]), the presented method employs that the conservative interface-interaction method of Hu et al. [51] prescribes interface boundary conditions in a flux-based formulation. This corresponds directly to the energy fluxes on the right-hand-side of the Stefan condition, eq. (1.6), which include the Gibbs-Thomson relation, eq. (1.5). Comparisons to the analytical solution of the one-dimensional Stefan problem [13] and to experimental and numerical reference data for the stable growth of a two-dimensional parabolic dendrite [75–77, 87, 116] yield good agreement. The proposed method is more sensitive to detect physical tip-splitting instabilities than previous models, as presented by comparison with reference work for the unstable growth of a four-fold symmetric crystal [80, 127]. This is in line with the previously reported improved representation of interfacial instabilities of the level-set scheme with conservative interface interaction for aerodynamic fragmentation. An extension of the interface-interaction model to binary and multi-component alloys, which are relevant for more realistic applications such as additive manufacturing, is subject of ongoing work.

In conclusion, the level-set approach with conservative interface interaction, coupled with spatial and temporal adaptation techniques, has proven to be very well suited to solve a variety of complex multi-phase flow configurations. This work presents new modeling techniques which improve the stability of the overall scheme, and enforce conservation at the interface. This enforced conservation, together with the low numerical dissipation of the level-set method, enables an accurate prediction of interfacial instabilities for both flow-field-driven and interface-driven multi-phase problems at high accuracy. This is underlined by the numerical investigations of aerodynamic fragmentation and liquid-solid phase transition in this work. This versatility makes the method directly applicable for a wide range of fluid-dynamics applications in research and industry.

Chapter A

Peer-Reviewed Journal Publications

A.1 An adaptive local time-stepping scheme for multiresolution simulations of hyperbolic conservation laws

Please note that the publication

> **Jakob W. J. Kaiser, Nils Hoppe, Stefan Adami, Nikolaus A. Adams:** *An adaptive local time-stepping scheme for multiresolution simulations of hyperbolic conservation laws.* Journal of Computational Physics: X, Volume 4, 100038, 2019. https://doi.org/10.1016/j.jcpx.2019.100038

Munich, 10.11.2020

Journal of Computational Physics: X 4 (2019) 100038

Contents lists available at ScienceDirect

Journal of Computational Physics: X

www.elsevier.com/locate/jcpx

An adaptive local time-stepping scheme for multiresolution simulations of hyperbolic conservation laws

Jakob W.J. Kaiser *, Nils Hoppe, Stefan Adami, Nikolaus A. Adams

Technical University of Munich, Department of Mechanical Engineering, Chair of Aerodynamics and Fluid Mechanics, Boltzmannstraße 15, 85748 Garching, Germany

ARTICLE INFO

Article history:
Received 3 December 2018
Received in revised form 9 July 2019
Accepted 20 August 2019
Available online 14 October 2019

Keywords:
Adaptive time stepping
Local time stepping
Multiresolution simulations
Shock-bubble interaction

ABSTRACT

We present an adaptive local time-stepping (ALTS) scheme for a block-structured multiresolution scheme of hyperbolic conservation laws for fluid flow. The stability of standard local time-stepping (LTS) schemes with level-dependent time-step sizes is improved by local time-step size adaptation when progressing through the underlying multi-stage time integration scheme. The novelty of the approach is that it merges flux computation and time integration of the state vector with projection and prediction operations of the multiresolution scheme [15]. This enables consistent time integration of subdomains with different refinement levels without the need for intermediate time synchronization which can be prohibitively expensive in parallel computations. Consequently, coarser subdomains are advanced in time only once finer subdomains have advanced to the same time instant. Full spatial resolution adaptivity for integrated regions after each substep is maintained.

The new scheme exhibits significantly improved numerical stability as compared to previous LTS schemes due to the local time-step size adaptation at each substep. The computational overhead of the incurred additional operations is small. In applications, the ALTS scheme demonstrates the same computational efficiency as standard LTS schemes.

The new scheme can be applied to any explicit single-step time-integration scheme and is independent of the employed spatial discretization scheme. The improved stability is demonstrated with several one- and two-dimensional examples of flows with one and two phases, applying second- and third-order Runge-Kutta time integration schemes.

1. Introduction

Computational simulations of complex flows remain a challenge even today. The large range of temporal and spatial scales in combustive or turbulent flows or flow cavitation challenges the performance of even the largest parallel computers [26]. While a wide range of spatial scales causes high memory consumption, small temporal scales lead to small time-step sizes that inversely proportionally increase the number of required computational operations. Although the smallest spatial and temporal scales predominantly govern the flow evolution, in particular interfacial flows or flows with reaction fronts require the highest spatial resolution levels on co-dimension one-manifolds. Therefore, spatial and temporal resolution adaption schemes have been and are being developed as a remedy to reduce computational cost.

* Corresponding author.
E-mail addresses: jakob.kaiser@tum.de (J.W.J. Kaiser), nils.hoppe@tum.de (N. Hoppe), stefan.adami@tum.de (S. Adami), nikolaus.adams@tum.de (N.A. Adams).

https://doi.org/10.1016/j.jcpx.2019.100038

As an approach for spatial adaptivity, Harten [15,16] proposed a multiresolution (MR) framework for the spatial discretization of hyperbolic conservation laws to improve the efficiency of existing finite-volume solvers. The concept, which has been further developed to provide full spatial adaptivity [4], relies on a wavelet-based representation of the flow fields. This allows for compressing data to the minimum necessary amount for representing a field function at desired accuracy. Starting from a solution on a coarse mesh, higher-order wavelet coefficients are added successively to achieve the required accuracy using an increasingly finer mesh. In smooth flow regions only few wavelet coefficients may suffice to approximate the solution with the required accuracy on a coarse grid. In regions where the solution has strong local gradients, higher-wavenumber wavelets need to be used to represent the solution which results in a locally refined grid. The underlying refinement strategy is based on dyadic refinement, where the cell spacing is halved in each direction for every additional set of wavelet coefficients. Compared to other spatial adaption methods, such as adaptive mesh refinement (AMR), MR techniques result in improved CPU and memory compression rates for the same truncation-error order discretizations of hyperbolic conservation laws [6].

Spatially varying grid resolution affects the temporal integration of the governing equations. The choice of a stable time-step size Δt from a stability criterion, such as the CFL condition, depends on the local cell sizes. Constant time-stepping (CTS) schemes choose the minimum Δt based on the globally maximum wave speed $|u \pm c|$ together with the smallest occurring cell size to ensure stability in the entire domain [10,29]. Although formally and algorithmically simple, this approach is not very efficient as larger cells could use larger time-step sizes.

As a remedy, Osher and Sanders [25] introduced a local time-stepping (LTS) scheme for solving one-dimensional conservation laws on grids with varying spatial cell size. Each level of refinement uses its specific cell size to scale the time-step size Δt. For dyadic refinement in one dimension, the time step at each successively coarser level l is twice the time-step size of the finer level $l+1$, thus the required number of time integration steps are strongly reduced compared to the CTS scheme. The LTS scheme has been combined with the MR approach by Domingues et al. [7–9] and Lopes et al. [22]. In their approach, the time-step size is fixed during each full cycle on the coarsest resolution level. At intermediate stages, interpolation is required in cells at resolution jumps. Müller and Stiriba [24] introduced transition zones between coarser and finer cells. This enables updating the time-step size after each full cycle on the finest levels and propagating this change upwards to coarser grid regions. Their scheme has been successfully employed for multi-fluid simulations [5]. However, their LTS algorithm is limited to stepwise grid refinements and cell-flux reconstruction schemes which require two adjacent cells only. Han et al. [12,13] applied the local time-stepping approach on a block-structured multiresolution scheme, with a fixed time-step size during each full cycle on the coarsest resolution level.

Several works [2,18,28] have demonstrated that the LTS approach with MR outperforms the computational efficiency of CTS. The minimum time-step size, however, can be determined only after each full cycle on the coarsest mesh, regardless of the interim local flow evolution on the finest mesh. Hence, the method does not deliver instantaneous time-step size adaptivity [8], and eventually may violate the stability criterion. Flows with strong temporal gradients, i.e. fast physical processes such as collapsing bubbles during cavitation [1] or chemical reactions [2] reveal such a deficiency of the LTS scheme. In the standard LTS approach, stability for such cases can be achieved by choosing a smaller CFL number, thus decreasing overall efficiency. Alternatively, the number of refinement levels can be reduced to allow more frequent time-step size adjustments, which decreases memory compression.

In this work, we present a revised LTS scheme without limitations on the spatial and temporal adaptivity for a block-structured MR scheme. Projection and prediction operations of Harten [15] are applied on the numerical divergence of the flux vector rather than the state vector of the finite-volume discretization of the governing equations, similar to the approach of Bihari and Harten [3]. By advancing also halo cells of cell blocks in time, time-step size adaptation for different resolutions in different domain regions without additional synchronization on coarser resolution levels is obtained. The time-step size is adapted after each full cycle on the finest level, thus recovering the stability properties of the CTS approach. This is not limited to single-stage time-integration schemes, but also applies to multi-stage time integration schemes, e.g., the two-stage second order Runge-Kutta (RK) Total Variation Diminishing (TVD) scheme [11,14]. In addition, the scheme does not constrain spatial discretization. Hence, it can be used with high-order spatial schemes, such as WENO, and does not limit the resolution jumps between neighboring domain regions.

The organization of the paper is the following: in section 2, the adaptive MR scheme for the finite volume (FV) method is reviewed. In section 3, we describe the new adaptive local time-stepping scheme. In section 4, we present simulation results of our fully adaptive scheme for one- and two-dimensional problems. We compare our simulation results with exact solutions and other numerical schemes to discuss the accuracy and stability of the new scheme. In section 5, we conclude our results.

2. Multiresolution scheme

2.1. Finite volume representation

We consider a finite-volume representation of hyperbolic conservation laws

$$\frac{\partial \overline{u}}{\partial t} + \nabla \cdot f(\overline{u}) = 0 \tag{1}$$

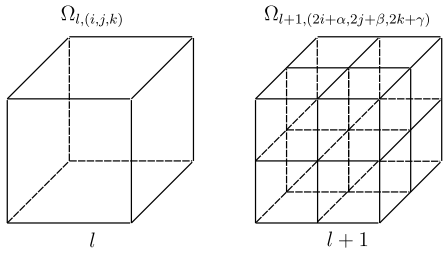

Fig. 1. Dyadic refinement scheme in 3D, following Domingues et al. [8].

on a Cartesian grid $(x, y, z, t) \in \Omega \times [0, \infty), \Omega \subset \mathbb{R}^3$ to evolve the state vector $\overline{u}$. The governing equations (1) constitute an initial-boundary value problem with $\overline{u}(x, y, z, 0) = \overline{u}_0(x, y, z)$ and appropriate boundary conditions on the boundary $\Gamma = \partial\Omega$. In the finite volume approach, the cell-averaged numerical solution $\overline{U}$ can be advanced in time by solving the ordinary differential equation (ODE) system

$$\frac{d\overline{U}}{dt} + \mathcal{D}(\overline{U}) = 0\,, \tag{2}$$

where $\mathcal{D}(\overline{U})$ represents the divergence of the evaluated numerical flux function. High-order shock capturing is achieved in this paper with a 5th-order WENO shock-capturing scheme for the reconstruction of the numerical flux function [19]. The ALTS scheme, however, can be applied with every other linear or nonlinear finite-volume or finite-difference scheme.

The semi-discrete ODE system (2) is integrated in time using the 2nd-order RK-TVD scheme

$$\overline{U}^{(n+1/2)} = \overline{U}^{(n)} + \Delta t^{(n)}\, \mathcal{D}\left(\overline{U}^{(n)}\right) \tag{3}$$

$$\overline{U}^{(n+1)} = \overline{U}^{(n)} + \Delta t^{(n)}\, \frac{1}{2}\left[\mathcal{D}\left(\overline{U}^{(n)}\right) + \mathcal{D}\left(\overline{U}^{(n+1/2)}\right)\right] \tag{4}$$

of Gottlieb and Shu [11]. The solution at time $t^{(n)}$ and $t^{(n+1)} = t^{(n)} + \Delta t^{(n)}$ is denoted as $\overline{U}^{(n)}$ and $\overline{U}^{(n+1)}$, respectively. The intermediate stage of the RK scheme is denoted as $\overline{U}^{(n+1/2)}$. The time-step size Δt is chosen according to a Courant-Friedrichs-Lewy (CFL) stability criterion

$$\Delta t \leq \mathrm{CFL}\left(\sum_i \frac{||u_i \pm c||_\infty}{\Delta x_i}\right)^{-1} \tag{5}$$

with $\mathrm{CFL} \leq 1$, where c, u_i and Δx_i are the local speed of sound, the velocity component in i-direction, and the cell size in i-direction of the Cartesian mesh, respectively [11]. We use the discrete evolution operator

$$\mathcal{E} = \mathcal{E}\left(\overline{U}^{(n)}, \mathcal{D}(\overline{U}_1), \mathcal{D}(\overline{U}_2), \Delta t^{(n)}\right) \tag{6}$$

as short notation for a single RK step [29]. For the first stage, it is $\mathcal{D}(\overline{U}_1) = \mathcal{D}(\overline{U}_2) = \mathcal{D}(\overline{U}^{(n)})$, for the second stage $\mathcal{D}(\overline{U}_1) = \mathcal{D}(\overline{U}^{(n)})$ and $\mathcal{D}(\overline{U}_2) = \mathcal{D}(\overline{U}^{(n+1/2)})$.

2.2. Multiresolution representation

Following the original concept of Harten [15], the cell average solution $\overline{U}$ is represented by the combination of data on a coarse grid and a series of values on successively finer grids. We use a Cartesian grid with global indices i, j, and k, where each cell can be refined dyadically into 2^D children cells, with D being the number of dimensions. Starting from the parent cell states $\overline{U}_{l,(i,j,k)}$ at level l, the children at the next-finer level $l+1$ are denoted as $\overline{U}_{l+1,(2i+\alpha,2j+\beta,2k+\gamma)}$, $\alpha, \beta, \gamma \in \{0, 1\}$. A sketch of this dyadic refinement strategy is shown in Fig. 1.

Two basic operations are introduced to exchange data between consecutive levels l and $l+1$ [15]. Cell averages at level l are estimated from a finer level $l+1$ by the *projection* operation $\mathcal{Q}(l+1 \to l)$

$$\overline{U}_{l,(i,j,k)} = \mathcal{Q}\overline{U}_{l+1} = \frac{1}{2^D}\sum_{\alpha=0}^{1}\sum_{\beta=0}^{1}\sum_{\gamma=0}^{1}\overline{U}_{l+1,(2i+\alpha,2j+\beta,2k+\gamma)}\,. \tag{7}$$

Note that we formulate the projection operator for 3D data sets. For lower dimensions, the indices k (2D) or j and k (1D) as well as γ and β are omitted. This operation is exact for cell-averaged data.

The *prediction* operation $\mathcal{P}(l \to l+1)$ is used to estimate cell averages at level $l+1$ from a coarser level l and is given by

$$\begin{aligned}\hat{U}_{l+1,(2i+i_0,2j+j_0,2k+k_0)} &= \mathcal{P}\overline{U}_l \\ &= \overline{U}_{l,(i,j,k)} + (-1)^{i_0} Q_x^s + (-1)^{j_0} Q_y^s + (-1)^{k_0} Q_z^s + \\ &\quad (-1)^{(i_0+j_0)} Q_{xy}^s + (-1)^{(i_0+k_0)} Q_{xz}^s + \\ &\quad (-1)^{(j_0+k_0)} Q_{yz}^s + (-1)^{(i_0+j_0+k_0)} Q_{xyz}^s \end{aligned} \tag{8}$$

with

$$\begin{aligned}
Q_x^s &= \sum_{m=1}^{s} \gamma_m \left(\overline{U}_{l,(i+m,j,k)} - \overline{U}_{l,(i-m,j,k)}\right), \\
Q_y^s &= \sum_{n=1}^{s} \gamma_n \left(\overline{U}_{l,(i,j+n,k)} - \overline{U}_{l,(i,j-n,k)}\right), \\
Q_z^s &= \sum_{o=1}^{s} \gamma_o \left(\overline{U}_{l,(i,j,k+o)} - \overline{U}_{l,(i,j,k-o)}\right), \\
Q_{xy}^s &= \sum_{m=1}^{s} \gamma_m \sum_{n=1}^{s} \gamma_n \left(\overline{U}_{l,i+m,j+n,k} - \overline{U}_{l,i+m,j-n,k} - \overline{U}_{l,i-m,j+n,k} + \overline{U}_{l,i-m,j-n,k}\right), \\
Q_{xz}^s &= \sum_{m=1}^{s} \gamma_m \sum_{o=1}^{s} \gamma_o \left(\overline{U}_{l,i+m,j,k+o} - \overline{U}_{l,i+m,j,k-o} - \overline{U}_{l,i-m,j,k+o} + \overline{U}_{l,i-m,j,k-o}\right), \\
Q_{yz}^s &= \sum_{n=1}^{s} \gamma_n \sum_{o=1}^{s} \gamma_o \left(\overline{U}_{l,i,j+n,k+o} - \overline{U}_{l,i,j+n,k-o} - \overline{U}_{l,i,j-n,k+o} + \overline{U}_{l,i,j-n,k-o}\right), \\
Q_{xyz}^s &= \sum_{m=1}^{s} \gamma_m \sum_{n=1}^{s} \gamma_n \sum_{o=1}^{s} \gamma_o \left(\overline{U}_{l,i+m,j+n,k+o} - \overline{U}_{l,i+m,j+n,k-o} - \overline{U}_{l,i+m,j-n,k+o}\right. \\
&\quad - \overline{U}_{l,i-m,j+n,k+o} + \overline{U}_{l,i+m,j-n,k-o} + \overline{U}_{l,i-m,j+n,k-o} + \overline{U}_{l,i-m,j-n,k+o} \\
&\quad \left. - \overline{U}_{l,i-m,j-n,k-o}\right)
\end{aligned}$$

and $i_0, j_0, k_0 \in \{0, 1\}$ depending on the location of the finer cell. The order of this central interpolation scheme is $r = 2s + 1$, with the stencil half-width s. The interpolation coefficients are $\gamma_1 = \{1/8\}$ for a 3rd order scheme ($s = 1$) and $\gamma_i = \{-22/128, 3/128\}$ for a 5th order scheme ($s = 2$). For lower dimensions, the prediction operation is given by eq. (8) without higher-dimensional terms (2D: $Q_{xyz}^s = Q_{xz}^s = Q_{yz}^s = Q_z^s = 0$, 1D: additionally $Q_{xy}^s = Q_y^s = 0$). These operations can be applied on both the cell-averaged state vector and the numerical divergence of the flux functions [3].

Projection and prediction operations are *local* and *consistent* ($\mathcal{Q} \circ \mathcal{P} = Id$), but not commutative ($\mathcal{P} \circ \mathcal{Q} \neq Id$). This motivates the definition of the so-called *details* d as the difference between the exact solution and the predicted solution

$$d_{l+1,(2i,2j,2k)} = \overline{U}_{l+1,(2i,2j,2k)} - \hat{U}_{l+1,(2i,2j,2k)} \,. \tag{9}$$

This definition shows that knowing the cell average of the coarsest cell and details of all successively finer cells is equivalent to knowing the cell-averaged values of all finer cells. Implicit mesh adaption is achieved by considering details larger than a pre-defined level-dependent threshold ε, only. As details become negligible, i.e. $||d|| < \varepsilon$, further grid refinement is not necessary, as a finer mesh does not lead to significantly better results than interpolation from a coarser grid.

For efficiency reasons, we follow the approach of Rossinelli et al. [27] and apply $\mathcal{P}$, $\mathcal{Q}$, and all other operations, e.g. the numerical flux estimation, always on a set of multiple cells, which is called a *block*. The refinement of cells occurs block-wise, too, i.e., all cells of a block are refined as soon as one single cell in the block triggers refinement. A two-dimensional example of the resulting tree structure for a maximum refinement level of $l_{max} = 3$ is shown in Fig. 2. In this example, we start with one single block on the coarsest level, which is successively refined three times to give the maximum resolution in the region of interest.

The following definitions are introduced for the tree-structure to reflect the relationship between different blocks. Taking the single block at the coarsest level $l = 0$ from Fig. 2, the four blocks which are at the next finer level $l = 1$ are called *children*, the blocks at the next level $l = 2$ are correspondingly the *grandchildren*. Vice versa, we speak of *parent* and *grandparent* blocks. When a block does not have any children, it is called a *leaf*. The governing equations are evolved in time only on leaves, all other blocks receive their values from their children by the projection operation eq. (7).

When performing $\mathcal{E}$ (or other operations) close to the edge of a block, data from neighboring blocks are required. We apply the approach of Han et al. [12] who use halo cells for each block to facilitate these operations without requiring

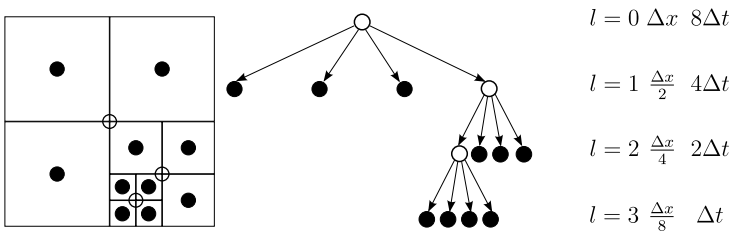

Fig. 2. Sketch of the multiresolution discretization: Grid representation with locally refined regions (left) with $l_{max} = 3$ in two dimensions. The graph shows the tree-structure with corresponding level labels, cell sizes, and time-step sizes for a local time-stepping algorithm. In the grid representation and the tree, existing blocks are shown as circles, where empty circles denote further refined blocks and filled circles mark leaves.

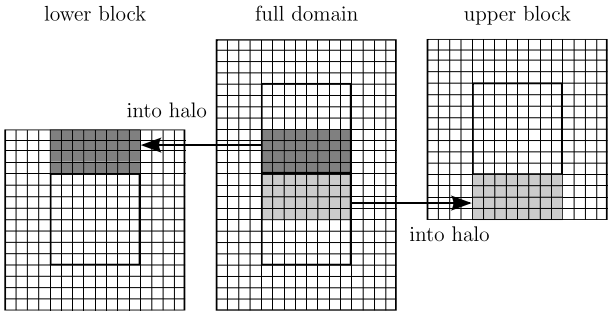

Fig. 3. Relationship of internal cells and halo cells for two neighboring blocks on the same level. In the center, the actual domain of two blocks with surrounding halo cells for external boundary conditions is shown. Each block is displayed separately to the left and right with its own halo cells. The internal cells which are halo cells for these blocks are marked grey.

frequent data exchange with neighboring blocks. Halo cells overlap with internal cells from neighboring blocks or external boundary conditions and contain copies of their states without being evolved themselves. These halo cells are then used to update the solution of internal cells in time. Halo cells need to be updated after each stage to be consistent. A 2D example for a domain with two blocks is shown in Fig. 3.

When evaluating the divergence of the numerical flux function $\mathcal{D}(\overline{U})$ at resolution jumps, conservation may be violated. For two neighboring leaves at levels l and $l+m$, with the outgoing flux being computed at level l and the incoming flux at level $l+m$ at their block boundaries, the flux-reconstruction operation performed on different levels may result in a mismatch of the incoming and outgoing fluxes. This mismatch is corrected by overwriting the fluxes of the coarser cell at the resolution jump with the fluxes computed on the finer mesh [29]. Note that fluxes of successive iterations need to be scaled with the different time-step sizes to ensure conservation. This way, we maintain strict conservation at cell patches between leaves on different resolution levels.

3. Adaptive local time-stepping scheme

The fixed cell-size ratio of successive refinement levels allows for the efficient formulation of a local time-stepping (LTS) scheme [8]. The level-dependent increment Δt_l is scaled from the finest admissible stepsize at the maximum refinement level $\Delta t_{l_{max}}$

$$\Delta t_l = \Delta t_{l_{max}} \cdot 2^{l_{max}-l} \tag{10}$$

for an arbitrary level l, where l_{max} is the maximum number of refinement levels, and $\Delta t_{l_{max}}$ the time-step size computed with the cell size of the finest level. This leads to an improved efficiency of the scheme as compared to the CTS approach, where all cells are integrated in time with $\Delta t_{l_{max}}$ regardless of their resolution. Drawbacks of the LTS scheme are the necessary time synchronization at resolution jumps and the constant time-step size Δt_l within each full cycle of the coarsest level [8]. Therefore, the time-step size adaption loses efficiency with increasing number of refinement levels. For example, for a setup with $l_{max} = 4$, $\Delta t_{l_{max}}$ is updated only after $2^4 = 16$ full cycles on l_{max}. For a setup with $l_{max} = 8$, the earliest possible adjustment of $\Delta t_{l_{max}}$ occurs after $2^8 = 256$ full cycles on l_{max}. In case of strong non-linear effects such as wave-steepening or bubble collapse events, this procedure may result in severe stability issues.

In this work, we propose a fully adaptive local time-stepping (ALTS) algorithm for multiresolution simulations to solve the aforementioned limitations. We split the evolution operation $\mathcal{E}$ into the evaluation of the divergence of the numerical flux functions $\mathcal{F} = \mathcal{F}(\overline{U})$, and the time integration $\mathcal{T} = \mathcal{T}\left(\overline{U}^{(n)}, \mathcal{D}(\overline{U}_1), \mathcal{D}(\overline{U}_2), \Delta t^{(n)}\right)$, so that

$$\mathcal{T} \circ \mathcal{F} = \mathcal{E}\,. \tag{11}$$

The key step to allow for instantaneous time-step size adaptivity is to apply the projection and prediction operations to the numerical divergence of the flux functions in halo cells at resolution jumps. The halo cells are integrated in time together

with the internal cells according to their level-dependent time-step size. This is mathematically equivalent to performing first the time integration of the internal cells followed by the projection and prediction to update the halo cells, which is shown in the following derivation.

The projection operation (7) with an Euler-forward time update can be written as

$$
\begin{aligned}
\overline{U}^{(n+1)}_{l,(i,j,k)} &= \mathcal{Q}\overline{U}^{(n+1)}_{l+1,(2i,2j,2k)} \\
&= \frac{1}{2^D}\sum_{\alpha=0}^{i_{max}}\sum_{\beta=0}^{j_{max}}\sum_{\gamma=0}^{k_{max}} \overline{U}^{(n+1)}_{l+1,(2i+\alpha,2j+\beta,2k+\gamma)} \\
&= \frac{1}{2^D}\sum_{\alpha=0}^{i_{max}}\sum_{\beta=0}^{j_{max}}\sum_{\gamma=0}^{k_{max}} \left[\overline{U}^{(n)}_{l+1,(2i+\alpha,2j+\beta,2k+\gamma)} + \Delta t_{l+1}\mathcal{D}\left(\overline{U}^{(n)}_{l+1,(2i+\alpha,2j+\beta,2k+\gamma)}\right)\right] \\
&= \frac{1}{2^D}\sum_{\alpha=0}^{i_{max}}\sum_{\beta=0}^{j_{max}}\sum_{\gamma=0}^{k_{max}} \overline{U}^{(n)}_{l+1,(2i+\alpha,2j+\beta,2k+\gamma)} \\
&\quad + \Delta t_{l+1}\frac{1}{2^D}\sum_{\alpha=0}^{i_{max}}\sum_{\beta=0}^{j_{max}}\sum_{\gamma=0}^{k_{max}} \mathcal{D}\left(\overline{U}^{(n)}_{l+1,(2i+\alpha,2j+\beta,2k+\gamma)}\right) \\
&= \overline{U}^{(n)}_{l,(i,j,k)} + \Delta t_{l+1}\mathcal{Q}\mathcal{D}\left(\overline{U}^{(n)}_{l+1,(2i,2j,2k)}\right) \\
&= \overline{U}^{(n)}_{l,(i,j,k)} + \Delta t_{l+1}(\mathcal{Q}\circ\mathcal{F})\overline{U}^{(n)}_{l+1,(2i,2j,2k)} .
\end{aligned}
$$

The prediction operation (8) yields

$$
\begin{aligned}
\hat{U}^{(n+1)}_{l+1,(2i+i_0,2j+j_0,2k+k_0)} &= \mathcal{P}\overline{U}^{(n+1)}_{l,(i,j,k)} \\
&= \overline{U}^{(n+1)}_{l,(i,j,k)} + \\
&\quad (-1)^{i_0}Q_x^{s,(n+1)} + (-1)^{j_0}Q_y^{s,(n+1)} + (-1)^{k_0}Q_z^{s,(n+1)} + \\
&\quad (-1)^{(i_0+j_0)}Q_{xy}^{s,(n+1)} + (-1)^{(i_0+k_0)}Q_{xz}^{s,(n+1)} + \\
&\quad (-1)^{(j_0+k_0)}Q_{yz}^{s,(n+1)} + (-1)^{(i_0+j_0+k_0)}Q_{xyz}^{s,(n+1)} \\
&= \overline{U}^{(n)}_{l,(i,j,k)} + \Delta t_l\mathcal{D}\left(\overline{U}^{(n)}_{l,(i,j,k)}\right) + \\
&\quad (-1)^{i_0}Q_x^{s,(n+1)} + (-1)^{j_0}Q_y^{s,(n+1)} + (-1)^{k_0}Q_z^{s,(n+1)} + \\
&\quad (-1)^{(i_0+j_0)}Q_{xy}^{s,(n+1)} + (-1)^{(i_0+k_0)}Q_{xz}^{s,(n+1)} + \\
&\quad (-1)^{(j_0+k_0)}Q_{yz}^{s,(n+1)} + (-1)^{(i_0+j_0+k_0)}Q_{xyz}^{s,(n+1)} .
\end{aligned}
$$

The $Q_\alpha^{s,(n+1)}$ terms change accordingly, for any component α. For example, $\alpha = x$ can be written as

$$
\begin{aligned}
Q_x^{s,(n+1)} &= \sum_{m=1}^{s}\gamma_m\left(\overline{U}^{(n+1)}_{l,(i+m,j,k)} - \overline{U}^{(n+1)}_{l,(i-m,j,k)}\right) \\
&= \sum_{m=1}^{s}\gamma_m\left(\overline{U}^{(n)}_{l,(i+m,j,k)} + \Delta t_l\mathcal{D}\left(\overline{U}^{(n)}_{l,(i+m,j,k)}\right) - \overline{U}^{(n)}_{l,(i-m,j,k)} - \Delta t_l\mathcal{D}\left(\overline{U}^{(n)}_{l,(i-m,j,k)}\right)\right) \\
&= \sum_{m=1}^{s}\gamma_m\left(\overline{U}^{(n)}_{l,(i+m,j,k)} - \overline{U}^{(n)}_{l,(i-m,j,k)}\right) + \\
&\quad \Delta t_l\sum_{m=1}^{s}\gamma_m\left(\mathcal{D}\left(\overline{U}^{(n)}_{l,(i+m,j,k)}\right) - \mathcal{D}\left(\overline{U}^{(n)}_{l,(i-m,j,k)}\right)\right) \\
&= Q_x^{s,(n)} + \Delta t_l\sum_{m=1}^{s}\gamma_m\left(\mathcal{D}\left(\overline{U}^{(n)}_{l,(i+m,j,k)}\right) - \mathcal{D}\left(\overline{U}^{(n)}_{l,(i-m,j,k)}\right)\right) \\
&= Q_x^{s,(n)} + \Delta t_l Q_{\mathcal{D},x}^{s,(n)} .
\end{aligned}
$$

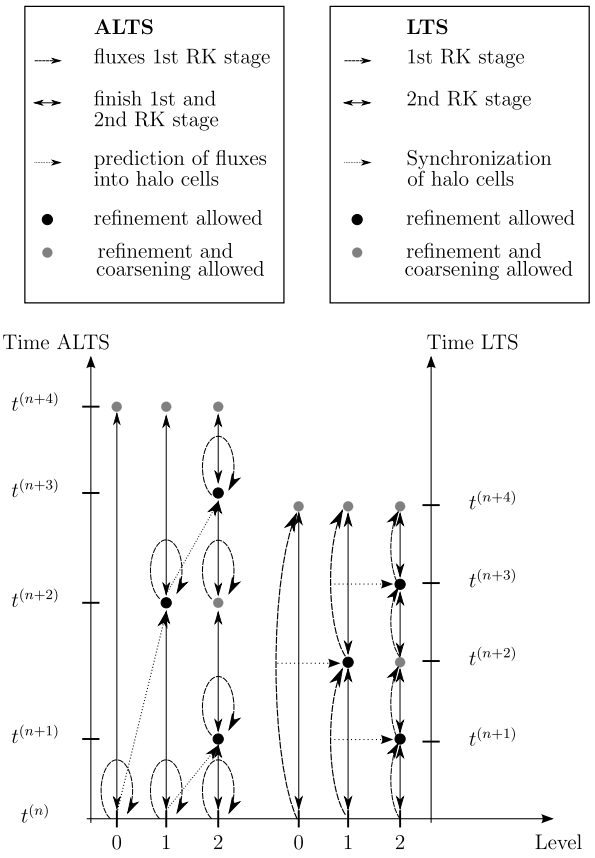

Fig. 4. Sketch of the time integration scheme: ALTS with $\Delta t^{(n+i)} \neq \Delta t^{(n+j)}$, $i \neq j$ (left) and classical LTS (right). See also Domingues et al. [8] for a similar presentation of LTS.

Combining these operations for all terms $Q_\alpha^{s,(n+1)}$ demonstrates the equivalence of the new approach with the standard time integration and projection operations of cell-averaged values (here for $i_0 = j_0 = k_0 = 0$)

$$\begin{aligned}\hat{U}^{(n+1)}_{l+1,(2i,2j,2k)} = {} & \overline{U}^{(n)}_{l,(i,j,k)} + Q_x^{s,(n)} + Q_y^{s,(n)} + Q_z^{s,(n)} + \\ & Q_{xy}^{s,(n)} + Q_{xz}^{s,(n)} + Q_{yz}^{s,(n)} + Q_{xyz}^{s,(n)} + \\ & \Delta t_l \left[\mathcal{D}\left(\overline{U}^{(n)}_{l,(i,j,k)}\right) + Q_{\mathcal{D},x}^{s,(n)} + Q_{\mathcal{D},y}^{s,(n)} + Q_{\mathcal{D},z}^{s,(n)} + \right. \\ & \left. Q_{\mathcal{D},xy}^{s,(n)} + Q_{\mathcal{D},xz}^{s,(n)} + Q_{\mathcal{D},yz}^{s,(n)} + Q_{\mathcal{D},xyz}^{s,(n)} \right] \\ = {} & \hat{U}^{(n)}_{l+1,(2i,2j,2k)} + \Delta t_l (\mathcal{P} \circ \mathcal{F}) \overline{U}^{(n)}_{l,(i,j,k)} \,.\end{aligned}$$

In other words, instead of integrating cells close to resolution jumps in time, we only compute the divergence of cell-face fluxes for both coarser and finer cells at the resolution jump. Then, we exchange them in the halo cells and integrate them in time for the finer block with its level-dependent time-step size. Halo cells at resolution jumps are now at the same time instant as the internal cells, hence we avoid costly synchronization in time which is necessary for the standard LTS scheme. In fact, the temporal integration of the coarser level is postponed until all finer levels reach the same time. This allows for adapting the time-step size after every full cycle on the finest level, and ensures strongly improved time-step size adaptivity.

Our scheme imposes no limits on the number of resolution jumps between two neighboring leaves. Assume two neighboring blocks, with block A being a leaf at level l and block B a leaf at level $l+m$ with $m = 2$. First, halo values are exchanged at level l, thus the grandparent block of block B has updated halo values. Second, the halo cells are predicted twice, first to the parent block of block B, and from there to block B itself. Third, the predictions in the halo cells at level $l+2$ are evaluated 2^2 times until the neighboring levels are synchronous again. This scheme works accordingly for $m > 2$.

Fig. 4 illustrates our new algorithm in comparison to the classical LTS. The basic algorithm works as follows: the divergence of cell-face fluxes on all parent and child levels are computed. They are projected to update divergences of parent blocks in the full tree, exchanged with neighboring blocks in their halo cells, and then predicted to update halo cells at resolution jumps. The evolution is finished by finally performing the integration in time on the target level. In short notation, the full step is abbreviated with the updated evolution operator

$$\tilde{\mathcal{E}} = \mathcal{T} \circ \mathcal{P} \circ \mathcal{Q} \circ \mathcal{F} \,. \tag{12}$$

Following Domingues et al. [8], the three basic steps to evolve the numerical solution from $\overline{U}^{(n)}$ to $\overline{U}^{(n+1)}$ can be expressed as

1. **Refinement**: $\mathcal{R}\overline{U}^{(n)} \rightarrow \overline{U}^{(n+)}$
2. **Evolution**: $\tilde{\mathcal{E}}\overline{U}^{(n+)} \rightarrow \tilde{\overline{U}}^{(n+1)}$
3. **Coarsening**: $\mathcal{C}(\varepsilon)\tilde{\overline{U}}^{(n+1)} \rightarrow \overline{U}^{(n+1)}$.

Here $\mathcal{R}$ is the refinement operator and $\mathcal{C}(\varepsilon)$ the coarsening operator with the coarsening threshold ε.

The main aspects of one time-step iteration in this scheme are:

1. Each macro cycle extends from $t^{(n)}$ to $t^{(n+2^{l_{max}})}$.
2. Each sub-cycle can be described by the tuple (τ, ς). $0 \leq \tau < 2^{l_{max}}$ describes the number of full time-step iterations on the finest level (micro time step) per iteration on the coarsest level (macro time step). $0 \leq \varsigma < \varsigma_{max}$ describes the number of intermediate steps for the explicit time integration scheme. E.g., for the 2nd-order RK-TVD scheme employed here, $\varsigma_{max} = 2$.
3. All sub-cycles τ with $\varsigma = 0$ start with an update of the current time-step size at the finest level $\Delta t^{\tau}_{l_{max}}$. Time-step sizes on all coarser levels accumulate the evolved steps and yield
$$\Delta t^{\tau}_{l} = \sum_{i=0}^{2^{(l_{max}-l)}-1} \Delta t^{\tau+i}_{l_{max}}. \tag{13}$$
4. In the first cycle of each macro time step, i.e. cycle $(0, 0)$, we compute the divergence of the fluxes $(\mathcal{F})$ for the first RK stage for all levels. We then perform the projection and prediction of the divergence to update halo cells at resolution jumps $(\mathcal{Q}, \mathcal{P})$.
5. In each following sub-cycle (τ, ς), leaves at all levels l which fulfill the constraint
$$(\tau + \varsigma) \bmod 2^{l_{max}-l} = 0$$
are integrated in time $(\mathcal{T})$. Afterwards, cells at the parent levels are updated through cell average projection $(\mathcal{Q})$. Then, flux divergences are computed $(\mathcal{F})$, projection is performed, and halo cells at jump conditions are filled by prediction $(\mathcal{Q}, \mathcal{P})$.
6. In each sub-cycle, refinement $(\mathcal{R})$ and coarsening $(\mathcal{C})$ can be performed after time integration $(\mathcal{T})$. The condition for refining level l again is
$$(\tau + \varsigma) \bmod 2^{l_{max}-l} = 0,$$
i.e. this level was integrated in this sub-cycle. For coarsening, the more restrictive condition
$$(\tau + \varsigma) \bmod 2^{l_{max}-(l-1)} = 0$$
is applied. Note that a leaf at level l can only be removed when also the parent level was updated in time during this iteration. This is required to allow for a consistent computation of the details as refinement criterion.
7. The last sub-cycle $(2^{l_{max}} - 1, \varsigma_{max} - 1)$ ends with the time integration of the second RK stage for all levels.

The scheme allows an update of $\Delta t^{\tau}_{l_{max}}$ during each full cycle at the finest level. The update ensures that the CFL-condition is fulfilled at every level at all times τ, which is demonstrated in the following, for simplicity, for the two finest levels l_{max} and $l_{max} - 1$. The maximum wave-speed $||u_i \pm c||^{\tau}_{\infty}$ is computed at all levels from the last completed full RK step and is used to determine the time-step size $\Delta t^{\tau}_{l_{max}}$ from the CFL-condition (5), giving $\Delta t^{\tau}_{l_{max}}$. The timestep size $\Delta t^{\tau+1}_{l_{max}}$ is computed analogously from the maximum wave-speed $||u_i \pm c||^{\tau+1}_{\infty}$. The time-step size at level $l_{max} - 1$ is $\Delta t^{\tau}_{l_{max}-1} = \Delta t^{\tau}_{l_{max}} + \Delta t^{\tau+1}_{l_{max}}$. We analyze at which level the maximum wave-speed $||u_i \pm c||^{\tau}_{\infty}$ occurs during two time steps on the finest level to estimate whether the time-step size at levels l_{max} and $l_{max} - 1$ is within the bounds of the CFL-criterion:

- $||u_i \pm c||^{\tau}_{\infty} = ||u_i \pm c||^{\tau}_{\infty,l_{max}} > ||u_i \pm c||^{\tau}_{\infty,l_{max}-1}$ and $||u_i \pm c||^{\tau+1}_{\infty} = ||u_i \pm c||^{\tau+1}_{\infty,l_{max}} > ||u_i \pm c||^{\tau}_{\infty,l_{max}-1}$: the maximum wave-speed in the domain occurs for both time steps at level l_{max}, the maximum admitted time-step size at level $l_{max} - 1$ therefore is larger than $\Delta t^{\tau}_{l_{max}-1} = \Delta t^{\tau}_{l_{max}} + \Delta t^{\tau+1}_{l_{max}}$. Hence, the CFL-condition is fulfilled at $l_{max} - 1$ and l_{max}.
- $||u_i \pm c||^{\tau}_{\infty} = ||u_i \pm c||^{\tau}_{\infty,l_{max}-1} > ||u_i \pm c||^{\tau}_{\infty,l_{max}}$ and $||u_i \pm c||^{\tau+1}_{\infty} = ||u_i \pm c||^{\tau}_{\infty,l_{max}-1} > ||u_i \pm c||^{\tau+1}_{\infty,l_{max}}$: the maximum wave-speed in the domain occurs for both time steps at level $l_{max} - 1$, therefore $\Delta t^{\tau}_{l_{max}-1} = 2 \cdot \Delta t^{\tau}_{l_{max}} = 2 \cdot \Delta t^{\tau+1}_{l_{max}}$. Hence, the CFL-condition is fulfilled at $l_{max} - 1$ and l_{max}.

- $||u_i \pm c||^{\tau}_{\infty} = ||u_i \pm c||^{\tau}_{\infty,l_{max}-1} > ||u_i \pm c||^{\tau}_{\infty,l_{max}}$ and $||u_i \pm c||^{\tau+1}_{\infty} = ||u_i \pm c||^{\tau+1}_{\infty,l_{max}} > ||u_i \pm c||^{\tau}_{\infty,l_{max}-1}$: the level of the maximum wave-speed changes after the first time step. For level $l_{max}-1$, $\Delta t^{\tau}_{l_{max}-1} = 2 \cdot \Delta t^{\tau}_{l_{max}}$ satisfies the CFL-condition exactly, $2 \cdot \Delta t^{\tau+1}_{l_{max}} < 2 \cdot \Delta t^{\tau}_{l_{max}}$ is too restrictive, hence $\Delta t^{\tau}_{l_{max}-1} = \Delta t^{\tau}_{l_{max}} + \Delta t^{\tau+1}_{l_{max}}$ also satisfies the CFL-condition at both levels $l_{max}-1$ and l_{max}.

Thus, the ALTS scheme provides a CFL-number which globally is always within the bounds of the prescribed stability criterion for every RK cycle.

4. Examples

The following examples illustrate the accuracy, improved stability, and efficiency of the proposed scheme. Grid adaptation is employed using the MR analysis with level- and dimension-dependent error levels

$$\varepsilon_l = \varepsilon_{\text{ref}} \cdot \mathrm{e}^{(-D \cdot (l - l_{max}))}\,, \tag{14}$$

with the number of dimensions D. Unless stated otherwise, we use $\varepsilon_{\text{ref}} = 0.01$ for the refinement from $l_{max}-1$ to l_{max}, and each simulation is performed with one block at level 0 using 16 internal cells in each spatial direction.

4.1. Accuracy-order analysis

Two one-dimensional test cases are presented to demonstrate the accuracy of the underlying methods of our adaptive local time-stepping scheme. First, we solve the linear scalar advection equation

$$\frac{\partial u}{\partial t} + \frac{\partial u}{\partial x} = 0 \tag{15}$$

for a sinusoidal profile $u_0(x) = 1 + 0.25\sin(2\pi x)$ on the one-dimensional periodic domain $x \in [0, 1]$. The problem is advanced to a final time of $t = 1$, when the wave is again at its initial position. The second test case is the non-linear steepening of a sinusoidal pressure wave $p_0(x) = 1 + 0.25\sin(2\pi x)$ on the one-dimensional periodic domain $x \in [0, 1]$. The one-dimensional Euler equations

$$\begin{aligned} \frac{\partial \rho}{\partial t} + \frac{\partial u\rho}{\partial x} &= 0\,, \\ \frac{\partial \rho u}{\partial t} + \frac{\partial u\rho u}{\partial x} + \frac{\partial p}{\partial x} &= 0\,, \\ \frac{\partial \rho e}{\partial t} + \frac{\partial u(\rho e + p)}{\partial x} &= 0\,, \end{aligned} \tag{16}$$

govern the problem, where ρ is the density, u the velocity, p the pressure, and e the specific energy. The system is closed by the stiffened-gas equation-of-state

$$p = (\gamma - 1)\rho e - \gamma p_{\infty}\,, \tag{17}$$

with the material parameters γ for the ratio of specific heats and p_{∞} for the background pressure. Here, we use $\gamma = 1.4$ and $p_{\infty} = 0$. Initial conditions for velocity and density fields are obtained from the Rankine-Hugoniot conditions for an ideal gas ($\gamma = 1.4$, $p_{\infty} = 0$). The problem is advanced to a final time of $t = 0.2$, when the wave has steepened already but still is continuous. For both cases, we present convergence rates for the spatial scheme (WENO 5), the standard RK2-TVD time-integration scheme, and the RK3-TVD time-integration scheme to demonstrate the applicability to higher-order explicit time-integration schemes. The simulations for the spatial error are run with CFL = 10^{-3} to minimize the temporal error, and $\varepsilon_{\text{ref}} = 0.001$ for a refinement from level 0 to level 1. The simulations for the temporal error are computed on a mesh with maximum level $l_{max} = 4$.

Error plots of the L_1 norm of the density field

$$L_1 = \frac{1}{V} \sum_n \frac{|\rho_{n,exact} - \rho_{n,sim}|}{\rho_{n,exact}} dV_n\,, \tag{18}$$

are given in Fig. 5 for the two cases, numeric values are given in Table 1. The convergence rates of both the linear and the non-linear examples agree well with the values expected from theory. Only close to CFL= 1.0, the convergence rate of RK2 deviates from the expected value. Note that for RK3 the second-order treatment at resolution jumps [7,22] reduces the global order of the convergence to slightly less than three.

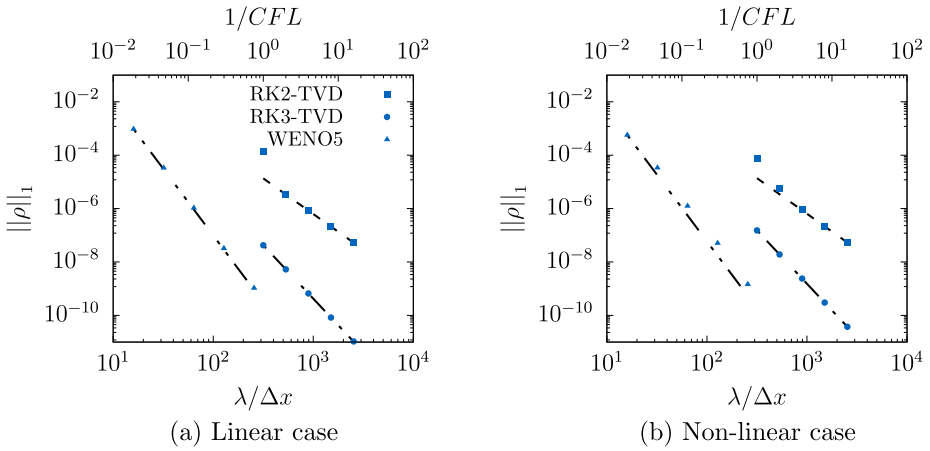

Fig. 5. Accuracy-order analysis for the linear (a) and non-linear (b) advection cases: temporal errors for RK2-TVD (■) and RK3-TVD (●), and spatial error for WENO5 (▲). For comparison, convergence plots for second (— —), third (— -), and fifth (— - -) order are given.

Table 1
The spatial and temporal accuracy of the linear sine-wave advection and non-linear sine-wave steepening for RK2-TVD, RK3-TVD, and WENO5 schemes.

Type	resolution	L_1 error linear	L_1 accuracy linear	L_1 error non-linear	L_1 accuracy non-linear
	1	1.3450E-4		7.7143E-5	
	0.5	3.3719E-6	6.32	5.4441E-6	3.76
temporal	0.25	8.4330E-7	2.00	8.8377E-7	2.48
(RK2-TVD)	0.125	2.1083E-7	2.00	2.1691E-7	2.02
	0.0625	5.2706E-8	2.00	5.3878E-8	2.01
	1	4.2420E-8		1.5239E-7	
	0.5	5.3045E-9	2.83	1.9113E-8	2.82
temporal	0.25	6.6339E-10	2.83	2.3964E-9	2.82
(RK3-TVD)	0.125	8.3011E-11	2.83	3.0006E-10	2.83
	0.0625	1.0551E-11	2.81	3.7514E-11	2.83
	16	9.4091E-4		5.6337E-4	
	32	3.3506E-5	5.30	3.3520E-5	4.10
spatial	64	1.0500E-6	5.65	1.2419E-6	5.20
(WENO5)	128	3.2178E-8	5.71	5.0419E-8	4.96
	256	1.0517E-9	5.53	1.4527E-9	5.89

4.2. One-dimensional examples

Two one-dimensional testcases with strong discontinuities and therefore strong temporal gradients in the wave-speeds are considered. The simulations are again governed by the compressible Euler equations (16).

The first setup is the inviscid shock-tube problem of Sod [30]. The initial conditions for a domain of length 1.0 are

$$(\rho, u, p) = \begin{cases} (1.0, 0.0, 1.0) & ,0.0 \leq x < 0.5 \\ (0.125, 0.0, 0.1) & ,0.5 \leq x \leq 1.0 \end{cases}. \tag{19}$$

The domain is refined to $l_{max} = 7$ and the final simulation time is $t = 0.2$.

The second one-dimensional case is the two blast-waves problem of Woodward and Colella [31]. The initial conditions are

$$(\rho, u, p) = \begin{cases} (1.0, 0.0, 1000.0) & ,0.0 \leq x < 0.1 \\ (1.0, 0.0, 0.01) & ,0.1 \leq x < 0.9 \\ (1.0, 0.0, 100.0) & ,0.9 \leq x \leq 1.0 \end{cases} \tag{20}$$

The domain is refined to $l_{max} = 7$ and the final simulation time is $t = 0.038$.

Results for both 1D test cases are shown in Fig. 6. The applied CFL-number is CFL= 1.0. The standard local time stepping cannot resolve the wave dynamics for this high CFL-number and becomes unstable within the first macro time step in both cases. The ALTS scheme allows for stable simulations in both cases. The results show good agreement with the ones from an equally-spaced grid without adaptive mesh. This underlines that the ALTS scheme shows the same temporal stability behavior as an homogeneous grid without local spatial adaptation, which is not the case for the classical LTS scheme.

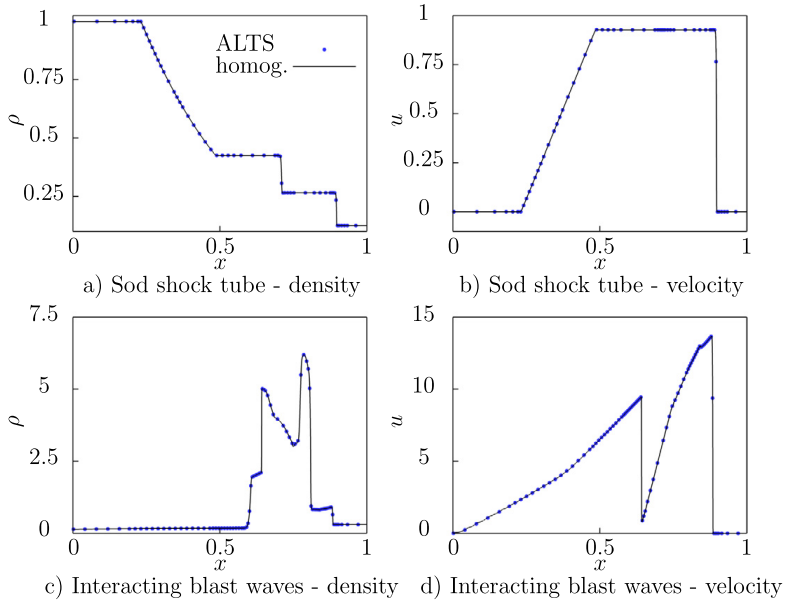

Fig. 6. One-dimensional examples. Upper half: Sod shock tube, density a) and velocity b) profiles at $t = 0.2$. Lower half: interacting blast waves, density c) and velocity d) at $t = 0.038$. Shown are results for a homogeneous grid (solid line) and an adaptive grid ($l_{max} = 7$) applying ALTS (dots) with CFL= 1.0. The results of every tenth cell are shown for ALTS.

4.3. Two-dimensional example

As two-dimensional test case we present the non-symmetric shock-induced collapse of a bubble near a rigid wall [20]. This problem is of practical relevance in a range of applications, e.g. shock-induced lithotripsy [21]. The wave-speed increases strongly during the bubble collapse, therefore instant adaption of the time-step size is required. Initial conditions for an axisymmetric domain $[4.0 \times 8.0]\,\mu$m, discretized with $l_{max} = 7$, two blocks in y-direction and one block in x-direction on $l = 0$ (effective resolution 2048×4096 cells), are

$$(\rho, u, v, p) = \begin{cases} (1011.05, 0.0, 21.36, 351 \times 10^5) & \text{post-shock water,} \\ (998.0, 0.0, 0.0, 10^5) & \text{pre-shock water,} \\ (1.2, 0.0, 0.0, 10^5) & \text{air bubble} \end{cases} \tag{21}$$

for a 35 MPa shock, which hits the bubble at $t = 0.0$. To model the second phase, we introduce a level-set function. The initial level-set field for the bubble is

$$\phi = -R_0 + \sqrt{(x - x_0)^2 + (y - y_0)^2} \tag{22}$$

with the bubble radius $R_0 = 50$ µm, $x_0 = 0$, and $y_0 = 0.7$ mm. This leads to a stand-off distance of $2R_0$ of the bubble center from the wall. The bubble is resolved with 256 cells per initial radius on l_{max}, and we use CFL= 0.9 for the simulation. A sketch of this setup, which was investigated by Johnsen and Colonius [20], is shown in Fig. 7. We consider the compressible Euler equations in axisymmetric formulation and employ a level-set approach for multi-phase flows. The system is closed by the complete stiffened-gas equation-of-state

$$p + \gamma p_\infty = (\gamma - 1)\rho(e + E_\infty)\,, \tag{23}$$

where E_∞ is the energy translation factor. We use $\gamma = 4.4$, $p_\infty = 6.0 \times 10^8$, $E_\infty = 7.456 \times 10^6$ for water, and $\gamma = 1.4$, $p_\infty = 0$, $E_\infty = 0$ for air [17,23].

The pressure and axial velocity fields are shown in Fig. 8 at $t = 2.47$ ms and $t = 2.48$ ms for both schemes. At $t = 2.47$ ms, the bubble is already strongly deformed. The maximum pressure regions are slightly shifted from the center axis, and coincide with the location where the bubble is thinnest (a). The high-speed water-jet has formed in the inner part of the bubble (b). For this instant, both schemes exhibit the same results. At $t = 2.48$ ms, the jet strikes the downstream bubble wall, and the bubble breaks up at the location of the maximum pressure in the previous instant. The jet accelerates even further, and a strong shock wave can be observed propagating away from the bubble (c, d). This leads to a strong increase in the wave speed, so the time-step size needs to be adapted immediately to satisfy the stability criterion. The LTS scheme cannot provide this immediate adaption, and spurious oscillations occur at the wave front of the water hammer. These oscillations indicate the onset of nonlinear numerical instability near the wave front. The ALTS provides immediate time-step size adaption, and does not exhibit such spurious oscillations.

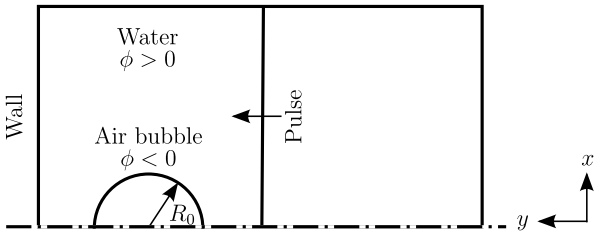

Fig. 7. Initial conditions for the shock-induced bubble collapse near a rigid wall in two dimensions.

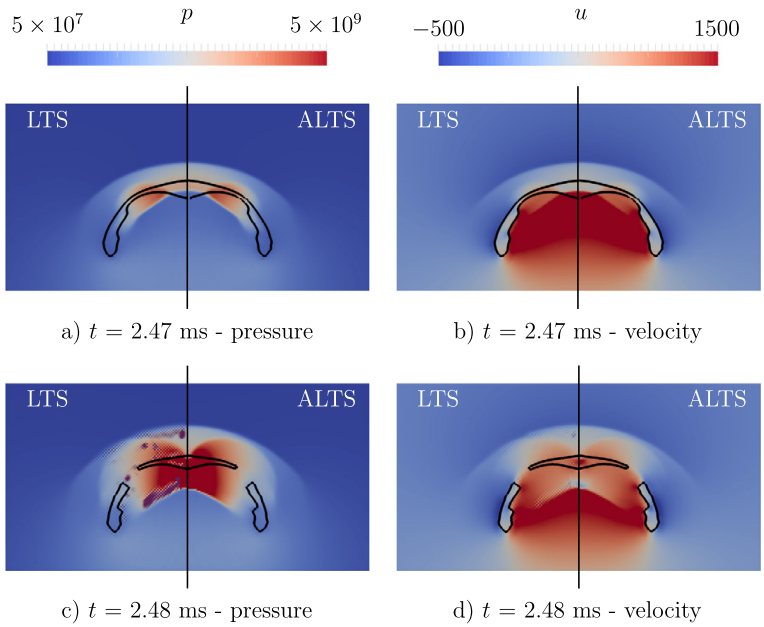

Fig. 8. Contour plots for LTS (left) and ALTS (right) at two different time instants: at $t = 2.47$ ms pressure (a) and streamwise velocity (b), and at $t = 2.48$ ms pressure (c) and streamwise velocity (d). The interface is denoted by the black line.

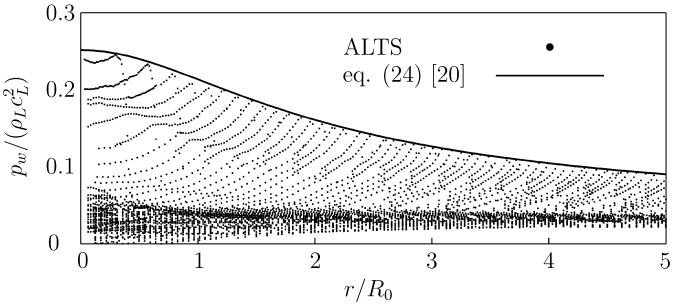

Fig. 9. Pressure profile along the wall at different instants with the analytical approximation of [20] (eq. (24)).

Johnsen and Colonius [20] have proposed an empirical analytical profile for the localized maximum wall pressure as function of the circular off-center distance along the wall

$$p_w\left(\frac{r}{R_0}\right) = \frac{c_1}{\sqrt{H_c^2 + (r/R_0)^2}} + c_2\,. \tag{24}$$

Here, c_1 and c_2 are two constants, which are determined from two arbitrary pressure profiles of the temporal evolution, and H_c is the stand-off distance at collapse time. For the given case, $H_c = 1.5$, $c_1 = 0.34$, and $c_2 = 0.025$. In Fig. 9, a series of radial wall-pressure profiles at several time instants is shown together with the asymptotical maximum wall-pressure function eq. (24). The time difference between two subsequent radial profiles is 20 µs, and the first profile shows the pressure profile at $t = 2.80$ ms. Due to the radial spreading, the maximum pressure decreases in time. The overall maximum pressure at the wall infact occurs not at the centerline, but is shifted slightly outwards as the collapsing bubble shields the wall from the incoming pressure wave. This maximum pressure is slightly larger than the prediction of Johnsen and Colonius [20], which was already found earlier for this model configuration [1].

Table 2
Percentage of different operations on computational cost during each full Runge-Kutta cycle. We separate between the update of the time-step size, functions which are introduced for ALTS (*ALTS related*), and other functions which appear both during LTS and ALTS (*common operations*).

simulation	update Δt	ALTS related	common operations
1D (single fluid)	4.9 %	10.7 %	84.4 %
2D (multi-fluid)	2.1 %	5.2 %	92.7 %

4.4. Performance estimation

Finally, we analyze the additional cost due to computational operations which were introduced for the ALTS scheme: the projection and prediction of flux functions and the temporal integration of halo cells. We analyze the results for the one-dimensional single-fluid shock-tube simulation ($l_{max} = 7$) and the two-dimensional multi-fluid shock-bubble interaction ($l_{max} = 8$) presented in sections 4.2 and 4.3. We have performed our numerical tests on a homogeneous cluster of Intel Xeon E5-2697 v3 "Haswell" CPUs with 28 cores at 2.7 GHz and 2.3 GB memory. One-dimensional single-fluid simulations are executed sequentially, on one core only. Two-dimensional multi-fluid results are run in parallel on all 28 cores using 28 MPI ranks. Operations of a full Runge-Kutta cycle are split into three main categories: the update of the time-step size, additional operations that were introduced with the ALTS algorithm (*ALTS related*), and operations that are required for both LTS and ALTS schemes (*common operations*). We compute for each category its share of the compute time over several macro time steps. Results are given in Table 2.

The share of each category varies with the simulation type: the time step size update and ALTS-related operations account for approximately 16% of computational cost in the one-dimensional single-phase simulation, and for approximately 7% in the two-dimensional multi-phase simulation. We conclude that the additional cost has no significant adverse impact on the overall computing efficiency.

5. Conclusion and outlook

We have presented an adaptive local time-stepping scheme for a block-based multiresolution algorithm. The key improvement of the new approach is the projection and prediction of the right-hand-side terms of the governing equations and additional halo-cell time integration. The benefit of the improved time-stepping scheme is full adaptivity of the numerical time-step size down to blocks with highest resolution and, thus, improved stability for larger CFL numbers.

The ALTS scheme is applied to various one- and two-dimensional examples with strong velocity gradients to demonstrate its advantages. Even for large CFL numbers up to CFL = 1.0, our approach allows for stable and accurate simulations. The scheme is not limited to single-phase simulations, but can also be used for multiple phases without constraints on, e.g., the variation of the wave speed across the material interface.

Despite the fact that additional operations are required during each iteration (projection and prediction of the numerical divergence of the flux function, time integration of halo cells), the additional work of the ALTS scheme in comparison to the LTS scheme is negligible for multi-dimensional realistic flow problems. The numerical stability is improved as compared to the classical LTS scheme. Overall, the stability behavior of the constant time-stepping scheme is recovered, which was lost with the introduction of the LTS scheme.

Declaration of competing interest

The authors declare that they have no known competing financial interests or personal relationships that could have appeared to influence the work reported in this paper.

Acknowledgements

The lead author has received funding from German Research Foundation (Deutsche Foschungsgesellschaft, project No. 277161739). The third and fourth author have received funding from the European Research Council (ERC) under the European Union's Horizon 2020 research and innovation programme (grant agreement No. 667483). The authors gratefully acknowledge the Gauss Centre for Supercomputing e.V. for funding this project by providing computing time on the GCS Supercomputer SuperMUC at Leibniz Supercomputing Centre.

References

[1] S. Adami, J. Kaiser, N.A. Adams, I. Bermejo-Moreno, Numerical modeling of shock waves in biomedicine, in: Center for Turbulence Research Proceedings of the Summer Program, 2016.
[2] M. Bendahmane, R. Bürger, R.R. Baier, K. Schneider, Adaptive multiresolution schemes with local time stepping for two-dimensional degenerate reaction-diffusion systems, Appl. Numer. Math. 57 (7) (2009) 1668–1692.
[3] B.L. Bihari, A. Harten, Multiresolution schemes for the numerical solution of 2-D conservation laws I, J. Sci. Comput. 18 (2) (1997) 315–354.

[4] A. Cohen, S. Kaber, S. Müller, M. Postel, Fully adaptive multiresolution finite volume schemes for conservation laws, Math. Comput. 72 (241) (2001) 183–225.
[5] F. Coquel, Q.L. Nguyen, M. Postel, Q.H. Tran, Local time stepping applied to implicit-explicit methods for hyperbolic systems, Multiscale Model. Simul. 8 (2) (2010) 540–570.
[6] R. Deiterding, M.O. Domingues, S.M. Gomes, K. Schneider, Comparison of adaptive multiresolution and adaptive mesh refinement applied to simulations of the compressible Euler equations, J. Sci. Comput. 38 (5) (2016) 173–193.
[7] M.O. Domingues, S.M. Gomes, O. Roussel, K. Schneider, An adaptive multiresolution scheme with local time stepping for evolutionary PDEs, J. Comput. Phys. 227 (8) (2008) 3758–3780.
[8] M.O. Domingues, S.M. Gomes, O. Roussel, K. Schneider, Space-time adaptive multiresolution methods for hyperbolic conservation laws: applications to compressible Euler equations, Appl. Numer. Math. 59 (9) (2009) 2303–2321.
[9] M.O. Domingues, O. Roussel, K. Schneider, An adaptive multiresolution method for parabolic PDEs with time-step control, Int. J. Numer. Methods Eng. 78 (2009) 652–670.
[10] A.K.F. Gomes, M.O. Domingues, K. Schneider, O. Mendes, R. Deiterding, An adaptive multiresolution method for ideal magnetohydrodynamics using divergence cleaning with parabolic-hyperbolic correction, Appl. Numer. Math. 95 (2015) 199–213.
[11] S. Gottlieb, C.-W. Shu, Total variation diminishing Runge-Kutta schemes, Math. Comput. 67 (221) (1998) 73–85.
[12] L.H. Han, X.Y. Hu, N.A. Adams, Adaptive multi-resolution method for compressible multi-phase flows with sharp interface model and pyramid data structure, J. Comput. Phys. 262 (2014) 131–152.
[13] L.H. Han, T. Indinger, X.Y. Hu, N.A. Adams, Wavelet-based adaptive multi-resolution solver on heterogeneous parallel architecture for computational fluid dynamics, Comput. Sci. Res. Dev. 26 (2011) 197–203.
[14] A. Harten, High resolution schemes for hyperbolic conservation laws, J. Comput. Phys. 135 (1983) 260–278.
[15] A. Harten, Adaptive multiresolution schemes for shock computations, J. Comput. Phys. 115 (2) (1994) 319–338.
[16] A. Harten, Multiresolution algorithms for the numerical solution of hyperbolic conservation laws, Commun. Pure Appl. Math. 48 (1995) 1305–1342.
[17] N.A. Hawker, Y. Ventikos, Interaction of a strong shockwave with a gas bubble in a liquid medium: a numerical study, J. Fluid Mech. 701 (2012) 59–97.
[18] B. Hejazialhosseini, D. Rossinelli, M. Bergdorf, P. Koumoutsakos, High order finite volume methods on wavelet-adapted grids with local time-stepping on multicore architectures for the simulation of shock-bubble interactions, J. Comput. Phys. 229 (22) (2010) 8364–8383.
[19] G.-S. Jiang, C.-W. Shu, Efficient implementation of weighted ENO schemes, J. Comput. Phys. 126 (1996) 202–228.
[20] E. Johnsen, T. Colonius, Numerical simulations of non-spherical bubble collapse, J. Fluid Mech. 629 (2009) 231.
[21] K. Kobayashi, T. Kodama, H. Takahira, Shock wave–bubble interaction near soft and rigid boundaries during lithotripsy: numerical analysis by the improved ghost fluid method, Phys. Med. Biol. 56 (19) (2011) 6421–6440.
[22] M.M. Lopes, M.O. Domingues, K. Schneider, O. Mendes, Local time-stepping for adaptive multiresolution using natural extension of Runge–Kutta methods, J. Comput. Phys. 382 (2019) 291–318.
[23] R. Menikoff, B.J. Plohr, The Riemann problem for fluid flows of real materials, Rev. Mod. Phys. 61 (1) (1989) 75–130.
[24] S. Müller, Y. Stiriba, Fully adaptive multiscale schemes for conservation laws employing locally varying time stepping, J. Sci. Comput. 30 (3) (2007) 493–531.
[25] S. Osher, R. Sanders, Numerical approximations to nonlinear conservation laws with locally varying time and space grids, Math. Comput. 41 (164) (1983) 321–336.
[26] D. Rossinelli, B. Hejazialhosseini, P. Hadjidoukas, C. Bekas, A. Curioni, A. Bertsch, S. Futral, S.J. Schmidt, N.A. Adams, P. Koumoutsakos, 11 pflop/s simulations of cloud cavitation collapse, in: Proceedings of the International Conference on High Performance Computing, Networking, Storage and Analysis, SC '13 3, ACM, New York, NY, USA, 2013, pp. 1–13.
[27] D. Rossinelli, B. Hejazialhosseini, D.G. Spampinato, P. Koumoutsakos, Multicore/multi-gpu accelerated simulations of multiphase compressible flows using wavelet adapted grids, J. Sci. Comput. 33 (2) (2011) 512–540.
[28] O. Roussel, K. Schneider, Adaptive multiresolution computations applied to detonations, Z. Phys. Chem. 229 (6) (2015) 931–953.
[29] O. Roussel, K. Schneider, A. Tsigulin, H. Bockhorn, A conservative fully adaptive multiresolution algorithm for parabolic PDEs, J. Comput. Phys. 188 (2003) 493–523.
[30] G.A. Sod, A survey of several finite difference methods for systems of nonlinear hyperbolic conservation laws, J. Comput. Phys. 27 (1) (1978) 1–31.
[31] P. Woodward, P. Colella, The numerical simulation of two-dimensional fluid flow with strong shocks, J. Comput. Phys. 54 (1) (1984) 115–173.

A.2 Investigation of interface deformation dynamics during high-Weber number cylindrical droplet breakup

Investigation of interface deformation dynamics during high-Weber number cylindrical droplet breakup

Author: J.W.J. Kaiser,J.M. Winter,S. Adami,N.A. Adams

Publication: International Journal of Multiphase Flow

Publisher: Elsevier

Date: November 2020

International Journal of Multiphase Flow 132 (2020) 103409

Contents lists available at ScienceDirect

International Journal of Multiphase Flow

journal homepage: www.elsevier.com/locate/ijmulflow

Investigation of interface deformation dynamics during high-Weber number cylindrical droplet breakup

J.W.J. Kaiser*, J.M. Winter, S. Adami, N.A. Adams

Technical University of Munich, Department of Mechanical Engineering, Chair of Aerodynamics and Fluid Mechanics, Boltzmannstraße 15, 85748 Garching, Germany

ARTICLE INFO

Article history:
Received 24 March 2020
Revised 17 June 2020
Accepted 8 July 2020
Available online 17 July 2020

Keywords:
Drop breakup
Shock waves
Shock-interface interaction
Level-set
Multiresolution

ABSTRACT

In this work, we study the interface deformation during the early-stages of breakup of a water column in an ambient flow field by high-resolution numerical simulation. The compressible Navier–Stokes equations govern the motion of the two fluids, and capillary forces and viscous effects are considered. We model the multiphase flow with a level-set based sharp-interface method with conservative interface interaction. The governing equations are discretized with a finite-volume approach with low-dissipation flux reconstruction at cell faces based on a fifth-order WENO scheme, and a third-order Runge–Kutta TVD explicit time integration scheme. We validate our numerical simulations by comparison with experimental reference data.

We achieve an accurate prediction of wave dynamics and interface deformation of the liquid column. Both flattening of the cylinder (first stage) and shearing of the sheet at the droplet equator (second stage) are reproduced. We show that a distinct pressure-wave pattern forms in the supersonic flow region near the cylinder equator after shock passage. These waves interact with the phase interface, resulting in local interface disturbances that coincide with the onset of the second stage. Resolving these waves is essential for the prediction of the hat-like structure at the upstream face of the cylinder during the second stage of the breakup, which so far only has been observed in experimental visualizations of this particular breakup mode. Our results support the connection of the sheet-stripping mechanism with the local formation of recirculation zones. Extending previous work, our high-resolution results indicate that recirculation zones appear at multiple locations along the interface, and are directly linked to the growth of water sheet-forming interface disturbances.

1. Introduction

The breakup of a spherical liquid drop into smaller fragments is of fundamental importance for many technological applications and environmental phenomena, ranging from internal liquid-fuel combustion engines to manufacturing of medical drugs and splatter of rain drops on supersonic aircrafts (Villermaux, 2007). The initial deformation of the drop is driven by the relative velocity with respect to the ambient flow field, which may be realized by injection into a crossflow or sudden acceleration by shock waves, eventually resulting in drop breakup. The characteristics of the breakup process are determined by the relation of inertial forces, viscous forces, and capillary forces acting on the drop.

The breakup process can be classified by two non-dimensional numbers: the Weber number and the Ohnesorge number, which describe the ratio of inertial to capillary forces and the ratio of viscous to capillary forces, respectively. Different breakup modes have been observed in experimental investigations upon variations of these two parameters, resulting in the postulation of five fundamental breakup regimes: vibrational, bag, multi-mode, sheet-stripping, and catastrophic breakup (Guildenbecher et al., 2009). At small Ohnesorge numbers ($Oh < 0.1$), vibrational and bag modes have been observed for small Weber numbers, and sheet-stripping and catastrophic modes for high Weber numbers. The multi-mode breakup has been assumed to be a transitional mode from bag breakup to sheet-stripping (Dai and Faeth, 2001). It occurs either as bag/plume or plume/sheet-stripping breakup. Theofanous et al.

* Corresponding author.
E-mail addresses: jakob.kaiser@tum.de (J.W.J. Kaiser), josef.winter@tum.de (J.M. Winter), stefan.adami@tum.de (S. Adami), nikolaus.adams@tum.de (N.A. Adams).

https://doi.org/10.1016/j.ijmultiphaseflow.2020.103409

(2004) suggested a re-classification of the breakup mechanisms, which is motivated by fundamental physical mechanisms that dominate the breakup process: Rayleigh-Taylor piercing (RTP) and shear-induced entrainment (SIE). RTP is the main instability mode for small Weber numbers, and SIE is the terminal instability mode for increasing Weber numbers. The RTP regime is characterized by ambient fluid penetrating the liquid bulk of the drop. The SIE regime, in comparison, exhibits a shearing of liquid material from the "edge" of the drop.

Systematic experimental and numerical investigations of drop breakup for wide parameter ranges have improved the understanding of the breakup process, we refer to reviews by Guildenbecher et al. (2009) and Theofanous (2011). With regard to numerical investigations, Khosla et al. (2006) were among the first to consider a fully three-dimensional setup. They investigated the breakup process in the low Weber number regime. Since then, further three-dimensional studies of the breakup process in the different regimes have been performed, assuming incompressible flow in the RTP regime (Yang et al., 2017) and fully compressible fluid flow in the SIE regime (Meng and Colonius, 2018). Numerical studies often apply (quasi) two-dimensional setups to decrease the required computational cost for breakup simulations. Supporting this simplification, previous experimental studies observed phenomenological similarity of early-stage interface deformation for (quasi) two-dimensional water columns and three-dimensional spherical drops in crossflow in the shear breakup regime (Igra et al., 2002; Igra and Takayama, 2001a), in particular regarding the flattening of the drop / cylinder and shearing at the equator. Experimental results of shock-column interaction (Igra and Takayama, 2001c; 2003; Sembian et al., 2016) often have been used in two-dimensional numerical studies for model validation on shock-interface interaction (Garrick et al., 2017; Igra and Sun, 2010; Ireland and Desjardins, 2016; Nonomura et al., 2014; Schmidmayer et al., 2017; Terashima and Tryggvason, 2009; Wan et al., 2019; Wang et al., 2018; Xiang and Wang, 2017; Yang and Peng, 2019). Also, more detailed physical investigations of the sheet-stripping process have been performed (Aslani and Regele, 2018; Chen, 2008). More specifically, the experimental setup of Igra and Takayama (2001c) has been used in the seminal work of Meng and Colonius for two-dimensional simulations of the breakup of a liquid column in the SIE regime (Meng and Colonius, 2015). Later, they presented fully three-dimensional simulation results of the breakup of a spherical liquid drop at the same flow conditions (Meng and Colonius, 2018). Analyzing both the breakup of the liquid column and the transient flow field, the important role of near-interface recirculation zones in the sheet-stripping process was reported. These zones appeared at the drop equator and in the wake of the drop. Due to the high Weber number and the low Ohnesorge number of the setup, viscous and capillary forces were explicitly suppressed in these simulations.

In the current work, we consider effects of viscous and capillary forces during breakup of a liquid column in the SIE regime. The setup follows that of Igra and Takayama (2001c). We apply a finite volume approach with low-dissipation shock capturing based on WENO reconstruction (Jiang and Shu, 1996) for an accurate representation of small-scale flow structures, and a third-order strongly-stable Runge–Kutta scheme for explicit time integration (Gottlieb and Shu, 1998). A level-set sharp interface method represents the liquid-gas phase interface, and conservative interface-exchange terms determine the interaction of the two phases (Hu et al., 2006; Luo et al., 2015). A block-structured multiresolution scheme with adaptive local timestepping allows for full spatial and temporal adaptivity (Han et al., 2014; Kaiser et al., 2019). The multiresolution compression enables high computational efficiency even at late stages of the interface deformation, as the mesh adapts to the ongoing liquid-column deformation.

Table 1
Material parameters for the stiffened-gas equation-of-state for water and air.

Fluid	γ [-]	p_∞ [GPa]	μ [Pa s]	σ [10^{-3} N/m]
Water	6.12	0.343	1.0×10^{-3}	72.75
Air	1.4	0.0	1.8×10^{-5}	

The structure of the paper is the following: in Section 2, we briefly discuss the physical model. The numerical model is described in Section 3. In Section 4, we study the results of the shock-induced breakup of a liquid column with an initial diameter of $D_0 = 4.8$mm at a shock Mach number of $Ma_S = 1.47$. We compare our results to experimental data of Igra et al. (2002), Igra and Takayama (2001b,c) and Theofanous et al. (2012), and investigate the influence of viscous and capillary effects. We discuss the formation of a hat-like structure on the upstream face of the cylinder which is known from experimental investigations and link it to the interaction of pressure disturbances with the phase interface during the early deformation stages. For quantitative comparison, we introduce the skewness of the axial deformation to quantify small scales during the ongoing deformation and the main breakup stages. We conclude the work in Section 5.

2. Physical model

The governing equations including viscous and capillary forces read in vector notation

$$\frac{\partial \mathbf{U}}{\partial t} + \nabla^T \cdot \mathbf{F} + \nabla^T \cdot \mathbf{F}_v = \mathbf{X} \tag{1}$$

with

$$\mathbf{U} = \begin{pmatrix} \rho \\ \rho \mathbf{u} \\ E \end{pmatrix}, \qquad \mathbf{F} = \begin{pmatrix} \mathbf{u}\rho \\ \rho \mathbf{u} \otimes \mathbf{u} + p\mathbf{I} \\ \mathbf{u}(E+p) \end{pmatrix}, \qquad \text{and} \qquad \mathbf{F}_v = \begin{pmatrix} 0 \\ \mathbf{T} \\ \mathbf{T} \cdot \mathbf{u} \end{pmatrix}$$

denoting the vector of conservative states, the convective flux vector, and the viscous flux vector, respectively. Here, ρ denotes the density, t the time, $\mathbf{u}$ the velocity vector, p the pressure, $\mathbf{I}$ the identity matrix, $\mathbf{T}$ the Cauchy stress tensor, and E the total energy

$$E = \rho e + \frac{1}{2}\rho \mathbf{u} \cdot \mathbf{u}\,, \tag{2}$$

composed of the internal energy (ρe) and the kinetic energy ($1/2\rho \mathbf{u} \cdot \mathbf{u}$). The vector $\mathbf{X}$ denotes exchange terms between the two phases air and water including capillary and viscous effects, for more details see the following Section 3. The system of equations is closed by the stiffened-gas equation-of-state (EOS)

$$p = (\gamma - 1)\rho e - \gamma p_\infty\,, \tag{3}$$

where the ratio of specific heats γ and the background pressure p_∞ are empirically determined parameters. The stiffened-gas EOS has been widely used in simulations with multiple immiscible compressible fluids. We use this EOS for both fluids air and water, for model parameters see Table 1. Note that for the gas phase with $p_\infty = 0$, the stiffened-gas EOS degenerates to the ideal-gas EOS. The parameters for water are calibrated for the given setup following the procedure described in Johnsen and Colonius (2007) with the experimental data of Gojani et al. (2016), see also Meng and Colonius (2015). Note that the stiffened-gas EOS is an incomplete EOS, providing an inaccurate prediction of the temperature. Since we neglect heat transfer, this deficit is not relevant. For a more detailed discussion as well as an extended EOS the reader is referred to Hawker and Ventikos (2012).

As mentioned above, the breakup behavior during aerodynamic fragmentation is dominated by inertial, viscous, and capillary forces. Inertial forces result in a deformation of the drop,

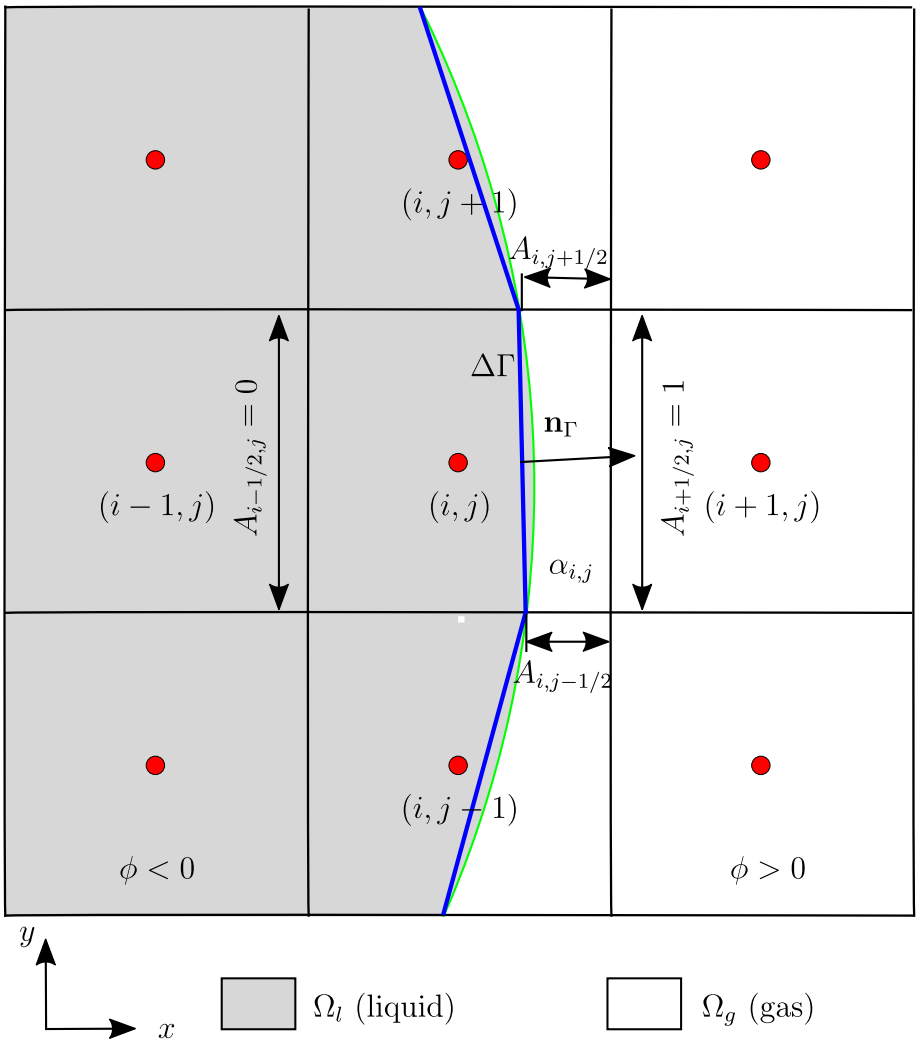

Fig. 1. Schematic finite-volume discretization of the domain Ω on Cartesian square cells. The green line denotes the exact solution, the blue line the linearized approximation by the level-set function. (For interpretation of the references to color in this figure legend, the reader is referred to the web version of this article.)

eventually causing its disintegration, while viscous forces retard the deformation, and capillary forces cause the drop to preserve its spherical shape. Two non-dimensional numbers characterize the breakup process: the Weber number *We* and the Ohnesorge number *Oh*. They describe the ratio of inertial to capillary forces and the ratio of viscous to capillary forces, respectively, and are defined as

$$We = \frac{\rho_{g,s} u_{g,s}^2 D_0}{\sigma} \tag{4}$$

$$Oh = \frac{\mu_l}{\sqrt{\rho_l d_0 \sigma}} \tag{5}$$

with the post-shock density of the gas phase $\rho_{g,s}$, the post-shock velocity of the gas phase $u_{g,s}$, the initial droplet diameter D_0, the surface-tension coefficient σ, the dynamic viscosity of the liquid phase μ_l, and the density of the liquid phase ρ_l. Other non-dimensional numbers used to classify secondary atomization are the Reynolds number

$$Re = \frac{\rho_{g,s} u_{g,s} D_0}{\mu_g} \tag{6}$$

describing the surrounding flow field, the Mach number Ma_S of the shock wave that initiates the breakup process, and the density ratio $\varepsilon = \rho_l / \rho_{g,s}$.

3. Numerical model

3.1. Finite-volume based sharp-interface model with conservative interface interaction

The governing equations (1) are discretized by a finite-volume approach on Cartesian square cells in the domain Ω, which is divided into two subdomains Ω_l (liquid phase) and Ω_g (gaseous phase) by a time-evolving interface Γ. Fig. 1 shows a sketch of the two subdomains with a sharp interface. We integrate Eq. (1) in each computational cell $\Delta_{i,j}$ of each subdomain Ω_m and apply Gauß' theorem to obtain

$$\int_{t^{(n)}}^{t^{(n+1)}} dt \int_{\Delta_{i,j}\cap\Omega_m} d\Delta_{i,j} \frac{\partial \mathbf{U}}{\partial t} + \int_{t^{(n)}}^{t^{(n+1)}} dt \oint_{\partial(\Delta_{i,j}\cap\Omega_m)} (\mathbf{F} + \mathbf{F}_v) \cdot \mathbf{n} \; d\big(\partial\Delta_{i,j}\big) = \int_{t^{(n)}}^{t^{(n+1)}} dt \oint_{\Gamma} \mathbf{X} \cdot \mathbf{n}_\Gamma d\Gamma \tag{7}$$

where $\Delta_{i,j} = \Delta x_1 \, \Delta x_2$ denotes the cell volume in two dimensions, $\Delta_{i,j} \cap \Omega_m$ each cell volume of phase m, $\partial(\Delta_{i,j} \cap \Omega_m)$ the cell face, $\mathbf{n}$ the cell-face normal unit vector, and $\mathbf{n}_\Gamma$ the interface-normal unit vector. We replace $\Delta_{i,j} \cap \Omega_m$ by $\Delta_{i,j}\alpha_{i,j}$, where $\alpha_{i,j}$ is the time-dependent volume fraction of phase m, with $0 \leq \alpha_{i,j} \leq 1$. The cell

face $\partial(\Delta_{i,j} \cap \Omega_m)$ can be approximated by the cell-face apertures A, $0 \leq A \leq 1$, and the segment of the interface Γ inside this cell, $\Delta\Gamma_{i,j}$. Eq. (7) is then rewritten for a single forward-time integration step of phase m as

$$\begin{aligned}\alpha_{i,j}^{(n+1)}\mathbf{U}_{i,j}^{(n+1)} &= \alpha_{i,j}^{(n)}\mathbf{U}_{i,j}^{(n)} \\ &+ \frac{\Delta t}{\Delta x_1}\left[A_{i-1/2,j}^{(n)}\left(\mathbf{F}_{i-1/2,j}^{(n)} + \mathbf{F}_{v,i-1/2,j}^{(n)}\right) - A_{i+1/2,j}^{(n)}\left(\mathbf{F}_{i+1/2,j}^{(n)} + \mathbf{F}_{v,i+1/2,j}^{(n)}\right)\right] \\ &+ \frac{\Delta t}{\Delta x_2}\left[A_{i,j-1/2}^{(n)}\left(\mathbf{F}_{i,j-1/2}^{(n)} + \mathbf{F}_{v,i,j-1/2}^{(n)}\right) - A_{i,j+1/2}^{(n)}\left(\mathbf{F}_{i,j+1/2}^{(n)} + \mathbf{F}_{v,i,j+1/2}^{(n)}\right)\right] \\ &+ \frac{\Delta t}{\Delta x_1 \Delta x_2}\mathbf{X}_{i,j}^{(n)}(\Delta\Gamma_{i,j}) \end{aligned} \tag{8}$$

where Δt denotes the timestep size, $\mathbf{U}_{i,j}$ the cell-averaged state vector of the considered phase in cell (i, j), and $\mathbf{F}_{i,j}$ the fluxes in or out of this cell. The term $\mathbf{X}_{i,j}$ describes momentum and energy exchange between the two fluids in a cell cut by the interface ("cut cell"), and includes inviscid, viscous and capillary effects.

Convective fluxes at cell faces are approximated by the fifth-order WENO (Weighted Essentially Non-Oscillatory) scheme on characteristic fluxes, split by the global Lax-Friedrich (GLF) scheme (Jiang and Shu, 1996; Roe, 1981). Viscous fluxes are discretized with a fourth-order central scheme. For temporal discretization, we use a strongly stable third-order Runge–Kutta scheme (Gottlieb and Shu, 1998; Harten, 1983). The maximum admissible timestep size is determined from a Courant–Friedrichs–Lewy (CFL) stability criterion considering the maximum wave speed, viscous diffusion, and propagation of capillary waves at the interface

$$\Delta t = \mathrm{CFL} \cdot \min\left(\frac{\Delta x}{\sum |u_i \pm c|_\infty}, \frac{3}{14}\frac{(\Delta x)^2 \rho}{\mu}, \sqrt{\frac{\rho_l + \rho_g}{8\pi\sigma}\Delta x^3}\right) \tag{9}$$

where c is the speed of sound (Sussman et al., 1994). In all simulations we use CFL= 0.5. Advancing the flow field by this timestep size may lead to an unstable fluid state in cells with small volume fraction α. Therefore, we apply a mixing procedure in cells with $\alpha < 0.5$ to maintain numerical stability (Hu et al., 2006).

3.2. Multi-phase treatment

The interaction of the two fluids is solved with the level-set-based conservative interface-interaction model of Hu et al. (2006) with the extension for viscous and capillary forces of Luo et al. (2015). The water-air phase interface is described by a level-set function ϕ. The level-set represents the interface as the zero-crossing of a multi-dimensional continuous function. The liquid subdomain Ω_l is indicated by the negative level-set $\phi(\mathbf{x}) < 0$, the gaseous subdomain Ω_g by the positive level-set $\phi(\mathbf{x}) > 0$, and the interface Γ by the zero-level-set $\phi(\mathbf{x}) = 0$. The absolute value of $\phi(\mathbf{x})$ describes the normal signed distance of the cell center $\mathbf{x}$ to the interface Γ. The level-set is evolved in time with the advection equation

$$\frac{\partial \phi}{\partial t} + u_\phi \mathbf{n}_\Gamma \cdot \nabla\phi = 0\,, \tag{10}$$

with u_ϕ being the level-set advection velocity.

In cut-cells, the level-set advection velocity is equal to the interface velocity u_Γ, which is the contact-wave solution of a two-material Riemann problem at the phase interface, see Luo et al. (2015). The interface velocity u_Γ and the interface pressures $p_{\Gamma,l}$ and $p_{\Gamma,g}$ are obtained from a linearized two-material Riemann solver

$$u_\Gamma = \frac{\rho_l c_l u_l + \rho_g c_g u_g + p_l - p_g - \sigma\kappa}{\rho_l c_l + \rho_g c_g} \tag{11}$$

$$p_{\Gamma,l} = \frac{\rho_l c_l (p_g + \sigma\kappa) + \rho_g c_g p_l + \rho_l c_l \rho_g c_g (u_l - u_g)}{\rho_l c_l + \rho_g c_g} \tag{12}$$

$$p_{\Gamma,g} = \frac{\rho_l c_l p_g + \rho_g c_g (p_l - \sigma\kappa) + \rho_l c_l \rho_g c_g (u_l - u_g)}{\rho_l c_l + \rho_g c_g}\,. \tag{13}$$

If capillary effects are neglected, i.e. the pressure jump at the interface due to surface tension vanishes, the interface pressures coincide $p_{\Gamma,l} = p_{\Gamma,g} = p_\Gamma$. The curvature κ is the divergence of the interface-normal vector $\kappa = \nabla \cdot \mathbf{n}_\Gamma$, and is numerically obtained from $\mathbf{n}_\Gamma = \nabla\phi/|\nabla\phi|$. The curvature is evaluated at the cell center and then subjected to a subcell correction step to take into account the distance between the cell center and the interface

$$\kappa_\Gamma = \frac{(D-1)\kappa}{D - 1 - \phi\kappa}\,, \tag{14}$$

where D is the number of spatial dimensions (Luo et al., 2015). In non-cut cells, the level-set advection velocity is equal to the extrapolated interface velocity $\tilde{u}_\Gamma$, which is determined from the steady-state solution of the extension equation

$$\frac{\partial \tilde{u}_\Gamma}{\partial \tau} + \mathbf{n}_\Gamma \cdot \nabla\tilde{u}_\Gamma = 0\,. \tag{15}$$

The numerical solution of the level-set advection does not maintain the signed-distance property $|\nabla\phi| = 1$. Therefore, the re-initialization equation

$$\frac{\partial \phi}{\partial \tau} + \mathrm{sign}(\phi_0)(|\nabla\phi| - 1) = 0 \tag{16}$$

is iterated in pseudo time τ to steady state to restore the signed-distance property after each timestep (Sussman et al., 1994). Here, ϕ_0 is the level-set field prior the re-initialization step.

Similarly to the interface velocity extrapolation from cut cells to adjacent bulk cells, the fluid states are extrapolated across the interface to define a "ghost" fluid within the opposing phase (Fedkiw et al., 1999). These ghost-fluid states are used in the reconstruction of the cell-face fluxes near the interface. This approach assures the sharp-interface property of the method.

Momentum and energy exchange across the interface are modeled for phase m by explicit exchange terms

$$\mathbf{X}_m = \mathbf{X}_{p,m} + \mathbf{X}_\nu \tag{17}$$

where

$$\mathbf{X}_{p,m} = (0,\ p_{\Gamma,m}\Delta\Gamma\mathbf{n}_\Gamma,\ u_\Gamma p_{\Gamma,m}\Delta\Gamma)^T \tag{18}$$

represents the inviscid exchange including the pressure jump due to capillarity in liquid ($m = l$) and gas ($m = g$), and

$$\mathbf{X}_\nu = (0,\ \mathcal{F}_\nu\Delta\Gamma\mathbf{n}_\Gamma,\ (\mathcal{F}_\nu\Delta\Gamma\mathbf{n}_\Gamma)\cdot\mathbf{n}_\Gamma u_\Gamma)^T \tag{19}$$

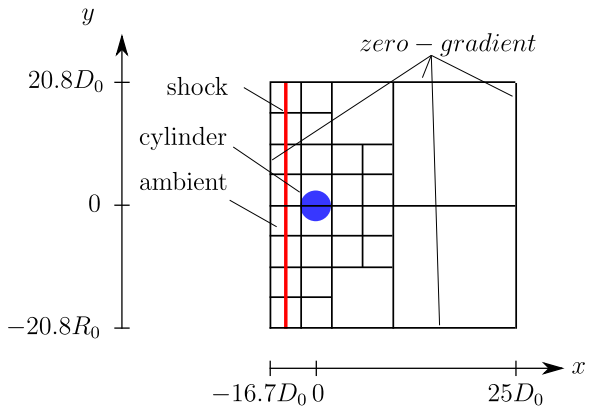

Fig. 2. Sketch of the simulation domain, including an exemplary multiresolution mesh. The water column is sketched in blue, the shock in red. Note that the water column is not drawn to scale. (For interpretation of the references to color in this figure legend, the reader is referred to the web version of this article.)

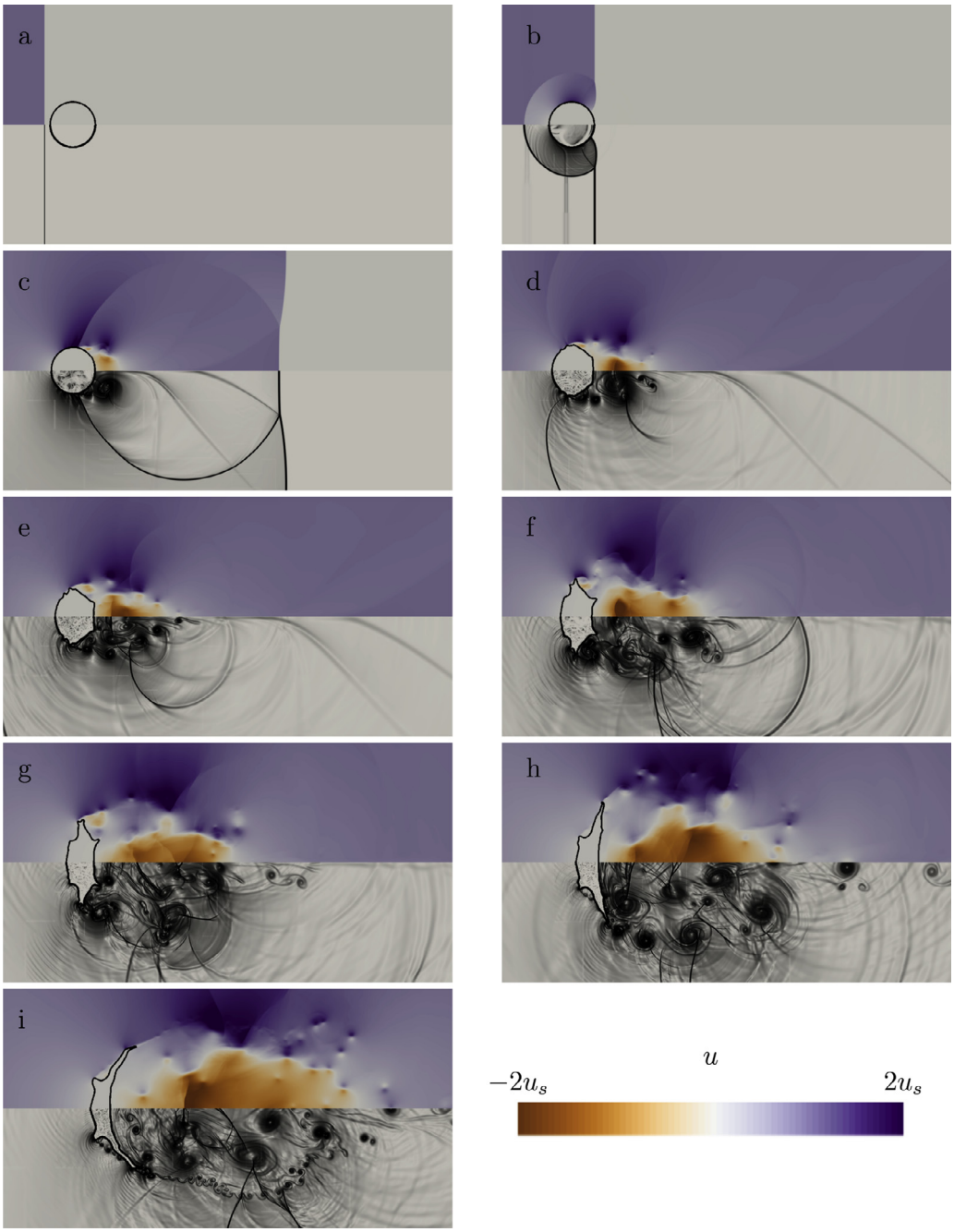

Fig. 3. Normalized streamwise velocity (top) and numerical schlieren images (bottom) of the breakup of a water cylinder with diameter $D_0 = 4.8$mm, initiated by a shock wave with $Ma_S = 1.47$. Shown are different time instants $t^* \in \{0.00, 0.02, 0.11, 0.19, 0.26, 0.44, 0.54, 0.76, 0.98\}$ for the subfigures (a)–(i) (left to right, top to bottom).

models the viscous exchange. Here, $\mathcal{F}_v = [\tau_{xx}, \tau_{xy}; \tau_{yx}, \tau_{yy}]$ is the viscous stress tensor. The length of the interface segment in each cut-cell $\Delta\Gamma_{i,j}$ is computed from the cell-face apertures following

$$\Delta\Gamma_{i,j} = \Delta x \sqrt{\left(A_{i+1/2,j} - A_{i-1/2,j}\right)^2 + \left(A_{i,j+1/2} - A_{i,j-1/2}\right)^2} \tag{20}$$

(Lauer et al., 2012). Note that more details on the model and in particular generic test cases for model validation can be found in Hu et al. (2006) for the base model and in Luo et al. (2015) for the extended model including capillary and viscous effects.

3.3. Wavelet-based multiresolution approach with adaptive local timestepping

High grid resolution is required to resolve the interface deformation and the surrounding flow field accurately. A coarser resolution is sufficient further away from the cylinder. Therefore, spatial and temporal adaptation techniques are necessary to efficiently solve the breakup process numerically.

We apply a block-structured wavelet-based multiresolution approach based on the work of Harten (1994) to adapt the mesh to the deforming phase interface and the evolving flow field (Han et al., 2014; Hoppe et al., 2019; Rossinelli et al., 2011). The procedure is described in detail in Hoppe et al. (2019). The cell-averaged solution is represented in a hierarchical data structure. Two basic

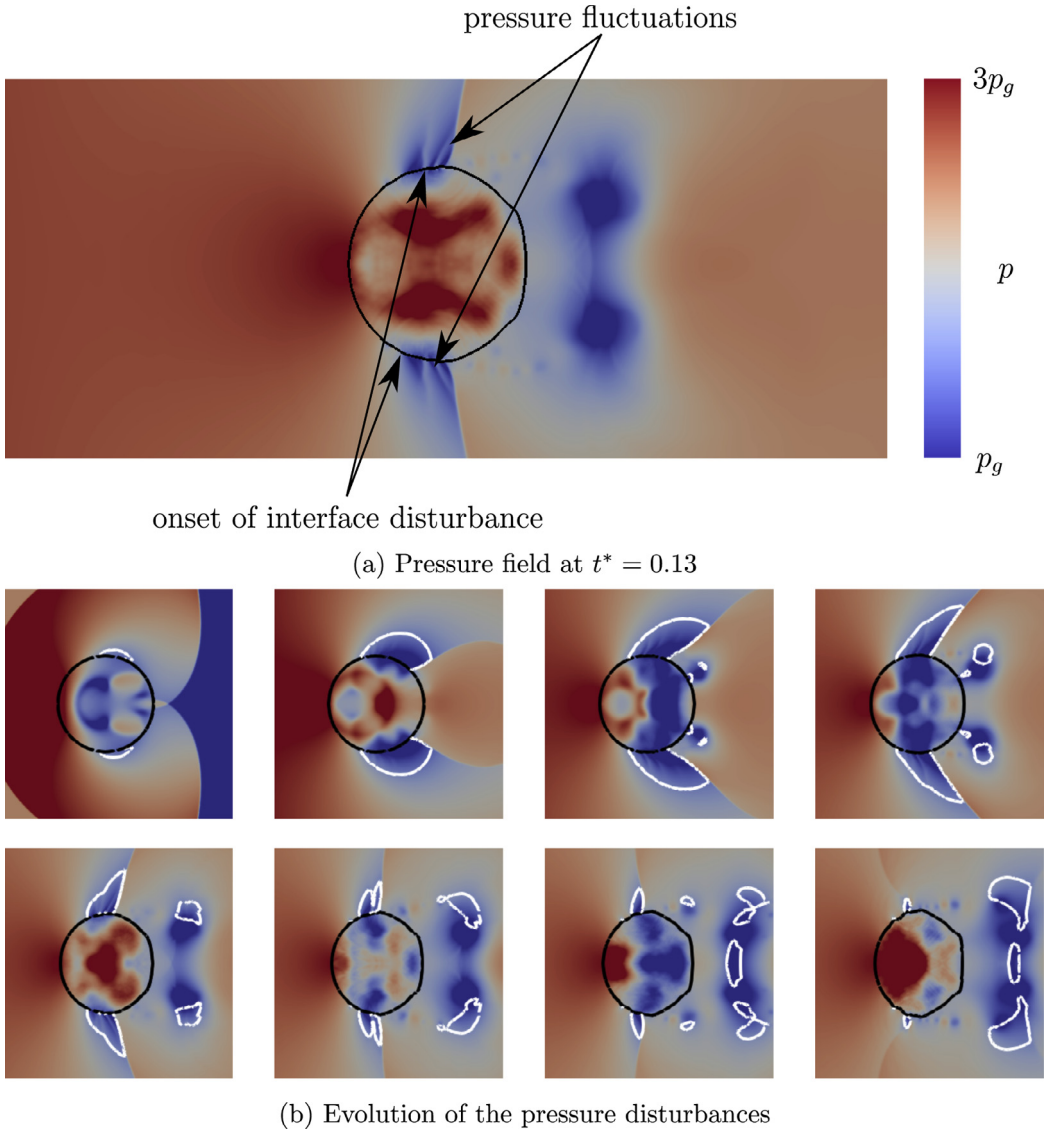

Fig. 4. (a) Pressure field around the deforming cylinder at $t^* = 0.13$. Pressure fluctuations appear near the equator on the upstream side of the secondary wave system, which is where interface instabilities grow. (b) Temporal evolution of the pressure disturbances. The first frame is at $t^* = 0.033$, subsequent frames follow with $\Delta t^* = 0.022$ from left to right and top to bottom. The white line denotes $Ma = 1$.

operations enable data transfer between successive refinement levels: projection and prediction. The projection operation is applied to obtain data on a refinement level l from the finer level $l+1$ and corresponds to averaging the cell-states on the finer level. The prediction operation approximates data on level $l+1$ from level l, and corresponds in our work to a fifth-order interpolation. Projection and prediction are local and consistent, but not commutative: applying first prediction to send data from level l to level $l+1$ and afterwards projection to send data from level $l+1$ to level l results in exactly the same solution on level l. To the contrary, applying first projection to send data from level $l+1$ to level l and afterwards prediction to send data from level l to level $l+1$ results in an error on level $l+1$. This motivates the definition of the so called details as the deviation between the exact solution and the predicted solution on any level l. The exact solution on any level l can thus be represented by the exact solution on the coarsest level and the details of all successively finer levels.

Implicit mesh adaption is performed by considering only those details that are larger than a level-dependent threshold

$$\varepsilon_l = \varepsilon_{\text{ref}} \cdot \mathrm{e}^{(-D\cdot(l_{max}-l))}, \tag{21}$$

where l_{max} denotes the maximum level to which the mesh is refined, and ε_{ref} is the admissible relative error on this level. We apply a dyadic refinement strategy, where each cell can be refined into 2^D smaller cells, with a reference error $\varepsilon_{\text{ref}} = 0.01$.

Efficient time integration is obtained by applying a local timestepping approach, where each refinement level is advanced with its level-dependent timestep size (Osher and Sanders, 1983). We use an improved version of this local timestepping scheme which allows for adapting the timestep size after each full Runge–Kutta cycle on the finest refinement level (Kaiser et al., 2019).

4. Results

4.1. Configuration and simulation setup

The numerical domain of the water-cylinder breakup simulation is shown in Fig. 2, together with a schematic multiresolution block structure for this case. Note that we simulate the full cylinder ($D_0 = 4.8$mm), as our previous work indicated asymmetric flow-field patterns in the wake of the cylinder already at early breakup stages (Kaiser et al., 2017). We prescribe zero-gradient boundary

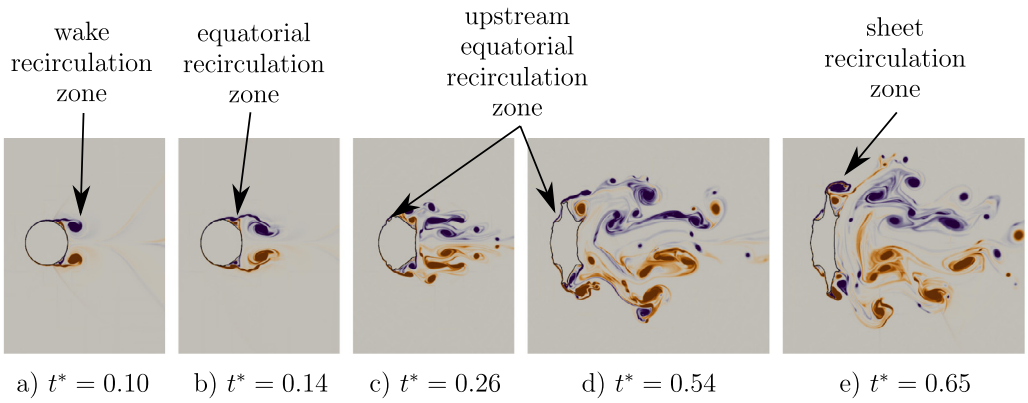

Fig. 5. Positive (orange) and negative (purple) z-vorticity streams that interact and form multiple recirculation zones at various instants. (For interpretation of the references to color in this figure legend, the reader is referred to the web version of this article.)

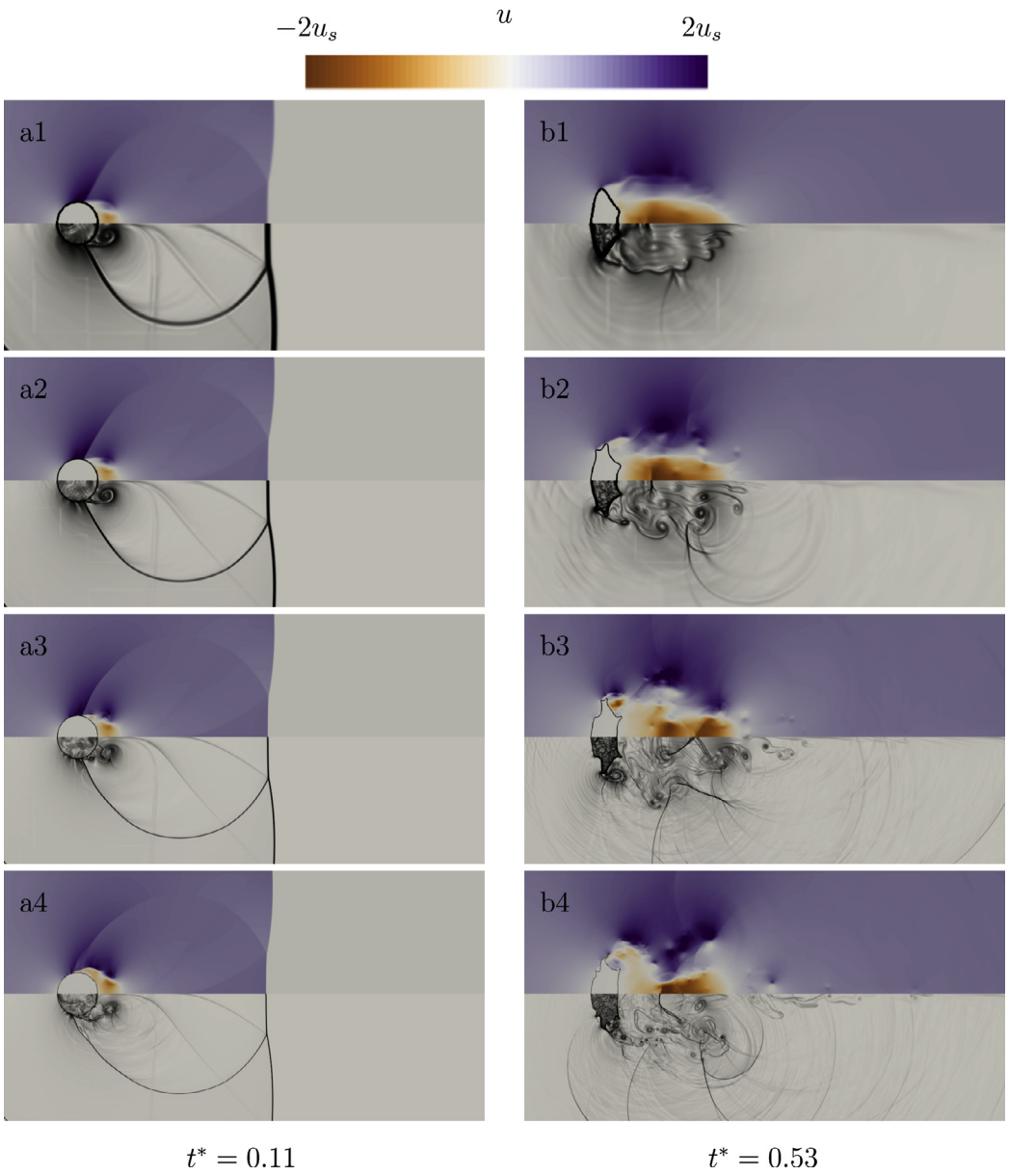

Fig. 6. The flow field in the vicinity of the water column for resolutions of 50 ((a1) – (b1)), 100 ((a2) – (b2)), 200 ((a3) – (b3)), and 300 ((a4) – (b4)) cells per initial diameter at $t^* = 0.11$ and $t^* = 0.53$. The upper half of each image shows the normalized axial velocity, the lower half numerical schlieren images.

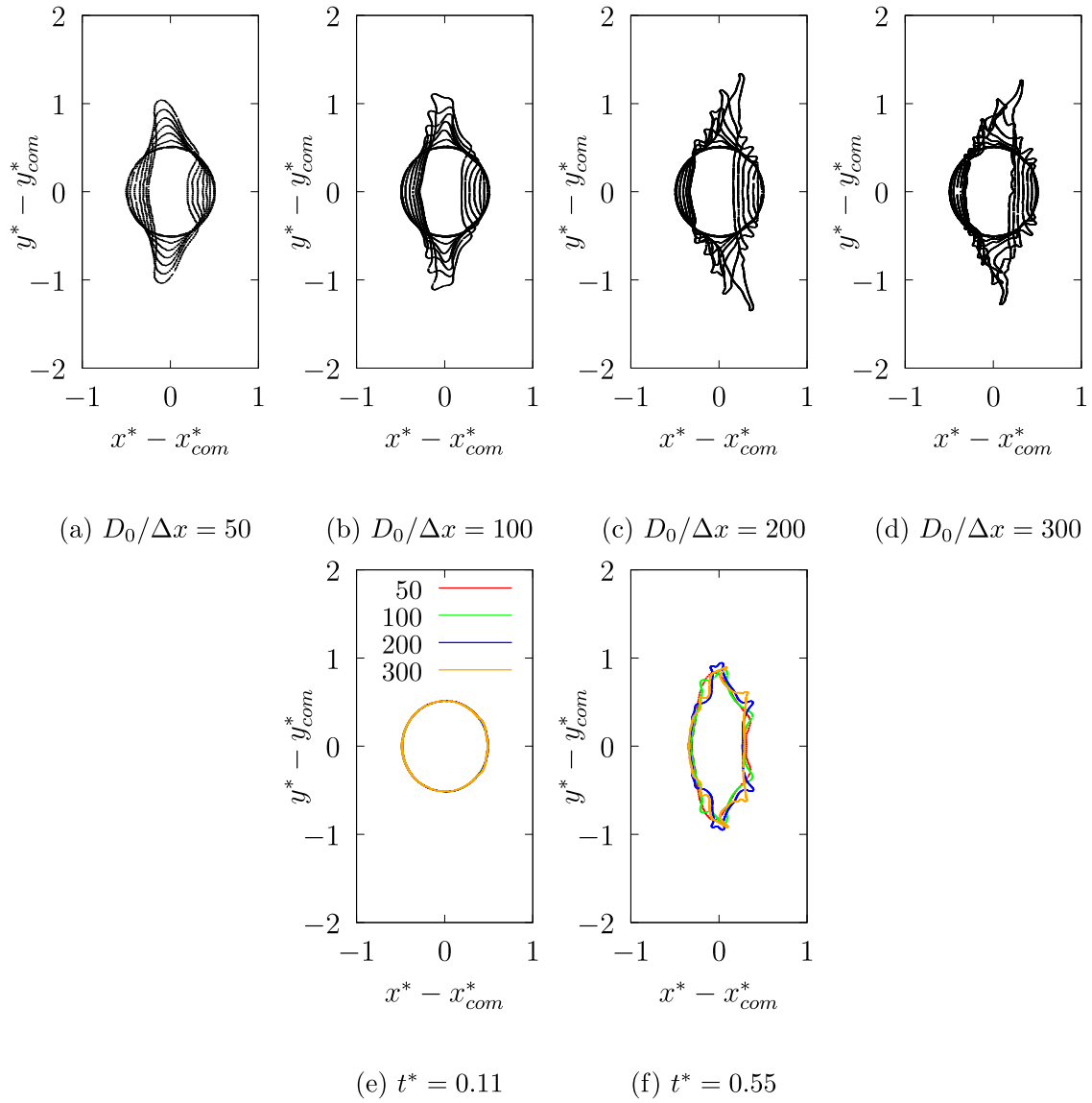

Fig. 7. (a)–(d): Comparison of deformed cylinder interface for resolutions of $D_0/\Delta x = 50$, 100, 200 and 300. The time interval between two subsequent interface contour lines is $\Delta t^* = 0.11$. (e)–(f): the deformed cylinder for these resolutions at $t^* = 0.11$ (e) and $t^* = 0.55$ (f).

conditions at all external boundaries. The domain size is chosen sufficiently large to prevent spurious effects of wave reflections at the domain boundaries.

The ambient uniform flow field is generated by a shock wave. This wave interacts with the cylinder at $t = 0$. Pre-shock air and water are at rest at standard conditions ($\rho_g = 1.20\text{kg/m}^3$, $\rho_l = 1000.0\text{kg/m}^3$, $p_g = p_l = 1.0\text{atm}$). Post-shock conditions follow from the Rankine-Hugoniot relation for a shock Mach number of $Ma_S = 1.47$ ($\rho_{g,s} = 2.18\text{kg/m}^3$, $p_{g,s} = 2.35\text{atm}$, $u_{g,s} = 225.9\text{m/s}$). Material parameters for air and water are given in Table 1. The Weber number of this case is $We = 7.3 \times 10^3$, the Ohnesorge number $Oh = 1.7 \times 10^{-3}$, the Reynolds number $Re = 1.3 \times 10^5$, and the density ratio $\varepsilon = 459$, thus SIE is expected to be the dominating breakup mode. We first perform simulations including viscous and capillary forces with a grid resolution of 200 cells per initial cylinder diameter, which relates to an effective resolution of 8192 × 8192 cells in the entire domain. Grid-resolution effects are analyzed by varying the resolution from 50 to 300 cells per initial cylinder diameter, which relates to effective resolutions of 2048 × 2048, 4096 × 4096, 8192 × 8192, and 12288 × 12288 cells. Note that a full resolution of capillary waves with

$$We_\Delta = \frac{(\rho_l + \rho_{g,s}) u_{g,s}^2 \Delta x}{4\pi\sigma} \ll 1\,, \tag{22}$$

where We_Δ is the cell Weber number (Popinet, 2018), would imply a resolution of approximately 3×10^5 cells per initial cylinder diameter. Thus, our simulations do not resolve the terminal disintegration of the liquid sheet due to capillary effects. Good agreement with experimental and numerical reference data indicates that the numerical resolution suffices to capture the early stages of the breakup process (see Sections 4.3 and 4.4).

We non-dimensionalize our results using the initial cylinder diameter D_0, the post-shock velocity $u_{g,s}$, the pre-shock pressure p_g, and the characteristic time by Ranger and Nicholls (1969) given by $(D_0\sqrt{\varepsilon})/u_{g,s}$. All non-dimensionalized quantities are denoted by an asterisk (*). Flow direction in all contour plots is from left to right.

4.2. Overall breakup evolution

Fig. 3 shows the temporal evolution of the numerical breakup simulation results for a resolution of 200 cells per initial diameter,

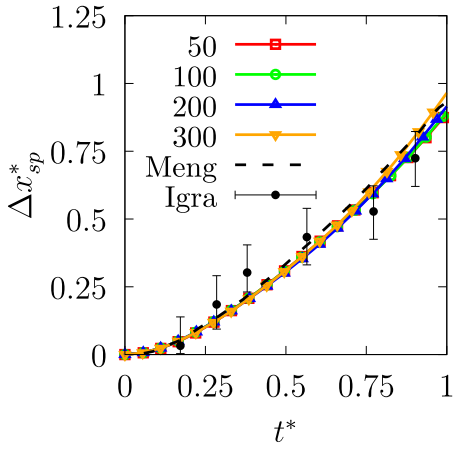

(a) Normalized upstream stagnation point drift

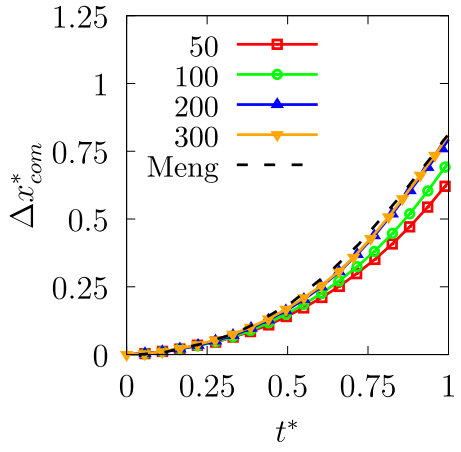

(b) Normalized center-of-mass drift

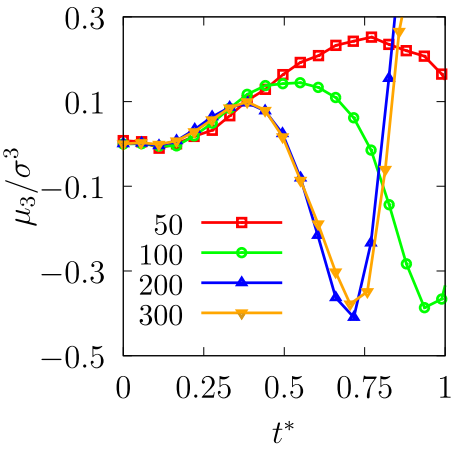

(c) Skewness

Fig. 8. Evolution of the normalized upstream stagnation point drift (a), the normalized center-of-mass drift (b) and the skewness (c) for various grid resolutions. Where applicable, present results are compared to experimental data of Igra et al. (2002) and Igra and Takayama (2001c) (symbols) and numerical data of Meng and Colonius (2015) (dashed line).

at time instants $t^* \in \{0.00, 0.02, 0.11, 0.19, 0.26, 0.44, 0.54, 0.76, 0.98\}$ (left to right, top to bottom). In each subfigure, the upper half domain displays the streamwise velocity field, and the lower a numerical schlieren image. Following Quirk and Karni (1996), the numerical schlieren images are computed with

$$\phi = e^{-k|\nabla\rho|/\max(|\nabla\rho|)}, \tag{23}$$

where the parameter k is used for scaling the schlieren of different fluids. Here, we use $k = 40$ and $k = 400$ for the air and water phase, respectively (Johnsen and Colonius, 2007; Meng and Colonius, 2015).

The wave patterns in the vicinity of the cylinder agree well with current state-of-the-art simulation results in literature (Meng and Colonius, 2015). Initially, the cylinder is unaffected by the shock passage, as the shock-passage time is much shorter than the relaxation time of the cylinder (Aalburg et al., 2003). The shock wave is partially reflected at the upstream side of the cylinder. Once the angle between the initial shock wave and the water-air interface exceeds a critical value, the reflected shock wave transforms to a Mach reflection (Igra and Takayama, 2001a). The Mach stems merge once the incident shock wave has passed the cylinder and form a secondary wave system, which eventually travels further upstream along the cylinder's surface (Fig. 3(a)–(c)).

The non-uniform pressure field along the interface results in the flattening of the cylinder (Fig. 3(c)–(e)). At the same time, regular wave-like interface disturbances develop at the equator (Fig. 3(d)). Interface disturbances are related to small pressure fluctuations at the phase interface. These fluctuations are detailed in Fig. 4(a), and their temporal evolution is shown in Fig. 4(b). We observe the formation of a supersonic flow region near the cylinder equator from the location of the sonic line (isoline for $Ma = ||\mathbf{u}||/c = 1$ in white). The pressure fluctuations appear once this supersonic zone reaches the windward side of the cylinder, but do not form on the leeward side. These characteristic waves do not travel upstream with the progressing secondary wave system, but remain at the same location until they merge with the secondary wave system. The pressure waves finally vanish once the secondary wave system detaches from the cylinder interface, and the supersonic flow region disappears. The pressure fluctuations coincide with the onset of the interface waves. We believe that the interaction of these local pressure waves with the phase interface generates small disturbances that trigger interface waves. The in-

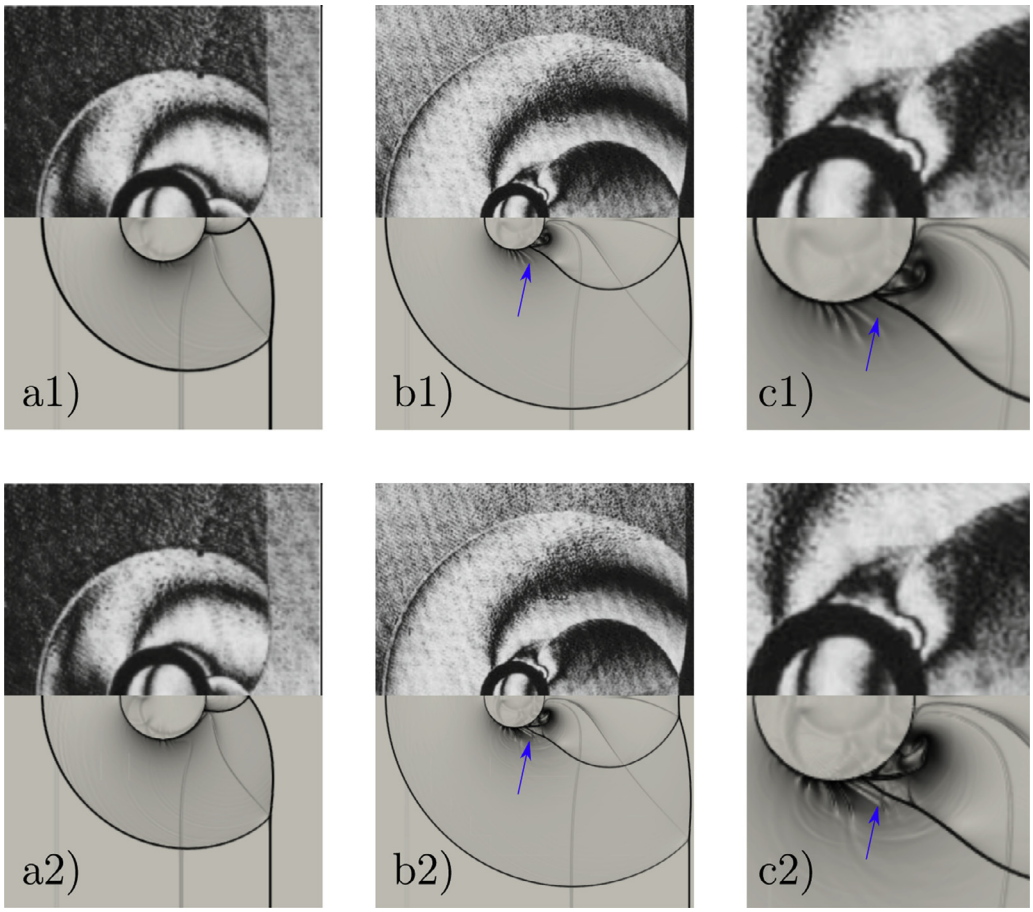

Fig. 9. (a)–(b) Comparison of experimental visualizations of Igra and Takayama (2001b) (upper half) and numerical schlieren images (lower half) at $t^* = 0.035$ ((a); $t = 16.18\mu s$) and $t^* = 0.07$ ((b); $t = 32.14\mu s$). (c) Flow field in the vicinity of the attached secondary wave at $t^* = 0.07$. Shown are results for simulations with resolutions of 200 cells ((a1)–(c1)) and 300 cells ((a2)–(c2)) per initial cylinder diameter. Reprinted from Igra and Takayama (2001b) with permission from Springer.

terface disturbances eventually develop cusps, which merge into a single large water sheet and are stripped off from the cylinder equator (Fig. 3(e)–(h)). The thin sheet is advected further downstream, where it is subjected to strongly fluctuating forces in the unsteady wake of the cylinder and, eventually, breaks up. Our simulations do not resolve this terminal breakup of the sheet. The smallest sheet dimension is limited by the smallest computational cell size.

The simulation confirms the development of a hat-like shape (Fig. 3(f)–(i)) with a smooth windward region and two distinct cusps near the edge, which so far has been reported only in experimental investigations (Theofanous et al., 2012). It is further discussed in the following Section 4.4.

Moreover, multiple recirculation zones establish around the cylinder interface forming during the simulated time until $t^* = 0.98$, whereas Meng and Colonius (2015) have reported a single recirculation zone each in the wake of the cylinder and at the cylinder equator. They play an important role during the deformation and sheet-stripping process, and are initiated by unsteady vortex shedding at the cylinder equator. Fig. 5 shows the z-vorticity at various time instants. Unsteady vortex shedding after the shock passage results in the formation of the wake recirculation zone ($t^* = 0.10$). The shed vortex originating from the cylinder equator is diverted at the downstream stagnation point of the cylinder. It interacts with the vorticity stream near the cylinder equator, which leads to the formation of the equatorial recirculation zone ($t^* = 0.14$). We extend these observations, which agree well with that of Meng and Colonius, by the detection of additional recirculation zones along the interface, which can be related to local unsteady vortex shedding at the deformed interface. Previously mentioned interface disturbances upstream of the cylinder equator are linked to the formation of a recirculation zone on the upstream side of the cylinder near the equator ($t^* = 0.26$), which occurs at later time instants between the hat-like structure on the upstream side and the developing liquid sheet ($t^* = 0.54$). Another recirculation zone forms at the tip of the liquid sheet due to the interaction of multiple vortices in this area, and contributes to the observed flapping of the sheet in the wake of the cylinder ($t^* = 0.65$).

4.3. Grid resolution

We have investigated the effect of the spatial resolution on the numerical results for the cylinder deformation. Fig. 6 depicts contour plots for resolutions of 50 ((a1) – (b1)), 100 ((a2) – (b2)), 200 ((a3) – (b3)), and 300 ((a4) – (b4)) cells per initial cylinder diameter at $t^* = 0.11$ and $t^* = 0.53$. The upper half of each image shows the normalized axial velocity, the lower half shows numerical schlieren.

At $t^* = 0.11$, recirculation zones have formed in the wake of the cylinder and at the equator. Flattening and shift of the upstream stagnation point are similar for all four resolutions. The primary wave system, which consists of the incident and the reflected shock wave, is at the same position for all investigated resolutions. The secondary wave system, which forms near the rear stagnation point once the Mach stems on both sides converge, is attached to the cylinder interface downstream of the equator up

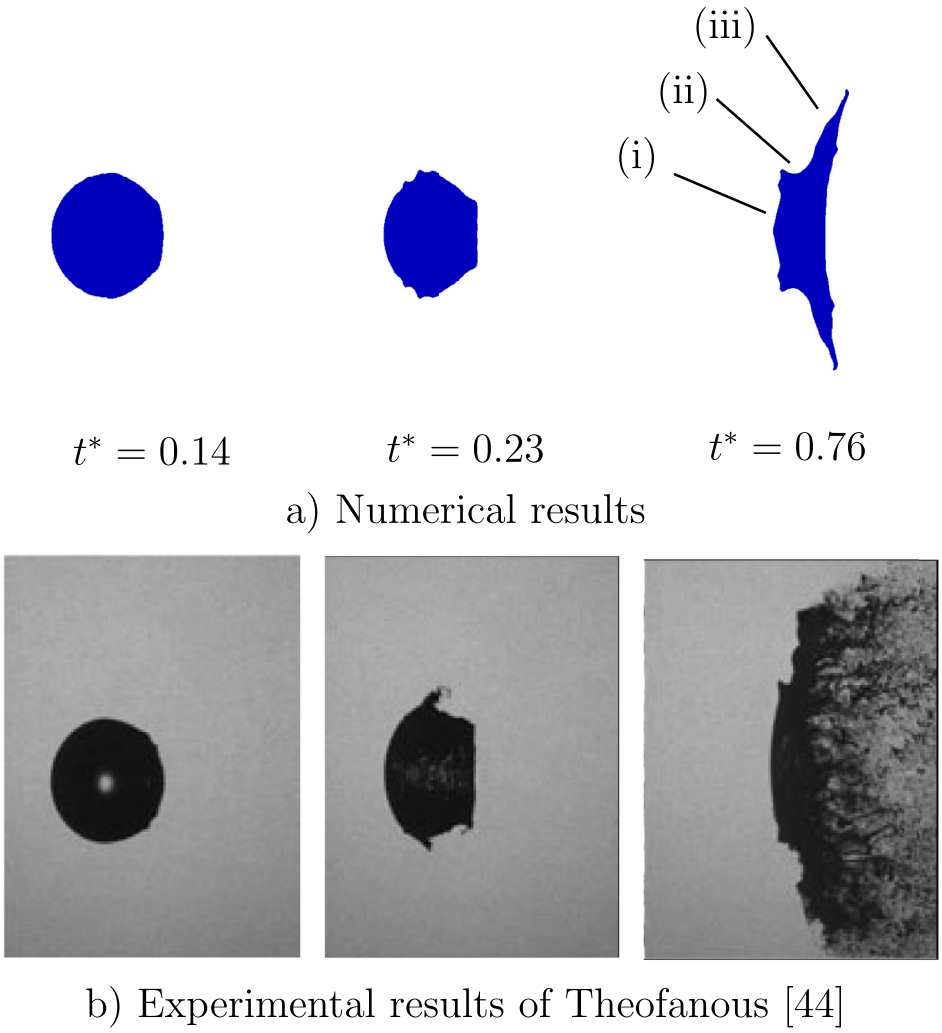

Fig. 10. Qualitative comparison of the interface deformation process. The experimental figures are obtained from online-available videos. Reprinted from Theofanous et al. (2012), with the permission from AIP Publishing.

to a resolution of 200 cells per diameter. With 300 cells, more details of the local wave-interface interaction are reproduced, and the secondary wave system crosses the cylinder equator slightly earlier (Fig. 6(a4)). This also affects the development of the pressure waves, that are visible in the Schlieren image. They only appear for a resolution of at least 100 cells. For a resolution of 300 cells, the secondary wave system moves further upstream, the supersonic flow region is about to disappear, and pressure waves almost vanish. The resolution of the interface disturbance at the equator requires more than 100 cells per initial diameter (Fig. 6(a1) and (a2)). From grid resolutions of 200 cells per cylinder diameter, interface waves are resolved that are responsible for hat formation and denote the onset of the sheet stripping (Fig. 6(a3) and (a4)).

A similar behavior is found for the results at $t^* = 0.53$. General features such as the recirculation zones are reproduced for all resolutions. Resolutions of at least 200 cells per diameter reproduce the hat-like structure on the upstream side of the cylinder (Fig. 6(b3) and (b4)), while simulations with coarser resolutions exhibit a smooth interface (Fig. 6(b1) and (b2)). Only with sufficient grid resolution, implying sufficiently small numerical dissipation, interface disturbances are accurately resolved and the hat shape develops. This is also the case for the formation of the sheet, which is strongly affected by proper resolution of interface disturbances. With increasing resolution, the sheet exhibits finer details, see for example the multiple cusps at the edges, each of which is associated with a local recirculation zone (Fig. 6(b2)–(b4)).

Fig. 7 shows the evolution of the phase interface for resolutions of $D_0/\Delta x = 50,\ 100,\ 200$ and 300 ((a)–(d)), and overlapping at times $t^* = \{0.11, 0.55\}$ ((e)–(f)). The plots are centered at the respective centers-of-mass

$$\mathbf{x}^*_{com} = \frac{\int_{\Omega_l} \mathbf{x}^* \rho \, dV}{\int_{\Omega_l} \rho \, dV} = \frac{\sum_i \mathbf{x}^*_i \rho_i V_i}{\sum_i \rho_i V_i}, \tag{24}$$

where x^* stands for the cell-center location and Ω_l denotes the liquid subdomain. The time interval between two subsequent grid lines is $\Delta t^* = 0.11$. At the coarsest resolution (Fig. 7(a)), flattening is reproduced, while stripping at the droplet equator is underestimated. The liquid sheet appears for the finer resolution of $D_0/\Delta x = 100$ (Fig. 7(b)). For resolutions of $D_0/\Delta x = 200,\ 300$, (Fig. 7(c) and (d)) additionally the hat-shaped structure is observed. The overlapping contour lines in subfigures (e) and (f) indicate that coarser grids have a minor effect on typical geometrical parameters. At both instants, the interface overlaps near the upstream and downstream stagnation points, and the extend in streamwise direction is similar. Yet, interface waves are more pronounced for finer resolutions (Fig. 7(e)), and result in a more detailed representation of the sheet and the hat-like structure (Fig. 7(f)).

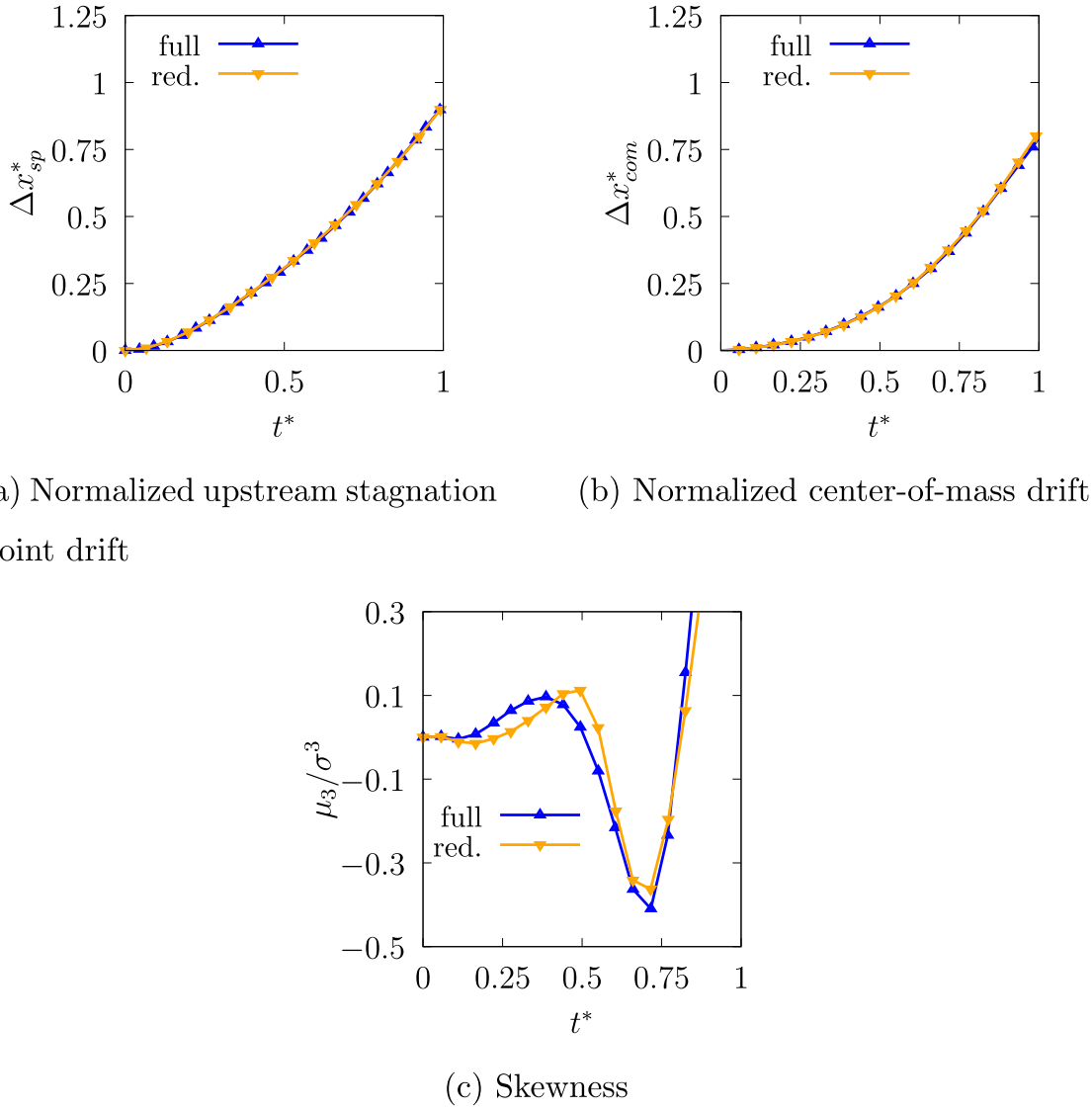

(a) Normalized upstream stagnation point drift

(b) Normalized center-of-mass drift

(c) Skewness

Fig. 11. Evolution of the normalized upstream stagnation point drift (a), the normalized center-of-mass drift (b) and the skewness (c) for simulations with and without capillary and viscous forces.

A quantitative comparison of the normalized upstream stagnation point drift Δx^*_{sp}, the normalized center-of-mass drift Δx^*_{com}, and the third moment of the axial displacement $\mu_3/\mu_2^{3/2}$ is shown in Fig. 8. Higher-order moments are computed following

$$\mu_k = \int_{\Omega_l} (x^* - x^*_{com})^k \rho dV = \frac{\sum_i (x^*_i - x^*_{com})^k \rho_i V_i}{\sum_i \rho_i V_i}. \tag{25}$$

The second moment ($k = 2$) μ_2 is the variance, and the normalized third moment ($k = 3$) $\mu_3/\mu_2^{3/2}$ the skewness of the mass distribution. The skewness measures the asymmetry between the upstream and the downstream side of the cylinder. For the upstream stagnation point drift, we also show experimental results of Igra et al. (2002) and Igra and Takayama (2001c), and numerical results of Meng and Colonius (2015) for comparison. For the center-of-mass drift, numerical reference data of Meng and Colonius are included. In the study of Meng and Colonius, the authors apply a volume-of-fluid (VOF) approach, and the results are given for a volume faction of $\alpha_T = 0.5$.

The upstream stagnation point drift Δx^*_{sp} (Fig. 8(a)) is converged for the considered resolutions, and agrees well with reference numerical data of Meng and Colonius (2015) and experimental data of Igra et al. (2002) and Igra and Takayama (2001c). The normalized center-of-mass drift Δx^*_{com} (Fig. 8(b)) is converged for a resolution of 200 cells per initial cylinder radius, and agrees well with the reference solution of Meng and Colonius (2015). This underlines that such integral parameters are insensitive to small scale interface structures which are resolved only for finer meshes. The overall evolution of the cylinder drift is well captured already for fairly coarse resolutions, and remains unaffected by the artificial dissipation of the applied numerical scheme. The skewness plots (Fig. 8(c)) overlap for 200 and 300 cells per initial cylinder diameter, indicating grid convergence. At the higher resolutions, different stages of the drop deformation can be related to the skewness evolution. The initial increase is related to the flattening of the drop. The onset of the hat-like structure at $t^* \approx 0.3$ results in a strong decrease of skewness. From $t^* \approx 0.75$, the liquid sheet is advected downstream, which increases skewness.

In summary, cylinder flattening is least dependent on resolution, and appears already at the coarsest resolution of $D_0/\Delta x = 50$. The most resolution-critical features are interface waves and the formation of the hat shape at the upstream side, which is resolved with $D_0/\Delta x = 200,\ 300$. Geometrical parameters are less affected by resolution. However, the normalized third moment

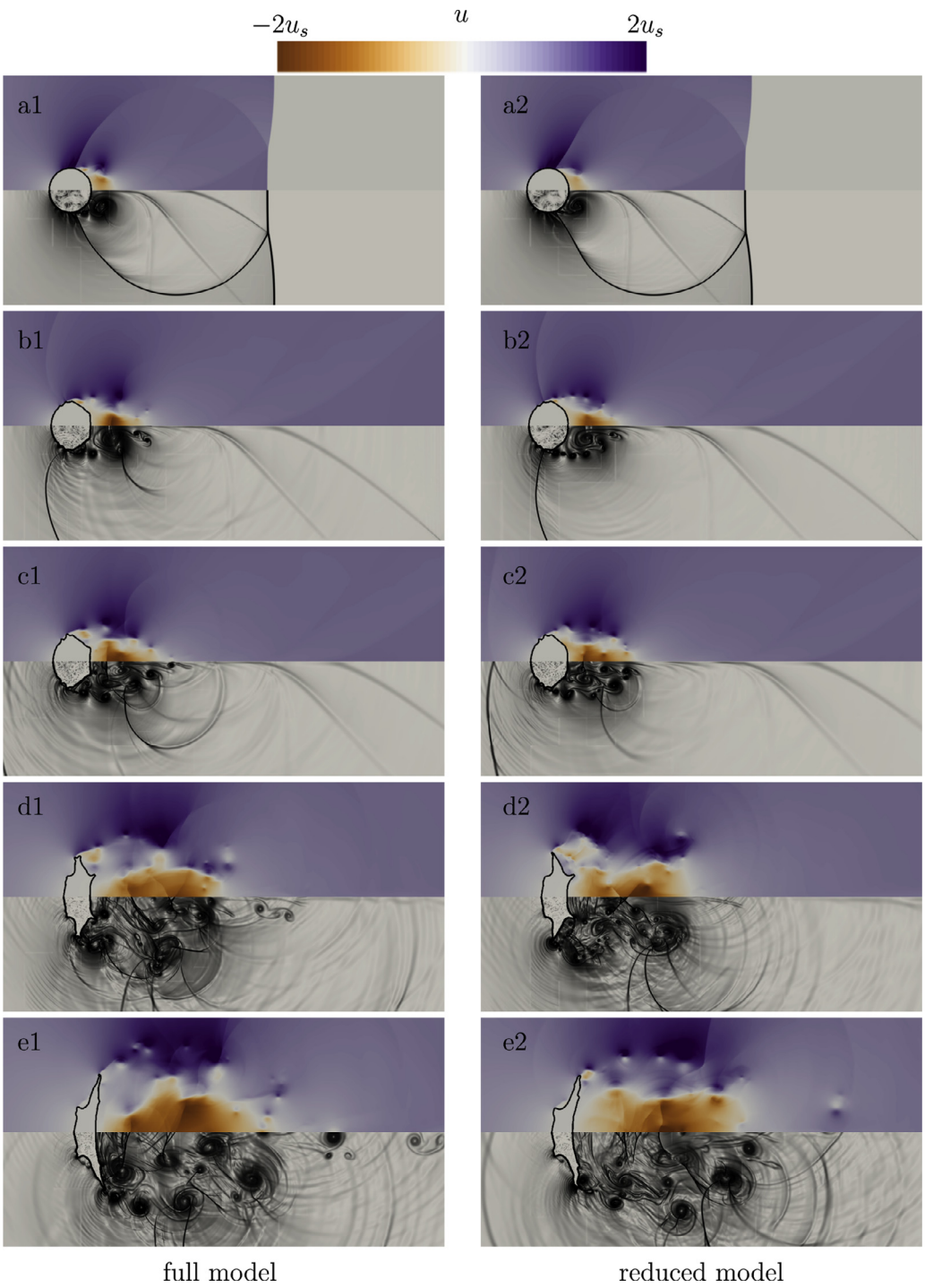

Fig. 12. The flow field in the vicinity of the water column for simulations with capillary and viscous forces ((a1) – (e1)) and without ((a2) – (e2)) for a mesh resolution of 200 cells per initial cylinder diameter at $t^* \in \{0.11, 0.19, 0.26, 0.44, 0.76\}$. The upper half of each image shows the normalized axial velocity field, the lower half numerical schlieren images.

(skewness) appears to deliver a good integral measure to detect the evolution of small-scale features. Our findings extend previously published results (Meng and Colonius, 2015), which showed grid convergence for a resolution of 100 cells per initial diameter. Our results indicate that higher resolutions of at least 200 cells per initial diameter are required, along with low-dissipation temporal and spatial discretization schemes, for resolving detailed breakup features, such as the formation of the upstream hat-shape structure.

4.4. Comparison with experimental visualizations

In the following, we compare our numerical results with available experimental visualizations. Schlieren images reveal wave patterns around the cylinder, as shown in Fig. 9 at times $t^* = 0.035$ (Fig. 9(a); $t = 16.18\mu s$) and $t^* = 0.07$ (Fig. 9(b) and (c); $t = 32.14\mu s$). The experimental images of Igra and Takayama (2001b) are depicted in the upper half, numerical schlieren images in the lower half. Fig. 9(a1)–(c1) give results for a resolution $D_0/\Delta x = 200$, and

Fig. 9(a2)–(c2) for $D_0/\Delta x = 300$. The time instants are chosen as described by Meng and Colonius (2015). At $t = 16.18\mu s$, the numerical simulation accurately reproduces the propagation of the primary wave system (initial and reflected shock), independent of the chosen resolution. The propagation of the secondary wave system, which consists of the converged Mach stems, is slightly underestimated for both resolutions. This delay has been reported previously in literature for this case, e.g. Meng and Colonius (2015). At $t = 32.14\mu s$, the primary waves are accurately predicted by the simulation. The propagation of the wave system close to the interface shows a dependency on the chosen mesh resolutions (see the area marked by the blue arrows in Fig. 9(b), and the focus on this area in Fig. 9(c)). For the higher-resolved simulation ($D_0/\Delta x = 300$), the interaction of the upstream-travelling wave with the increasingly disturbed interface results in a faster progression of the wave in comparison to the simulation with $D_0/\Delta x = 200$, and, thus, in a better agreement with the experimental data.

Igra et al. (2002) and Igra and Takayama (2001a) reported phenomenological similarities for the interface deformation and breakup of two-dimensional liquid columns and three-dimensional spherical drops in the shear breakup regime. With this motivation, we show in Fig. 10 snapshots of the deformed interface from our numerical study of two-dimensional liquid-column breakup (Fig. 10(a)), and qualitatively similar visualizations of three-dimensional drop-breakup experiments of Theofanous et al. (2012) (Fig. 10(b)). The experimental visualizations are taken from a breakup configuration in the SIE regime, with $We = 7.8 \times 10^2$, $Oh = 2.4 \times 10^{-3}$, and $Re = 2.2 \times 10^4$ (run W2 in Theofanous et al. (2012)). We consider the main flow characteristics as precise flow conditions and time information do not match, see also Meng and Colonius (2018) for a corresponding discussion. Nevertheless, the characteristic interface deformation patterns agree well in both visualizations. At $t^* = 0.14$, the cylinder flattens due to the non-uniform pressure distribution along the interface. The downstream side is nearly planar, with two small cusps near the equator. At $t^* = 0.23$, interface waves appear on the upstream side. These disturbances later form the hat-like structure and the liquid sheet, which is typical for this breakup mode ($t^* = 0.76$). The capillary breakup of the sheet in the wake of the cylinder cannot be observed in our simulation, most likely due to resolution limits (see Section 4.1). In summary, the main characteristics of the drop evolution agree with the experiment:

(i) hat-like upstream structure with smooth windward region and two cusps at the edge,
(ii) transition region between hat and sheet, and
(iii) sheet deformation in the wake of the cylinder.

4.5. Capillary and viscous forces

Capillary and viscous forces may be negligible at high Weber and low Ohnesorge numbers. We assess the significance of these forces on overall breakup evolution and on interface deformation for the given set of physical and numerical parameters. Fig. 11 shows the temporal evolution of the upstream stagnation point drift, the center-of-mass drift, and the skewness of the deformation in x-direction for simulations with and without capillary and viscous effects for a resolution of 200 cells per initial diameter. The upstream stagnation point drift Δx^*_{sp} (Fig. 11(a)) and the center-of-mass drift Δx^*_{com} (Fig. 11(b)) overlap, indicating that capillary and viscous effects are insignificant at the considered We and Oh. Generally, also the skewness (Fig. 11(c)) shows similar evolution through the main stages: increase during the flattening stage, decrease during the hat-formation, and subsquent increase during sheet stripping. However, for $t^* < 0.5$, the skewness differs more significantly, indicating that small scale interface structures at early deformation stages indeed are affected by surface tension and viscous forces. With progressing interface deformation, inertial forces dominate and overwhelm capillary and viscous effects.

Fig. 12 shows contour plots at time instants $t^* \in \{0.11, 0.19, 0.26, 0.44, 0.76\}$ (top to bottom) for the cases with ((a1) – (e1)) and without ((a2) – (e2)) capillary and viscous forces. The upper half domain shows the normalized axial velocity, the lower numerical schlieren images. The general flow-field and interface-deformation evolution agree well qualitatively for both cases. However, the formation of the two small water sheets on the leeward side of the cylinder is delayed ($t^* = 0.19, 0.26$) when neglecting capillary and viscous effects. Also, interface disturbances at the equator appear to be sharper ($t^* = 0.19, 0.26$), which has some effect on the shape of the sheet at later instants ($t^* = 0.76$). Nonetheless, flow field characteristics such as the recirculation zones are well reproduced in both cases. At $t^* = 0.76$, both cases exhibit the hat-shape structure at the upstream side and the liquid sheet at the downstream side.

5. Conclusion

We have analyzed interface deformation of shock-induced breakup of a liquid column by simulation with a high-resolution numerical scheme. The numerical model has beed validated by comparison with experimental results of Igra et al. (2002), Igra and Takayama (2001b,c) and Theofanous et al. (2012). The analysis focuses on the unsteady deformation of the water cylinder for different mesh resolutions, and on comparison of results for simulations with and without capillary and viscous forces.

The simulations accurately predict wave dynamics and interface deformation of the liquid column, reproducing the flattening of the cylinder (first stage) and the stripping of the sheet (second stage). Pressure waves form in a supersonic region upstream of the cylinder equator after shock impact and interact with the phase interface. This results in local interface disturbances, coinciding with the onset of the second stage. Resolving these interface waves is essential for a numerical prediction of a hat-shape structure at the upstream side of the cylinder during the second stage of the breakup, which is found in experimental results of Theofanous et al. (2012) for this breakup mode. To our knowledge, this structure has not been reproduced by numerical simulations in previous works. We assume that the pressure waves initiate the interface disturbances, since these pressure waves also appear for a coarser resolution of 100 cells per initial diameter, for which the interface remains smooth due to numerical dissipation. The results confirm the relation between the sheet-stripping mechanisms and the local formation of recirculation zones, as reported by Meng and Colonius (2015). Extending their findings, we find that additional recirculation zones appear at multiple locations near the interface, and are directly linked to the evolution of liquid sheets from interface disturbances. At very early stages of the shock-column interaction, correct prediction of the interaction between the secondary wave system and interface instabilities is critical for qualitative agreement between simulation and experimental results of Igra and Takayama (2001b). A comparative study shows that capillary and viscous forces have small effect on integral parameters for the considered Weber and Ohnesorge numbers and for the early stages of breakup. Late stages of breakup evolution increasingly develop three-dimensional flow structures. Simulations and analyses of three-dimensional configurations at late breakup stages are subject of ongoing work.

Declaration of Competing Interest

The authors declare that they have no known competing financial interests or personal relationships that could have appeared to influence the work reported in this paper.

CRediT authorship contribution statement

J.W.J. Kaiser: Conceptualization, Methodology, Software, Investigation, Formal analysis, Visualization, Writing - original draft. **J.M. Winter:** Methodology, Software, Investigation, Writing - original draft, Writing - review & editing. **S. Adami:** Writing - review & editing, Supervision, Resources, Project administration. **N.A. Adams:** Formal analysis, Writing - review & editing, Supervision, Funding acquisition, Project administration.

Acknowledgments

The first author is supported by the German Research Foundation (Deutsche Forschungsgesellschaft, DFG). The second, third, and fourth authors acknowledge funding from the European Research Council (ERC) under the European Union's Horizon 2020 research and innovation program (grant agreement No. 667483). The authors gratefully acknowledge the Gauss Centre for Supercomputing e.V. (www.gauss-centre.eu) for funding this project by providing computing time on the GCS Supercomputer SuperMUC at Leibniz Supercomputing Centre (www.lrz.de).

References

Aalburg, C., van Leer, B., Faeth, G.M., 2003. Deformation and drag properties of round drops subjected to shock-wave disturbances. AIAA J. 41 (12), 2371–2378.
Aslani, M., Regele, J.D., 2018. A localized artificial diffusivity method to simulate compressible multiphase flows using the stiffened gas equation of state. Int. J. Numer. Methods Fluids 88 (9), 413–433. doi:10.1002/fld.4668.
Chen, H., 2008. Two-dimensional simulation of stripping breakup of a water droplet. AIAA J. 46 (5), 1135–1143.
Dai, Z., Faeth, G.M., 2001. Temporal properties of secondary drop breakup in the multimode breakup regime. Int. J. Multiphase Flow 27, 217–236.
Fedkiw, R.P., Aslam, T.D., Merriman, B., Osher, S., 1999. A non-oscillatory Eulerian approach to interfaces in multimaterial flows (the ghost fluid method). J. Comput. Phys. 152 (2), 457–492.
Garrick, D.P., Owkes, M., Regele, J.D., 2017. A finite-volume HLLC-based scheme for compressible interfacial flows with surface tension. J. Comput. Phys. 339, 46–67. doi:10.1016/j.jcp.2017.03.007.
Gojani, A.B., Ohtani, K., Takayama, K., Hosseini, S.H., 2016. Shock Hugoniot and equations of states of water, castor oil, and aqueous solutions of sodium chloride, sucrose and gelatin. Shock Waves 26, 63–68.
Gottlieb, S., Shu, C.-W., 1998. Total variation diminishing Runge–Kutta schemes. Math. Comput. 67 (221), 73–85.
Guildenbecher, D.R., López-Rivera, C., Sojka, P.E., 2009. Secondary atomization. Exp. Fluids 46 (3), 371–402. doi:10.1007/s00348-008-0593-2.
Han, L.H., Hu, X.Y., Adams, N.A., 2014. Adaptive multi-resolution method for compressible multi-phase flows with sharp interface model and pyramid data structure. J. Comput. Phys. 262, 131–152. doi:10.1016/j.jcp.2013.12.061.
Harten, A., 1983. High resolution schemes for hyperbolic conservation laws. J. Comput. Phys. 135, 260–278. doi:10.1016/0021-9991(83)90136-5.
Harten, A., 1994. Adaptive multiresolution Schemes for Shock Computations. J. Comput. Phys. 115, 319–338.
Hawker, N.A., Ventikos, Y., 2012. Interaction of a strong shockwave with a gas bubble in a liquid medium: a numerical study. J. Fluid Mech. 701, 59–97. doi:10.1017/jfm.2012.132.
Hoppe, N., Pasichnyk, I., Allalen, M., Adami, S., Adams, N.A., 2019. Node-level optimization of a 3D block-based multiresolution compressible flow solver with emphasis on performance portability. In: Proceedings of the International Conference on High Performance Computing & Simulation (HPCS).
Hu, X., Khoo, B., Adams, N., Huang, F., 2006. A conservative interface method for compressible flows. J. Comput. Phys. 219 (2), 553–578. doi:10.1016/j.jcp.2006.04.001.
Igra, D., Ogawa, T., Takayama, K., 2002. A parametric study of water column deformation resulting from shock wave loading. At. Sprays 12, 577–591. doi:10.1615/AtomizSpr.v12.i56.20.
Igra, D., Sun, M., 2010. Shock–water column interaction, from initial impact to fragmentation onset. AIAA J. 48, 2763–2771.
Igra, D., Takayama, K., 2001. Investigation of aerodynamic breakup of a cylindrical water droplet. At. Sprays 11, 167–185.
Igra, D., Takayama, K., 2001. Numerical simulation of shock wave interaction with a water column. Shock Waves 11 (3), 219–228.
Igra, D., Takayama, K., 2001. A study of shock wave loading on a cylindrical water column. Technical Report. Institute of Fluid Science, Tohoku University.
Igra, D., Takayama, K., 2003. Experimental investigation of two cylindrical water columns subjected to planar shock wave loading. J. Fluids Eng. 125 (2), 325–331. doi:10.1115/1.1538628.
Ireland, P.J., Desjardins, O., 2016. Toward liquid jet atomization in supersonic crossflows. In: Proceedings of the ILASS AmericasTwenty-eighth Annual Conference on Liquid Atomization and Spray Systems.
Jiang, G.-S., Shu, C.-W., 1996. Efficient implementation of weighted ENO schemes. J. Comput. Phys. 126, 202–228.
Johnsen, E., Colonius, T., 2007. Numerical simulations of non-spherical bubble collapse with applications to shockwave lithotripsy. California Institute of Technology, Pasadena, CA.
Kaiser, J.W.J., Adami, S., Adams, N.A., 2017. Direct numerical simulation of shock-induced drop breakup with a sharp-interface-method. In: Proceedings of the Tenth International Symposium on Turbulence and Shear Flow Phenomena, TSFP 2017, pp. 1–6.
Kaiser, J.W.J., Hoppe, N., Adami, S., Adams, N.A., 2019. An adaptive local time-stepping scheme for multiresolution simulations of hyperbolic conservation laws. J. Comput. Phys. X 4, 1000038.
Khosla, S., Smith, C.E., Throckmorton, R.P., 2006. Detailed understanding of drop atomization by gas crossflow using the volume of fluid method. In: Proceedings of the Nineteenth Annual Conference on Liquid Atomization and Spray Systems (ILASS-Americas), Toronto, Canada.
Lauer, E., Hu, X.Y., Hickel, S., Adams, N.A., 2012. Numerical investigation of collapsing cavity arrays. Phys. Fluids 24 (5), 052104. doi:10.1063/1.4719142.
Luo, J., Hu, X., Adams, N., 2015. A conservative sharp interface method for incompressible multiphase flows. J. Comput. Phys. 284, 547–565. doi:10.1016/j.jcp.2014.12.044.
Meng, J.C., Colonius, T., 2015. Numerical simulations of the early stages of high-speed droplet breakup. Shock Waves 25, 339–414.
Meng, J.C., Colonius, T., 2018. Numerical simulation of the aerobreakup of a water droplet. J. Fluid Mech. 835, 1108–1135. doi:10.1017/jfm.2017.804.
Nonomura, T., Kitamura, K., Fujii, K., 2014. A simple interface sharpening technique with a hyperbolic tangent function applied to compressible two-fluid modeling. J. Comput. Phys. 258, 95–117. doi:10.1016/j.jcp.2013.10.021.
Osher, S., Sanders, R., 1983. Numerical approximations to nonlinear conservation laws with locally varying time and space grids. Math. Comput. 41 (164), 321–336.
Popinet, S., 2018. Numerical models of surface tension. Annu. Rev. Fluid Mech. 50 (1), 49–75. doi:10.1146/annurev-fluid-122316-045034.
Quirk, J.J., Karni, S., 1996. On the dynamics of a shock-bubble interaction. J. Fluid Mech. 318, 129–163.
Ranger, A.A., Nicholls, J.A., 1969. Aerodynamic shattering of liquid drops.. AIAA J. 7 (2), 285–290. doi:10.2514/3.5087.
Roe, P.L., 1981. Approximate Riemann solvers, parameter vectors, and difference schemes. J. Comput. Phys. 43 (2), 357–372.
Rossinelli, D., Hejazialhosseini, B., Spampinato, D.G., Koumoutsakos, P., 2011. Multicore/multi-gpu accelerated simulations of multiphase compressible flows using wavelet adapted grids. J. Sci. Comput. 33 (2), 512–540.
Schmidmayer, K., Petitpas, F., Daniel, E., Favrie, N., Gavrilyuk, S., 2017. A model and numerical method for compressible flows with capillary effects. J. Comput. Phys. 334, 468–496.
Sembian, S., Liverts, M., Tillmark, N., Apazidis, N., 2016. Plane shock wave interaction with a cylindrical water column. Phys. Fluids 28 (5). doi:10.1063/1.4948274.
Sussman, M., Smereka, P., Osher, S., 1994. A level set approach for computing solutions to incompressible two-phase flow. J. Comput. Phys. 114, 146–159.
Terashima, H., Tryggvason, G., 2009. A front-tracking/ghost-fluid method for fluid interfaces in compressible flows. J. Comput. Phys. 228 (11), 4012–4037. doi:10.1016/j.jcp.2009.02.023.
Theofanous, T., 2011. Aerobreakup of Newtonian and viscoelastic liquids. Annu. Rev. Fluid Mech. 43 (1), 661–690. doi:10.1146/annurev-fluid-122109-160638.
Theofanous, T., Mitkin, V.V., Ng, C.L., Chang, C.H., Deng, X., Sushchikh, S., 2012. The physics of aerobreakup. Part II. Viscous liquids. Phys. Fluids 24.
Theofanous, T.G., Li, G.J., Dinh, T.N., 2004. Aerobreakup in rarefied supersonic gas flows. J. Fluids Eng. 126 (4), 516. doi:10.1115/1.1777234.
Villermaux, E., 2007. Fragmentation. Annu. Rev. Fluid Mech. 39, 419–446. doi:10.1016/j.physa.2006.04.087.
Wan, Q., Deiterding, R., Eliasson, V., 2019. Numerical investigation of shock wave attenuation in channels using water obstacles. Multisc. Multidiscip. Model. Exp. Des. 2, 159–173.
Wang, B., Xiang, G., Hu, X.Y., 2018. An incremental-stencil WENO reconstruction for simulation of compressible two-phase flows. Int. J. Multiphase Flow 104, 20–31.
Xiang, G., Wang, B., 2017. Numerical study of a planar shock interacting with a cylindrical water column embedded with an air cavity. J. Fluid Mech. 825, 825–852. doi:10.1017/jfm.2017.403.
Yang, H., Peng, J., 2019. Numerical study of the shear-thinning effect on the interaction between a normal shock wave and a cylindrical liquid column. Phys. Fluids 31 (4). doi:10.1063/1.5083633.
Yang, W., Jia, M., Che, Z., Sun, K., Wang, T., 2017. Transitions of deformation to bag breakup and bag to bag-stamen breakup for droplets subjected to a continuous gas flow. Inter. J. Heat Mass Transf. 111, 884–894. doi:10.1016/j.ijheatmasstransfer.2017.04.012.

A.3 A semi-implicit conservative sharp-interface method for liquid-solid phase transition

A semi-implicit conservative sharp-interface method for liquid-solid phase transition

Author: J.W.J. Kaiser,S. Adami,I.S. Akhatov,N.A. Adams

Publication: International Journal of Heat and Mass Transfer

Publisher: Elsevier

Date: July 2020

International Journal of Heat and Mass Transfer 155 (2020) 119800

Contents lists available at ScienceDirect

International Journal of Heat and Mass Transfer

journal homepage: www.elsevier.com/locate/hmt

A semi-implicit conservative sharp-interface method for liquid-solid phase transition

J.W.J. Kaiser[a,*], S. Adami[a], I.S. Akhatov[b], N.A. Adams[a]

[a] Technical University of Munich, Department of Mechanical Engineering, Chair of Aerodynamics and Fluid Mechanics, Boltzmannstraße 15, Garching 85748, Germany

[b] Skolkovo Institute of Science and Technology, Skolkovo Innovation Center, 3 Nobel St., Moscow 143026, Russia

ARTICLE INFO

Article history:
Received 12 December 2019
Revised 20 March 2020
Accepted 12 April 2020

Keywords:
Solidification
Dendritic growth
Level-set method
Conservative interface-exchange terms
Sharp-interface method
Multiresolution

ABSTRACT

The solidification of an undercooled liquid is physically unstable. The dominating instability modes are affected by both the evolving temperature field in the solid and liquid phases, and characteristics of the phase interface such as the curvature and the propagation velocity. To capture the instability mode, therefore both the temperature field and the interface have to be represented accurately in a numerical model of the phase-change process. In this work, we develop conservative interface exchange terms for a sharp-interface formulation of liquid-solid phase transition. Conservation at the interface is maintained by explicit formulation of interface fluxes into both solid and liquid phases. We propose a semi-implicit level-set formulation to evolve the phase interface. A new formulation for the interface surface in a cut cell is derived, which includes the Stefan condition. We achieve low numerical dissipation by an explicit third-order Runge-Kutta scheme for time discretization, and a novel WENO-like (Weighted Essentially Non-Oscillatory) interface-gradient reconstruction. This distinguishes our level-set based sharp-interface model from previous level-set based approaches, which rely on finite-difference based interface treatment, and thus do not ensure discrete conservation at the interface. The flux terms in our approach take into account surface-tension and kinetic effects on the interface temperature (Gibbs-Thomson relation). The Stefan condition provides a relation between interface fluxes of mass and energy, and the interface-propagation velocity. Computational efficiency is maintained by a multiresolution approach for local mesh adaptation, and an adaptive local time-stepping scheme.

We present one- and two-dimensional simulation results for the growth of a planar solidification front and a single parabolic dendrite affected by surface tension. The results agree well with experimental and analytical reference data, showing that the model is capable to capture both stable (planar) and unstable (dendritic-like) growth processes in the heat-diffusion dominated regime. The convergence order for successively finer meshes in the one-dimensional case is one for the interface location and the temperature field, outperforming previously reported level-set based approaches. We present numerical data of a growing crystal with four-fold symmetry. Our results indicate that the artificial dissipation of the underlying numerical scheme affects its capability to reproduce consistently physical tip-splitting instabilities. The proposed low-dissipation scheme is able to resolve such instabilities. Finally, we demonstrate the capability of the method to simulate multiple growing crystals with anisotropic surface-tension and kinetic effects.

1. Introduction

Under suitable conditions, liquids can be cooled down to a temperature well below their solidification temperature. A disturbance of the undercooled liquid initiates sudden solidification processes, which manifest themselves as dendrites. Dendrites have a highly branched, tree-like structure. Anisotropic growth is caused by in-

* Corresponding author.
E-mail addresses: jakob.kaiser@tum.de (J.W.J. Kaiser), stefan.adami@tum.de (S. Adami), i.akhatov@skoltech.ru (I.S. Akhatov), nikolaus.adams@tum.de (N.A. Adams).

https://doi.org/10.1016/j.ijheatmasstransfer.2020.119800

homogeneities of the phase-change process in preferred crystal growth directions. Small perturbations of the initial state of the undercooled liquid or during the growth process may cause significant changes in the resulting crystalline structure [21]. Although the dendritic growth process itself is inherently unstable, a steady-state solution exists for the tip radius and the growth velocity, which depend on both the material properties and the degree of undercooling. The steady-state growth mechanism can be characterized by diffusion or interface kinetics [46]. For the diffusion-dominated regime, Langer and Müller-Krumbhaar [28–30,34] derived an analytical stability theory, which extends the seminal work of Ivantsov [20]. Their theory shows good agreement with experimental results [9,46–48] in the diffusion-dominated regime, but differs in the kinetics-dominated regime. Once tip radius and tip growth velocities exceed their stability region, tip-splitting or side-branching instabilities may occur that eventually lead again to a stable configuration.

The dendritic solidification process poses a Stefan problem at the phase interface, i.e. an initial-boundary value problem with moving boundary. Phase-interface dynamics are governed by the local temperature field and a Dirichlet boundary condition for the interface temperature considering local interface characteristics, such as the curvature or the propagation velocity. Therefore, an accurate representation of the topologically complex, time-dependent solidification front in multiple dimensions is necessary [11]. Various multiphase models have been applied to solve the Stefan problem numerically, both for mesh-free [50–52] and mesh-based discretization methods. For the mesh-based discretization, approaches can be related to either front-tracking [13,23,41] or front-capturing methods. Among the front-capturing methods, phase-field [2,3,10,14,25,27,35,49,57] and level-set [5–7,11,26,45,54–56] approaches are the most popular choices for representing the solidification front [21]. In the phase-field approach, an additional order parameter, the phase field variable, is introduced. This variable indicates the physical state at the location of interest. The phase interface is located in the transition region of this parameter, and the interface width is a model parameter. Hence, the interface is artificially thickened so it can be resolved on the given mesh. Phase-field models are therefore often classified as diffuse-interface model. The accuracy of the simulation depends on the thickness of the phase interface. Quantitatively accurate predictions of the phase front therefore require sufficiently small numerical grids, which may incur prohibitively high computational cost [21].

This difficulty is alleviated by the level-set approach. It also employs an order parameter, the level set, which describes the signed distance from the interface. The zero-level-set contour denotes the interface location. The sharp-interface property of the level set enables an accurate localization of the phase interface, and simplifies the computation of local interface characteristics. An approach to couple the interface velocity with the interface curvature was introduced by Osher and Sethian [37]. This work was a first step towards simulating dendritic solidification with the level-set method [44]. Chen et al. [6] extended this approach and proposed a model to solve the Stefan problem, focusing on crystal growth. They applied a finite difference approach to discretize the diffusion equation in solid and liquid phases on a homogenoeous grid, and used implicit time integration schemes. Their approach shows good agreement with the analytical solution obtained from solvability theory [26]. Higher-order stencils improved accuracy and convergence rates [11]. Overall computational efficiency was improved by a local mesh adaptation approach, which accounts for the different length scales near the phase interface [5]. Their approach was applied to compute the solidification of binary alloys by Theillard et al. [56]. An extended level-set model was introduced by Criscione et al. [7], who employed a finite-volume scheme using ghost cells to solve the temperature field. Good results were obtained for the simulation of both a stable, planar solidification front and the unstable growth of a single parabolic dendrite. Ramanuj et al. [39] presented simulations of unstable solidifying systems based on a second-order level-set approach [38]. They showed the advantages of high-order spatial schemes and explicit time integration schemes for dendrite-growth simulations. Yet, most previous works rely on implicit time integration schemes, introducing comparably large numerical dissipation and therefore require higher spatial resolutions to resolve topologically complex crystalline structures. In addition, non-conservative numerical interface models may compromise physically correct interface evolution.

In this work, we develop a conservative interface-interaction method for a sharp-interface formulation of liquid-solid phase transition of pure liquids. Conservation at the interface is maintained by explicit formulation of interface fluxes into both solid and liquid phases. We propose a semi-implicit level-set formulation to evolve the phase interface. A new formulation for the interface surface in a cut cell is derived, which includes the Stefan condition. We achieve low numerical dissipation by an explicit third-order Runge-Kutta scheme for time discretization [12,16], and a novel WENO-like (Weighted Essentially Non-Oscillatory) interface-gradient reconstruction [22]. This distinguishes our level-set based sharp-interface model from previously published level-set based approaches, which rely on finite-difference based interface treatment and may violate discrete conservation at the interface. The flux terms in our approach take into account surface-tension and kinetic effects on the interface temperature (Gibbs-Thomson relation), including anisotropic behavior. The Stefan condition provides a relation between interface fluxes of mass and energy, and the interface-propagation velocity. The sharp-interface property is ensured by extrapolating fluid states across the interface for the single-phase reconstruction of the cell-face fluxes near the interface [8]. Computational efficiency is improved by dynamic mesh adaptation with respect to the evolving interface and temperature field using the multiresolution approach of Harten [17]. We employ an adaptive local time-stepping scheme for efficient and robust time integration [24].

The structure of the paper is the following: in section 2, we describe the sharp-interface method for modeling solid-liquid phase-transition problems. The new conservative interface-interaction approach for liquid-solid phase transition is given in section 3, together with the employed level-set method. Section 4 provides one- and two-dimensional numerical example simulations for stable and unstable phase-change processes. We conclude the work in section 5.

2. Sharp-interface method for liquid-solid phase transition

The governing equations for the phase-change problem can be written as

$$\frac{\partial \mathbf{U}}{\partial t} = \nabla \cdot \mathbf{F}_k \,, \tag{1}$$

where $\mathbf{U} = (\rho, \rho c T)^T$ is the state vector of mass and energy, and $\mathbf{F}_k = (0, k\nabla T)^T$ represents heat conduction. Here, ρ is the density, c the specific heat capacity, T the temperature, and k the thermal conductivity. We solve eq. (1) separately for the solid and liquid subdomain, and assume the specific heat capacity c and the thermal conductivity k to be constant in each subdomain. The convection in the liquid phase is suppressed in order to focus on the phase-change model.

Eq. (1) needs to be completed by a set of interface conditions to fully describe the Stefan problem. We assume that the temperature field is continuous across the interface. The temperature at

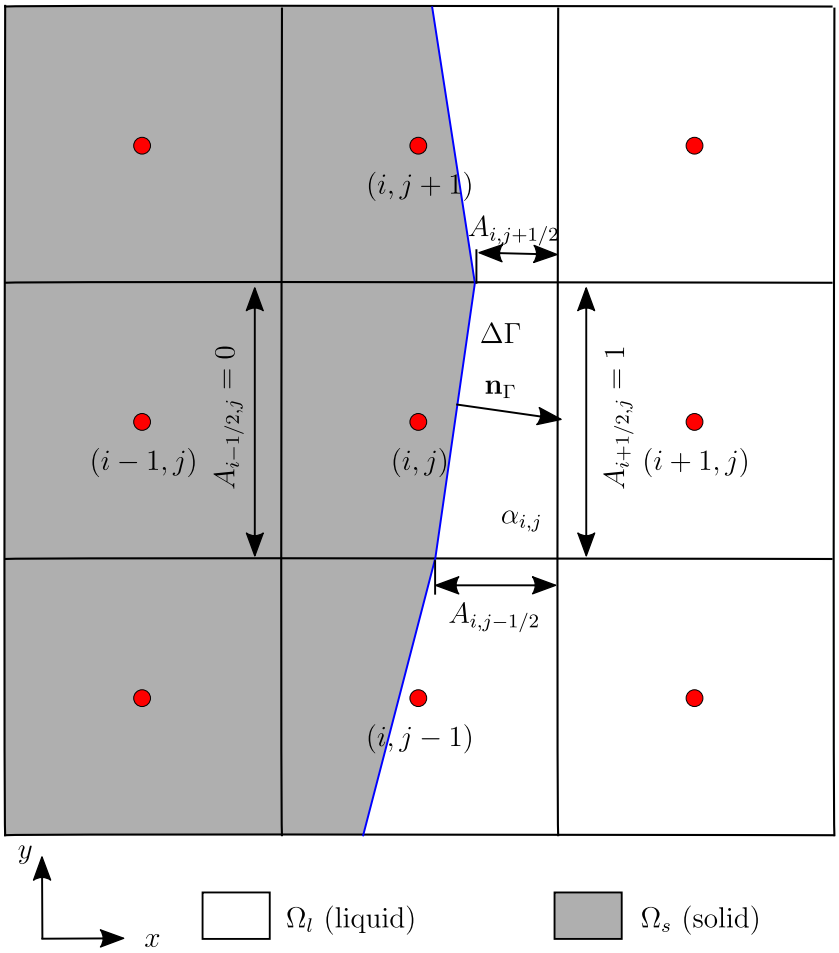

Fig. 1. Schematic finite volume discretization of the domain Ω on a Cartesian quadratic grid.

the interface T_Γ is prescribed as Dirichlet boundary condition, and follows from the Gibbs-Thomson relation

$$T_\Gamma = T_m - \frac{\gamma T_m}{\rho L}\kappa - \epsilon_u ||\mathbf{u}_\Gamma|| \tag{2}$$

including surface tension and kinetic effects. Here, T_m is the melting temperature of the material, γ the surface tension coefficient, L the latent heat, κ the interface curvature, ϵ_u the kinetic coefficient, and $\mathbf{u}_\Gamma$ the interface velocity vector. Unless noted otherwise, we assume isotropic surface tension and kinetic coefficients. The Stefan condition represents the balance of local heat fluxes and the latent heat released by phase change and yields

$$\begin{aligned}\dot{m}[L + (T_\Gamma - T_m)(c_l - c_s)] &= \rho \parallel \mathbf{u}_\Gamma \parallel [L + (T_\Gamma - T_m)(c_l - c_s)] \\ &= (k_s \nabla T_s - k_l \nabla T_l) \cdot \mathbf{n}_\Gamma.\end{aligned} \tag{3}$$

Here, $\dot{m}$ is the mass rate of solidifying liquid, $\nabla_n T_\Phi = \nabla T_\Phi \cdot \mathbf{n}_\Gamma$ is the interface-normal temperature gradient of the solid ($\Phi = s$) and liquid ($\Phi = l$) phases, and $\mathbf{n}_\Gamma$ is the interface-normal vector, which points from the solid to the liquid phase.

The governing equations (1) are discretized by a finite-volume approach in the domain Ω, which is divided into two subdomains Ω_l and Ω_s by a time-evolving interface Γ. Fig. 1 shows a sketch of the two subdomains with a sharp interface. We integrate eq. (1) in each computational cell S_{ij} of each subdomain Ω_Φ and apply Gauß' theorem to obtain

$$\int_{t^{(n)}}^{t^{(n+1)}} dt \int_{S_{ij}\cap\Omega_\Phi} dS_{ij} \frac{\partial \mathbf{U}}{\partial t} = \int_{t^{(n)}}^{t^{(n+1)}} dt \int_{\partial(S_{ij}\cap\Omega_\Phi)} dS_{ij}\, \mathbf{F}_k \cdot \mathbf{n} \tag{4}$$

where $dS_{ij} = \Delta x_1\, \Delta x_2$ denotes the cell volume in two dimensions, $S_{ij} \cap \Omega_\Phi$ each cell volume of phase Φ, $\partial(S_{ij} \cap \Omega_\Phi)$ the cell face, and $\mathbf{n}$ the surface normal of this cell face. We replace $S_{ij} \cap \Omega_\Phi$ by $S_{ij}\alpha_{ij}$, where α_{ij} is the time-dependent volume fraction of phase Φ, with $0 \le \alpha_{ij} \le 1$. The cell face $\partial(S_{ij} \cap \Omega_\Phi)$ can be approximated by the cell-face apertures A, $0 \le A \le 1$, and the segment of the interface Γ inside this cell, $\Delta\Gamma_{ij}$. Eq. (4) is then rewritten for a single forward-time integration step of phase Φ as

$$\begin{aligned}\alpha_{i,j}^{(n+1)}\mathbf{U}_{i,j}^{(n+1)} &= \alpha_{i,j}^{(n)}\mathbf{U}_{i,j}^{(n)} \\ &+ \frac{\Delta t}{\Delta x_1}(A_{i-1/2,j}^{(n)}\mathbf{F}_{\mathbf{k}_{i-1/2,j}}^{(n)} - A_{i+1/2,j}^{(n)}\mathbf{F}_{\mathbf{k}_{i+1/2,j}}^{(n)}) \\ &+ \frac{\Delta t}{\Delta x_2}(A_{i,j-1/2}^{(n)}\mathbf{F}_{\mathbf{k}_{i,j-1/2}}^{(n)} - A_{i,j+1/2}^{(n)}\mathbf{F}_{\mathbf{k}_{i,j+1/2}}^{(n)}) \\ &+ \frac{\Delta t}{\Delta x_1 \Delta x_2}\mathbf{X}_{\mathbf{S}_{i,j}}^{(n,n+1)}(\Delta\Gamma_{i,j})\end{aligned} \tag{5}$$

where Δt denotes the timestep size, $\mathbf{U}_{i,j}$ the cell-averaged state vector of the considered phase in cell (i, j), and $\mathbf{F}_{\mathbf{k}_{i,j}}$ the fluxes in or out of this cell. The term $\mathbf{X}_{\mathbf{S},i,j}$ describes the mass and energy exchange across the interface for the phase-change process. It vanishes if a cell is not a cut cell. We follow the approach of Hu et al. [19], and formulate the exchange terms as conservative interface fluxes. The fluxes also model the interface conditions (2) and (3). All terms on the right hand side are calculated at time $t^{(n)}$, except for the interface exchange term $\mathbf{X}_{\mathbf{S},i,j}$, which is further detailed in the following section 3.

In this work, cell-face heat fluxes are reconstructed by a second-order central difference scheme. Low-dissipation time integration is achieved by a strongly stable third-order Runge-Kutta scheme

$$\begin{aligned} u^{(1)} &= u^{(n)} + \Delta t\, L(u^{(n)}) \\ u^{(2)} &= \frac{3}{4}u^{(n)} + \frac{1}{4}u^{(1)} + \frac{1}{4}\Delta t\, L(u^{(1)}) \\ u^{(n+1)} &= \frac{1}{3}u^{(n)} + \frac{2}{3}u^{(2)} + \frac{2}{3}\Delta t\, L(u^{(2)}) \end{aligned} \tag{6}$$

[12,16]. The maximum admissible timestep size is determined from a CFL-type stability criterion considering the propagation speed of the phase interface and heat diffusion in both phases

$$\Delta t = \mathrm{CFL} \cdot \min\left(\frac{\Delta x}{|u_\Gamma|}, \frac{3}{14}\frac{(\Delta x)^2 \rho c}{k} \right). \tag{7}$$

In all examples we use CFL= 0.5. Advancing the flow field by this timestep size may lead to an unstable fluid state in cells with small volume fraction α. Therefore, we apply a mixing procedure in cells with $\alpha < 0.5$ to maintain numerical stability [19].

Resolution of all scales of dendritic solidification on a homogeneous mesh is computationally expensive. Several orders of magnitude lie between the wavelength of the dominating instability modes of a growing dendrite and the size of the dendrite itself [56]. Therefore, spatial adaptation techniques are necessary to efficiently solve dendritic solidification problems numerically. We apply a block-structured wavelet-based multiresolution approach based on the work of Harten [17] to adapt the mesh to the progressing solidification front and the evolving temperature field [15,18,42]. The procedure is in detail described in Hoppe et al. [18]. In the multiresolution approach, the cell-averaged solution is represented by cell-averaged data on a coarse grid and a series of values on successively finer refinement levels. In this tree-based structure, the two basic operations to communicate data between successive refinement levels are projection and prediction. The projection operation is applied to obtain data on a refinement level l from level $l+1$. Cell-averaged data on level $l+1$ can be interpolated from level l using the prediction operation. Projection and prediction operations are local and consistent, but not commutative, i.e:

- Applying first the prediction operation to obtain data on level $l+1$ from level l, and afterwards again the projection operation results in exactly the same solution on level l.
- Applying first the projection operation to obtain data on level l from level $l+1$, and interpolating afterwards the data on level $l+1$ from level l using the prediction operation results in an error for data on level $l+1$.

This motivates the definition of the so-called details d, which are the deviation of the predicted solution to the exact solution. The exact solution on the finest level can be replaced by a hierarchical data structure, which contains the exact solution on the coarsest level and the details of all successively finer levels. For implicit mesh adaptation, details are only considered when they are larger than a pre-defined level-dependent threshold

$$\varepsilon_l = \varepsilon_{\mathrm{ref}} \cdot \mathrm{e}^{(-D\cdot(l-l_{max}))}, \tag{8}$$

where l_{max} denotes the maximum level to which the mesh can be refined, D the number of dimensions, and $\varepsilon_{\mathrm{ref}}$ the admissible relative error on level l. If the details are sufficiently small, further grid refinement does not lead to significantly better results than interpolation from a coarser grid. In our simulations, we refine the mesh based on the local error of the energy field. In addition, the phase interface is enforced to be always on the finest level [15]. We apply dyadic refinement, where each cell can be refined into 2^D smaller cells. The reference error is set to $\varepsilon_{\mathrm{ref}} = 0.01$ for a refinement between the finest level and the next coarser one. Efficient time integration is obtained by applying a local time-stepping approach, where each refinement level is advanced with its level-dependent timestep size [36]. The method is described in detail in Kaiser et al. [24]. It allows for adapting the timestep size after each full Runge-Kutta cycle on the finest refinement level based on the CFL stability criterion (7).

3. Conservative interface-interaction model for liquid-solid phase transition

3.1. Conservative interface-exchange terms

The level-set function ϕ represents the phase interface as the zero-crossing of a multi-dimensional continuous function ϕ with>

$$\begin{aligned} &\mathbf{x} \in \Omega_s \rightarrow \phi(\mathbf{x}) < 0, \\ &\mathbf{x} \in \Omega_l \rightarrow \phi(\mathbf{x}) > 0, \text{ and} \\ &\mathbf{x} \in \Gamma \rightarrow \phi(\mathbf{x}) = 0. \end{aligned}$$

The absolute value of ϕ describes the normal distance of the cell center $\mathbf{x}$ to the interface Γ, which leads to the signed-distance property $|\nabla\phi| = 1$.

We develop conservative interface-exchange terms to model the phase-change process. We model mass and energy exchange across the interface, and for now suppress exchange of momentum. The interface fluxes for the solid phase are

$$\mathbf{X}_{\mathbf{S}_s} = (-\dot{m}\Delta\Gamma,\ -\dot{m}c_s T_\Gamma \Delta\Gamma + k_s(\nabla T_s \cdot \mathbf{n}_\Gamma)\Delta\Gamma)^T, \tag{9}$$

and for the liquid phase

$$\mathbf{X}_{\mathbf{S}_l} = (\dot{m}\Delta\Gamma,\ \dot{m}c_l T_\Gamma \Delta\Gamma + k_l(\nabla T_l \cdot \mathbf{n}_\Gamma)\Delta\Gamma)^T. \tag{10}$$

The first term of the energy exchange describes the material transport through the interface, and the second term the heat flux into each material due to the Stefan condition (3). The interface temperature T_Γ is obtained from the Gibbs-Thomson relation eq. (2). If kinetic effects are taken into account, the interface temperature is computed using the interface velocity at time $t^{(n)}$ [11].

In previous work, the area of the interface segment in a cut-cell $\Delta\Gamma$ is computed from cut-cell apertures [19,31]. For $\dot{m} = \rho||\mathbf{u}_\Gamma||$, the interface segment moves within the cut-cell by a distance $\Delta t||\mathbf{u}_\Gamma||$. The linearized volume-fraction change is $\Delta t\Delta\Gamma||\mathbf{u}_\Gamma||$. However, this formulation potentially violates conservation for multi-dimensional problems, see Fig. 2. The linearized volume-fraction change differs from the correct volume-fraction change for the given case. Therefore, we propose a new way for determining $\Delta\Gamma$ based on a semi-implicit level-set approach (see section 3.2). First, we compute the time derivative of the liquid volume fraction $\dot{\alpha}$ from level-set fields $\phi^{(n)}$ and $\phi^{(n+1)}$

$$\dot{\alpha} = \frac{\partial\alpha}{\partial t} \approx \frac{\alpha(\phi^{(n+1)}) - \alpha(\phi^{(n)})}{\Delta t}. \tag{11}$$

It is thus possible to reformulate the mass exchange across the interface in terms of $\dot{\alpha}$ as $\dot{m}\Delta\Gamma = \rho\dot{\alpha}V_c$, where V_c denotes the cell volume. Second, we formulate the energy conservation in a single cut cell based on the Stefan condition, eq. (3),

$$\begin{aligned} \dot{Q}_{\dot{\alpha}} &= \dot{Q}_\lambda \\ \dot{\alpha}\rho V_c[L + (T_\Gamma - T_m)(c_l - c_s)] &= (k_s\nabla T_s - k_l\nabla T_l)\cdot\mathbf{n}_\Gamma\Delta\Gamma \end{aligned}$$

where $\dot{Q}_{\dot{\alpha}}$ denotes the heat released in the phase-change process, and $\dot{Q}_\lambda$ the released heat into both solid and liquid phases due to heat conduction. The interface area $\Delta\Gamma$ follows from

$$\Delta\Gamma = \frac{\dot{\alpha}\rho V_c\left[L + \left(T_{\Gamma_{i,j}} - T_m\right)(c_l - c_s)\right]}{(k_s\nabla T_s - k_l\nabla T_l)\cdot\mathbf{n}_\Gamma} = \frac{\dot{\alpha}V_c}{\|\ \mathbf{u}_\Gamma\ \|} \tag{12}$$

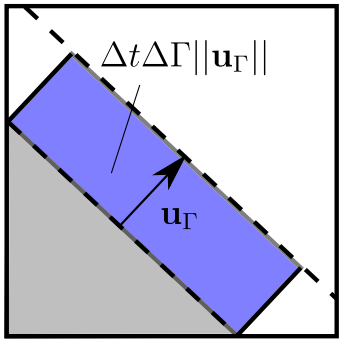

(a) Linearized approach

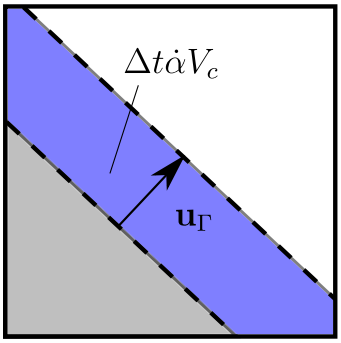

(b) Semi-implicit approach

Fig. 2. Schematic of the volume-fraction change in a single cell during an Euler step. The included volume-fraction change is shown in blue. Fig. (a): change for the linearized approach. Fig. (b): the new semi-implict level-set approach, which correctly predicts the entire volume-fraction change.

Thus, the interface-exchange terms eqs. (9) and (10) can be written as

$$\mathbf{X}_{\mathbf{S}_s} = (-\rho_s \dot{\alpha} V_c, \; -\rho_s \dot{\alpha} V_c c_s T_\Gamma + k_s (\nabla T_s \cdot \mathbf{n}_\Gamma) \Delta\Gamma)^T , \tag{13}$$

$$\mathbf{X}_{\mathbf{S}_l} = (\rho_l \dot{\alpha} V_c, \; \rho_l \dot{\alpha} V_c c_l T_\Gamma + k_l (\nabla T_l \cdot \mathbf{n}_\Gamma) \Delta\Gamma)^T . \tag{14}$$

We compare our approach with the linearized formulation in section 4.3.

The overall accuracy and stability of the method are sensitive to the evaluation of the interface-normal temperature gradient [7]. A common method provided in previous work is to reconstruct the temperature at one or multiple points in a fixed normal distance to the interface. The interface-normal temperature gradient then is computed by a finite-difference scheme [7,32,40]. Through extensive numerical tests we found that a directional splitting approach with weighting of local interface-normal temperature gradients based on third-order WENO smoothness indicators [22] provides the best approximation of $\nabla_n T$ in terms of efficiency and accuracy, see Fig. 3. Filled dots mark cells which are considered for computing the interface-normal temperature gradient. First, we compute the interface temperature gradient in each cell for each direction with a finite difference stencil

$$\begin{aligned} \left.\frac{\partial T}{\partial x_1}\right|_{i+l,j} &= \left|\left| \frac{T_{i+l,j} - T_\Gamma}{|\phi_{i,j}| + l\,\Delta x} \right|\right| \mathrm{sgn}(n_{\Gamma,x_1}), \quad \left.\frac{\partial T}{\partial x_2}\right|_{i,j+l} \\ &= \left|\left| \frac{T_{i,j+l} - T_\Gamma}{|\phi_{i,j}| + l\,\Delta x} \right|\right| \mathrm{sgn}(n_{\Gamma,x_2}) \end{aligned} \tag{15}$$

with $l \in \{1, 2, 3\}$, the sign function sgn() and n_{Γ,x_i} the component of the interface-vector in x_i-direction. We weight the cell-wise interface gradients based on the smoothness indicators of the third-order WENO scheme to obtain the overall interface-normal temperature gradient in the cut-cell (i,j) in each spatial direction $\partial T/\partial x_1$, $\partial T/\partial x_2$. These are then projected onto the normal direction

$$\nabla_n T = n_{\Gamma,x_1} \frac{\partial T}{\partial x_1} + n_{\Gamma,x_2} \frac{\partial T}{\partial x_2} . \tag{16}$$

Similar to Criscione et al. [7], the interface-normal temperature gradient finally is averaged within all direct neighbor cells. This procedure decreases spurious oscillations of the interface-normal temperature gradient.

3.2. Level-set evolution

The level-set field ϕ is evolved in time by an advection equation

$$\frac{\partial \phi}{\partial t} + \mathbf{u}_\Gamma \cdot \nabla \phi = 0 . \tag{17}$$

The level-set advection equation is solved for cut cells using the interface velocity $\mathbf{u}_\Gamma$, which is computed from the Stefan condition (eq. (3)) following

$$\| \mathbf{u}_\Gamma \| = \frac{k_s \nabla_n T_s - k_l \nabla_n T_l}{\rho [L + (T_\Gamma - T_m)(c_l - c_s)]} . \tag{18}$$

Non-cut cells are evolved using an interface velocity $\tilde{\mathbf{u}}_\Gamma$ extrapolated from adjacent cut cells, which is determined from the steady-state solution of the extrapolation equation

$$\frac{\partial \tilde{\mathbf{u}}_\Gamma}{\partial \tau} + \mathbf{n}_\Gamma \cdot \nabla \tilde{\mathbf{u}}_\Gamma = 0 . \tag{19}$$

The level-set field is evolved with the phase states at time $t^{(n)}$ before advecting the fluid field. Thus, the solid and liquid phases can be updated afterwards from time $t^{(n)}$ to $t^{(n+1)}$ using the interface locations $\phi^{(n)}$ and $\phi^{(n+1)}$, e.g. when computing $\dot{\alpha}$ in eq. (11). We have found that this type of operator splitting improves mass conservation of the overall level-set scheme, see section 4.3 for a numerical example.

The numerical solution of the level-set advection does not maintain the signed-distance property $|\nabla\phi| = 1$. Therefore, the re-initialization equation

$$\frac{\partial \phi}{\partial \tau} + \mathrm{sign}(\phi_0)(|\nabla \phi| - 1) = 0 \tag{20}$$

is iterated in pseudo time τ to steady state to restore the signed-distance property after each timestep [53]. Here, ϕ_0 is the level-set field prior the re-initialization step. Note that we also re-initialize cut cells to maintain the signed-distance property. The re-intialization of cells cut by the interface generally may affect the overall conservation of the level-set scheme by shifting the location of the zero-level-set [43]. This issue is, however, not relevant for the developed scheme, as the incorporation of the reinitialized level-set fields at $t^{(n)}$ and $t^{(n+1)}$ within the interface-exchange terms ensures local conservation, see section 3.1.

Similarly to the interface velocity extrapolation from the interface to the adjacent bulk cells, the fluid states are extrapolated across the interface to define a “ghost” fluid within the opposing phase [8]. These ghost-fluid states allow for the single-phase reconstruction of the cell-face fluxes near the interface. This maintains the sharp-interface property of the method.

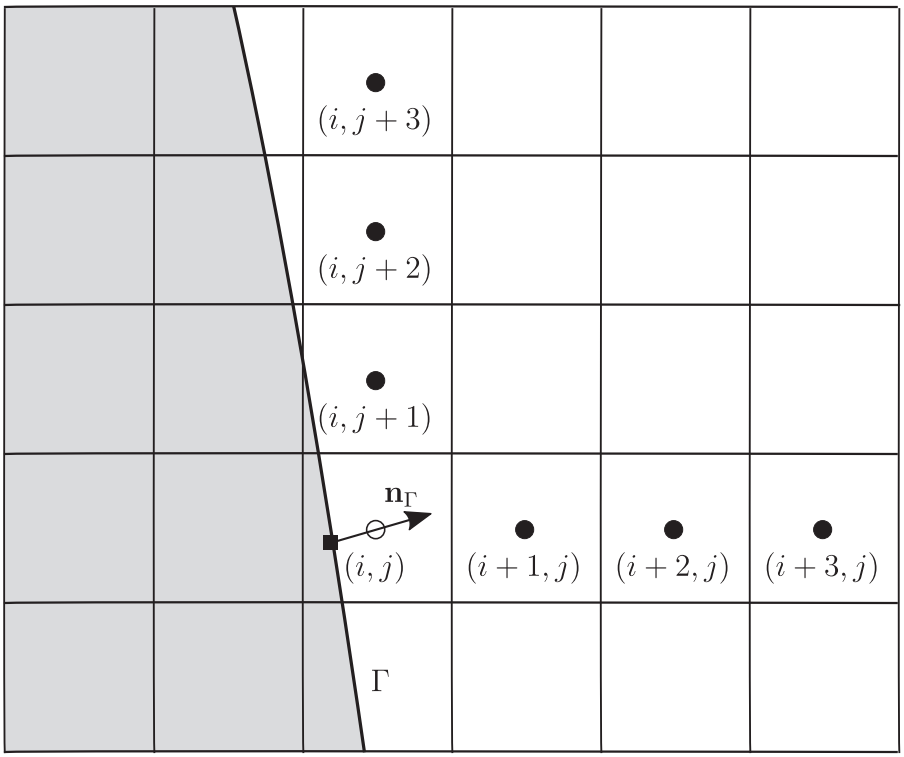

Fig. 3. Schematic of the relevant cells for the computation of the interface-normal temperature gradient. Filled dots mark cell centers which are used to reconstruct the interface-normal temperature gradient.

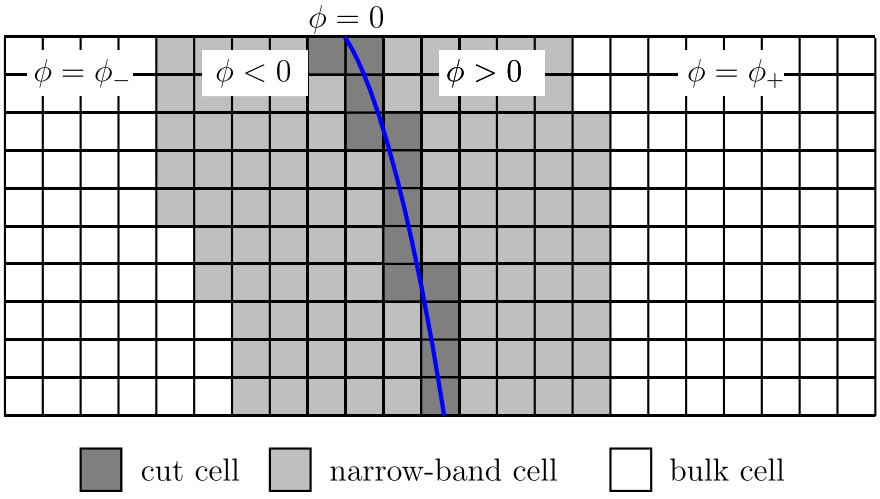

Fig. 4. Schematic of the narrow-band approach: shown are the interface (blue), cut cells (dark gray), narrow-band cells (light gray), and bulk cells (white). The solid phase is on the left side of the interface ($\phi < 0$), the liquid phase on the right side ($\phi > 0$).

We introduce a narrow band around the interface to further improve the overall efficiency of our method. The narrow-band concept is shown in Fig. 4. Three cell types are distinguished:

1. Cut cells: cells that are cut by the interface.
2. Narrow-band cells: cells which are in the vicinity of the interface. The width of the narrow band depends on the applied spatial and temporal discretization schemes. As example, a narrow band with a width of four cells is shown in the figure.
3. Bulk cells: cells that are far away from in the interface.

All previously mentioned level-set operations (advection, reinitialization, interface velocity and ghost cell extrapolation) are only performed in cut cells and narrow-band cells. All bulk cells are set to a constant level-set value depending on whether they contain liquid (ϕ_+) or solid (ϕ_-) states. This approach limits costly level-set related operations to only a fraction of the domain, thus improving overall performance, without adversely affecting the accuracy of the method.

The Gibbs-Thomson relation given in eq. (2) includes the interface temperature as function of the interface curvature. The curvature is the divergence of the interface-normal vector $\kappa = \nabla \cdot \mathbf{n}_\Gamma$, which is numerically obtained from $\mathbf{n}_\Gamma = \nabla\phi/|\nabla\phi|$. The curvature is evaluated at the cell center by

$$\kappa = \nabla \cdot \frac{\nabla\phi}{|\nabla\phi|}\,, \tag{21}$$

using a third-order WENO scheme. Finally, the interface curvature is subjected to a subcell correction step depending on spatial di-

Table 1
Material parameters for the one-dimensional Stefan problem: water at 243.15K and ice at 263.15K.

	ρ [kg/m^3]	c [J/(kg K)]	k [W/(m K)]	L [kJ/kg]	T_m [K]
water	1000	4864.0	0.4829	333.6	273.15
ice	1000	2030.0	2.319		

mensionality D

$$\kappa_\Gamma = \frac{(D-1)\kappa}{D-1-\phi\kappa} \tag{22}$$

to take into account the distance between the cell center and the interface [33].

4. Numerical results

4.1. Growth of a planar solidification front (Stefan problem)

The classical Stefan problem describes the non-stationary growth of a planar solidification front, and is solved to investigate the accuracy of the model for non-stationary problems. We simulate the propagation of an ice front in undercooled water, as proposed by Rauschenberger et al. [40]. In a domain of length 2.5 mm, the phase interface is initially located at $x_{\Gamma,0} = 0$ and propagates into the semi-infinite liquid subdomain $x_\Gamma(t) > x_{\Gamma,0}$. Both phases are initially at constant temperatures of $T_s = 263.15$ K (solid) and $T_l = 243.15$ K (liquid). Material parameters are provided in Table 1. We prescribe a constant temperature $T_w = T_s = 263.15$ K at the wall, and use a zero-gradient boundary condition to represent a semi-infinite liquid subdomain. The domain size is chosen sufficiently large to prevent spurious effects from the far-field zero-gradient boundary condition on the ice-layer growth.

The numerical solution of the temperature field is compared to the analytical solution given by Carslaw & Jaeger [4]

$$0 < x < x_\Gamma(t),\ t > 0 : T(x,t) = T_w + (T_m - T_w)\frac{\mathrm{erf}\left(\frac{x-x_{\Gamma,0}}{2\sqrt{\alpha_s t}}\right)}{\mathrm{erf}(\beta)}$$

$$x > x_\Gamma(t),\ t > 0 : T(x,t) = T_\infty + (T_m - T_\infty)\frac{\mathrm{erfc}\left(\frac{x-x_{\Gamma,0}}{2\sqrt{\alpha_l t}}\right)}{\mathrm{erfc}(\tilde{\alpha}\beta)} \tag{23}$$

with

$$\beta\sqrt{\pi} = \frac{St_s}{\mathrm{erfc}(\beta)}\mathrm{e}^{(-\beta^2)} + \frac{St_l}{\tilde{\alpha}\ \mathrm{erfc}(\tilde{\alpha}\,\beta)}\ \mathrm{e}^{(-\tilde{\alpha}^2\beta^2)} \tag{24}$$

and the ratio of the thermal conductivities $\tilde{\alpha} = \sqrt{\alpha_s/\alpha_l}$. The Stefan number St denotes the ratio of sensible heat to latent heat and is computed following

$$St_s = \frac{c_s(T_m - T_w)}{L}, \qquad St_l = \frac{c_l(T_m - T_\infty)}{L}.$$

Eq. (24) yields $\beta = 0.2685$ for the described case. The interface location at time t is given by

$$x_\Gamma(t) = x_{\Gamma,0} + 2\beta\sqrt{\alpha_s t}\,, \tag{25}$$

and the interface velocity is

$$u_\Gamma(t) = \frac{dx_\Gamma(t)}{dt} = \beta\sqrt{\frac{\alpha_s}{t}}\,. \tag{26}$$

The simulations are initialized with the analytical solution for the temperature field from eq. (23) at $t = 0.01$, and a corresponding level-set field with the interface located at $x_\Gamma(t = 0.01)$ from eq. (25).

A temporal series of simulated temperature profiles is shown in Fig. 5, together with the corresponding analytical solutions. The effective resolution for this case is 512 cells in the entire domain. The agreement with the reference is good at all time instants. Steep temperature gradients in both phases diminish over time, as solid and liquid phases absorb the latent heat released by the solidifying undercooled liquid. Therefore, the propagation of the phase interface slows down.

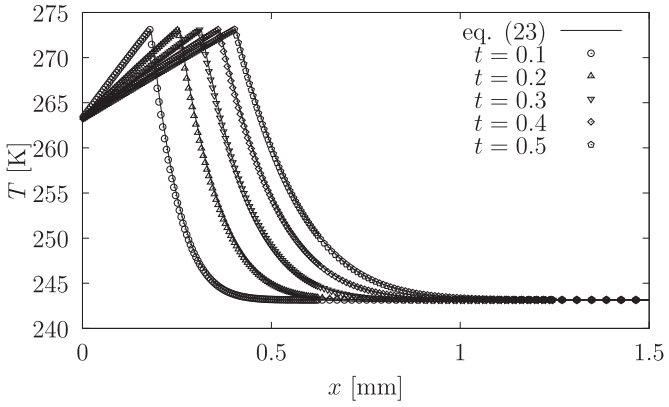

Fig. 5. Temperature profiles of the 1D Stefan problem at various instants for an effective resolution of 512 cells: analytical solution (−) and numerical results (symbols).

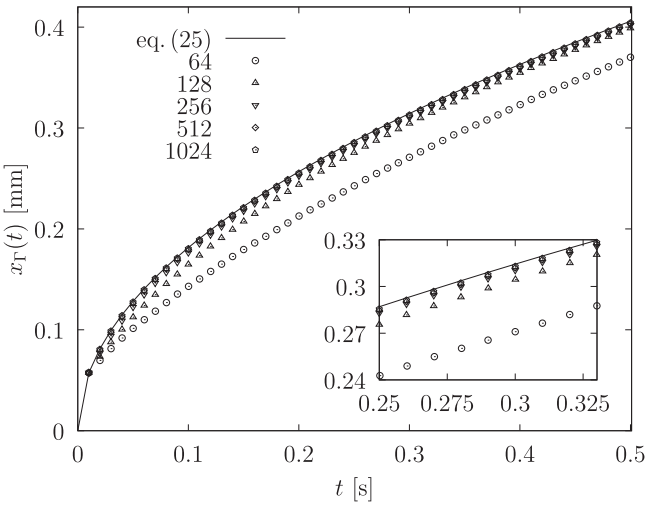

Fig. 6. Interface location for the one-dimensional Stefan problem for different resolutions: analytical solution (−) and numerical results (symbols).

The temporal evolution of the interface location is shown in Fig. 6 for successively finer meshes. The numerical results replicate the square-root behavior of the moving solidification front in time. The accuracy of the solution improves for successively finer meshes. Error plots are given in Fig. 7 for the interface location (left) and the temperature field (right) at $t = 0.5$, for effective mesh resolutions between 64 and 4096 cells. The temperature-field error is given as L_∞ norm, and as L_1 norm following

$$L_1 = \frac{1}{V}\sum_n \frac{||T_{n,exact} - T_{n,sim}||}{T_{n,exact}} dV_n\,, \tag{27}$$

with $T_{n,exact}$ being obtained from the analytical solution eq. (23). The global convergence order of the scheme is one for both the interface location and the temperature field, which is higher than for previously published level-set based approaches [40], underlining the advantages of applying high-order low-dissipation schemes.

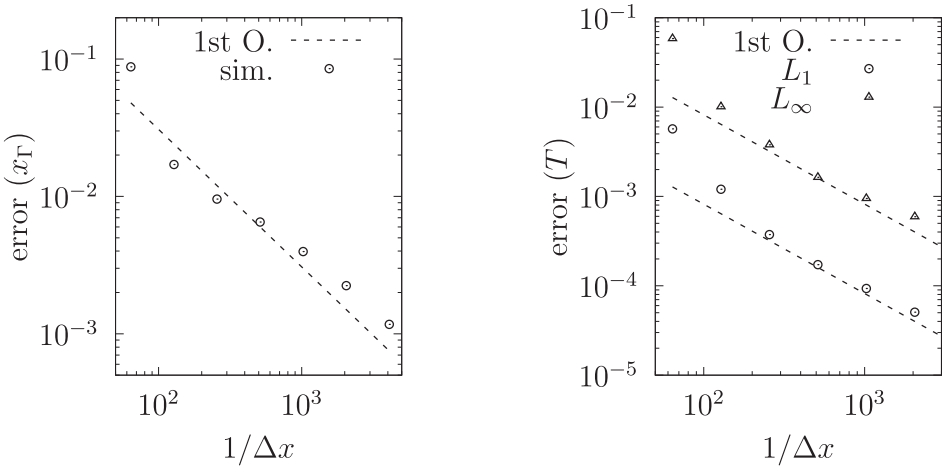

(a) Error of the interface position (b) Error of the temperature field

Fig. 7. Fig. (a): error of the interface location x_Γ at $t = 0.5$. Fig. (b): error of the temperature field (right) at $t = 0.5$. Given are reference convergence orders (dashed line) and simulation results (symbols).

4.2. Growth of a parabolic dendrite

The growth of a parabolic dendrite has been investigated analytically, experimentally, and numerically in the past. Based on the work of Ivantsov [20], Langer and Müller-Krumbhaar developed a stability theory for the growth of a single dendrite [28,29,34]. They derived a universal solution to compute the tip radius and velocity of a parabolic dendrite. First, the Péclet number of the growth process

$$Pe = \frac{r_t}{l} \tag{28}$$

is introduced, which describes the ratio of the tip radius r_t (i.e. the length scale of the growing dendrite) to the range of the diffusion field l given by

$$l = \frac{2\alpha}{u_\Gamma}. \tag{29}$$

Here, α denotes the thermal diffusivity of the melt and u_Γ is the interface velocity at the tip of the dendrite. For dendritic growth cases, $Pe < 0.1$ is usually valid. According to Langer et al. [29], the Stefan number and the Péclet number are related by

$$St \approx Pe \exp PeE_1(Pe) \tag{30}$$

if the dendrite is of parabolic shape, rotationally symmetric, and isothermal. Here, E_1 describes the exponential integral.

A second non-dimensional parameter

$$\sigma = \frac{l d_c}{r_t^2} \tag{31}$$

can be formulated, which relates the capillary length scale

$$d_c = \frac{\gamma c T_m}{\rho L^2} \tag{32}$$

to the diffusion length l and the tip radius r_t. The parameter σ plays a crucial role in the stability analysis of dendritic growth. Depending on the number of dimensions D, Müller-Krumbhaar & Langer [34] derived that only solutions which satisfy

$$\sigma^* = \begin{cases} 0.020 \pm 0.007 & D = 2 \\ 0.025 \pm 0.007 & D = 3 \end{cases} \tag{33}$$

are stable. Here, $\sigma = \sigma^*$ is the operating point of dendritic growth.

The tip radius and velocity for a given undercooling and material parameters are obtained as follows. First, eq. (30) is solved to obtain the Péclet number. Then, the formula for the growth velocity

$$V = \sigma Pe^2 = \frac{d_c u_\Gamma}{2\alpha} \tag{34}$$

is employed to compute the tip velocity and, eventually, the tip radius is found from eq. (28).

In the following, we compare the simulation results with both the analytical solution of the theory of Langer and Müller-Krumbhaar and experimental results [9,48] at various undercoolings ΔT. We prescribe a single dendrite of tip length l_D with the parametric function

$$x(s) = s \tag{35}$$

$$y(s) = -\frac{s^2}{r_t} + l_D, \tag{36}$$

$s \in [0, \sqrt{r_t l_D}/2]$. We choose $l_D = 3r_t$, and an initial tip-radius which is half the tip radius expected from theory. We simulate only half a dendrite in a domain of size $[20r_t \times 40r_t]$, utilizing the symmetry of the problem, see Fig. 8 for the initial interface location together with a sketch of the multiresolution block structure. Each phase is initialized at constant temperature, the ice subdomain with $T_s = T_m$ and the undercooled water subdomain with $T_l = T_m - \Delta T$. Material parameters for water and ice at 273.15K are given in Table 2. The domain is chosen big enough to eliminate boundary effects. We resolve the domain with 256×512 cells. All far-field boundary conditions are assumed to be adiabatic.

Fig. 9 shows the transient tip velocity for an undercooling of $\Delta T = 10$ K for various refinement levels (Fig. 9 (a)), and the temperature field in the growing crystal (Fig. 9 (b)). The discontinuous temperature field at initialization leads to an overestimation of the tip velocity at early times, and the dendrite grows rapidly. The energy released by the solidifying melt results in a flattening

Table 2
Material properties of ice and water at 273.15K [40].

	ρ [kg m^{-3}]	k [W (m K)$^{-1}$]	c [J (kg K)$^{-1}$]	L [kJ kg^{-1}]	γ [kg s^{-2}]
Ice	1000.0	2.216	2103.0	333.0	0.028
Water	1000.0	0.5624	4218.0		

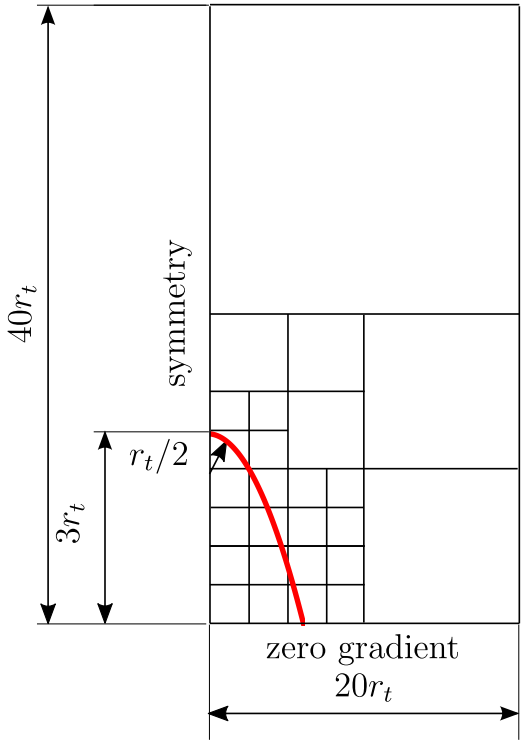

Fig. 8. Schematic of the simulation domain for the two-dimensional dendritic growth case, including the multiresolution block structure. The solidification front is shown in red. Note that the dendrite is not drawn to scale.

of the temperature gradient in both phases, and the tip velocity decreases. Note that the cell spacing only affects the early stages of the growth for $t < 200$ ns. Once a smooth temperature field has developed in the near field of the dendrite, the temporal evolution overlaps for different mesh sizes. Curvature effects on the interface temperature result in a heterogeneous temperature distribution in the parabolic dendrite (see Fig. 9 (b)). The minimum temperature occurs at the dendrite tip, which is where the interface velocity reaches its maximum.

Table 3
Relative error of the presented results to the analytical solution.

ΔT [K]	1	2	5	8	10	15	20
error (u_Γ) [%]	11.6	12.8	16.0	10.2	9.0	9.7	10.3

Based on these results, we performed multiple simulations with various undercoolings to compare our model with analytical, experimental, and numerical reference data. Note that the interface radius r_t decreases with increasing undercooling ΔT. Therefore, we adapt the cell size to maintain a constant resolution per tip radius for all investigated cases. The strong initial temperature gradient results in a high interface velocity, so that the crystal grows rapidly. To assure that the crystal does not grow beyond its stability limit due to the initial transient, we initialize the dendrite with a tip radius smaller than what is predicted from the analtical solution $r_{t,0} < r_{t,LM-K}$. Once a smooth temperature field has developed, the tip curvature decreases. We evaluate the interface velocity once the tip radius is equal to the radius of the theory of Langer and Müller-Krumbhaar $r_{t,LM-K}$ [40]. Our results are presented in Fig. 10, together with the analytical solution [29] and previously published experimental [9,48] and numerical [7,40] data. The deviation to the analytical solution for each undercooling is presented in Table 3. The results of our model lie within the experimental scatter, and numerical errors are similar to previously published level-set based models [7,40]. For $\Delta T > 10$ K, experimental results deviate from analytically and numerically determined tip velocities. This deviation can be attributed to kinetic effects [48], which play an increasingly important role for such large undercoolings, and are neither included in the simulation models nor in the analytical model.

4.3. Growth of a crystal with four-fold symmetry

Juric and Tryggvason [23] proposed a test problem for the unstable growth of a crystal with four-fold symmetry. The initial phase interface is given by the parametric function

$$x(s) = x_c + (R_0 + R_s \cos(8\pi s)) \cos(2\pi s) \tag{37}$$

$$y(s) = y_c + (R_0 + R_s \cos(8\pi s)) \sin(2\pi s) \tag{38}$$

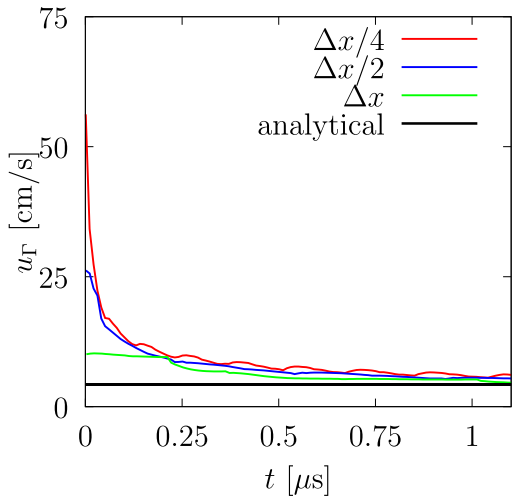

(a) Temporal evolution of the tip velocity

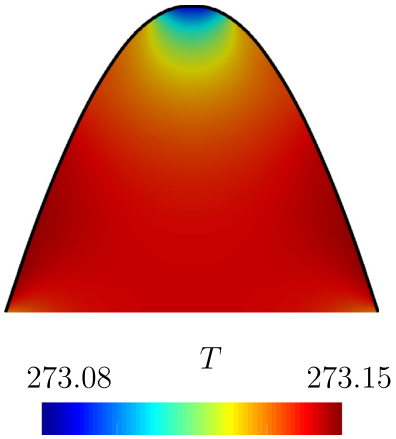

(b) Temperature field at the dendrite tip

Fig. 9. Fig. (a): temporal evolution of the tip velocity for $\Delta T = 10$ K for various grid resolutions and the analytical solution. Fig. (b): temperature field in the growing dendrite.

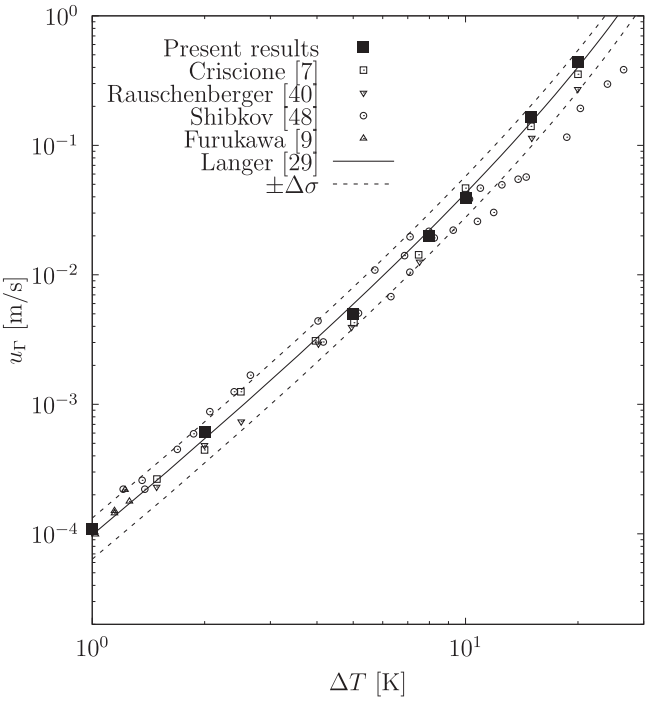

Fig. 10. Tip velocity as function of the undercooling ΔT from the presented numerical simulations, numerical reference data [7,40], experimental reference data [9,48], and analytical results [29]. Present numerical results are marked with filled symbols, open symbols denote reference data from literature, and the solid and dashed lines give the analytical results together with the variance $\Delta\sigma$.

with $s \in [0, 1]$, $R_0 = 0.1$, $R_s = 0.02$, and $x_c = y_c = 2$ in a domain of size $[0, 4] \times [0, 4]$ with periodic boundary conditions. We use constant material parameters for the densities $\rho_l = \rho_s = \rho = 1$, the specific heat capacities $c_l = c_s = c = 1$, the thermal conductivities $k_l = k_s = k = 1$, and the latent heat $L = 1$. The melting temperature is set to $T_m = 1$, and the initial temperature field in the solid ($T_s = T_m$) and liquid ($T_l = 0.5$) phase is constant. The surface-tension coefficient and the kinetic coefficient are set to $\gamma = 0.002$ and $\epsilon_u = 0.002$, respectively [23].

The Stefan number of this problem is

$$St = \frac{c(T_m - T_l)}{L} = 0.5 = X_s(t \to \infty)$$

and indicates that at equilibrium, half of the domain is solidified, while the other half remains in a liquid state at melting temperature. The temporal evolution of the solid volume fraction X_s and of the mass m normalized with the initial mass m_0 are given in Fig. 11 for effective grid resolutions of 256, 320, 384, 448, and 512 cells per spatial direction. For the coarsest resolution, we find an overprediction of the steady-state solid volume fraction, but with increasing resolution this overshoot vanishes. The temporal behavior converges for increasing mesh refinement, too. At steady state, the solid and the liquid mass each account for approximately one half of the total mass, as expected for this setup. The total mass (Fig. 11 (b)) remains constant during the simulated time, confirming the conservation property of our method. For comparison, Fig. 12 shows the relative local deviation of the simulated density field ρ_{sim} to the exact solution $\rho = 1$ for an effective resolution of 256 cells per spatial direction at $t = 0.4$ with the linearized approach, Fig. 12 (a), and the semi-implicit scheme proposed here, Fig. 12 (b). The linearized scheme exhibits large density errors in cut cells where the main direction of the crystal growth deviates from the main grid axes, see e.g. the area between two neighbouring fingers, Fig. 12 (a). For the present scheme, the density errors vanish, Fig. 12 (b)).

Fig. 13 shows the isolines of the evolving solid-liquid interface for the previously mentioned grid resolutions. The time interval between isolines is $\Delta t = 0.05$. The initial four protrusions develop each into a single dendrite. The tip-splitting instability occurs at each of these protrusions. In previous studies, the onset of this instability was reported at $t \approx 0.3$ (e.g. [32,55]). Our low-dissipation simulations indicate that the numerical dissipation of the underlying numerical discretization scheme is critical for observing the first occurrence of tip-splitting, which in our case is at $t = 0.15$. This underlines the advantageous effect of low-dissipative spatial and temporal discretization schemes on the occurrence of interfacial instabilities, as already mentioned by Gibou et al. [11]. Such high-order methods benefit from their low intrinsic numerical diffusion which does not prevail over the physical instability mechanism. With increasing refinement, the secondary dendrites flatten, and the onset of additional tip-splitting instabilities is observed, see the results in Fig. 13 for resolutions above 384 cells. To the authors' knowledge, this kind of instability has not been reported for numerical simulations of this test case in previous literature.

The temperature field at $t = 0.6$ and $t = 1$ is given in Fig. 14. The anisotropic growth behavior is a consequence of the non-uniform temperature distribution in the solid and liquid phases, see $t = 0.6$. Between two neighboring fingers, the liquid temperature is close to the melting temperature, leading to a low growth velocity. Near the tips of the crystal, the liquid is still undercooled. In combination with the lower interface temperature at the tips, which follows from the Gibbs-Thomson relation for curved interfaces (eq. (2)), this results in a local increase of the growth velocity. At $t = 1$, the temperature is approximately homogeneous in solid and liquid phases. This results in small interface temperature gradients, thus the crystal ceases to grow.

4.4. Growth of multiple crystals with four-fold symmetry

Finally, we simulate the growth of a complex multi-crystal growth configuration in an undercooled liquid to mimic a realistic solidification microstructure. On a domain of size $[0, 8] \times [0, 4]$, we initialize four spherical seeds with initial radius $r = 0.2$. The arbitrarily chosen seed centers are located at $(1, 2)$, $(2.5, 3.5)$, $(4, 1)$, and $(6, 2)$. The initial temperature is $T_l = 0.2$ for the undercooled liquid, and $T_s = T_m = 1$ in the solid seeds. We use constant material parameters for the densities $\rho_l = \rho_s = \rho = 1$, the specific heat capacities $c_l = c_s = c = 1$, the thermal conductivities $k_l = k_s = k = 1$, the latent heat $L = 1$, and the kinetic coefficient $\epsilon_u = 0.002$. For the anisotropic surface tension, we use

$$\gamma(\Theta) = \gamma_0 \left\{ 1 + A_s \left[\frac{8}{3} \sin^4 \left(\frac{1}{2} m_s (\Theta - \Theta_0) \right) - 1 \right] \right\} \tag{39}$$

[1]. Here, γ_0 describes the undisturbed surface tension coefficient, A_s the magnitude of anisotropy, Θ the angle between the interface normal and the x-axis, Θ_0 the angle between the symmetry axis of the crystal and the x-axis, and m_s the symmetry mode of the crystal. We choose $\gamma_0 = 0.002$, $A_s = 0.4$, $\Theta_0 = 0$, and $m_s = 4$ for a crystal with four-fold symmetry. The maximum mesh resolution of the adaptive grid is 1024×512 cells, and periodic boundary conditions are applied in x- and y-direction.

Interface contour lines are given in Fig. 15, with an equal time spacing of $\Delta t = 0.005$ between isolines. The initial growth stages are similar to the growth of a single nucleus in an undercooled melt, since the growing crystals do not influence each other yet. The four-fold anisotropy of the surface tension causes the crystal to grow along four main directions, similarly to the case presented in section 4.3. Interfacial instabilities at the tip of each of the protrusions result in the characteristic tip-splitting patterns. At later stages, the growing crystals interact with each other and block each others growth, which results in the locally degenerated

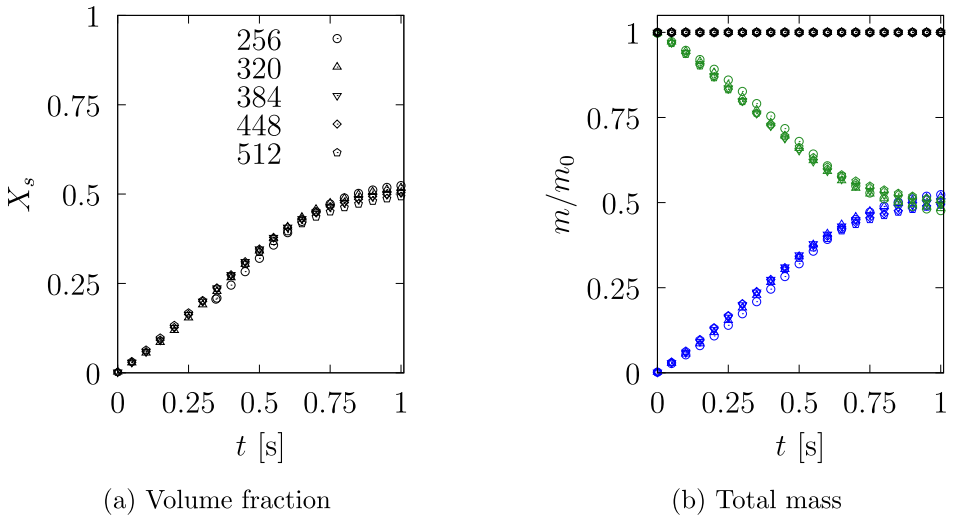

(a) Volume fraction (b) Total mass

Fig. 11. Fig. (a): evolution of the solid volume fraction for successively finer meshes. Fig. (b): evolution of the total mass, the liquid mass, and the solid mass for various resolutions. The total mass for for the different resolutions is shown in black, the mass in the liquid phase in green, and the mass in the solid phase in blue.

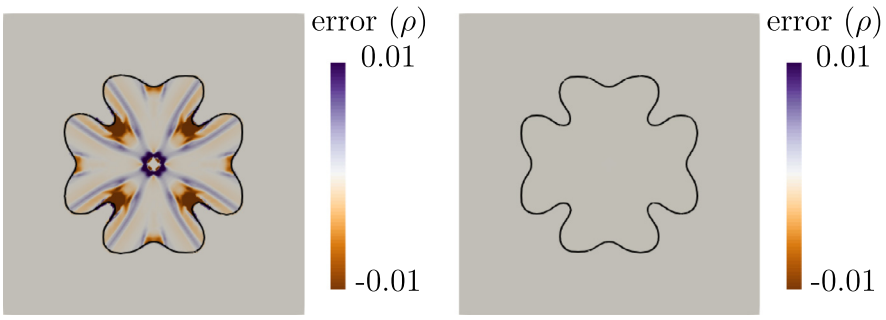

(a) Linearized approach (b) Semi-implicit approach

Fig. 12. Relative error of the density field at $t = 0.4$. Fig (a): linearized approach. Fig. (b): semi-implicit approach.

fingers. This behavior is connected to inhomogeneities in the temperature field, which is shown in Fig. 16 at $t = 0.03$ and $t = 0.07$. At $t = 0.03$, temperature-field inhomogeneities are restricted to the near field of each single crystal, while their surrounding consists of homogeneous undercooled liquid. Therefore, the shape of all four crystals is comparable to that of a single-crystal growth case, and symmetric to the main growth directions. The ongoing heat release during phase transition results in a temperature increase in the ambient undercooled liquid. At $t = 0.07$, the liquid between crystals 1 and 2 has reached the melting temperature locally, and the growth ceases. The low numerical dissipation of the model ensures that the liquid areas between the solid crystals are preserved, and are not merged with each other. Between crystals 1 and 3, the fluid is still undercooled, thus the crystals grow in this direction.

5. Conclusion and outlook

We have presented a conservative interface-interaction method for a sharp-interface formulation of liquid-solid phase transition. Conservation at the interface is maintained by explicit formula-

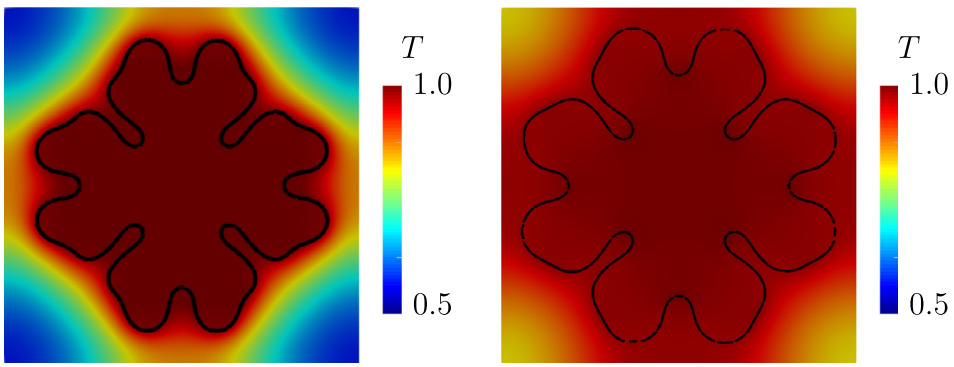

(a) $t = 0.6$ (b) $t = 1.0$

Fig. 14. The temperature field for an effective resolution of 512 cells in each spatial direction. The solidification front is shown in black. Fig. (a): $t = 0.6$. Fig. (b): $t = 1.0$

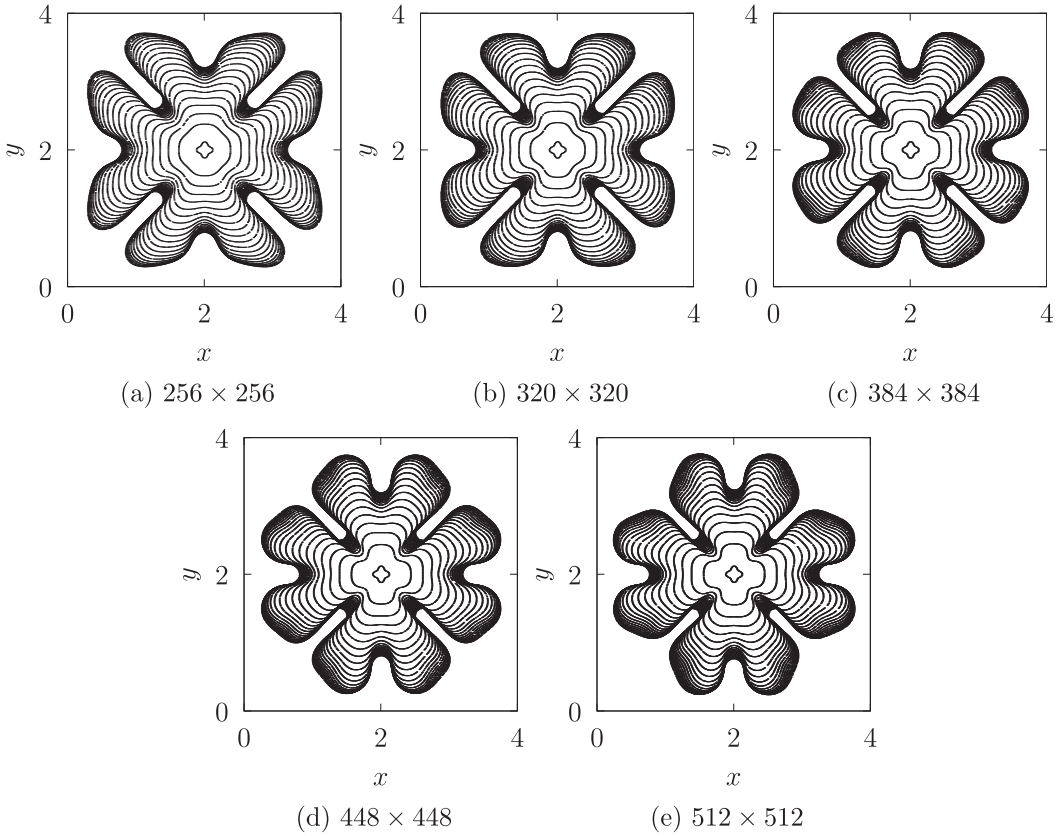

Fig. 13. The solid-liquid interface for various grid resolutions. The time interval between isolines is $\Delta t = 0.05$.

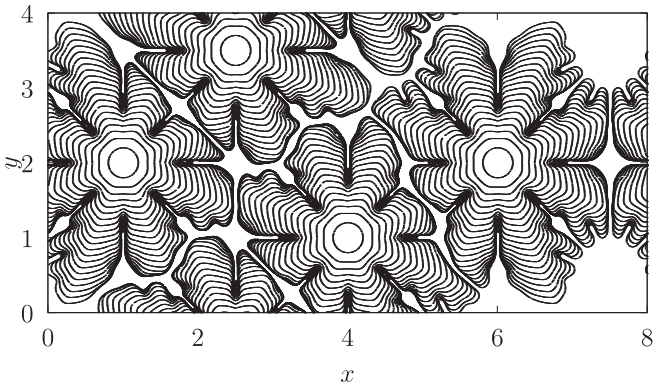

Fig. 15. The solid-liquid interface for the growth of multiple cystals subjected to four-fold anisotropic surface tension. The time interval between two successive isolines is $\Delta t = 0.005$.

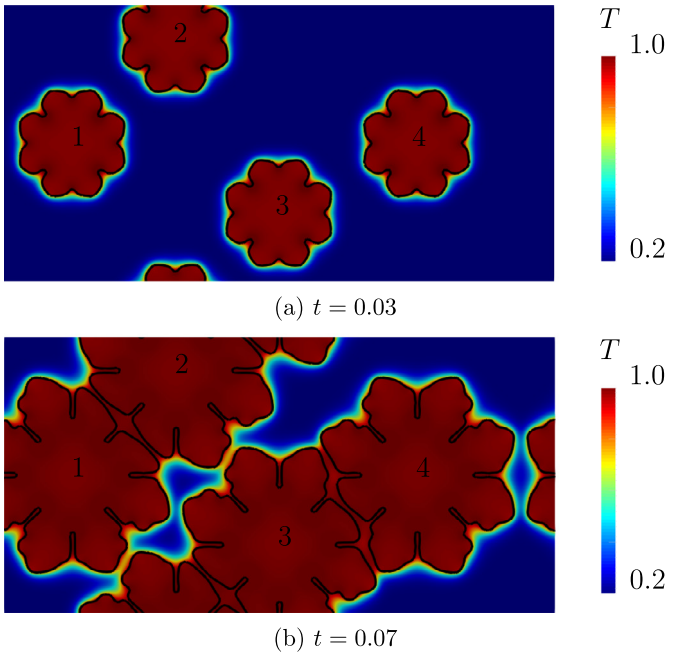

Fig. 16. The temperature field of the multi-crystal growth case. The solidification front is shown in black. Fig. (a): $t = 0.03$. Fig (b): $t = 0.07$.

tion of interface fluxes into both solid and liquid phases. A semi-implicit level-set formulation is applied to evolve the phase interface. A new formulation for the interface surface in a cut cell has been derived, which includes the Stefan condition. The reconstruction of interface gradients based on third-order WENO smoothness indicators [22] and an explicit third-order Runge-Kutta scheme for time discretization [12,16] ensures low numerical dissipation. The interface-interaction model takes into account surface-tension and kinetic effects on the interface temperature (Gibbs-Thomson relation), including anisotropic behavior. The Stefan condition provides a relation between interface fluxes of mass and energy, and the interface-propagation velocity. The sharp-interface property is ensured by extrapolating fluid states across the interface for the single-phase reconstruction of the cell-face fluxes near the interface [8]. Computational efficiency is improved by dynamic mesh adaptation with respect to the evolving interface and temperature field using the multiresolution approach of Harten [17], and an adaptive local time-stepping scheme for efficient and robust time integration [24].

We have validated the presented method with analytical solutions for the one-dimensional Stefan problem and the growth of a two-dimensional parabolic dendrite. This shows that the model is capable to capture both unstable (dendritic-like) and stable (planar) growth processes accurately. Numerical results of a growing single crystal with four-fold symmetry and multiple crystals with four-fold symmetry demonstrate the capabilities of the method to model crystal-growth problems with complex interfaces, and that it recovers the tip-splitting instability correctly. Our results indicate that the numerical dissipation of the underlying numerical scheme is critical for the prediction of tip-splitting instabilities. Our simulation predicts an earlier onset of this instability than reported in previous literature which is consistent with lower numerical dissipation. The numerical examples presented here are limited to one and two dimensions, extension to three dimensions is subject of ongoing work.

Declaration of Competing Interest

The authors declare that they have no known competing financial interests or personal relationships that could have appeared to influence the work reported in this paper.

CRediT authorship contribution statement

J.W.J. Kaiser: Conceptualization, Methodology, Software, Formal analysis, Visualization, Writing - original draft. **S. Adami:** Writing - review & editing, Supervision, Formal analysis, Resources, Project administration. **I.S. Akhatov:** Writing - review & editing, Supervision, Funding acquisition. **N.A. Adams:** Conceptualization, Writing - review & editing, Supervision, Funding acquisition, Project administration.

Acknowlgedgments

The first author is supported by the German Research Foundation (Deutsche Forschungsgesellschaft, DFG). The second and fourth author acknowledge funding from the European Research Council (ERC) under the European Union's Horizon 2020 research and innovation program (grant agreement No. 667483). The authors gratefully acknowledge the Gauss Centre for Supercomputing e.V. (www.gauss-centre.eu) for funding this project by providing computing time on the GCS Supercomputer SuperMUC at Leibniz Supercomputing Centre (www.lrz.de). This project is part of the Skoltech-TUM cooperation agreement.

References

[1] R. Almgren, Variational Algorithms and Pattern Formation in Dendritic Solidification, J. Comput. Phys. 106 (2) (1993) 337–354, doi:10.1016/S0021-9991(83)71112-5.
[2] D.M. Anderson, G.B. McFadden, A.A. Wheeler, A phase-field model of solidification with convection, Physica D 135 (2000) 175–194, doi:10.1016/S0167-2789(99)00109-8.
[3] C. Beckermann, H.J. Diepers, I. Steinbach, A. Karma, X. Tong, Modeling Melt Convection in Phase-Field Simulations of Solidification, J. Comput. Phys. 154 (1999) 468–496, doi:10.1006/jcph.1999.6323.
[4] , Conduction of heat in solids, H.S. Carslaw, J.C. Jaeger (Eds.), Oxford University Press, 1959.
[5] H. Chen, C. Min, F. Gibou, A numerical scheme for the Stefan problem on adaptive Cartesian grids with supralinear convergence rate, J. Comput. Phys. 228 (16) (2009) 5803–5818, doi:10.1016/j.jcp.2009.04.044.
[6] S. Chen, B. Merriman, P. Smereka, S. Osher, A simple level set method for Stefan problems, J. Comput. Phys. 135 (1997) 8–29.
[7] A. Criscione, D. Kintea, Ž. Tuković, S. Jakirlić, I.V. Roisman, C. Tropea, Crystallization of supercooled water: A level-set-based modeling of the dendrite tip velocity, Int. J. Heat Mass Transf. 66 (2013) 830–837.
[8] R.P. Fedkiw, T.D. Aslam, B. Merriman, S. Osher, A Non-oscillatory Eulerian Approach to Interfaces in Multimaterial Flows (The Ghost Fluid Method), J. Comput. Phys. 152 (2) (1999) 457–492.
[9] Y. Furukawa, W. Shimada, Three-dimensional pattern formation during growth of ice dendrites - its relation to universal law of dendritic growth, J. Cryst. Growth 128 (1993) 234–239, doi:10.1016/0022-0248(93)90325-Q.
[10] M. Gaoyang, X. Lingda, W. Chunming, J. Ping, Z. Guoli, Two-dimensional phase–field simulations of competitive dendritic growth during laser welding, Mater. Design 181 (2019) 107980.
[11] F. Gibou, R. Fedkiw, R. Caflisch, S. Osher, A level set approach for the numerical simulation of dendritic growth, J. Sci. Comput. 19 (1) (2003) 183–199.
[12] S. Gottlieb, C.-W. Shu, Total variation diminishing Runge-Kutta schemes, Math. Comput. 67 (221) (1998) 73–85.
[13] R.D. Groot, Second order front tracking algorithm for Stefan problem on a regular grid, J. Comput. Phys. 372 (2018) 956–971.
[14] Z. Guo, P. Lin, A thermodynamically consistent phase-field model for two-phase flows with thermocapillary effects, J. Fluid Mech. 766 (2015) 226–271, doi:10.1017/jfm.2014.696.
[15] L.H. Han, X.Y. Hu, N.A. Adams, Adaptive multi-resolution method for compressible multi-phase flows with sharp interface model and pyramid data structure, J. Comput. Phys. 262 (2014) 131–152, doi:10.1016/j.jcp.2013.12.061.
[16] A. Harten, High resolution schemes for hyperbolic conservation laws, J. Comput. Phys. 135 (1983) 260–278, doi:10.1016/0021-9991(83)90136-5.
[17] A. Harten, Adaptive Multiresolution Schemes for Shock Computations, J. Comput. Phys. 115 (1994) 319–338.
[18] N. Hoppe, I. Pasichnyk, M. Allalen, S. Adami, N.A. Adams, Node-Level Optimization of a 3D Block-Based Multiresolution Compressible Flow Solver with Emphasis on Performance Portability, in: International Conference on High Performance Computing & Simulation (HPCS), 2019.
[19] X.Y. Hu, B.C. Khoo, N.A. Adams, F.L. Huang, A conservative interface method for compressible flows, J. Comput. Phys. 219 (2) (2006) 553–578, doi:10.1016/j.jcp.2006.04.001.
[20] G. Ivantsov, Doklady Akademii Nauk SSSR (1947) 558–567.
[21] M.A. Jaafar, D.R. Rousse, S. Gibout, J.P. Bédécarrats, A review of dendritic growth during solidification: Mathematical modeling and numerical simulations, Renew. Sust. Energ. Rev. 74 (March 2016) (2017) 1064–1069, doi:10.1016/j.rser.2017.02.050.
[22] G.-S. Jiang, C.-W. Shu, Efficient implementation of weighted ENO schemes, J. Comput. Phys. 126 (1996) 202–228.
[23] D. Juric, G. Tryggvason, A Front-Tracking Method for Dendritic Solidification, J. Comput. Phys. 123 (1996) 127–148.
[24] J.W.J. Kaiser, N. Hoppe, S. Adami, N.A. Adams, An adaptive local time-stepping scheme for multiresolution simulations of hyperbolic conservation laws, J. Comput. Phys. X 4 (2019) 100038.
[25] A. Karma, W.-J. Rappel, Phase-field method for computationally efficient modeling of solidification with arbitrary interface kinetrics, Phys. Rev. E 53 (1996).
[26] Y.-T. Kim, N. Goldenfeld, J. Dantzig, Computation of Dendritic Microstructures using a Level Set Method, Phys. Rev. E 62 (2) (2000) 2471–2474.
[27] R. Kobayashi, Modeling and numerical simulations of dendritic crystal growth, Physica D 63 (1993) 410–423, doi:10.1016/0167-2789(93)90120-P.
[28] J.S. Langer, H. Müller-Krumbhaar, Theory of dendritic growth-I. Elements of a stability analysis, Acta Metall. 26 (11) (1978a) 1681–1687, doi:10.1016/0001-6160(78)90078-0.
[29] J.S. Langer, H. Müller-Krumbhaar, Theory of dendritic growth-II. Instabilities in the limit of vanishing surface tension, Acta Metall. 26 (11) (1978b) 1689–1695, doi:10.1016/0001-6160(78)90079-2.
[30] J.S. Langer, J. Müller-Krumbhaar, Stability effects in dendritic crystal growth, J. Cryst. Growth 42 (C) (1977) 11–14, doi:10.1016/0022-0248(77)90171-3.
[31] E. Lauer, X.Y. Hu, S. Hickel, N.A. Adams, Numerical investigation of collapsing cavity arrays, Phys. Fluids 24 (5) (2012) 052104, doi:10.1063/1.4719142.
[32] K. Ling, W.Q. Tao, A sharp-interface model coupling VOSET and IBM for simulations on melting and solidification, Comput. Fluids 178 (2019) 113–131.
[33] J. Luo, X. Hu, N.A. Adams, A conservative sharp interface method for incompressible multiphase flows, J. Comput. Phys. 284 (2015) 547–565, doi:10.1016/j.jcp.2014.12.044.
[34] H. Müller-Krumbhaar, J.S. Langer, Theory of dendritic growth-III. Effects of surface tension, Acta Metall. 26 (11) (1978) 1697–1708, doi:10.1016/0001-6160(78)90080-9.
[35] B. Nestler, A.A. Wheeler, L. Ratke, C. Stöcker, Phase-field model for solidification of a monotectic alloy with convection, Physica D 141 (2000) 133–154, doi:10.1016/S0167-2789(00)00035-X.
[36] S. Osher, R. Sanders, Numerical Approximations to Nonlinear Conservation Laws With Locally Varying Time and Space Grids, Math. Comput. 41 (164) (1983) 321–336.
[37] S. Osher, J.A. Sethian, Fronts Propagating With Curvature Dependent Speed: Algorithms Based on Hamilton-Jacobi Formulations, J. Comput. Phys. 79 (1988) (1988) 12–49.
[38] V. Ramanuj, R. Sankaran, High Order Anchoring and Reinitialization of Level Set Function for Simulating Interface Motion, J. Sci. Comput. 81 (3) (2019) 1963–1986, doi:10.1007/s10915-019-01076-0.
[39] V. Ramanuj, R. Sankaran, B. Radhakrishnan, A sharp interface model for deterministic simulation of dendrite growth, Comput. Mater. Sci. 169 (May) (2019) 109097, doi:10.1016/j.commatsci.2019.109097.
[40] P. Rauschenberger, A. Criscione, K. Eisenschmidt, D. Kintea, S. Jakirlić, Ž. Tuković, I.V. Roisman, B. Weigand, C. Tropea, Comparative assessment of Volume-of-Fluid and Level-Set methods by relevance to dendritic ice growth in supercooled water, Comput. Fluids 79 (2013) 44–52, doi:10.1016/j.compfluid.2013.03.010.
[41] A.R. Roosen, J.E. Taylor, Modeling Crystal Growth in a Diffusion Field Using Fully Faceted Interfaces, J. Comput. Phys. 114 (1994) 113–128, doi:10.1006/jcph.1994.1153.

[42] D. Rossinelli, B. Hejazialhosseini, D.G. Spampinato, P. Koumoutsakos, Multicore/multi-gpu accelerated simulations of multiphase compressible flows using wavelet adapted grids, J. Sci. Comput. 33 (2) (2011) 512–540.
[43] G. Russo, P. Smereka, A Remark on Computing Distance Functions, J. Comput. Phys. 163 (2000) 51–67.
[44] J.A. Sethian, J. Straint, Crystal growth and dendritic solidification, J. Comput. Phys. 98 (2) (1992) 231–253, doi:10.1016/0021-9991(92)90140-T.
[45] J. Shaikh, A. Sharma, R. Bhardwaj, On sharp-interface level-set method for heat and/or mass transfer induced Stefan problem, Int. J. Heat Mass Transf. 96 (2016) 458–473, doi:10.1016/j.ijheatmasstransfer.2015.12.074.
[46] A.A. Shibkov, Y.I. Golovin, M.A. Zheltov, A.A. Korolev, A.A. Leonov, Morphology diagram of nonequilibrium patterns of ice crystals growing in supercooled water, Physica A 319 (2003) 65–79, doi:10.1016/S0378-4371(02)01517-0.
[47] A.A. Shibkov, Y.I. Golovin, M.A. Zheltov, A.A. Korolev, A.A. Vlasov, Kinetics and morphology of nonequilibrium growth of ice in supercooled water, Crystallogr. Rep. 46 (3) (2001) 496–502, doi:10.1134/1.1376484.
[48] A.A. Shibkov, M.A. Zheltov, A.A. Korolev, A.A. Kazakov, A.A. Leonov, Crossover from diffusion-limited to kinetics-limited growth of ice crystals, J. Cryst. Growth 285 (2005) 215–227.
[49] R. van der Sman, Phase field simulations of ice crystal growth in sugar solutions, Int. J. Heat Mass Transf. 95 (2016) 153–161.
[50] D. Sun, S. Pan, Q. Han, B. Sun, Numerical simulation of dendritic growth in directional solidification of binary alloys using a lattice Boltzmann scheme, Int. J. Heat Mass Transf. 103 (2016) 821–831.
[51] D. Sun, Y. Wang, H. Yu, Q. Han, A lattice Boltzmann study on dendritic growth of a binary alloy in the presence of melt convection, Int. J. Heat Mass Transf. 123 (2018) 213–226.
[52] D. Sun, M. Zhu, J. Wang, B. Sun, Lattice Boltzmann modeling of bubble formation and dendritic growth in solidification of binary alloys, Int. J. Heat Mass Transf. 94 (2016) 474–487.
[53] M. Sussman, P. Smereka, S. Osher, A Level Set Approach for Computing Solutions to Incompressible Two-Phase Flow, J. Comput. Phys. 114 (1994) 146–159.
[54] L. Tan, N. Zabaras, Modeling the growth and interaction of multiple dendrites in solidification using a level set method, J. Comput. Phys. 226 (2007) 131–155, doi:10.1016/j.jcp.2007.03.023.
[55] L. Tan, Z. Zabaras, A level set simulation of dendritic solidification with combined features of front-tracking and fixed-domain methods, J. Comput. Phys. 211 (2006) 36–63, doi:10.1016/j.jcp.2005.05.013.
[56] M. Theillard, F. Gibou, T. Pollock, A Sharp Computational Method for the Simulation of the Solidification of Binary Alloys, J. Sci. Comput. 63 (2015) 330–354, doi:10.1007/s10915-014-9895-0.
[57] H. Xing, K. Ankit, X. Dong, H. Chen, K. Jin, Growth direction selection of tilted dendritic arrays in directional solidification over a wide range of pulling velocity: A phase-field study, Int. J. Heat Mass Transf. 117 (2018) 1107–1114, doi:10.1016/j.ijheatmasstransfer.2017.10.086.

Chapter B

Copyright Permission for Adopted and Reproduced Material

Copyright Clearance Center Marketplace™

Annual Reviews, Inc. - License Terms and Conditions

This is a License Agreement between Jakob Kaiser ("You") and Annual Reviews, Inc. ("Publisher") provided by Copyright Clearance Center ("CCC"). The license consists of your order details, the terms and conditions provided by Annual Reviews, Inc., and the CCC terms and conditions.

All payments must be made in full to CCC.

Order Date	11-Nov-2020	**Type of Use**	Republish in a thesis/dissertation
Order license ID	1076763-1		
ISSN	1545-4479	**Publisher**	ANNUAL REVIEWS
		Portion	Chart/graph/table/figure

LICENSED CONTENT

Publication Title	Annual review of fluid mechanics	**Rightsholder**	Annual Reviews, Inc.
		Publication Type	e-Journal
Date	01/01/1969	**URL**	http://arjournals.annualreviews.org/loi/fluid
Language	English		
Country	United States of America		

REQUEST DETAILS

Portion Type	Chart/graph/table/figure	**Distribution**	Worldwide
Number of charts / graphs / tables / figures requested	1	**Translation**	Original language of publication
		Copies for the disabled?	No
Format (select all that apply)	Print, Electronic	**Minor editing privileges?**	No
Who will republish the content?	Academic institution	**Incidental promotional use?**	No
Duration of Use	Life of current and all future editions	**Currency**	EUR
Lifetime Unit Quantity	Up to 499		
Rights Requested	Main product		

NEW WORK DETAILS

Title	Modeling Interfacial Instabilities with the Level Set Method	**Institution name**	Technical University of Munich
		Expected presentation date	2021-03-01
Instructor name	Prof. Dr.-Ing. Nikolaus A. Adams		

ADDITIONAL DETAILS

Order reference number	N/A

The requesting person / organization to appear on the license	Jakob Kaiser

REUSE CONTENT DETAILS

Title, description or numeric reference of the portion(s)	Figure 1	**Title of the article/chapter the portion is from**	Fragmentation
Editor of portion(s)	N/A	**Author of portion(s)**	E. Villermaux
Volume of serial or monograph	39	**Issue, if republishing an article from a serial**	N/A
Page or page range of portion	421	**Publication date of portion**	2007-01-21

CCC Republication Terms and Conditions

1. Description of Service; Defined Terms. This Republication License enables the User to obtain licenses for republication of one or more copyrighted works as described in detail on the relevant Order Confirmation (the "Work(s)"). Copyright Clearance Center, Inc. ("CCC") grants licenses through the Service on behalf of the rightsholder identified on the Order Confirmation (the "Rightsholder"). "Republication", as used herein, generally means the inclusion of a Work, in whole or in part, in a new work or works, also as described on the Order Confirmation. "User", as used herein, means the person or entity making such republication.

2. The terms set forth in the relevant Order Confirmation, and any terms set by the Rightsholder with respect to a particular Work, govern the terms of use of Works in connection with the Service. By using the Service, the person transacting for a republication license on behalf of the User represents and warrants that he/she/it (a) has been duly authorized by the User to accept, and hereby does accept, all such terms and conditions on behalf of User, and (b) shall inform User of all such terms and conditions. In the event such person is a "freelancer" or other third party independent of User and CCC, such party shall be deemed jointly a "User" for purposes of these terms and conditions. In any event, User shall be deemed to have accepted and agreed to all such terms and conditions if User republishes the Work in any fashion.

3. Scope of License; Limitations and Obligations.

    3.1. All Works and all rights therein, including copyright rights, remain the sole and exclusive property of the Rightsholder. The license created by the exchange of an Order Confirmation (and/or any invoice) and payment by User of the full amount set forth on that document includes only those rights expressly set forth in the Order Confirmation and in these terms and conditions, and conveys no other rights in the Work(s) to User. All rights not expressly granted are hereby reserved.

    3.2. General Payment Terms: You may pay by credit card or through an account with us payable at the end of the month. If you and we agree that you may establish a standing account with CCC, then the following terms apply: Remit Payment to: Copyright Clearance Center, 29118 Network Place, Chicago, IL 60673-1291. Payments Due: Invoices are payable upon their delivery to you (or upon our notice to you that they are available to you for downloading). After 30 days, outstanding amounts will be subject to a service charge of 1-1/2% per month or, if less, the maximum rate allowed by applicable law. Unless otherwise specifically set forth in the Order Confirmation or in a separate written agreement signed by CCC, invoices are due and payable on "net 30" terms. While User may exercise the rights licensed immediately upon issuance of the Order Confirmation, the license is automatically revoked and is null and void, as if it had never been issued, if complete payment for the license is not received on a timely basis either from User directly or through a payment agent, such as a credit card company.

    3.3. Unless otherwise provided in the Order Confirmation, any grant of rights to User (i) is "one-time" (including

the editions and product family specified in the license), (ii) is non-exclusive and non-transferable and (iii) is subject to any and all limitations and restrictions (such as, but not limited to, limitations on duration of use or circulation) included in the Order Confirmation or invoice and/or in these terms and conditions. Upon completion of the licensed use, User shall either secure a new permission for further use of the Work(s) or immediately cease any new use of the Work(s) and shall render inaccessible (such as by deleting or by removing or severing links or other locators) any further copies of the Work (except for copies printed on paper in accordance with this license and still in User's stock at the end of such period).

3.4. In the event that the material for which a republication license is sought includes third party materials (such as photographs, illustrations, graphs, inserts and similar materials) which are identified in such material as having been used by permission, User is responsible for identifying, and seeking separate licenses (under this Service or otherwise) for, any of such third party materials; without a separate license, such third party materials may not be used.

3.5. Use of proper copyright notice for a Work is required as a condition of any license granted under the Service. Unless otherwise provided in the Order Confirmation, a proper copyright notice will read substantially as follows: "Republished with permission of [Rightsholder's name], from [Work's title, author, volume, edition number and year of copyright]; permission conveyed through Copyright Clearance Center, Inc. " Such notice must be provided in a reasonably legible font size and must be placed either immediately adjacent to the Work as used (for example, as part of a by-line or footnote but not as a separate electronic link) or in the place where substantially all other credits or notices for the new work containing the republished Work are located. Failure to include the required notice results in loss to the Rightsholder and CCC, and the User shall be liable to pay liquidated damages for each such failure equal to twice the use fee specified in the Order Confirmation, in addition to the use fee itself and any other fees and charges specified.

3.6. User may only make alterations to the Work if and as expressly set forth in the Order Confirmation. No Work may be used in any way that is defamatory, violates the rights of third parties (including such third parties' rights of copyright, privacy, publicity, or other tangible or intangible property), or is otherwise illegal, sexually explicit or obscene. In addition, User may not conjoin a Work with any other material that may result in damage to the reputation of the Rightsholder. User agrees to inform CCC if it becomes aware of any infringement of any rights in a Work and to cooperate with any reasonable request of CCC or the Rightsholder in connection therewith.

4. Indemnity. User hereby indemnifies and agrees to defend the Rightsholder and CCC, and their respective employees and directors, against all claims, liability, damages, costs and expenses, including legal fees and expenses, arising out of any use of a Work beyond the scope of the rights granted herein, or any use of a Work which has been altered in any unauthorized way by User, including claims of defamation or infringement of rights of copyright, publicity, privacy or other tangible or intangible property.

5. Limitation of Liability. UNDER NO CIRCUMSTANCES WILL CCC OR THE RIGHTSHOLDER BE LIABLE FOR ANY DIRECT, INDIRECT, CONSEQUENTIAL OR INCIDENTAL DAMAGES (INCLUDING WITHOUT LIMITATION DAMAGES FOR LOSS OF BUSINESS PROFITS OR INFORMATION, OR FOR BUSINESS INTERRUPTION) ARISING OUT OF THE USE OR INABILITY TO USE A WORK, EVEN IF ONE OF THEM HAS BEEN ADVISED OF THE POSSIBILITY OF SUCH DAMAGES. In any event, the total liability of the Rightsholder and CCC (including their respective employees and directors) shall not exceed the total amount actually paid by User for this license. User assumes full liability for the actions and omissions of its principals, employees, agents, affiliates, successors and assigns.

6. Limited Warranties. THE WORK(S) AND RIGHT(S) ARE PROVIDED "AS IS". CCC HAS THE RIGHT TO GRANT TO USER THE RIGHTS GRANTED IN THE ORDER CONFIRMATION DOCUMENT. CCC AND THE RIGHTSHOLDER DISCLAIM ALL OTHER WARRANTIES RELATING TO THE WORK(S) AND RIGHT(S), EITHER EXPRESS OR IMPLIED, INCLUDING WITHOUT LIMITATION IMPLIED WARRANTIES OF MERCHANTABILITY OR FITNESS FOR A PARTICULAR PURPOSE. ADDITIONAL RIGHTS MAY BE REQUIRED TO USE ILLUSTRATIONS, GRAPHS, PHOTOGRAPHS, ABSTRACTS, INSERTS OR OTHER PORTIONS OF THE WORK (AS OPPOSED TO THE ENTIRE WORK) IN A MANNER CONTEMPLATED BY USER; USER UNDERSTANDS AND AGREES THAT NEITHER CCC NOR THE RIGHTSHOLDER MAY HAVE SUCH ADDITIONAL

RIGHTS TO GRANT.

7. Effect of Breach. Any failure by User to pay any amount when due, or any use by User of a Work beyond the scope of the license set forth in the Order Confirmation and/or these terms and conditions, shall be a material breach of the license created by the Order Confirmation and these terms and conditions. Any breach not cured within 30 days of written notice thereof shall result in immediate termination of such license without further notice. Any unauthorized (but licensable) use of a Work that is terminated immediately upon notice thereof may be liquidated by payment of the Rightsholder's ordinary license price therefor; any unauthorized (and unlicensable) use that is not terminated immediately for any reason (including, for example, because materials containing the Work cannot reasonably be recalled) will be subject to all remedies available at law or in equity, but in no event to a payment of less than three times the Rightsholder's ordinary license price for the most closely analogous licensable use plus Rightsholder's and/or CCC's costs and expenses incurred in collecting such payment.

8. Miscellaneous.

    8.1. User acknowledges that CCC may, from time to time, make changes or additions to the Service or to these terms and conditions, and CCC reserves the right to send notice to the User by electronic mail or otherwise for the purposes of notifying User of such changes or additions; provided that any such changes or additions shall not apply to permissions already secured and paid for.

    8.2. Use of User-related information collected through the Service is governed by CCC's privacy policy, available online here:https://marketplace.copyright.com/rs-ui-web/mp/privacy-policy

    8.3. The licensing transaction described in the Order Confirmation is personal to User. Therefore, User may not assign or transfer to any other person (whether a natural person or an organization of any kind) the license created by the Order Confirmation and these terms and conditions or any rights granted hereunder; provided, however, that User may assign such license in its entirety on written notice to CCC in the event of a transfer of all or substantially all of User's rights in the new material which includes the Work(s) licensed under this Service.

    8.4. No amendment or waiver of any terms is binding unless set forth in writing and signed by the parties. The Rightsholder and CCC hereby object to any terms contained in any writing prepared by the User or its principals, employees, agents or affiliates and purporting to govern or otherwise relate to the licensing transaction described in the Order Confirmation, which terms are in any way inconsistent with any terms set forth in the Order Confirmation and/or in these terms and conditions or CCC's standard operating procedures, whether such writing is prepared prior to, simultaneously with or subsequent to the Order Confirmation, and whether such writing appears on a copy of the Order Confirmation or in a separate instrument.

    8.5. The licensing transaction described in the Order Confirmation document shall be governed by and construed under the law of the State of New York, USA, without regard to the principles thereof of conflicts of law. Any case, controversy, suit, action, or proceeding arising out of, in connection with, or related to such licensing transaction shall be brought, at CCC's sole discretion, in any federal or state court located in the County of New York, State of New York, USA, or in any federal or state court whose geographical jurisdiction covers the location of the Rightsholder set forth in the Order Confirmation. The parties expressly submit to the personal jurisdiction and venue of each such federal or state court.If you have any comments or questions about the Service or Copyright Clearance Center, please contact us at 978-750-8400 or send an e-mail to support@copyright.com.

v 1.1

Bibliography

[1] Adami, S., Kaiser, J., Adams, N. A., and Bermejo-Moreno, I. “Numerical modeling of shock waves in biomedicine”. In: *Center for Turbulence Research Proceedings of the Summer Program 2016*. 2016.

[2] Adami, S. “Modeling and Simulation of Multiphase Phenomena with Smoothed Particle Hydrodynamics”. PhD Thesis. Technical University of Munich, 2014.

[3] Allaire, G., Clerc, S., and Kokh, S. “A five-equation model for the simulation of interfaces between compressible fluids”. In: *Journal of Computational Physics* 181.2 (2002), pp. 577–616. ISSN: 00219991. DOI: 10.1006/jcph.2002.7143.

[4] Allen, S. M. and Cahn, J. W. “A microscopic theory for antiphase boundary motion and its application to antiphase domain coarsening”. In: *Acta Metallurgica* 27 (1979), pp. 1085–1095.

[5] Almgren, R. “Variational Algorithms and Pattern Formation in Dendritic Solidification”. In: *J. Comput. Phys.* 106.2 (1993), pp. 337–354. ISSN: 10902716. DOI: 10.1016/S0021-9991(83)71112-5.

[6] Anderson, D. M., McFadden, G. B., and Wheeler, A. A. “A phase-field model of solidification with convection”. In: *Physica D* 135 (2000), pp. 175–194. ISSN: 01672789. DOI: 10.1016/S0167-2789(99)00109-8.

[7] Aslam, T., Luo, S., and Zhao, Z. “A static PDE approach for multidimensional extrapolation using fast sweeping methods”. In: *SIAM J. Sci. Comput.* 36.6 (2014), A2907–A2928. ISSN: 10957200. DOI: 10.1137/140956919.

[8] Beckermann, C., Diepers, H. J., Steinbach, I., Karma, A., and Tong, X. “Modeling Melt Convection in Phase-Field Simulations of Solidification”. In: *J. Comput. Phys.* 154 (1999), pp. 468–496. ISSN: 00219991. DOI: 10.1006/jcph.1999.6323.

[9] Bendahmane, M., Bürger, R., Baier, R. R., and Schneider, K. “Adaptive multiresolution schemes with local time stepping for two-dimensional degenerate reaction-diffusion systems”. In: *Appl. Numer. Math.* 57.7 (2009), pp. 1668–1692.

[10] Ben-Jacob, E. and Garik, P. “The formation of patterns in non-equilibrium growth”. In: *Nature* 343.6258 (1990), pp. 523–530. ISSN: 00280836. DOI: 10.1038/343523a0.

[11] Boettinger, W. J., Warren, J. A., Beckermann, C., and Karma, A. “Phase-field simulation of solidification”. In: *Annual Review of Materials Science* 32 (2002), pp. 163–194. ISSN: 00846600. DOI: 10.1146/annurev.matsci.32.101901.155803.

[12] Cahn, J. W. and Hilliard, J. E. “Free energy of a nonuniform system. I. Interfacial Free Energy”. In: *J. Chem. Phys.* 28.2 (1958), pp. 258–267.

[13] Carslaw, H. S. and Jaeger, J. C., eds. *Conduction of heat in solids*. Oxford University Press, 1959.

[14] Chen, H., Min, C., and Gibou, F. “A numerical scheme for the Stefan problem on adaptive Cartesian grids with supralinear convergence rate”. In: *J. Comput. Phys.* 228.16 (2009), pp. 5803–5818. ISSN: 00219991. DOI: 10.1016/j.jcp.2009.04.044. URL: http://dx.doi.org/10.1016/j.jcp.2009.04.044.

[15] Chen, S., Merriman, B., Smereka, P., and Osher, S. “A simple level set method for Stefan problems”. In: *J. Comput. Phys.* 135 (1997), pp. 8–29.

[16] Cohen, A., Kaber, S., Müller, S., and Postel, M. “Fully adaptive multiresolution finite volume schemes for conservation laws”. In: *Math. Comput* 72.241 (2001), pp. 183–225. URL: http://www.ams.org/mcom/2003-72-241/S0025-5718-01-01391-6/.

[17] Coquel, F., Nguyen, Q. L., Postel, M., and Tran, Q. H. “Local time stepping applied to implicit-explicit methods for hyperbolic systems”. In: *Multiscale Model. Simul.* 8.2 (2010), pp. 540–570. DOI: 10.1137/070708500.

[18] Criscione, A., Kintea, D., Tuković, Ž., Jakirlić, S., Roisman, I. V., and Tropea, C. “Crystallization of supercooled water: A level-set-based modeling of the dendrite tip velocity”. In: *Int. J. Heat Mass Transf.* 66 (2013), pp. 830–837. ISSN: 00179310.

[19] Deiterding, R., Domingues, M. O., Gomes, S. M., and Schneider, K. “Comparison of adaptive multiresolution and adaptive mesh refinement applied to simulations of the compressible Euler equations”. In: *J. Sci. Comput.* 38.5 (2016), pp. 173–193.

[20] Desjardins, O., Moureau, V., and Pitsch, H. “An accurate conservative level set/ghost fluid method for simulating turbulent atomization”. In: *Journal of Computational Physics* 227.18 (2008), pp. 8395–8416. ISSN: 00219991. DOI: 10.1016/j.jcp.2008.05.027. URL: http://linkinghub.elsevier.com/retrieve/pii/S0021999108003112.

[21] Domingues, M. O., Gomes, S. M., Roussel, O., and Schneider, K. “Space – time adaptive multiresolution methods for hyperbolic conservation laws : Applications to compressible Euler equations”. In: *Appl. Numer. Math.* 59.9 (2009), pp. 2303–2321. ISSN: 0168-9274. DOI: 10.1016/j.apnum.2008.12.018.

[22] Faghri, A. and Zhang, Y. *Fundamentals of Multiphase Heat Transfer and Flow*. Springer Nature Switzerland, 2020.

[23] Fedkiw, R. P., Aslam, T. D., Merriman, B., and Osher, S. “A Non-Oscillatory Eulerian Approach to Interfaces in Multimaterial Flows (The Ghost Fluid Method)”. In: *J. Comput. Phys.* 152.2 (1999), pp. 457–492.

[24] Fleischmann, N., Adami, S., and Adams, N. A. “A shock-stable modification of the HLLC Riemann solver with reduced numerical dissipation”. In: *Journal of Computational Physics* (2020), p. 109762. ISSN: 0021-9991. DOI: https://doi.org/10.1016/j.jcp.2020.109762. URL: http://www.sciencedirect.com/science/article/pii/S0021999120305362.

[25] Fu, L., Hu, X. Y., and Adams, N. A. “A family of high-order targeted ENO schemes for compressible-fluid simulations”. en. In: *Journal of Computational Physics* 305 (2016), pp. 333–359. ISSN: 10902716. DOI: 10.1016/j.jcp.2015.10.037. URL: http://linkinghub.elsevier.com/retrieve/pii/S0021999115007147.

[26] Fu, L., Hu, X. Y., and Adams, N. A. “Single-step reinitialization and extending algorithms for level-set based multi-phase flow simulations”. In: *Computer Physics Communications* 221.September (2017), pp. 63–80. ISSN: 00104655. DOI: 10.1016/j.cpc.2017.08.002. URL: http://dx.doi.org/10.1016/j.cpc.2017.08.002.

[27] Furukawa, Y. and Shimada, W. “Three-dimensional pattern formation during growth of ice dendrites - its relation to universal law of dendritic growth”. In: *J. Cryst. Growth* 128 (1993), pp. 234–239. ISSN: 00220248. DOI: 10.1016/0022-0248(93)90325-Q.

[28] Gaoyang, M., Lingda, X., Chunming, W., Ping, J., and Guoli, Z. “Two-dimensional phase-field simulations of competitive dendritic growth during laser welding”. In: *Mater. Design* 181 (2019), p. 107980.

[29] Garrick, D. P., Owkes, M., and Regele, J. D. “A finite-volume HLLC-based scheme for compressible interfacial flows with surface tension”. In: *J. Comput. Phys.* 339 (2017), pp. 46–67. ISSN: 10902716. DOI: 10.1016/j.jcp.2017.03.007. URL: http://dx.doi.org/10.1016/j.jcp.2017.03.007.

[30] Ge, Z., Loiseau, J. C., Tammisola, O., and Brandt, L. “An efficient mass-preserving interface-correction level set/ghost fluid method for droplet suspensions under depletion forces”. In: *Journal of Computational Physics* 353 (2018), pp. 435–459. ISSN: 10902716. DOI: 10.1016/j.jcp.2017.10.046. arXiv: 1701.07385. URL: https://doi.org/10.1016/j.jcp.2017.10.046.

[31] Gibou, F., Fedkiw, R., Caflisch, R., and Osher, S. “A level set approach for the numerical simulation of dendritic growth”. In: *J. Sci. Comput.* 19.1 (2003), pp. 183–199. ISSN: 0885-7474.

[32] Gibou, F., Fedkiw, R., and Osher, S. “A review of level-set methods and some recent applications”. In: *Journal of Computational Physics* 353 (2018), pp. 82–109. DOI: 10.1016/j.jcp.2017.10.006. URL: www.elsevier.com/locate/jcp.

[33] Glicksman, M. E., Schaefer, R. J., and Ayers, J. D. “Dendritic growth-A test of theory”. In: *Metallurgical Transactions A* 7.11 (1976), pp. 1747–1759. ISSN: 03602133. DOI: 10.1007/BF03186673.

[34] Glimm, J., Grove, J., Li, X. L., Shyue, K. M., Zeng, Y. N., and Zhange, Q. “Three Dimensional Front Tracking, Communication”. In: *SIAM J. Sci. Comput.* 19 (1998), pp. 703–727.

[35] Gomes, A. K. F., Domingues, M. O., Schneider, K., Mendes, O., and Deiterding, R. “An adaptive multiresolution method for ideal magnetohydrodynamics using divergence cleaning with parabolic-hyperbolic correction”. In: *Appl. Numer. Math.* 95 (2015), pp. 199–213. DOI: 10.1016/j.apnum.2015.01.007.

[36] Gottlieb, S. and Shu, C.-W. “Total variation diminishing Runge-Kutta schemes”. In: *Math. Comput.* 67.221 (1998), pp. 73–85.

[37] Groot, R. D. “Second order front tracking algorithm for Stefan problem on a regular grid”. In: *J. Comput. Phys.* 372 (2018), pp. 956–971.

[38] Guildenbecher, D. R., López-Rivera, C., and Sojka, P. E. “Secondary Atomization”. en. In: *Exp. Fluids* 46.3 (Mar. 2009), pp. 371–402. ISSN: 0723-4864, 1432-1114. DOI: 10.1007/s00348-008-0593-2. (Visited on 08/05/2016).

[39] Guo, Z. and Lin, P. “A thermodynamically consistent phase-field model for two-phase flows with thermocapillary effects”. In: *J. Fluid Mech.* 766 (2015), pp. 226–271. DOI: 10.1017/jfm.2014.696. eprint: 1401.5793.

[40] Han, L. H., Hu, X. Y., and Adams, N. A. “Adaptive multi-resolution method for compressible multi-phase flows with sharp interface model and pyramid data structure”. In: *J. Comput. Phys.* 262 (2014), pp. 131–152. ISSN: 00219991. DOI: 10.1016/j.jcp.2013.12.061.

[41] Han, L. H., Indinger, T., Hu, X. Y., and Adams, N. A. “Wavelet-based adaptive multi-resolution solver on heterogeneous parallel architecture for computational fluid dynamics”. en. In: *Computer Science - Research and Development*. Vol. 26. 3-4. 2011, pp. 197–203. DOI: 10.1007/s00450-011-0167-z. URL: http://link.springer.com/10.1007/s00450-011-0167-z%20https://link.springer.com/content/pdf/10.1007%7B%5C%%7D2Fs00450-011-0167-z.pdf.

[42] Harten, A. “Adaptive Multiresolution Schemes for Shock Computations”. In: *J. Comput. Phys.* 115.2 (1994), pp. 319–338. ISSN: 00219991. DOI: 10.1006/jcph.1994.1199.

[43] Hawker, N. A. and Ventikos, Y. “Interaction of a strong shockwave with a gas bubble in a liquid medium: A numerical study”. In: *J. Fluid Mech.* 701 (2012), pp. 59–97. ISSN: 00221120. DOI: 10.1017/jfm.2012.132.

[44] Hejazialhosseini, B., Rossinelli, D., Bergdorf, M., and Koumoutsakos, P. “High order finite volume methods on wavelet-adapted grids with local time-stepping on multicore architectures for the simulation of shock-bubble interactions”. In: *J. Comput. Phys.* 229.22 (2010), pp. 8364–8383. ISSN: 00219991. DOI: 10.1016/j.jcp.2010.07.021.

[45] Hinze, J. O. “Critical speeds and sizes of liquid globules”. In: *Appl. Sci. Res.* 1 (1949), pp. 273–288.

[46] Hirt, C. W., Amsden, A. A., and Cook, J. L. “An arbitrary Lagrangian-Eulerian computing method for all flow speeds”. In: *Journal of Computational Physics* 14.3 (1974), pp. 227–253. ISSN: 10902716. DOI: 10.1016/0021-9991(74)90051-5.

[47] Hirt, C. W. and Nichols, B. D. “Volume of fluid (VOF) method for the dynamics of free boundaries”. In: *J. Comput. Phys.* 39.1 (1981), pp. 201–225.

[48] Hoppe, N., Winter, J., Adami, S., and Adams, N. “ALPACA - A level-set based sharp-interface solver for conservation laws”. In: *in preparation* (2020).

[49] Hsiang, L.-P. and Faeth, G. M. “Near-limit drop deformation and secondary breakup”. In: *International Journal of Multiphase Flow* 18.5 (1992), pp. 635–652. URL: http://www.sciencedirect.com/science/article/pii/030193229290036G.

[50] Hu, X. and Khoo, B. “An interface interaction method for compressible multifluids”. en. In: *Journal of Computational Physics* 198.1 (2004), pp. 35–64. ISSN: 00219991. DOI: 10.1016/j.jcp.2003.12.018. URL: http://linkinghub.elsevier.com/retrieve/pii/S0021999104000178.

[51] Hu, X., Khoo, B., Adams, N., and Huang, F. “A Conservative Interface Method for Compressible Flows”. en. In: *J. Comput. Phys.* 219.2 (Dec. 2006), pp. 553–578. ISSN: 00219991. DOI: 10.1016/j.jcp.2006.04.001. (Visited on 07/19/2016).

[52] Igra, D., Ogawa, T., and Takayama, K. “A parametric study of water column deformation resulting from shock wave loading”. In: *At. Sprays* 12 (2002), pp. 577–591. ISSN: 10445110. DOI: 10.1615/AtomizSpr.v12.i56.20.

[53] Igra, D. and Sun, M. “Shock—Water Column Interaction, from Initial Impact to Fragmentation Onset”. In: *AIAA J.* 48 (Dec. 2010), pp. 2763–2771.

[54] Igra, D. and Takayama, K. *A study of shock wave loading on a cylindrical water column*. Tech. rep. Institute of Fluid Science, Tohoku University, 2001, pp. 19–36.

[55] Igra, D. and Takayama, K. “Investigation of Aerodynamic Breakup of a Cylindrical Water Droplet”. In: *At. Sprays* 11 (2001), pp. 167–185.

[56] Igra, D. and Takayama, K. “Experimental investigation of two cylindrical water columns subjected to planar shock wave loading”. In: *J. Fluids Eng.* 125.2 (2003), pp. 325–331. ISSN: 00982202. DOI: 10.1115/1.1538628.

[57] Ireland, P. J. and Desjardins, O. “Toward liquid jet atomization in supersonic crossflows”. In: *ILASS Americas 28th Annual Conference on Liquid Atomization and Spray Systems*. 2016.

[58] Ivantsov, G. In: *Doklady Akademii Nauk SSSR* (1947), pp. 558–567.

[59] Jaafar, M. A., Rousse, D. R., Gibout, S., and Bédécarrats, J. P. “A review of dendritic growth during solidification: Mathematical modeling and numerical simulations”. In: *Renew. Sust. Energ. Rev.* 74.March 2016 (2017), pp. 1064–1069. ISSN: 18790690. DOI: 10.1016/j.rser.2017.02.050.

[60] Jiang, G.-S. and Shu. “Efficient Implementation of Weighted ENO Schemes”. In: *Journal of Computational Physics* 126 (1996), pp. 202–228.

[61] Johnsen, E. and Colonius, T. “Shock-induced collapse of a gas bubble in shockwave lithotripsy.” In: *The Journal of the Acoustical Society of America* 124.4 (2008), pp. 2011–20. ISSN: 1520-8524. DOI: 10.1121/1.2973229. URL: http://www.pubmedcentral.nih.gov/articlerender.fcgi?artid=2600620%7B%5C&%7Dtool=pmcentrez%7B%5C&%7Drendertype=abstract.

[62] Johnsen, E. and Colonius, T. “Numerical simulations of non-spherical bubble collapse”. en. In: *J. Fluid Mech.* 629 (2009), p. 231. ISSN: 0022-1120, 1469-7645. DOI: 10.1017/S0022112009006351. URL: http://www.journals.cambridge.org/abstract%7B%5C_%7DS0022112009006351.

[63] Juric, D. and Tryggvason, G. “A Front-Tracking Method for Dendritic Solidification”. In: *J. Comput. Phys.* 123 (1996), pp. 127–148.

[64] Kaiser, J. W. J., Adami, S., Akhatov, I. S., and Adams, N. A. “A semi-implicit conservative sharp-interface method for liquid-solid phase transition”. In: *International Journal of Heat and Mass Transfer* 155 (2020), p. 119800. ISSN: 0017-9310. DOI: 10.1016/j.ijheatmasstransfer.2020.119800. URL: https://doi.org/10.1016/j.ijheatmasstransfer.2020.119800.

[65] Kaiser, J. W. J., Hoppe, N., Adami, S., and Adams, N. A. “An adaptive local time-stepping scheme for multiresolution simulations of hyperbolic conservation laws”. In: *J. Comput. Phys. X* 4 (2019), p. 100038.

[66] Kaiser, J. W., Winter, J. M., Adami, S., and Adams, N. A. “Investigation of interface deformation dynamics during high-Weber number cylindrical droplet breakup”. In: *International Journal of Multiphase Flow* 132 (2020). ISSN: 03019322. DOI: 10.1016/j.ijmultiphaseflow.2020.103409.

[67] Kaiser, J. W. J., Adami, S., and Adams, N. A. “Three-Dimensional Direct Numerical Simulation of Shock-Induced Bubble Collapse Near Gelatin”. In: *Proceedings of the 11th International Symposium on Turbulence and Shear Flow Phenomena (TSFP11),* 2019.

[68] Kaiser, J. W., Adami, S., and Adams, N. A. “Direct numerical simulation of shock-induced drop breakup with a sharp-interface-method”. In: *Proceedings of the 10th International Symposium on Turbulence and Shear Flow Phenomena (TSFP10)*. 2017.

[69] Kapila, A. K., Menikoff, R., Bdzil, J. B., Son, S. F., and Stewart, D. S. “Two-phase modeling of deflagration-to-detonation transition in granular materials: Reduced equations”. In: *Physics of Fluids* 13.10 (2001), pp. 3002–3024. ISSN: 10706631. DOI: 10.1063/1.1398042.

[70] Karma, A. and Rappel, W.-J. “Phase-field method for computationally efficient modeling of solidification with arbitrary interface kinetrics”. In: *Phys. Rev. E* 53 (1996). ISSN: 1060-6823.

[71] Khosla, S., Smith, C. E., and Throckmorton, R. P. “Detailed Understanding of Drop Atomization by Gas Crossflow Using the Volume of Fluid Method”. In: *19th Annual Conference on Liquid Atomization and Spray Systems (ILASS-Americas), Toronto, Canada*. 2006. (Visited on 08/17/2016).

[72] Kim, Y.-T., Goldenfeld, N., and Dantzig, J. “Computation of Dendritic Microstructures using a Level Set Method”. In: *Phys. Rev. E* 62.2 (2000), pp. 2471–2474.

[73] Kobayashi, K., Kodama, T., and Takahira, H. “Shock wave–bubble interaction near soft and rigid boundaries during lithotripsy: numerical analysis by the improved ghost fluid method”. In: *Phys. Med. Biol.* 56.19 (2011), pp. 6421–6440. ISSN: 0031-9155, 1361-6560. DOI: 10.1088/0031-9155/56/19/016. URL: http://stacks.iop.org/0031-9155/56/i=19/a=016?key=crossref.91e5f69265a8f30154666c8a0123b4f2.

[74] Kobayashi, R. “Modeling and numerical simulations of dendritic crystal growth”. In: *Physica D* 63 (1993), pp. 410–423. ISSN: 01672789. DOI: 10.1016/0167-2789(93)90120-P.

[75] Langer, J. S. and Müller-Krumbhaar, H. “Theory of dendritic growth-I. Elements of a stability analysis”. In: *Acta Metall.* 26.11 (1978), pp. 1681–1687. ISSN: 00016160. DOI: 10.1016/0001-6160(78)90078-0.

[76] Langer, J. S. and Müller-Krumbhaar, H. “Theory of dendritic growth-II. Instabilities in the limit of vanishing surface tension”. In: *Acta Metall.* 26.11 (1978), pp. 1689–1695. ISSN: 00016160. DOI: 10.1016/0001-6160(78)90079-2.

[77] Langer, J. S. and Müller-Krumbhaar, J. “Stability effects in dendritic crystal growth”. In: *J. Cryst. Growth* 42.C (1977), pp. 11–14. ISSN: 00220248. DOI: 10.1016/0022-0248(77)90171-3.

[78] Lauer, E., Hu, X. Y., Hickel, S., and Adams, N. A. “Numerical Investigation of Collapsing Cavity Arrays”. en. In: *Phys. Fluids* 24.5 (2012), p. 052104. ISSN: 10706631. DOI: 10.1063/1.4719142. (Visited on 08/10/2016).

[79] LeVeque, R. J. *Finite Volume Methods for Hyperbolic Problems*. Cambridge, U.K.: Cambridge University Press, 2002.

[80] Ling, K. and Tao, W. Q. “A sharp-interface model coupling VOSET and IBM for simulations on melting and solidification”. In: *Comput. Fluids* 178 (2019), pp. 113–131.

[81] Luo, J., Hu, X., and Adams, N. “A Conservative Sharp Interface Method for Incompressible Multiphase Flows”. en. In: *J. Comput. Phys.* 284 (Mar. 2015), pp. 547–565. ISSN: 00219991. DOI: 10.1016/j.jcp.2014.12.044. (Visited on 08/18/2016).

[82] Meng, J. C. and Colonius, T. “Numerical simulations of the early stages of high-speed droplet breakup”. In: *Shock Waves* 25 (2015), pp. 339–414.

[83] Meng, J. C. and Colonius, T. “Numerical simulation of the aerobreakup of a water droplet”. In: *J. Fluid Mech.* 835 (2018), pp. 1108–1135. DOI: 10.1017/jfm.2017.804.

[84] Monaghan, J. J. “Smoothed particle hydrodynamics and its diverse applications”. In: *Annual Review of Fluid Mechanics* 44 (2011), pp. 323–346. ISSN: 00664189. DOI: 10.1146/annurev-fluid-120710-101220.

[85] Monaghan, J. J., Huppert, H. E., and Worster, M. G. “Solidification using smoothed particle hydrodynamics”. In: *Journal of Computational Physics* 206.2 (2005), pp. 684–705. ISSN: 00219991. DOI: 10.1016/j.jcp.2004.11.039.

[86] Müller, S. and Stiriba, Y. “Fully Adaptive Multiscale Schemes for Conservation Laws Employing Locally Varying Time Stepping”. In: *J. Sci. Comput.* 30.3 (2007), pp. 493–531. ISSN: 0885-7474. DOI: 10.1007/s10915-006-9102-z.

[87] Müller-Krumbhaar, H. and Langer, J. S. “Theory of dendritic growth-III. Effects of surface tension”. In: *Acta Metall.* 26.11 (1978), pp. 1697–1708. ISSN: 00016160. DOI: 10.1016/0001-6160(78)90080-9.

[88] Nestler, B., Wheeler, A. A., Ratke, L., and Stöcker, C. “Phase-field model for solidification of a monotectic alloy with convection”. In: *Physica D* 141 (2000), pp. 133–154. ISSN: 01672789. DOI: 10.1016/S0167-2789(00)00035-X.

[89] Neumann, J. von and Richtmyer, R. D. “A method for the numerical calculation of hydrodynamic shocks”. In: *Journal of Applied Physics* 21.3 (1950), pp. 232–237. ISSN: 00218979. DOI: 10.1063/1.1699639.

[90] Nonomura, T., Kitamura, K., and Fujii, K. “A simple interface sharpening technique with a hyperbolic tangent function applied to compressible two-fluid modeling”. In: *J. Comput. Phys.* 258 (2014), pp. 95–117. ISSN: 10902716. DOI: 10.1016/j.jcp.2013.10.021. URL: http://dx.doi.org/10.1016/j.jcp.2013.10.021.

[91] Nourgaliev, R., Liou, M.-S., and Theofanous, T. “Numerical prediction of interfacial instabilities: Sharp interface method (SIM)”. In: *Journal of Computational Physics* 227.8 (2008), pp. 3940–3970. ISSN: 00219991. DOI: 10.1016/j.jcp.2007.12.008. URL: http://linkinghub.elsevier.com/retrieve/pii/S0021999107005566.

[92] Osher, S. and Sanders, R. “Numerical Approximations to Nonlinear Conservation Laws With Locally Varying Time and Space Grids”. In: *Math. Comput.* 41.164 (1983), pp. 321–336.

[93] Osher, S. and Sethian, J. A. “Fronts Propagating With Curvature Dependent Speed: Algorithms Based on Hamilton-Jacobi Formulations”. In: *J. Comput. Phys.* 79.1988 (1988), pp. 12–49.

[94] Pan, S., Han, L., Hu, X., and Adams, N. A. “A conservative interface-interaction method for compressible multi-material flows”. In: *Journal of Computational Physics* 371 (2018), pp. 870–895. ISSN: 10902716. DOI: 10.1016/j.jcp.2018.02.007. arXiv: 1704.00519. URL: http://arxiv.org/abs/1704.00519.

[95] Pan, S., Lyu, X., Hu, X. Y., and Adams, N. A. “High-order time-marching reinitialization for regional level-set functions”. In: *Journal of Computational Physics* 354 (2018), pp. 311–319. ISSN: 10902716. DOI: 10.1016/j.jcp.2017.10.054. URL: www.elsevier.com/locate/jcp.

[96] Patel, P. and Theofanous, T. “Hydrodynamic fragmentation of drops”. In: *J. Fluid Mech.* 103 (1981), pp. 207–223.

[97] Paula, T., Adami, S., and Adams, N. A. “Analysis of the early stages of liquid-water-drop explosion by numerical simulation”. In: *Physical Review Fluids* 4.4 (2019). ISSN: 2469990X. DOI: 10.1103/PhysRevFluids.4.044003.

[98] Pieper, J. L., Schranner, F. S., and Adams, N. A. “Sharp-Interface Simulations of Heat-Driven Flows with Marangoni Effect”. In: *Proceedings of the 10th International Symposium on Turbulence and Shear Flow Phenomena (TSFP10)*. 2017.

[99] Pilch, M. and Erdmann, C. A. “Use of breakup time data and velocity history data to predict the maximum size of stable fragments for acceleration-induced breakup of a liquid drop”. In: *International Journal of Multiphase Flow* 13.6 (1987), pp. 741–757.

[100] Ramanuj, V. and Sankaran, R. “High Order Anchoring and Reinitialization of Level Set Function for Simulating Interface Motion”. In: *J. Sci. Comput.* 81.3 (2019), pp. 1963–1986. ISSN: 15737691. DOI: 10.1007/s10915-019-01076-0. URL: https://doi.org/10.1007/s10915-019-01076-0.

[101] Ramanuj, V., Sankaran, R., and Radhakrishnan, B. “A sharp interface model for deterministic simulation of dendrite growth”. In: *Comput. Mater. Sci.* 169.May (2019), p. 109097. ISSN: 09270256. DOI: 10.1016/j.commatsci.2019.109097. URL: https://doi.org/10.1016/j.commatsci.2019.109097.

[102] Rauschenberger, P., Criscione, A., Eisenschmidt, K., Kintea, D., Jakirlić, S., Tuković, Ž., Roisman, I. V., Weigand, B., and Tropea, C. “Comparative assessment of Volume-of-Fluid and Level-Set methods by relevance to dendritic ice growth in supercooled water”. In: *Comput. Fluids* 79 (2013), pp. 44–52. ISSN: 00457930. DOI: 10.1016/j.compfluid.2013.03.010.

[103] Roe, P. L. “Approximate Riemann Solvers, Parameter Vectors, and Difference Schemes”. In: *J. Comput. Phys.* 43.2 (1981), pp. 357–372. (Visited on 08/12/2016).

[104] Roosen, A. R. and Taylor, J. E. “Modeling Crystal Growth in a Diffusion Field Using Fully Faceted Interfaces”. In: *J. Comput. Phys.* 114 (1994), pp. 113–128. ISSN: 00219991. DOI: 10.1006/jcph.1994.1153.

[105] Rossinelli, D., Hejazialhosseini, B., Hadjidoukas, P., Bekas, C., Curioni, A., Bertsch, A., Futral, S., Schmidt, S. J., Adams, N. A., and Koumoutsakos, P. “11 PFLOP/s Simulations of Cloud Cavitation Collapse”. In: *Proceedings of the International Conference on High Performance Computing, Networking, Storage and Analysis*. SC ’13 3. Denver, Colorado: ACM, 2013, 3:1–3:13. DOI: 10.1145/2503210.2504565. URL: http://doi.acm.org/10.1145/2503210.2504565.

[106] Rossinelli, D., Hejazialhosseini, B., Spampinato, D. G., and Koumoutsakos, P. “Multicore/multi-gpu accelerated simulations of multiphase compressible flows using wavelet adapted grids”. In: *J. Sci. Comput.* 33.2 (2011), pp. 512–540.

[107] Roussel, O. and Schneider, K. “Adaptive multiresolution computations applied to detonations”. In: *Z. Phys. Chem.* 229.6 (2015), pp. 931–953.

[108] Roussel, O., Schneider, K., Tsigulin, A., and Bockhorn, H. “A conservative fully adaptive multiresolution algorithm for parabolic PDEs”. In: *J. Comput. Phys.* 188 (2003), pp. 493–523. DOI: 10.1016/S0021-9991(03)00189-X.

[109] Russo, G. and Smereka, P. “A Remark on Computing Distance Functions”. In: *J. Comput. Phys.* 163 (2000), pp. 51–67.

[110] Saurel, R. and Abgrall, R. “A Multiphase Godunov Method for Compressible Multifluid and Multiphase Flows”. In: *J. Comput. Phys.* 150.2 (1999), pp. 425–467.

[111] Saurel, R. and Pantano, C. “Diffuse-Interface Capturing Methods for Compressible Two-Phase Flows”. In: *Annual Review of Fluid Mechanics* 50 (2018), pp. 105–130. ISSN: 00664189. DOI: 10.1146/annurev-fluid-122316-050109.

[112] Schmidmayer, K., Petitpas, F., Daniel, E., Favrie, N., and Gavrilyuk, S. “A model and numerical method for compressible flows with capillary effects”. In: *J. Comput. Phys.* 334 (2017), pp. 468–496.

[113] Sembian, S., Liverts, M., Tillmark, N., and Apazidis, N. “Plane shock wave interaction with a cylindrical water column”. In: *Phys. Fluids* 28.5 (2016). ISSN: 10897666. DOI: 10.1063/1.4948274. URL: http://dx.doi.org/10.1063/1.4948274.

[114] Sethian, J. A. and Straint, J. “Crystal growth and dendritic solidification”. In: *J. Comput. Phys.* 98.2 (1992), pp. 231–253. ISSN: 10902716. DOI: 10.1016/0021-9991(92)90140-T.

[115] Shaikh, J., Bhardwaj, R., and Sharma, A. “ScienceDirect IUTAM Symposium on Multiphase flows with phase change: challenges and opportunities A Ghost Fluid Method based Sharp Interface Level Set Method for Evaporating Droplet”. In: *Procedia IUTAM* 15.15 (2015), pp. 124–131. ISSN: 2210-9838. DOI: 10.1016/j.piutam.2015.04.018. URL: www.sciencedirect.com.

[116] Shibkov, A. A., Zheltov, M. A., Korolev, A. A., Kazakov, A. A., and Leonov, A. A. “Crossover from diffusion-limited to kinetics-limited growth of ice crystals”. In: *J. Cryst. Growth* 285 (2005), pp. 215–227. ISSN: 00220248.

[117] Singer-Loginova, I. and Singer, H. M. “The phase field technique for modeling multiphase materials”. In: *Reports on Progress in Physics* 71.10 (2008). ISSN: 00344885. DOI: 10.1088/0034-4885/71/10/106501.

[118] Sman, R. van der. “Phase field simulations of ice crystal growth in sugar solutions”. In: *Int. J. Heat Mass Transf.* 95 (2016), pp. 153–161.

[119] Sod, G. A. “A survey of several finite difference methods for systems of nonlinear hyperbolic conservation laws”. In: *J. Comput. Phys.* 27.1 (1978), pp. 1–31. ISSN: 10902716. DOI: 10.1016/0021-9991(78)90023-2.

[120] Stride, E. P., Coussios, C. C., and Wells, P. N. T. “Cavitation and contrast: the use of bubbles in ultrasound imaging and therapy”. In: *P. I. Mech. Eng. H* 224.2 (2010), pp. 171–191. ISSN: 0954-4119, 2041-3033. DOI: 10.1243/09544119JEIM622. URL: http://sdj.sagepub.com/lookup/10.1243/09544119JEIM622.

[121] Sun, D., Pan, S., Han, Q., and Sun, B. “Numerical simulation of dendritic growth in directional solidification of binary alloys using a lattice Boltzmann scheme”. In: *Int. J. Heat Mass Transf.* 103 (2016), pp. 821–831.

[122] Sun, D., Wang, Y., Yu, H., and Han, Q. “A lattice Boltzmann study on dendritic growth of a binary alloy in the presence of melt convection”. In: *Int. J. Heat Mass Transf.* 123 (2018), pp. 213–226.

[123] Sun, D., Zhu, M., Wang, J., and Sun, B. “Lattice Boltzmann modeling of bubble formation and dendritic growth in solidification of binary alloys”. In: *Int. J. Heat Mass Transf.* 94 (2016), pp. 474–487.

[124] Sussman, M., Smereka, P., and Osher, S. “A Level Set Approach for Computing Solutions to Incompressible Two-Phase Flow”. In: *J. Comput. Phys.* 114 (1994), pp. 146–159.

[125] Tan, L. and Zabaras, N. “A level set simulation of dendritic solidification of multi-component alloys”. In: *J. Comput. Phys.* 221.1 (2007), pp. 9–40. ISSN: 10902716. DOI: 10.1016/j.jcp.2006.06.003.

[126] Tan, L. and Zabaras, N. “Modeling the growth and interaction of multiple dendrites in solidification using a level set method”. In: *J. Comput. Phys.* 226 (2007), pp. 131–155. ISSN: 00219991. DOI: 10.1016/j.jcp.2007.03.023.

[127] Tan, L. and Zabaras, Z. “A level set simulation of dendritic solidification with combined features of front-tracking and fixed-domain methods”. In: *J. Comput. Phys.* 211 (2006), pp. 36–63. ISSN: 00219991. DOI: 10.1016/j.jcp.2005.05.013.

[128] Terashima, H. and Tryggvason, G. “A front-tracking/ghost-fluid method for fluid interfaces in compressible flows”. In: *J. Comput. Phys.* 228.11 (2009), pp. 4012–4037. ISSN: 10902716. DOI: 10.1016/j.jcp.2009.02.023. URL: http://dx.doi.org/10.1016/j.jcp.2009.02.023.

[129] Theillard, M., Gibou, F., and Pollock, T. “A Sharp Computational Method for the Simulation of the Solidification of Binary Alloys”. In: *J. Sci. Comput.* 63 (2015), pp. 330–354. ISSN: 08857474. DOI: 10.1007/s10915-014-9895-0.

[130] Theofanous, T. G. and Li, G. J. “On the physics of aerobreakup”. In: *Physics of Fluids* 20.5 (2008), p. 052103. ISSN: 1070-6631. DOI: 10.1063/1.2907989. URL: http://aip.scitation.org/doi/10.1063/1.2907989.

[131] Theofanous, T. G., Li, G. J., and Dinh, T. N. “Aerobreakup in Rarefied Supersonic Gas Flows”. en. In: *Journal of Fluids Engineering* 126.4 (2004), p. 516. ISSN: 00982202. DOI: 10.1115/1.1777234. URL: http://fluidsengineering.asmedigitalcollection.asme.org/article.aspx?articleid=1430001.

[132] Theofanous, T. “Aerobreakup of Newtonian and Viscoelastic Liquids”. en. In: *Annual Review of Fluid Mechanics* 43.1 (2011), pp. 661–690. ISSN: 0066-4189, 1545-4479. DOI: 10.1146/annurev-fluid-122109-160638. URL: http://www.annualreviews.org/doi/abs/10.1146/annurev-fluid-122109-160638.

[133] Theofanous, T., Mitkin, V. V., Ng, C. L., Chang, C. H., Deng, X., and Sushchikh, S. “The physics of aerobreakup. Part II. Viscous liquids”. en. In: *Phys. Fluids* 24 (2012).

[134] Tonks, M. R. and Aagesen, L. K. “The Phase Field Method: Mesoscale Simulation Aiding Material Discovery”. In: *Annual Review of Materials Research* 49 (2019), pp. 79–102. ISSN: 15317331. DOI: 10.1146/annurev-matsci-070218-010151.

[135] Toro, E. *Riemann Solvers and Numerical Methods for Fluid Dynamics: A Practical Introduction*. Berlin: Springer, 2009.

[136] Villermaux, E. “Fragmentation”. In: *Annu. Rev. Fluid Mech.* 39 (2007), pp. 419–446.

[137] Wan, Q., Deiterding, R., and Eliasson, V. “Numerical investigation of shock wave attenuation in channels using water obstacles”. In: *Multiscale and Multidisciplinary Modeling, Experiments and Design* 2 (2019), pp. 159–173. ISSN: 2520-8179. URL: https://doi.org/10.1007/s41939-018-00041-y.

[138] Wang, B., Xiang, G., and Hu, X. Y. “An incremental-stencil WENO reconstruction for simulation of compressible two-phase flows”. In: *Int. J. Multiphase Flow* 104 (2018), pp. 20–31.

[139] Winter, J. M., Kaiser, J. W. J., Adami, S., and Adams, N. A. “Numerical Investigation of 3D Drop-Breakup Mechanisms Using a Sharp Interface Level-Set Method”. In: *Proceedings of the 11th International Symposium on Turbulence and Shear Flow Phenomena (TSFP11)*. 2019.

[140] Woodward, P. and Colella, P. “The numerical simulation of two-dimensional fluid flow with strong shocks”. In: *J. Comput. Phys.* 54.1 (1984), pp. 115–173. ISSN: 10902716. DOI: 10.1016/0021-9991(84)90142-6.

[141] Xiang, G. and Wang, B. “Numerical study of a planar shock interacting with a cylindrical water column embedded with an air cavity”. In: *J. Fluid Mech.* 825 (2017), pp. 825–852. ISSN: 14697645. DOI: 10.1017/jfm.2017.403.

[142] Xing, H., Ankit, K., Dong, X., Chen, H., and Jin, K. “Growth direction selection of tilted dendritic arrays in directional solidification over a wide range of pulling velocity: A phase-field study”. In: *Int. J. Heat Mass Transf.* 117 (2018), pp. 1107–1114. ISSN: 00179310. DOI: 10.1016/j.ijheatmasstransfer.2017.10.086. URL: https://doi.org/10.1016/j.ijheatmasstransfer.2017.10.086.

[143] Yang, H. and Peng, J. “Numerical study of the shear-thinning effect on the interaction between a normal shock wave and a cylindrical liquid column”. In: *Phys. Fluids* 31.4 (2019). ISSN: 10897666. DOI: 10.1063/1.5083633. URL: http://dx.doi.org/10.1063/1.5083633.

[144] Yang, W., Jia, M., Che, Z., Sun, K., and Wang, T. “Transitions of deformation to bag breakup and bag to bag-stamen breakup for droplets subjected to a continuous gas flow”. In: *Inter. J. Heat Mass Transf.* 111 (2017), pp. 884–894. ISSN: 00179310. DOI: 10.1016/j.ijheatmasstransfer.2017.04.012. URL: http://dx.doi.org/10.1016/j.ijheatmasstransfer.2017.04.012.

[145] Ye, Q. and Chen, S. “Numerical Modeling of Metal-Based Additive Manufacturing Using Level Set Methods”. In: *Journal of Manufacturing Science and Engineering* 139.7 (2017), p. 071019. ISSN: 1087-1357. DOI: 10.1115/1.4036290. URL: http://manufacturingscience.asmedigitalcollection.asme.org/article.aspx?doi=10.1115/1.4036290.

[146] Zeng, Q., Gonzalez-Avila, S. R., Dijkink, R., Koukouvinis, P., Gavaises, M., and Ohl, C.-D. “Wall shear stress from jetting cavitation bubbles”. In: *J. Fluid Mech.* 846 (2018), pp. 341–355. ISSN: 14697645. DOI: 10.1017/jfm.2018.286.

[147] Zhang, M., Zhang, H., and Zheng, L. “Application of smoothed particle hydrodynamics method to free surface and solidification problems”. In: *Numerical Heat Transfer, Part A: Applications: An International Journal of Computation and Methodology* 52.4 (2007), pp. 299–314.